Doctoral theses at NTNU, 2022:274

Elisabeth Thronsen

The effect of natural ageing on clustering and precipitation in heat-treatable aluminium alloys

An advanced TEM study

Doctoral thesis

NTNU
Norwegian University of Science and Technology
Thesis for the Degree of
Philosophiae Doctor

NTNU
Norwegian University of
Science and Technology

Elisabeth Thronsen

The effect of natural ageing on clustering and precipitation in heat-treatable aluminium alloys

An advanced TEM study

Thesis for the Degree of Philosophiae Doctor

Trondheim, September 2022

Norwegian University of Science and Technology
Department of Physics
Faculty of Natural Sciences

NTNU
Norwegian University of
Science and Technology

NTNU
Norwegian University of Science and Technology

Thesis for the Degree of Philosophiae Doctor

Department of Physics
Faculty of Natural Sciences

ISBN 978-82-326-6788-8 (printed ver.)
ISBN 978-82-326-5977-7 (electronic ver.)
ISSN 1503-8181 (printed ver.)
ISSN 2703-8084 (online ver.)

Doctoral theses at NTNU, 2022:274

Printed by NTNU Grafisk senter

Abstract

Heat-treatable aluminium (Al) alloys gain their strength from the formation of nanoscale, metastable precipitates upon artificial ageing at elevated temperatures. The precipitates are preceded by solute clusters or Guinier-Preston (GP) zones formed in the initial stages of artificial ageing or during natural ageing at room temperature prior to artificial ageing. Understanding the atomic structure of both clusters, GP zones and precipitates and how they evolve is important for developing new alloys and also for modelling the mechanical properties of Al alloys. One of the most powerful methods for characterising materials on the nanoscale is transmission electron microscopy (TEM). TEM was the main characterisation tool in this work. In particular, atomically resolved high-angle annular dark-field (HAADF)-scanning transmission electron microscopy (STEM) and scanning precession electron diffraction (SPED) have been the main characterisation methods to investigate the materials. HAADF-STEM enables incoherent imaging of crystal lattices, with the advantage of yielding a contrast that increases monotonously with the atomic number. In SPED, a precessing probe is scanned across a region of interest in the sample and a diffraction pattern is recorded for each probe position, yielding a four-dimensional dataset. With this technique, information about the distribution of precipitate phases is attainable and regions up to μm^2 can be probed. This enables phase mapping of precipitates or clusters and gives better statistics of the relative phase fraction in comparison to HAADF-STEM. Such datasets require more sophisticated data analysis as compared to traditional image analysis.

This thesis contains six research papers. The first three concerns the GP zones forming in Al-Zn-Mg alloys during natural ageing and their influence on artificial ageing. The next two papers are related to the effect of heavy deformation and natural ageing on precipitation in an Al-Cu-Mg-Si alloy. A majority of the publications relies on analysing SPED data and the last paper is dedicated to comparing data analysis approaches for phase mapping of precipitates in Al alloys by SPED.

Paper I presents the first HAADF-STEM images revealing the atomic structure of the GPI zones in Al-Zn-Mg alloys. Atomic models were prepared based on the images and both density functional theory calculations and electron diffraction simulations verified the models. A unit with high Zn/Mg ratio was found to be the fundamental building block for all GPI zones. The unit is referred to as a truncated cube octahedron (TCO) since the atomic configuration can be explained as a partial substitution of Mg and Zn on the Al lattice and its surrounding TCO shell. The unit was found to connect along different Al directions to form larger zones and the individual zones exhibited variations in atomic structure.

Paper II presents the first experimental PED patterns of single GPI zones in Al-Zn-Mg alloys. The PED patterns were compared with multislice electron diffraction simulations from different density functional theory relaxed models. The study provided evidence that the octahedral site of the central column in the TCO unit was sometimes occupied.

Paper III concerns the evolution of precipitates from the naturally aged state, consisting of a dense distribution of GPI zones and a small population of η' precipitates, to the peak aged condition during artificial ageing. Upon the initial stages of artificial ageing, the hardness rapidly decreased. Based on APT, this condition had clusters of similar size and number density as in the naturally aged condition. HAADF-STEM revealed that the clusters in this condition showed less ordering as compared to the GPI zones in the naturally aged condition. The presence of η' also increased from 2% to 18%. The decrease in hardness was attributed to the η' precipitates and clusters in this condition contributing less to hardness as compared to the GPI zones in the naturally aged condition. In the peak aged condition η' co-existed with η_1, η_2 and T′ phases. The assumingly first PED pattern from a single T′ phase was presented.

Paper IV studies the effect of combined heavy pre-deformation and naturally ageing on the precipitation in an Al-Cu-Mg-Si alloy. SPED and HAADF-STEM enabled a detailed characterisation of the precipitates in the pre-deformed conditions. In the undeformed material, L phases and structural units of Guinier-Preston-Bagaryatsky zones were the only observed precipitates. The L phase was the dominant phase in the undistorted regions of the Al lattice in the pre-deformed conditions. In the vicinity of the deformation induced defects, the C and E phases were the dominant phases. The E phase had previously been reported, but its crystal structure was elucidated on in this work. This phase has was shown to nucleate preferentially on dislocations and has never been observed in undeformed 6xxx alloys.

Paper V investigates the effect of adding Fe to the Al-Cu-Mg-Si alloy in Paper V. The thermomechanical treatment consisted of naturally ageing, 80% pre-deformation, artificial ageing to peak age, 50% deformation before a short, final artificial ageing treatment. The Fe added alloy and the standard alloy were characterised both in the undeformed and deformed conditions. The presence of primary bcc α-AlFeSi particles were twice as high in the Fe added alloy as compared to the standard alloy. This caused a lower number density of precipitates in the undeformed condition. In the deformed conditions, SPED revealed that the addition of Fe affected the relative ratio of precipitates nucleated on deformation induced defects as compared to precipitates nucleated in the bulk. The precipitation in the Fe added alloy was more heterogeneous as compared to the precipitation in the standard alloy.

Paper VI is concerned with comparing different strategies for phase mapping of precipitates by SPED in Al alloys. The strategies included non-negative matrix factorisation, a vector analysis approach, template matching and artificial neural networks. A dataset was obtained from an Al-Cu-Mg-Li alloy containing T1 and θ' precipitates. These precipitates had different orientation relationships and morphologies and were thus discernible in images. A ground truth image was created and compared with the phase maps obtained from all four approaches. The goal of this work was to compare different strategies for phase mapping in terms of accuracy and reproducibility.

Preface

This thesis has been submitted to the Norwegian University of Science and Technology (NTNU) as a part of the fulfilment of the requirements for the degree of Philosophiae doctor (PhD). The scientific work was conducted between 2018 to 2022 at the TEM gemini centre at NTNU, Trondheim. Professor Randi Holmestad has been the main supervisor with doctor Sigurd Wenner, professor Antonius T. J. van Helvoort and professor Jaakko Akola as co-supervisors.

This work has been conducted as part of the *AllDesign* project in the NTNU Digitalization project. The goal of the AllDesign project is to create a digital materials platform for intermetallic alloy design with focus on aluminium-based alloys. This requires microstructural investigations at the nanoscale, which in this thesis is provided by TEM studies of wrought, heat-treatable aluminium alloys.

This thesis is divided into three main parts. Part I provides the background and motivation for the thesis and introduces aluminium and precipitation hardening as well as TEM. Part II presents the research and includes an overview of the alloys studied and microscopes used in the thesis. The results are summarised and discussed. Part III contains the results presented as six journal publications. The publications are either accepted or soon ready to be submitted to peer-review journals of international standards.

Publication list

Papers included in this thesis

Paper I — Atomic structure of solute clusters in Al-Zn-Mg alloys
A. Lervik, E. Thronsen, J. Friis, C.D. Marioara, S. Wenner, A. Bendo, K. Matsuda, R. Holmestad, S.J. Andersen
Acta Materialia (2021) **205** 116574

Paper II — Studying GPI zones in Al-Zn-Mg alloys by 4D-STEM
E. Thronsen, J. Frafjord, J. Friis, C.D. Marioara, S. Wenner, S.J. Andersen, R. Holmestad
Materials Characterization (2022) **185** 111675

Paper III — The evolution of precipitates in an Al-Zn-Mg alloy
E. Thronsen, S. Shah, C. Hatzoglou, C.D. Marioara, S. Wenner, S.J. Andersen, B. Holmedal, R. Holmestad
To be submitted

Paper IV — The effect of heavy deformation on the precipitation in an Al-1.3Cu-1.0Mg-0.4Si wt.% alloy
E. Thronsen, C.D. Marioara, J.K. Sunde, K. Minakuchi, T. Katsumi, I. Erga, S.J. Andersen, J. Friis, K. Marthinsen, K. Matsuda, R. Holmestad
Materials & Design (2020) **186** 108203

Paper V — The effect of small additions of Fe and heavy deformation on the precipitation in an Al-1.1Mg-0.5Cu-0.3Si at.% alloy
E. Thronsen, H. Mørkeseth, C.D. Marioara, K. Minakuchi, T. Katsumi, K. Marthinsen, K. Matsuda, R. Holmestad
Metallurgical and Materials Transactions A (2022) **In press**

Paper VI — Scanning precession electron diffraction data analysis approaches for phase mapping of precipitates in aluminium alloys
E. Thronsen, T. Bergh, T. I. Thorsen, E. F. Christiansen, J. Frafjord, P. Crout, A. T. J. van Helvoort, P. A. Midgley, R. Holmestad
To be submitted

Papers not included in this thesis

Paper A — Copper enrichment on aluminium surfaces after electropolishing and its effect on electron imaging and diffraction
S. Wenner, A. Lervik, E. Thronsen, C.D. Marioara, S. Kubowicz, R. Holmestad
Materials Characterization (2021) **172** 110846

Paper B — Precipitation behavior of Al-Si-Cu-Mg(-Fe) alloys by a deformation-semisolid extrusion process
D. Kim, J. Kim, S. Wenner, E. Thronsen, C.D. Marioara, R. Holmestad, E. Kobayashi
Materials Characterization (2021) **173** 110863

Paper C — AutomAl 6000: Semi-automatic structural labeling of HAADF-STEM images of precipitates in Al-Mg-Si(-Cu) alloys
H. Tvedt, C.D. Marioara, E. Thronsen, C. Hell, S.J. Andersen, R. Holmestad
Ultramicroscopy (2022) **236** 113493

Paper D — Effect of cyclic ageing on the early-stage clustering in Al–Zn–Mg(-Cu) alloys
S. Shah, E. Thronsen, C. Hatzoglou, S. Wenner, C.D. Marioara, R. Holmestad, B. Holmedal
Materials Science and Engineering: A (2022) **846** 143280

Datasets

Dataset for "Studying GPI zones in Al-Zn-Mg alloys by 4D-STEM"
E. Thronsen; *Zenodo* (2021) 10.5281/zenodo.5654427

Dataset for "The effect of small additions of Fe and heavy deformation on the precipitation in an Al-1.1Mg-0.5Cu-0.3Si at.% alloy"
E. Thronsen; *Zenodo* (2021) 10.5281/zenodo.5636674

Dataset for "The evolution of precipitates in an Al-Zn-Mg alloy"
E. Thronsen, S. Shah, C. Hatzoglou, C.D. Marioara, S. Wenner, S.J. Andersen, B. Holmedal, R. Holmestad; *Zenodo* (2022) 10.5281/zenodo.6655410

Dataset for "Scanning precession electron diffraction data analysis approaches for phase mapping of precipitates in aluminium alloys"
E. Thronsen, T. Bergh, T. I. Thorsen, E. F. Christiansen, J. Frafjord, P. Crout, A. T. J. van Helvoort, P. A. Midgley, R. Holmestad; *Zenodo* (2022) 10.5281/zenodo.6645396

Acknowledgements

This thesis had not been possible without the effort of a great many people, both direct and indirectly. First and foremost, I am forever grateful to my supervisor Randi Holmestad, who also was my supervisor during my master thesis in 2017-2018. Thank you for trusting in me and giving me this opportunity. Your positive and enthusiastic way of being has been motivating through both good and bad days. Without you, this thesis could not have been realised. I have always looked forward to our weekly meetings, and even though we sometimes talk about something completely different than science, it has always left me motivated to continue my work.

My co-supervisors, Jaakko, Sigurd and Antonius 'Ton', have been valuable to me through the years. To Jaakko I am grateful for hiring me as a PhD in the AllDesign project, where he is the project leader. Sigurd has helped a lot with everything related to aluminium, has co-authored Paper I-III and read through the aluminium, results and discussion parts of this thesis, which I am grateful for. Ton has been an important driving force for the data analysis development in our group and has held monthly SPED meetings, which have been very useful and interesting. He is the co-author on Paper IV and has given insightful feedback on the TEM part of this thesis. Needless to say, I am grateful to all three of you.

I have really appreciated the excellent working environment that we have in the TEM group. Especially the bond between the temporary staff is amazing. Christoph, Jonas, Tina, Inger-Emma, Dipanwita, Gregory, Jørgen, Tor-Inge, Oskar, Gregory, Iryna, Sivert, Håkon, Hogne and formerly Jonas, Adrian, Haakon and Emil (wow, we are a whole bunch), thank you for all the casuals coffees, ice creams, cinnamon buns and fruitful discussions. To the professors in the TEM group, Randi, Ton and Magnus, I am grateful for the working environment you have created and keep on pushing to maintain. Lastly, to the engineers in the TEM group, Bjørn, Emil and formerly Ragnhild, I am grateful for teaching me TEM and sample preparation and for always being available (even during the weekends) and Per Erik for training me on the ARM.

During my master thesis, I had the opportunity to be in Japan for one month. As a 'rooky' aluminium and TEM researcher, I really appreciated the time I spent working at YKK where I learnt a lot about aluminium and saw how important the research I was doing was for the industry. I am grateful for Iven, Katsumi, Minakuchi, Kita and Koizumi for making my stay memorable and that we were able to continue the collaboration throughout my PhD work as well. I would also like to thank professor Matsuda and doctor Lee at the University of Toyama for making my stay there meaningful.

I was lucky enough to have a two month stay as a visiting researcher at Monash University in Melbourne in late 2019 together with Randi, right before the world shut down due to Covid-19. Bryan, Eva, Ben, Laure, Phil and Jo, thank you for making my stay a memory for life. Sadly, none of the results we obtained there is included in my thesis, but I learnt a lot and Paper II is highly influenced by the work we did there.

The SumAl project is also acknowledged since I have been affiliated with that project. The SumAl project is funded by the Norwegian research council and three partners from the aluminium industry: Hydro, Benteler and Neuman. In that regards, I would like to thank Calin, who has acted as my co-supervisor without being it, Sigmund, Ruben, Jesper and Inga for all the fruitful discussions we have had during the years. I really look forward to becoming your colleague in August. Sohail, Bjørn Holmedal and Constantinos co-authored Paper III and we

have had many interesting scientific discussions in our biweekly meetings. I am grateful to you for your insight on atom probe tomography and aluminium from a slightly different perspective than mine. It has been a delight working with you and I am really proud of we achieved in our work.

The IDUN cluster at the high performance computing group at NTNU is acknowledged for the use of their computing resources in this thesis [1].

There has also been people outside the TEM or aluminium research field that have contributed to motivating me to work hard on my thesis, and that is the people 'back home'. This is better done in Norwegian. Til alle mine gode venner: Trine, Ellen, Marthe, Mia, Guro, Malin, Oda, Marita og Nina, takk for alle middagene, turene, treningsøktene osv. Og for at dere viser interesse for forskningen min, selv om dere ikke har noen forutsetning for å forstå hva jeg driver med. Jeg er også svært takknemlig for å å ha en veldig fin og omsorgsfull svigerfamilie, spesielt Siv og Jostein, Emil, Maiken og Thea og Tone og Tore. I tillegg har jeg også verdens beste mamma og pappa, som har gitt gode råd og vært mine største støttespillere gjennom hele livet. Takk for at dere alltid er tilgjengelige og hjelpsomme og for at dere viser genuin interesse for forskningen min. Sist, men ikke minst, takk til min kjære, Robin. Takk for at du alltid har støttet meg, vært forståelsesfull og tatt hånd om hjemmet vårt og Toyo i hektiste perioder.

Acronyms

AA artificial ageing.

ADF annular dark-field.

ANN artificial neural network.

APT atom probe tomography.

BF bright-field.

BSE backscattered electrons.

CBED convergent beam electron diffraction.

CCD charge-coupled device.

CRSS critical resolved shear stress.

CTEM conventional transmission electron microscopy.

DF dark-field.

DFT density functional theory.

DQE detective quantum efficiency.

EDS energy-dispersive X-ray spectroscopy.

EELS electron energy loss spectroscopy.

EM electron microscopy.

FCC face-centred cubic.

FEG field emission gun.

FOLZ first-order Laue zone.

GIF Gatan imaging filter.

GP Guinier-Preston.

GPB Guinier-Preston-Bagaryatsky.

HAADF high-angle annular dark-field.

HOLZ higher-order Laue zones.

NA natural ageing.

NBD nanobeam diffraction.

NMF non-negative matrix factorisation.

NTNU Norwegian university of science and technology.

PCA principal component analysis.

RT room temperature.

SAED selected area electron diffraction.

SE secondary electrons.

SEM scanning electron microscopy.

SGD stochastic gradient descent.

SHT solution heat treatment.

SOLZ second-order Laue zone.

SPED scanning precession electron diffraction.

SSSS supersatured solid solution.

STEM scanning transmission electron microscopy.

SVD singular value decomposition.

TCO truncated cube octahedron.

TDS thermal diffuse scattering.

TEM transmission electron microscopy.

UTS ultimate tensile strength.

VBF virtual bright-field.

VDF virtual dark-field.

YKK Yoshida Kōgyō Kabushiki-gaisha.

ZOLZ zeroth-order Laue zone.

Contents

Part I

Background

Chapter 1

Introduction

1.1 Motivation

When most people hear the word 'aluminium', they think of everyday convenience items such as soda cans and aluminium foil and not necessarily a high strength material. While this is true, aluminium is a versatile material - it can be designed to be thin and bendable, it can also be processed for applications where strength and durability are the most important considerations - from applications in the transport industry to the construction industry. Once more expensive than gold, the average price of aluminium has steadily decreased, albeit with local variations, since the 1900s. This is attributed to an increase in the production efficiency and today aluminium is the most heavily consumed non-ferrous metal in the world [2, 3]. Aluminium is the third most abundant element in the Earth's crust [3]. Its unique properties such as light weight, high strength and resistance to corrosion make it an ideal material for many applications, such as in the automotive-, construction and packaging industry. Pure aluminium however has a low strength, thus other elements are added, mainly to improve the strength. Typical tensile strengths range from 40 MPa of pure aluminium to strengths exceeding 700 MPa depending on composition and thermomechanical history of the alloy. The high strength, in combination with the low density of aluminium, has made it an attractive choice in applications where specific strength is a major design consideration. Worldwide, about 27% of the produced aluminium products are used in the transportation industry, enabling a weight reduction in automotive, aerospace and railway components [4]. The potential for reducing the CO_2 emissions from the transportation industry is considerable given that about 20% of our global energy and process CO_2 emissions originate from transportation, and about 20% of that could be reduced through lightweighting [4]. From a manufacturing perspective, aluminium alloys are ideal candidates for vehicular lightweighting due to their formability and high specific strength [5]. Thus, substituting steel with aluminium alloys in e.g. automotive applications can be an effective way of reducing the CO_2 emissions from the transportation industry.

Aluminium alloys are classified as either wrought or cast alloys, depending on whether they are worked or cast into their final shape. Wrought products account for 75-80% of the aluminium production [6]. The wrought alloys can be further divided into heat-treatable and non heat-treatable. The heat-treatable alloys undergo a heat treatment where the goal is to optimise the final properties of the alloy for its intended use. The final step of the heat treatment is called age hardening. Age hardening of aluminium alloys has been known since early 1900s when Dr. Alfred Wilm started work to improve the strength of aluminium alloys [7]. He was already aware that the strength of steels could be improved if the right compositions where cooled fast enough. Inspired by this, he prepared numerous Al-Cu alloys and quenched them at different rates only to realise that some of the alloys were even weakened by this treatment. The story tells that he interrupted his work to go sailing for the weekend. Upon his return, he was surprised to find that the hardness and tensile properties had improved significantly

during his two days of absence. He continued his experiments and by 1906 an aluminium alloy named duraluminum was patented [7]. The alloy is still used today, over 100 years after its discovery. Examination of the microstructure of duraluminum by optical microscopy failed to reveal any change that could account for the response to age hardening. In 1919, it was proposed that precipitation from a supersatured solid solution (SSSS) accounted for the increase in hardness [8]. The first experimental evidence of Cu-rich zones was by Guinier and Preston, working independently in 1937 [9, 10]. The zones were named GP zones after their discoverers, but was first observed by TEM in 1959 [11].

Today, we know that the hardening at room temperature discovered by Wilm is attributed to the formation of nano-sized clusters or GP zones. This phenomenon is called natural ageing (NA). The hardening process can be accelerated by aging at elevated temperatures, known as artificial ageing (AA). During AA, semi-coherent, metastable precipitates that significantly affect the mechanical properties, nucleate. Which type(s) of precipitates that nucleate and their distributions are determined by the composition and thermomechanical history of the alloy. Extensive research during the last 30 years has improved our understanding of the precipitates. Today the crystal structure of the most important precipitates is known [12]. Less is known about the crystal structure of the clusters. This is not surprising, considering that the size of the clusters is 1-3 nm which is small compared to the size of peak aged precipitates which typically extend through the whole TEM thickness ($\sim$ 30-100 nm).

It is well established that the presence of clusters or GP zones prior to AA affects the precipitation behaviour and thereby the final mechanical properties of the material. This is especially true for the Al-Mg-Si(-Cu) alloy system, where the clusters can be detrimental to the final properties of the alloy [13]. In Al-Zn-Mg alloys, the GP zones formed during NA cause a decrease in uniform elongation, which is undesired in engineering applications [14]. How the clusters affect the subsequent precipitation is highly dependent on the crystal structure of the clusters and zones. If a phase transformation can occur from clusters to precipitates, the ageing time will be decreased. In the event that a phase transformation cannot occur, the supersaturation will be lower as compared to the case of direct AA and the precipitation kinetics will hence be lowered. Another factor to consider is that vacancies can be bound to the clusters, hence lowering the vacancy concentration available for diffusion [15]. The effect of NA clusters on the formation of hardening precipitates during AA is hence also dependent on the AA temperature. If the clusters dissolve during AA, the bound vacancies will be redistributed in the solid solution, increasing the precipitation kinetics. The dissolution of clusters is dependent on the AA temperature and the alloy composition. Parts of this thesis concerns the crystal structure of GP-zones in Al-Zn-Mg alloys, along with how the GP-zones and clusters affect the final microstructure and properties of both Al-Mg-Si(-Cu) and Al-Zn-Mg alloys in their aged condition. The main characterisation tool has been TEM.

TEM is a powerful and versatile tool for characterising materials on the nanoscale. One of its main advantages is the ability to detect different complementary signals from the same volume simultaneously, along with its sub-nanometer resolution and the ability to detect particles embedded in a host material. Improvement of existing techniques and the advent of new techniques related to TEM have improved our understanding of many solid state materials. As mentioned, the first direct observation of GP zones in Al-Cu alloys was enabled by the invention of TEM. The advent of aberration corrected TEMs revolutionised atomically resolved HAADF-STEM in the early 2000s [16], enabling accurate estimations of the crystal structure of the most common precipitate types in aluminium alloys. With this technique,

an incoherent image where the contrast of each atomic column increases monotonously with Z-number, is formed [17]. Today, in the 2020s, 4D-STEM has gained a reputation as a robust and versatile technique for various characterisation tasks [18]. In 4D-STEM, a convergent probe scans a 2D region of the specimen while recording the diffraction pattern for every probe position, creating a 4D dataset. Several gigabytes of data is usually collected in 4D-STEM and the analysis rely on more sophisticated data analysis strategies as compared to conventional image analysis. It is hence of interest to implement data analysis tools as open-source codes, freely available for the community. The TEM group at the TEM Gemini Centre has a long experience investigating precipitation in aluminium alloys both with HAADF-STEM [12, 19] and more recently with SPED [20, 21], a subcategory of 4D-STEM. In this thesis, HAADF-STEM has been combined with SPED to study aluminium alloys in both the NA and AA conditions. HAADF-STEM and SPED have been the main TEM techniques and novel data analysis approaches have been implemented to analyse the SPED datasets.

1.2 Objectives and scope

1.2.1 Objective

This PhD work is part of the NTNU Digital Transformation initiative *AllDesign*. One of the main objectives of AllDesign is to *provide fundamental insight on solid-state precipitation in aluminium alloys based on synergistic multiscale modelling, and its impact on macroscopic properties and manufacturing processes* [22]. The overall objective of this thesis has been to provide experimental results that can be used to develop a multiscale modelling framework. For this thesis, this overall objective is divided into three main objectives: (i) increasing the understanding of early stage ageing in Al-Zn-Mg alloys, (ii) investigating how NA and heavy deformation affects the precipitation in Al-Cu-Mg-Si alloys and (iii) developing data analysis approaches for phase mapping of both GP zones and precipitates in heat-treatable aluminium alloys.

1.2.2 Scope

It is important to state that several limitations apply to the work presented in this thesis. First of all, the work is experimentally oriented, with the exception of TEM image- and diffraction simulations to interpret experimental results. Some of the results are supported by density functional theory calculations and atom probe tomography, executed by colleagues working in collaborative projects. The main characterisation tool in this work was transmission electron microscopy along with hardness measurements. The purpose of the study was not to provide theoretical insight to the solute clustering process, but rather to provide fundamental microstructural studies of features only accessible by state-of-the-art instrumentation. Increasing the understanding of microstructural development during AA is the main focus of this work. A majority of the work has relied on SPED and hence the development of data analysis approaches has also been an objective for this thesis.

Chapter 2

Aluminium alloys and precipitation

2.1 Aluminium and its alloys

Aluminium (Al) is well known for its low density, 2.7 g/cm^3 and high electrical- and thermal conductivity [3]. It is resistant to atmospheric corrosion, owed to the formation of an adhesive oxide layer protecting the material further attack. In its pure form, Al has a face-centred cubic (FCC) crystal structure. It belongs to spacegroup number 225 (Fm$\bar{3}$m). The lattice constant of Al at room temperature is 4.045 Å.

Metals are seldom used in their pure form in commercial applications. Instead, fractions of one or more other elements are alloyed with the base metal to tailor the properties of the material [23]. One of the most common reasons for alloying is to improve the strength. Al is no exception in this context: Al in its pure form has a low strength and is not suitable in applications where resistance to deformation is of concern. Whereas pure Al has a tensile strength of around 40 MPa, the strongest alloys exhibit tensile strengths exceeding 700 MPa [24]. The low density combined with high strength have made Al alloys attractive in applications where specific strength is a major design consideration. The properties of Al is highly dependent on the complex interaction of chemical composition and microstructural features developed during thermomechanical processing. Al alloys can be categorised as either cast or wrought alloys, depending on whether they are cast or worked into their final shape, respectively. Heat-treatable alloys, alloys that hardened by heating at elevated temperatures, exist in both categories. An overview of the wrought alloys, their main alloying elements and heat-treatability is given in Table 2.1 [2]. These alloys are denoted using a four digit system, where the first digit denotes the the main alloying element(s). Main alloying elements include Copper (Cu), Magnesium (Mg), Manganese (Mn), Silicon (Si) and Zinc (Zn).

Table 2.1: Overview of the wrought alloys and major alloying elements.

Series	Major alloying elements	Heat treatable
1xxx	Al > 99%	No
2xxx	Cu(, Mg)	Yes
3xxx	Mn	No
4xxx	Si	No
5xxx	Mg	No
6xxx	Mg, Si(, Cu)	Yes
7xxx	Zn, Mg(, Cu)	Yes
8xxx	Other elements	No/yes

2.2 Material properties and microstructure

The strength of a material is determined by its resistance to plastic deformation when loaded beyond its elastic limit [23]. Plastic deformation occurs by *glide*, the passage of dislocations along the certain crystallographic planes of the material. For Al, having an FCC crystal structure, glide occurs along the $\{111\}$ planes in the $\langle\bar{1}10\rangle$ direction. The different strengthening mechanisms aim at increasing the resistance for dislocations to glide. There are several ways of increasing the resistance. For Al, the most important strengthening mechanisms include: solid solution hardening, strain hardening, grain refining and age hardening. The mechanisms are made possible by thermomechanical treatments in combination with the addition of alloying elements. The thermomechanical treatments change the microstructure, i.e. the grain size, dislocation density, phase distribution and the texture of the material. These parameters strongly influence the macroscopical properties of the material. For this reason, control of microstructure during thermomechanical processing is important [25].

2.2.1 Stress strain behaviour of materials

One common way to measure the stress-strain behaviour of materials is with uniaxial deformation performing a *tensile test* [26]. A specimen with initial cross section q_0 and length l_0 is mounted into a mechanical testing machine where it is elongated with a constant speed, and both the elongation Δl and the applied force F are measured. The engineering stress is obtained by $\sigma = F/q_0$, while the engineering strain is defined as the elongation normalised by the initial length, $\varepsilon = \Delta l/l_0$. An example of an engineering stress-strain curve is schematically shown in Fig. 2.1.

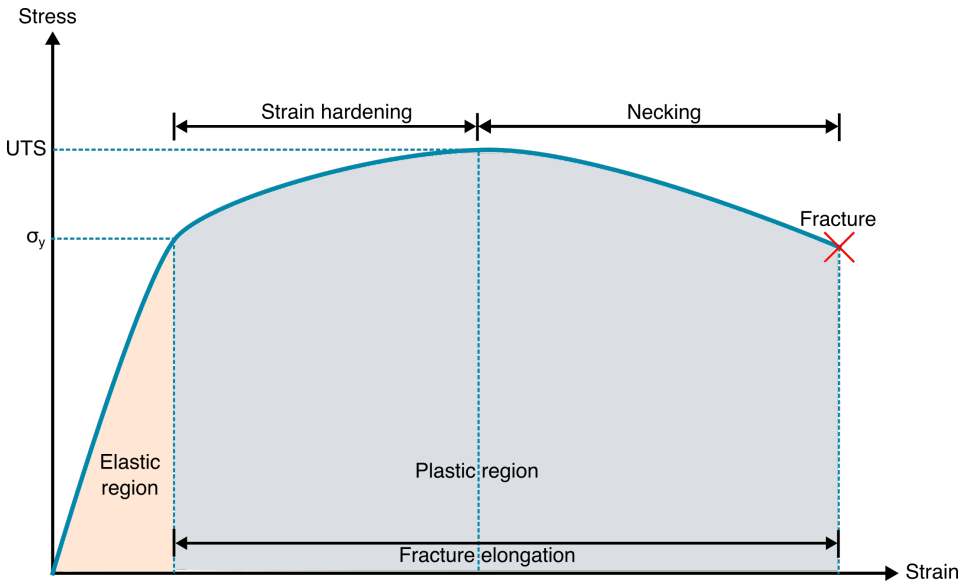

Figure 2.1: Schematic illustration of the engineering stress-strain curve of ductile materials.

Upon the initial stages of deformation, the engineering stress is proportional to the engineering strain. This relation is known as Hooke's law and constitutes the elastic region of the stress-strain curve. It is characteristic for elastic deformation that the solid spontaneously re-

verts to its original, undeformed shape when the forces are removed. Certain materials can be deformed to strains much larger than the elastic limit before they fracture, owed to their ability to deform plastically. During plastic deformation, the shape of the material is changed upon unloading. Materials exhibiting this behaviour are called ductile as opposed to brittle materials which fracture without significant plastic deformation. The end of the elastic region is marked by the *yield stress*, σ_y. Beyond this limit, the material deforms plastically and the stress increases with increasing strain, this is known as *strain hardening*. At a certain strain, the stress reaches a maximum known as *ultimate tensile strength (UTS)*. Beyond the UTS, the stress decreases until finally the material fractures. The stress-strain curves can take many shapes and forms depending on the material and the thermomechanical history. The yield strength, fracture elongation and UTS are important properties used to measure the performance of Al alloys.

2.2.2 Thermomechanical processing of heat-treatable aluminium alloys

Fig. 2.2 shows the different steps in a typical thermomechanical treatment of heat-treatable Al alloys along with the microstructure associated with each step.

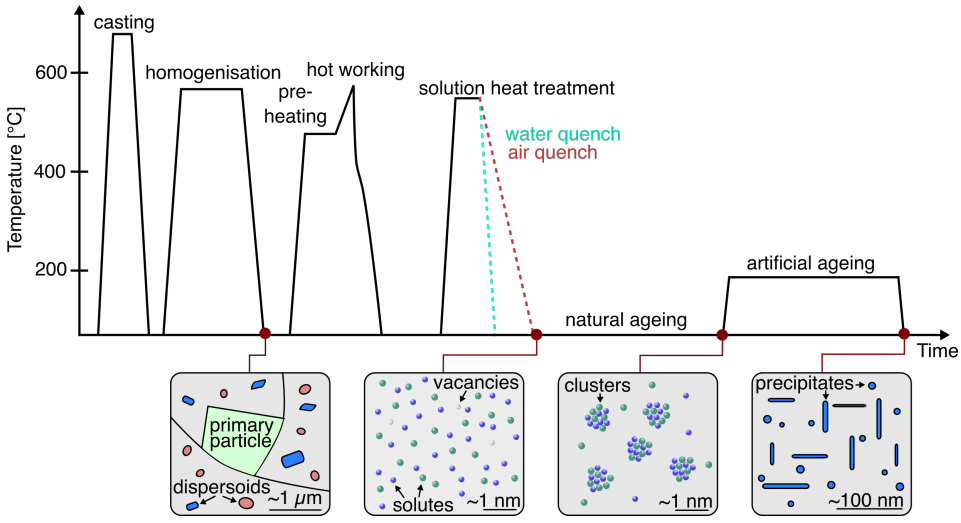

Figure 2.2: The typical thermomechanical processing steps and corresponding microstructure of heat-treatable Al alloys. Figure adapted from Ref. [25].

When the Al is cast, the solidification process produces equilibrium or metastable *primary particles* [25]. These coarse particles are often insoluble in the solid state after casting and are also often incoherent with the matrix. Due to the low solubility of iron (Fe) in Al and the inevitable presence of Fe as an impurity from bauxite, the primary particles often contain Fe. The presence of primary particles can be detrimental to the strength and one of the main purposes of the homogenisation is to produce a more uniform microstructure by a redistribution of the elements [27]. For instance, the β-AlFeSi intermetallic particle is transformed to the more favourable α-AlFeSi phase in this step [28]. Homogenisation also facilitates the precipitation of other fine particles known as *dispersoids*. Elements such as Zr, Cr and Mn are often added to Al alloys to precipitate dispersoids to inhibit recrystallisation. The subsequent step involves hot working, which can include hot rolling or extrusion, depending on the applica-

tion of the product. Prior to hot working, the metal is pre-heated to dissolve particles that may have formed to soften the material. In the hot working process, the billet is subjected to high temperatures and plastic deformation. Significant dynamic recovery usually occurs during hot working, whereby the dislocations rearrange themselves to form sub-grains.

After hot working, the alloy may undergo *solution heat treatment (SHT)* to create a *SSSS*. The SHT is followed by quenching, i.e. rapid cooling, to maintain the SSSS and to quench in vacancies, i.e. vacant lattice sites. The vacancy concentration may be several orders of magnitude higher than normal, depending on the quenching rate and temperature. By quenching, the vacancy concentration of the high temperature is maintained. This state is unstable and if kept at room temperature (RT), *clusters* form accompanied by a gradual increase in hardness [29, 30]. This process is known as *NA*. When the clusters achieve periodicity in one or more spatial dimensions, they are often referred to as *GP* zones after their discoverers in 1938 [9, 10]. During the subsequent *AA* performed at elevated temperatures, *precipitates* nucleate. In the following subsection, the influence of the introduced microstructural features will be discussed in terms of strengthening mechanisms commonly seen in heat-treatable Al alloys.

2.2.3 Lattice defects and strengthening mechanisms of aluminium

Fig. 2.3 shows an illustration of various defects in the Al lattice and their corresponding strain fields. Compressive and tensile strain fields are illustrated by green and red gradients, respectively.

Point defects and solid solution hardening
If an Al atom is removed from the lattice, a *vacancy* is formed. A vacancy contracts the site diameter by approximately 20% [3]. Atoms of different elements are always present in Al alloys, either they are intentionally added to tailor the properties of the alloy, or they are unwanted elements from the processing stage. The solutes have a different effective diameter compared to Al. Depending on the size of the solute, the solutes either substitute the Al atoms or they are placed in an interstitial position, i.e. we distinguish between substitutional and interstitial solutes. The atomic radii of the substitutional solutes compared to the atomic radii of Al determine whether their incorporation into the lattice causes compressive or tensile stresses. The solutes will distort the lattice and the distortion by the solid solution will impede dislocation glide. This is called *solid solution hardening* and the contribution from the solid solution to the yield stress can be expressed as [31, 32]:

$$\sigma_{\text{ss}} = \Sigma_i k_i C_i^{2/3}, \tag{2.1}$$

where C_i is the concentration of a specific alloying element in solid solution and k_i is the corresponding scaling factor.

Dislocations and strain hardening
Dislocations are line defects in crystals and as mentioned, they contribute to the deformation of the crystal. Two types of ideal dislocations exist, namely *edge* and *screw dislocations*. In general, most dislocations consist of a combination of edge and screw components. Edge dislocations can be interpreted as an extra half-plane of atoms in the lattice, as shown in Fig. 2.3. The long-range strain field associated with an edge dislocation is compressive where the extra half-plane is inserted and tensile at the opposite side. A dislocation is characterised by the magnitude and direction of the slip movement, which is called the *Burgers vector* $\vec{b}$. For

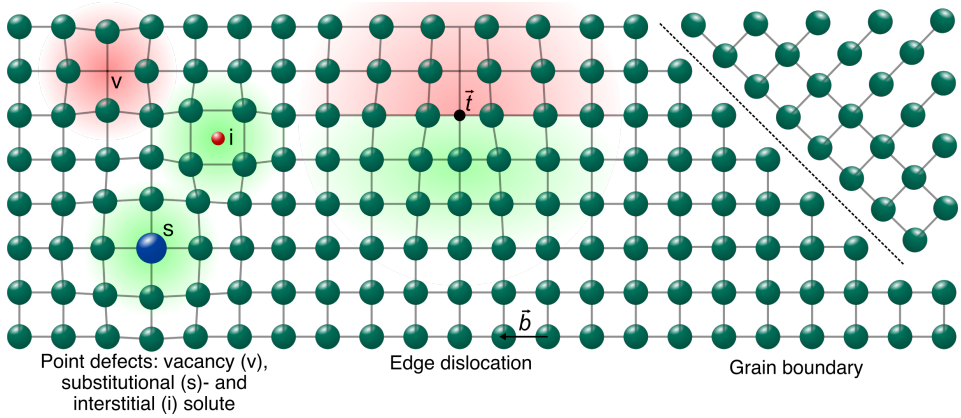

Figure 2.3: Lattice defects in the Al lattice along with their distortions in the lattice. Compressive- and tensile strain fields are illustrated by green and red gradients, respectively. Figure adapted from Ref. [3].

Al, the magnitude of the Burgers vector is equal to $\langle 110 \rangle a/2$ = 2.86 Å. The line vector $\vec{t}$ is perpendicular to the Burgers vector for edge dislocations, while for screw dislocations the two quantities are parallel. The yield stress σ_y characterises the start of plastic deformation. The start of plastic flow is equivalent to the onset of large scale dislocation motion. Dislocations become mobile when subjected to a force which has a component parallel to the slip plane in the slip direction. In a single crystal, the stress at which dislocations glide freely is called the *critical resolved shear stress (CRSS)*. For polycrystals, the CRSS is related to the yield stress through the Taylor factor, M. Dislocations interact via their elastic strain fields. A positive edge dislocation attracts a negative edge dislocation lying on the same slip plane so that their respective strain fields should cancel. Not all dislocations can glide in the usual manner, they can act as obstacles for other dislocations. As deformation proceeds, the dislocation density ρ_d increases when dislocation generation and multiplication occur faster than dislocation annihilation. This is mechanism is causing the strain hardening. The contribution from the dislocations to the yield stress can be expressed as [3, 31, 32]:

$$\sigma_d = M \alpha G b \sqrt{\rho_d}, \tag{2.2}$$

where α is a constant of the order 0.2-0.3, depending on the alloy composition, and G is the shear modulus.

Grain refining

Al is usually polycrystalline, i.e. it consists of many different, individually oriented crystals known as *grains*. The atoms in the three-dimensional regions between the individual grains constitute the *grain boundaries* of the metal and are not aligned with either crystal. Therefore, the grain boundaries are in a higher energy state than the grains. A grain boundary is schematically illustrated in Fig. 2.3. A dislocation reaching the grain boundary cannot continue its slip motion into another grain because of the difference in orientation between two adjacent grains. Hence, grain boundaries act as obstacles to gliding dislocations and the dislocations pile up at the grain boundaries. Increasing the amount of grain boundaries therefore decreases the distance dislocations can travel before reaching a grain boundary, resulting in

higher strength. This strengthening mechanism is known as *grain refining*. The contribution from the grain boundaries to the yield stress can be expressed through the Hall-Petch equation [3]:

$$\sigma_{\mathrm{gb}} = kd^{-1/2}, \tag{2.3}$$

where d is the average grain diameter and k is a constant, affected by the alloying elements. k is relatively low (0.065 MPam^{-1} for pure Al [3]) and grain size is not a major factor in strengthening of Al alloys.

Precipitates and age hardening

The phase transitions occurring during AA of heat-treatable alloys are described using sequences of different precipitates. This is known as the *precipitation sequence* and can in general be described as:

$$\begin{aligned} \mathrm{SSSS} \rightarrow \text{solute clusters} \rightarrow \text{GP zones} \rightarrow \text{peak aged precipitates} \\ \rightarrow \text{over-aged precipitates} \rightarrow \text{equilibrium particles}. \end{aligned} \tag{2.4}$$

Precipitate type(s) and distribution are determined by the thermomechanical history and composition of the alloy. Alloying elements are brought in solid solution at the SHT temperature and quenched to RT. At intermediate temperatures, very fine particles are precipitated from the SSSS resulting in a substantial increase in strength. This is known as *age hardening*. The effect of the age hardening is determined by several parameters including the chemical composition of the SSSS, the composition of the precipitates formed upon decomposition of the SSSS, the kinetics of precipitation, AA temperature and time and the properties of the precipitates, such as morphology, composition and hardness. The SSSS state is shown schematically on the left hand side in Fig. 2.4.

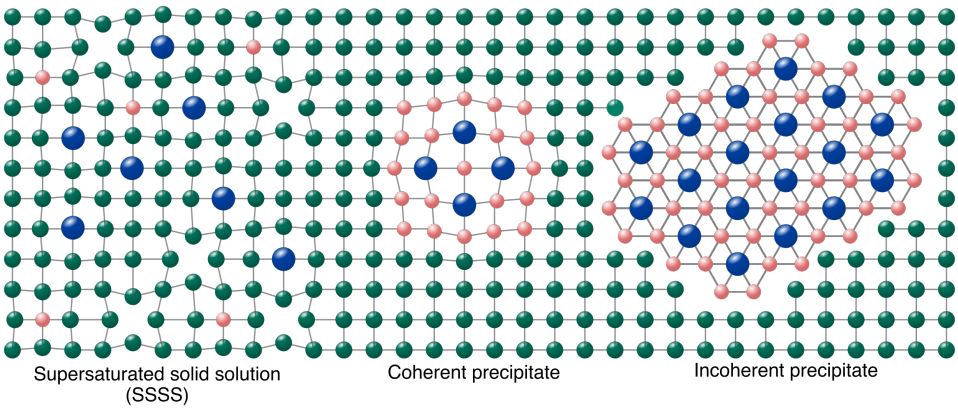

Figure 2.4: Illustration of a supersatured solid solution, coherent precipitate and incoherent precipitate in a simple cubic lattice. Figure adapted from Ref. [23]

The composition of the SSSS is controlled by the quenching rate and the SHT temperature and is in general different from the alloy composition, since some of the alloying elements

are locked in primary particles and dispersoids and hence are not contributing to the SSSS [3]. The presence of excess vacancies promotes diffusion and the formation of precipitates is substantially faster than under normal conditions. The precipitation usually starts with the segregation of solute atoms into solute clusters. Then, the clusters acquire their own crystal structure, first similar to that of the matrix. These particles are coherent with the matrix and referred to as GP zones. An example of a coherent precipitate and its effect on the Al lattice is shown in Fig. 2.4. The subsequent metastable phases formed during precipitation are (semi)coherent. The metastable precipitates have their own crystal structure and coherency is usually maintained only along certain directions. After prolonged ageing, the precipitates become coarse and incoherent, exemplified in Fig. 2.4. If the temperature is high enough or if the alloy is aged for a very long time, the equilibrium particles will form.

The precipitation sequence in Eq. 2.4 is often monitored by performing hardness tests at the different stages of AA. During the nucleation and growth of solute clusters and GP zones, the hardness increases. This is known as the *under-aged condition*. At a certain point, the hardness typically reaches a peak. The peak is associated with a high number density of metastable, semi-coherent precipitates and is known as *peak aged condition*. As the AA advances, the hardness decreases due to the transformation into a coarser microstructure. This state is usually referred to as the *over-aged condition*.

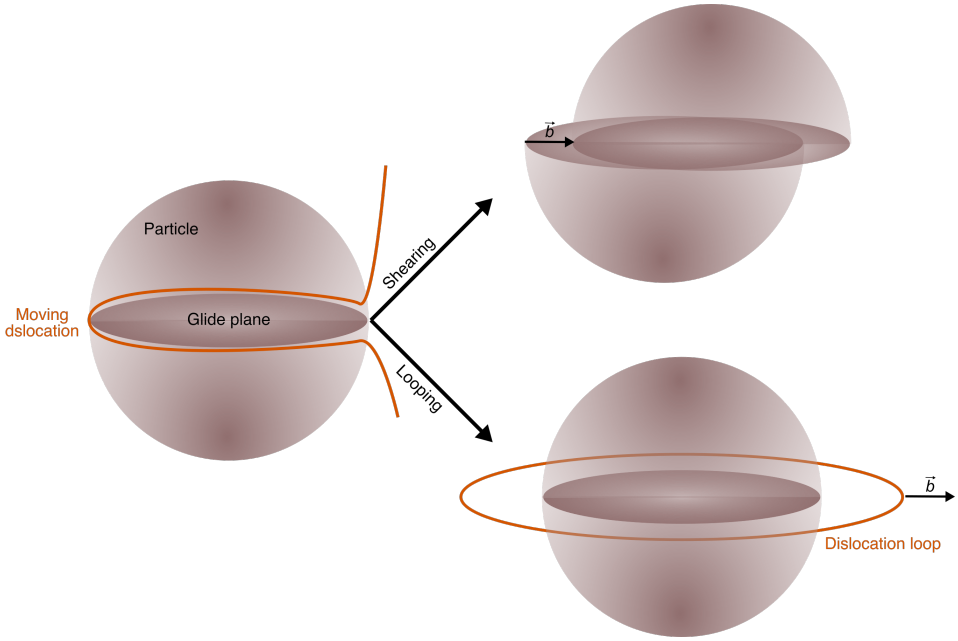

Figure 2.5: Schematic illustration of a moving dislocation interacting with a spherical precipitate. The precipitate is either sheared or looped by the dislocation. The figure is adapted from Ref. [33].

The degree of strengthening obtained during age hardening is highly dependent on the alloy system, the volume fraction and size of the precipitates in addition to the nature of the interaction of the precipitates and the dislocations [33]. Depending on the size, spacing and degree of coherency, the precipitates are either sheared or looped by the dislocations during plastic deformation. Fig. 2.5 shows the two possible interactions between a dislocation and a pre-

cipitate. Small precipitates that are coherent or semi-coherent with the Al matrix are typically sheared, while the incoherent phase boundaries act on dislocations like grain boundaries, i.e. the dislocations can not move from the Al matrix into the precipitate. The only way for the dislocations to circumvent incoherent precipitates is by bowing out between the particles. This is known as the *Orowan mechanism* and leads to a dislocation loop around the particle.

The contribution from precipitates to the yield strength is dependent on the precipitate size distribution $f(R)$, the obstacle strength $F(R)$, the average particle spacing on the dislocation L, the magnitude of the Burgers vector b and the Taylor factor M and can for homogeneous precipitation be estimated as [34]:

$$\sigma_p = M\bar{F}bL = MbL\int_0^\infty f(R)F(R)dR, \tag{2.5}$$

where $\bar{F}$ is the mean obstacle strength. The obstacle strength depends on the precipitate-dislocation interaction. For a detailed description of strength models for age hardening, c.f. Ref. [31, 32, 34].

Overall yield strength

If one assumes that the individual strength contributions can be added linearly, the resultant expression for the yield strength is obtained [32]:

$$\sigma_y = \sigma_i + \sigma_{\text{ss}} + \sigma_d + \sigma_{\text{gb}} + \sigma_p, \tag{2.6}$$

where σ_i is the intrinsic yield strength of pure Al.

2.3 Precipitation in heat-treatable aluminium alloys

This subsection describes the relevant precipitation sequences occurring in the alloys studied in this thesis.

Al-Cu-Mg and Al-Li-Cu(-Mg) alloys

Different precipitates form in the Al-Cu-Mg alloy system depending on the Cu/Mg ratio of the alloy. The isothermal section of the ternary Al-Cu-Mg phase diagram at 200°C is shown in Fig. 2.6. In the following, only the phases relevant for the this thesis will be considered.

For alloys in the α + S region of the ternary Al-Cu-Mg phase diagram, the decomposition process starts with the segregation of copper and magnesium atoms into solute clusters. These clusters are precursors to the more structurally developed Guinier-Preston-Bagaryatsky (GPB) zones. Bagaryatsky reported the following precipitation sequence in such alloys [36]:

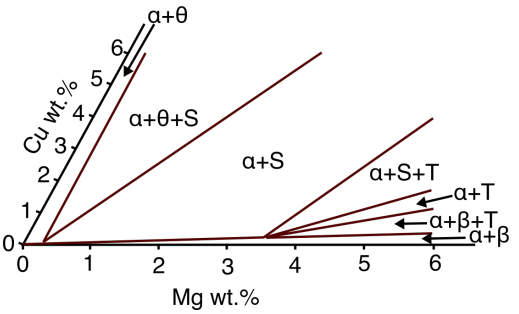

Figure 2.6: Isothermal section of the ternary Al-Cu-Mg phase diagram at 200°C. α = Al, θ = $CuAl_2$, S = Al_2CuMg, T = Al_6CuMg_4 and β = $Al_{12}Mg_{17}$. The figure is adapted from Ref. [35].

$$\text{SSSS} \rightarrow \text{solute clusters} \rightarrow \text{GPB zones} \rightarrow \text{S}'' \rightarrow \text{S}' \rightarrow \text{S-CuMgAl}_2. \tag{2.7}$$

These alloys usually experience a hardness plateau upon AA. The first increase is believed to be attributed to the solute clusters, rather than the formation of more structurally developed GPB zones [37, 38]. At the second plateau, the GPB zones co-exist with the S′ phase. The GPB zones are metastable, rod-like precipitates and are comprised of different structural units [39, 40]. The structural units have perfect translational periodicity along the [100] growth direction and the lattice parameter along this direction is equal to the Al matrix lattice parameter, a_{Al}. An overview of the different structural units of the GPB zones, their crystal structure and composition is given in Ref. [40]. The S″ and S′ phases are precursors to the equilibrium S phase and exhibit different degrees of coherency with the Al matrix [41]. The most widely reported orientation relationship between S and the Al matrix is [35, 42]:

$$(001)_{\text{S}} \,//\, (021)_{\text{Al}}, [100]_{\text{S}} \,//\, [100]_{\text{Al}}. \tag{2.8}$$

The S phase grows as laths on $\{021\}_{\text{Al}}$ habit planes and is elongated along $\langle 100\rangle_{\text{Al}}$. Other orientation relationships have also been observed [42]. The S phase has an orthorombic structure and belongs to the Cmcm space group with lattice parameters a = 0.400 nm, b = 0.923 nm, c = 0.714 nm [43]. The S phase is often seen to nucleate heterogeneously on dislocations as well as in the matrix of Al-Cu-Mg alloys [44].

In the $\alpha + \theta$ + S region of the phase diagram, the S phase and its precursors may co-exist with the θ phase and its precursors from the Al-Cu alloy system. The precipitation sequence for the θ phase is as follows [12]:

$$\text{SSSS} \rightarrow \text{GPI zones} \rightarrow \theta'' \rightarrow \theta' \rightarrow \theta\text{-Al}_2\text{Cu}. \tag{2.9}$$

The θ phase is incoherent with the Al matrix and thus contributes little to hardening. It has a a tetragonal I4/mcm structure with a = 0.601 nm and c = 0.488 nm [45]. It is preceded by the metastable θ' phase, which has a tetragonal crystal structure and belongs to space group $I\bar{4}m2$ [46]. The lattice parameters are a = 0.404 nm and c = 0.580 nm. This phase grows as plates on the $\{100\}_{\text{Al}}$ planes and exhibits the following orientation relationship with the Al matrix [35]:

$$(100)_{\theta'} \,//\, (100)_{\text{Al}}, [001]_{\theta'} \,//\, [001]_{\text{Al}}. \tag{2.10}$$

The θ'' precursor is also called GPII zone and has a composition of Al_3Cu and consists of two or more Cu planes in parallel replacing every fourth Al plane [12], while the GPI zone is even simpler: Cu replaces Al atoms on the $\{100\}_{\text{Al}}$ planes as plates.

If Li is added to the Al-Cu(-Mg) system, the plate-like T_1-Al_2LiCu phase may also form, often co-existing with θ and its precursor and/or S and its precursors, depending on the alloy composition and heat treatment. The orientation relationship between T_1 with the Al matrix is [35]:

$$(0001)_{\text{T}_1} \,//\, (111)_{\text{Al}}, [1\bar{1}00]_{\text{T}_1} \,//\, [1\bar{1}0]_{\text{Al}}. \tag{2.11}$$

The space group, lattice parameter and atomic positions for the θ'- and T_1 phases are shown in Tab. 2.2.

Table 2.2: Space group, lattice parameter and atomic positions for the θ' phase [46] and T_1 phase [47]. Note that the Cu- and Li- atomic positions for the T_1 phase are Cu- and Li-rich, respectively, and such sites are also partially occupied by Al.

Phase	Space group	Lattice parameter (nm)	Atomic positions x	y	z	Atom
θ'	$I\bar{4}m2$	$a = 0.404$, $c = 0.580$	0.00	0.00	0.00	Al
			0.00	0.00	0.50	Al
			0.00	0.50	0.25	Cu
T_1	P6/mmm	$a = 0.496$, $b = 1.418$	1/3	0.00	0.00	Al
			0.00	0.50	0.406	Al
			2/3	1/3	0.161	Cu
			1/2	0.00	0.324	Cu
			0.00	0.00	0.199	Li
			1/3	2/3	0.500	Li

Al-Mg-Si(-Cu) alloys

The precipitation sequence in the Al-Mg-Si system is usually given as [19]:

$$\text{SSSS} \rightarrow \text{solute clusters} \rightarrow \text{GP zones} \rightarrow \beta'' \rightarrow \beta', \text{U1}, \text{U2}, \text{B}' \rightarrow \beta\text{-Mg}_2\text{Si} \tag{2.12}$$

All precipitates, except the equilibrium phases, have their main coherency and growth direction along $\langle 001 \rangle_{\text{Al}}$, yielding a lattice parameter of a_{Al} along one of their crystallographic directions. Given a particular alloy composition, the phases formed depend on the thermomechanical treatment and the distribution of microstructural features such as grain boundaries and dislocations. As always, the decomposition from SSSS starts with the formation of solute clusters, preceded by the formation of GP zones. The peak aged condition of these alloys usually incorporates a dense population of needle-like, semi-coherent β'' precipitates, which is the main hardening phase. The post-β'' phases that form during over-ageing are coherent along the $\langle 001 \rangle_{\text{Al}}$ direction, but exhibit less coherency in the cross-sectional planes compared to β''. All post-β'' precipitate phases incorporate the so-called Si-network [48]. These precipitates can be described as different arrangements of Al and Mg on a projected hexagonal Si grid, i.e. the Si-network. Along $\langle 001 \rangle_{\text{Al}}$, the network is near hexagonal in projection, with a lattice spacing of about 0.4 nm, equal to the lattice parameter of Al. Depending on the precipitated phase, the Si network is oriented along $\langle 100 \rangle_{\text{Al}}$ or $\langle 510 \rangle_{\text{Al}}$ directions. The main hardening phase, β'', does not contain a perfect Si network such as the aforementioned phases, but exhibits a partially discontinuous network. An overview over of different precipitate phases in Al-Mg-Si alloys along with their space group, composition and lattice parameters is shown in Tab. 2.3. Structural unit cell models projected along $\langle 001 \rangle_{\text{Al}}$ for the metastable precipitates are shown in Fig. 2.7.

Several orientation relationships have been reported for the β' phase [59]. All β' precipitates exhibit a perfectly coherent interface along $[0001]_{\beta'} // [001]_{\text{Al}}$, while exhibiting a lattice misfit

Table 2.3: Overview of the precipitate phases forming in Al-Mg-Si alloys along with their composition, space group, lattice parameters and references.

Phases	Composition	Space group	Lattice parameters (nm)	Ref.
GP zones	Variable	C2/m	$a = 1.480$, $b = 0.405$, $c = 0.648$, $\beta = 105.3°$	[49]
β''	$Mg_{6-x}Al_{1+x}Si_4$ [a]	C2/m	$a = 1.516$, $b = 0.405$, $c = 0.674$, $\beta = 105.3°$	[50, 51]
β'	Mg_9Si_5	$P6_3/m$	$a = b = 0.715$, $c = 0.405$, $\gamma = 120°$	[52, 53]
U1	$MgAl_2Si_2$	$P\bar{3}m1$	$a = b = 0.405$, $c = 0.674$, $\gamma = 120°$	[54]
U2	MgAlSi	Pnma	$a = 0.675$, $b = 0.405$, $c = 0.794$	[55]
B′	$Mg_9Al_3Si_7$	$P\bar{6}$	$a = b = 10.3$, $c = 0.405$ $\gamma = 120°$	[56, 57]
β	Mg_2Si	$Fm\bar{3}m$	$a = 0.635$	[58]

[a] $0 \leq x \leq 2$

in the cross-sectional plane. Weng *et al.* [59] found that the angle between the $\langle 2\bar{1}\bar{1}0\rangle_{\beta'}$ direction and the nearest $\langle 100\rangle_{Al}$ varied from 6.1° to 14.1° for rod-shapes precipitates, while for the lath-like β' precipitate, the angle was 0°. The other precipitates observed in the over-aged conditions also exhibit multiple orientation relationships [54, 55], while for β'' the orientation relationship can be expressed as [60]:

$$(010)_{\beta''} \,//\, \{001\}_{Al}, [001]_{\beta''} \,//\, \langle 310\rangle_{Al}, [100]_{\beta''} \,//\, \langle 230\rangle_{Al}. \tag{2.13}$$

The rotation of the projected Si-network along the growth direction of the precipitates results in different orientation relationships of precipitates. For β'', exhibiting a partially discontinuous Si-network, the rotation is not possible, yielding a constant orientation relationship [59].

The addition of Cu to Al-Mg-Si alloys alters the precipitation sequence in Eq. 2.12 and new phases form during AA. Which phases form is heavily dependent on the Mg/Si ratio of the alloy, along with the amount of Cu added. In general, the precipitation sequence in Al-Mg-Si-Cu alloys is given as [61–63]:

$$\text{SSSS} \rightarrow \text{solute clusters} \rightarrow \text{GP zones} \rightarrow \beta'', \text{L}, \text{C} \rightarrow \text{L}, \text{C}, \beta', \text{Q}', \beta'_{Cu} \tag{2.14}$$

$$\rightarrow \text{Q-}Al_3Cu_2Mg_9Si_7. \tag{2.15}$$

The L phase has a lath morphology and is a disordered structure [63] showing variation in composition [64]. It has been demonstrated that the L phase has a good thermal stability, contributing to a slower over-ageing behaviour [65]. The Mg/Si ratio is an important parameter to consider in alloy design of these alloys as it has a large influence on the type of precipitates

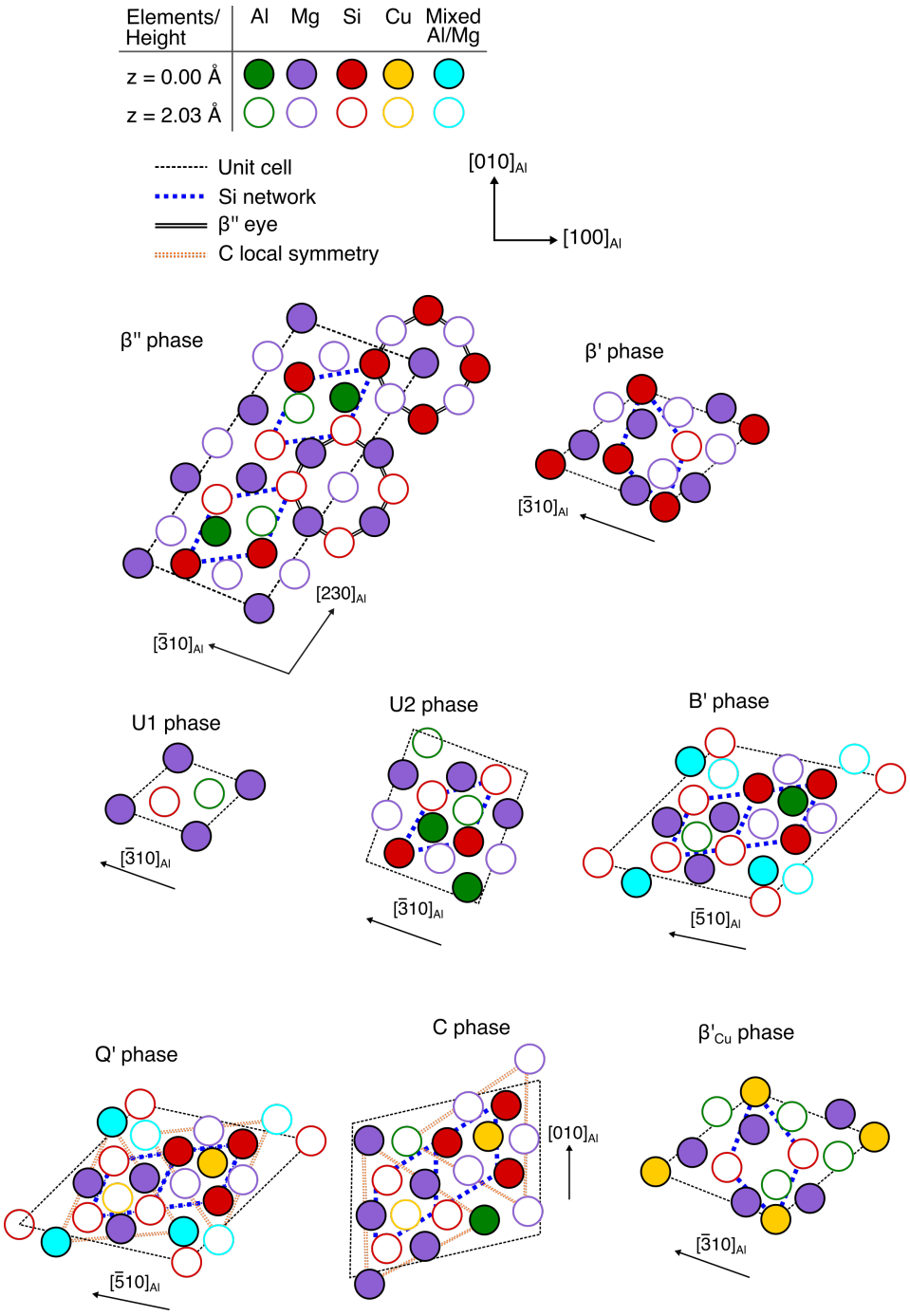

Figure 2.7: Structural unit cell models of metastable, precipitate phases in Al-Mg-Si(-Cu) alloys. Adapted from Ref. [19].

formed during AA. E.g., in Mg-rich alloys, the L phase is often favoured [66, 67]. The plate-like C phase has a monoclinic unit cell. Both the L- and C phase are elongated along $\langle 001 \rangle_{\mathrm{Al}}$ and have habit plane $\{100\}_{\mathrm{Al}}$, hence the L phase is often described as a disordered version of the C phase [63]. Both these phases are believed to be precursors to the Q′ phase. The Q′ phase is isostructural to the B' phase, having Cu substituting Al, and is encountered in the over-aged conditions [63]. There are multiple reported orientation relationships between Q′ and the Al matrix [68, 69]. The β_{Cu} phase is isostructural to β'_{Ag} [70]. All these precipitates incorporate the Si-network and the Cu atomic columns can either replace Si in the network, or be in-between the Si network columns. Structural unit cell models of the metastable precipitates in Al-Mg-Si(-Cu) alloys are schematically shown in Fig. 2.7 [19], while Tab. 2.4 shows an overview of the phases, along with their space groups and lattice parameters.

Table 2.4: Overview of the Cu-containing precipitate phases forming in Al-Mg-Si-Cu alloys.

Phases	Composition	Space group	Lattice parameters (nm)	Ref.
L	Variable	Disordered	-	[63]
C	$Mg_4AlSi_{3.3}Cu_{0.7}$	$P2_1/m$	a = 1.032, b = 0.405, c = 0.810 β = 100.9°	[71]
β'_{Cu}	$Mg_3Al_3Si_2Cu$	$P\bar{6}2m$	$a = b$ = 0.690, c = 0.405 γ = 120°	[19, 72]
Q′	$Al_3Cu_2Mg_9Si_7$	$P\bar{6}$	$a = b$ = 1.032, c = 0.405 γ = 120°	[62, 73]
Q	$Al_3Cu_2Mg_9Si_7$	$P\bar{6}$	$a = b$ = 1.032, c = 0.405 γ = 120°	[74]

The presence of solute clusters formed during NA prior to AA can yield a slower hardening reaction and lower the yield strength and UTS upon subsequent AA as compared to direct AA without NA [13]. This is referred to the *negative effect of NA* for Al-Mg-Si(-Cu) alloys. This is most pronounced in dense alloys. Lean alloys can exhibit some positive effect of NA [75, 76].

Al-Zn-Mg(-Cu) alloys

The precipitation sequence in Al-Zn-Mg alloys is usually given as [77]:

$$\text{SSSS} \rightarrow \text{GPI/GPII} \rightarrow \eta' + \eta_{1-14} \rightarrow \eta\text{-MgZn}_2. \tag{2.16}$$

Two types of GP zones have been observed in Al-Zn-Mg alloys, namely the spherical GPI and plate-like GPII zones [78]. The GPI zones form during NA and at temperatures below the GPI formation temperature, T_h [79, 80]. The GPII zones, on the other hand, are formed after quenching from temperatures above 450°C and at AA temperatures above 70°C [78]. The atomic structure of the GPI zones is the topic of Paper I in this thesis [81], and was up until recently described as a simple anti-phase ordering of solute based on diffraction patterns acquired from large regions [78]. In Paper I however, we show that the atomic structure can be explained as a partial substitution of Mg and Zn on the fcc Al cell and its surrounding TCO shell. A simple set of principles based on Frank-Kasper structures can explain how the basic units arrange with respect to each other to form larger zones. The GPII zones are less understood, Berg *et al.* [78] proposed that they could be described as Zn-rich layers on the $\{111\}_{\text{Al}}$ planes, based on diffraction patterns and high resolution transmission electron microscopy.

Cu is often added to Al-Zn-Mg alloys to increase the strength of these alloys. The addition of Cu does not contribute to the formation of new phases, rather it increases the number density of precipitates and refines the microstructure [82].

The AA treatment of these alloys is usually done in two steps. The aim of the first step ($\sim$ 100°C) is to form GP zones that can act as nucleation sites for the formation of metastable, hardening phases. During the second step ($\sim$ 140-160°), the alloy acquires its final properties [3]. The transformation from GP zones to the main hardening phase, η', is not well understood. This is the topic of Paper III in this thesis. In general, two different mechanisms are proposed in the literature [79, 80]:

- Partial reversion: The dissolution of the GP zones and the formation of η' overlap. This is often attributed to the model proposed by Lorimer and Nicholson [83]. According to this model, GP zones exceeding a certain critical radius do not dissolve and η' preferentially form at the sites of these over-critical GP zones.
- Complete reversion: The GP zones dissolve prior to the formation of η'. In spite of the complete dissolution of the zones, such treatments often result in finely distributed η'. In specimens directly quenched to the same AA temperature, only coarse, heterogeneously distributed η' phases are formed. I.e., the dissolving GP zones must leave behind traces that act as preferential nucleation sites for η' [79].

In the case of partial reversion, the mechanical properties do not reach the as-quenched level, while during complete reversion, the mechanical properties rapidly decrease to values corresponding to the as-quenched level [79].

At the peak aged condition, the microstructure consists of the metastable, hexagonal η' typically co-existing with hexagonal, semi-coherent η_{1-14} precipitates. Fourteen different orientation relationships are reported for η, these are summarised in Tab. 2.5. The table also shows

the orientation relationship of η' along with the morphologies of the different precipitates. In the following, any of the η_{1-14} precipitates will be referred to as η precipitates, while the incoherent η-$MgZn_2$ will be referred to as equilibrium η-$MgZn_2$ to differentiate between the semi-coherent and incoherent particles.

In general, the agreed crystal structure for the η' is hexagonal with a = 0.496 nm and c = 1.405 [84–87]. The most frequently observed phases at the peak aged condition include η', η_1, η_2 in the bulk, while η_4 is often observed to heterogeneously nucleate at defects [77, 88, 89]. Even though η' and the η precipitates have been known and investigated for decades [88, 90–93], it was not until the advent of atomically resolved HAADF-STEM that directly interpretable images were attained, revealing the atomic structure of the precipitate along with the precipitate-Al interface.

Table 2.5: Overview of the η' and η precipitates forming upon AA of Al-Zn-Mg alloys along with their orientation relationships and morphologies. The notations used according to Gjønnes *et al.* [93].

Phases	Orientation relationship		Morphology	Ref.	HAADF-STEM
η'	$(0001)_\eta // (1\bar{1}1)_{Al}$	$(10\bar{1}0)_\eta // (110)_{Al}$	Plate on $\{111\}_{Al}$	[94]	[77, 95–99]
η_2	$(0001)_\eta // (1\bar{1}1)_{Al}$	$(10\bar{1}0)_\eta // (110)_{Al}$	Plate on $\{111\}_{Al}$	[92]	[95–98, 100, 101]
η_3	$(0001)_\eta // (1\bar{1}1)_{Al}$	$(11\bar{2}0)_\eta // (110)_{Al}$	Plate on $\{111\}_{Al}$	[102]	-
η_{10}	$(0001)_\eta // (1\bar{1}1)_{Al}$	$(11\bar{2}0)_\eta // (1\bar{3}4)_{Al}$		[79]	-
η_1	$(0001)_\eta // (110)_{Al}$	$(10\bar{1}0)_\eta // (001)_{Al}$	Plate on $\{001\}_{Al}$	[92]	[77, 89, 100, 101, 103, 104]
η_9	$(0001)_\eta // (110)_{Al}$	$(11\bar{2}0)_\eta // (001)_{Al}$	Plate on $\{001\}_{Al}$	[88]	-
η_{11}	$(0001)_\eta // (110)_{Al}$	$(10\bar{1}0)_\eta // (1\bar{1}\bar{1})_{Al}$		[88]	-
η_4	$(11\bar{2}0)_\eta // (1\bar{1}\bar{1})_{Al}$	$(0001)_\eta // (110)_{Al}$	Rod/lath on $\{111\}_{Al}$	[92]	[77]
η_5	$(11\bar{2}0)_\eta // (1\bar{1}\bar{1})_{Al}$	11° to $\langle 110\rangle_{Al}$	Rod/lath on $\{111\}_{Al}$	[92]	-
η_6	$(11\bar{2}0)_\eta // (1\bar{1}\bar{1})_{Al}$	15° to $\langle 110\rangle_{Al}$	Rod/lath on $\{111\}_{Al}$	[92]	-
η_7	$(11\bar{2}0)_\eta // (1\bar{1}\bar{1})_{Al}$	25° to $\langle 110\rangle_{Al}$	Rod/lath on $\{111\}_{Al}$	[92]	-
η_8	$(11\bar{2}0)_\eta // (1\bar{1}2)_{Al}$	$(0001)_\eta // (31\bar{1})_{Al}$	Rod along $\langle 112\rangle_{Al}$	[93]	-
η_{12}	$(11\bar{2}0)_\eta // (110)_{Al}$	$(0001)_\eta // (1\bar{1}3)_{Al}$	On $\{1\bar{1}3\}_{Al}$	[100]	[100, 101]
η_{13}	$(0001)_\eta // (120)_{Al}$	$(2\bar{1}\bar{1}0)_\eta // (001)_{Al}$	Plate on $\{120\}_{Al}$	[103]	[101, 103]
η_{14}	$(0001)_\eta // (51\bar{3})_{Al}$	$(2\bar{1}\bar{1}0)_\eta // (112)_{Al}$	Plate on $\{51\bar{3}\}_{Al}$	[101]	[101]

Marioara *et al.* [96] presented the first atomically resolved HAADF-STEM images of the η' and η_2 precipitates along $\langle 211\rangle_{Al}$ and labeled them 'Type 1' and 'Type 2', respectively. These precipitates have the same orientation relationships, c.f. Tab. 2.5, and are thus separable based solely on their atomic structure. η' precipitates are comprised of one rhombohedral (R) layer and one orthorombic (O) layer, having a fixed width of $6d_{111}{}^{Al}$. η_2 on the other hand, consists of R layers, stacked pairwise or rotated 180° w.r.t. each other (R^{-1}) when viewed along $\langle 211\rangle_{Al}$ [95, 96, 99–101]. If the stacking is in a zigzag manner ($RR^{-1}RR^{-1}$..), η_2 and the equilibrium η-$MgZn_2$ are isostructural, when neglecting the solute-enriched $\{111\}_{Al}$ planes [96]. The equilibrium η-$MgZn_2$ belongs to space group $P6_3/mmc$ with unit cell parameters a = 0.52 nm and c = 0.86 nm [105]. Bendo *et al.* [89] investigated the η_1 precipitate and found that it consisted of a pairwise stacking of R- and R^{-1} layers when viewed along $[010]_{\eta 1} // [\bar{1}10]_{Al}$.

Although many orientation relationships are reported between η and the Al host lattice, only some of them have been observed with HAADF-STEM. The ones observed with HAADF-STEM, to the authors knowledge, are indicated in Tab. 2.5 along with the corresponding

reference.

In addition to the η precursor phases in Eq. 2.16, the equilibrium T-$Mg_{32}(AlZn)_{49}$ phase can also form in Al-Zn-Mg alloys with moderate to high Mg/Zn ratio [79, 106, 107]. The precipitation sequence for the T phase is usually given as [108]:

$$\text{SSSS} \rightarrow \text{T}' \rightarrow \text{T-Mg}_{32}(\text{AlZn})_{49}. \tag{2.17}$$

The T phase is cubic and belongs to space group Im3 with 162 atoms in the unit cell. The lattice parameter is a = 1.416 nm [106]. The T phase is preceded by the metastable, semi-coherent T′ phase [108–112]. Recently, Zou *et al.* [113–115] have reported a co-existence of Zn-rich T′ and η' precipitates in Al-Zn-Mg alloys. The orientation relationship between the T/T′ phases and the Al lattice is often reported as [79]:

$$(100)_{\text{T}} \,//\, (112)_{\text{Al}}, (001)_{\text{T}} \,//\, (1\bar{1}0)_{\text{Al}}. \tag{2.18}$$

Chapter 3

Electron microscopy

This chapter introduces the basic underlying principles of electron microscopy (EM), electron scattering and imaging with TEM and STEM. The kinematical diffraction theory will be presented and briefly compared to the dynamical theory of diffraction. Approaches to simulate diffraction patterns based on both the kinematical and dynamical theory will be presented. At the end of the chapter, SPED will be introduced and various data analysis approaches will be presented. Most of the theory is based on Williams and Carter [116] unless otherwise stated.

3.1 Introduction to electron microscopy

The electron is a negatively charged subatomic particle with elemental charge $e \approx 1.60 \cdot 10^{-19}$ C and mass $m_0 \approx 9.11 \cdot 10^{-31}$ kg. It exhibits wave-like properties, according to the particle-wave duality in quantum mechanics. Its wavelength λ is given by $\lambda = h/p$, where h is Planck's constant and $p = \sqrt{2mE_0}$ is the momentum [117]. Inside the EM, the electrons are accelerated to tens or hundreds of keV in energy, $E_0 = eV_a$, with V_a being the applied acceleration voltage of the instrument. For high voltages, the electron velocity approaches the speed of light c, and relativistic effects must be taken into consideration. For an electron accelerated through a 200 kV potential, the obtained speed is 2.086×10^8 m/s ($0.7c$). Correcting for relativistic effects, the wavelength of an electron is given by [118]:

$$\lambda = \frac{h}{\sqrt{2m_0 eV_a(1 + \frac{e}{2m_0c^2})V_a}}. \tag{3.1}$$

The wavelength of an electron in a TEM operated at 200 kV is thus 2.51 pm. Historically, EM was developed due to the limited spatial resolution in visible light microscopes, imposed by the wavelength of visible light through the Rayleigh criterion, which states that the smallest distance that can be resolved, δ, is approximately [116]:

$$\delta = \frac{0.61\lambda}{\mu \sin \beta}, \tag{3.2}$$

where λ is the wavelength of the illumination source, μ is the refractive index of the viewing medium and β is the collection semi-angle of the magnifying lens. For simplicity, $\mu \sin \beta$ can be approximated to unity and the resolution is equal to about half the wavelength. For green light, in the middle of the visible light spectra, the wavelength is around 550 nm, yielding a resolution of a good visible light microscope of 300 nm. For EM, the meaning of resolution is different for the different operation modes of the instrument, but for the state-of-the-art instruments it is well below the 1 Å barrier [116]. This is still far above the wavelength-limited resolution. Due to the electrostatic lenses of the EMs being imperfect, i.e. they have substantial

aberrations, the experimental resolution is lower than the theoretical resolution. Aberrations will be further discussed in Section 3.1.2.

When the incident electron beam interacts with the specimen, several events may occur. The incident electrons interact with the electrons and nuclei within the sample through Coulomb forces, resulting in scattering. Fig. 3.1 shows the various signals generated when a high-energy incident electron beam interacts with a thin specimen.

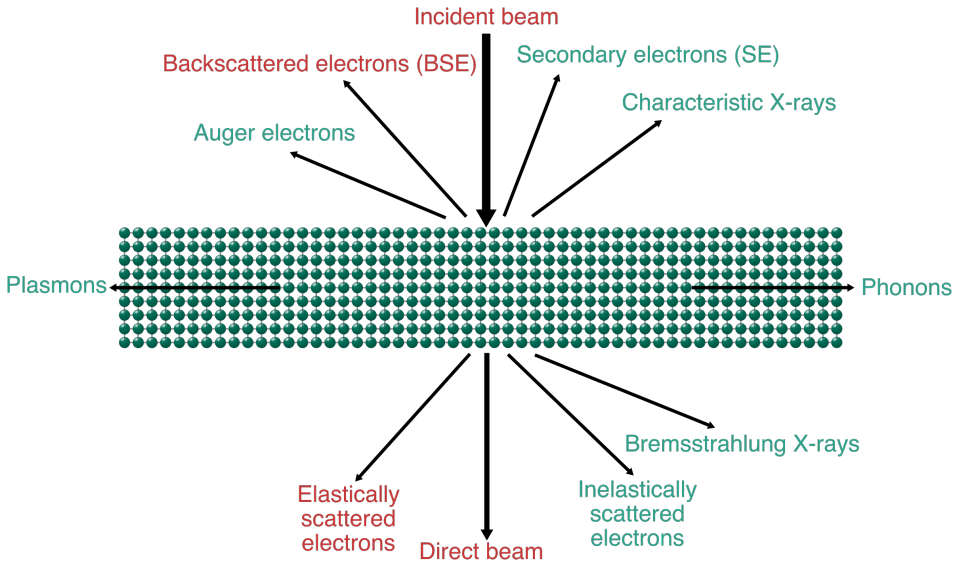

Figure 3.1: The different signals generated when high energy electrons interact with a thin specimen. The elastic scattering is indicated with red letters, whereas the inelastic scattering is indicated with green letters. Adapted from Figure 1.3 in Ref. [116].

The nature of the scattering can result in different angular distributions. The electrons can be either forward scattered or backscattered, referring to the scattering angle being $> 90°$ or $< 90°$ respectively. The *direct beam* contains mainly the electrons which are transmitted through the specimen in the same direction as the incident beam. Electron scattering can be classified as either *elastic* or *inelastic*, referring to scattering that conserves the energy or scattering that leads to some measurable loss in energy, respectively. In inelastic scattering, the energy transferred to the specimen can cause different signals such as *X-rays*, *Auger*- or *secondary electrons (SE)s*. There might also be inelastic scattering events following the creation of phonons or plasmons.

X-rays are generated by two main inelastic scattering mechanisms and hence two types of X-rays are observed in EM, namely *Bremsstrahlung*- and *characteristic X-rays*. The former have a continuous range of energies up to the energy of the incident electrons and are created by decelerated electrons deflected by the atom nuclei of the specimen. Characteristic X-rays are generated when more than a critical amount of energy is transferred to an inner-shell electron of the specimen and that electron is ejected, exciting the atom and leaving a hole. The hole is filled with an electron from a higher shell, this transition is accompanied by the emission of either an Auger electron or a characteristic X-ray. In both the Auger- and X-ray case, the

energy of the emission is the energy difference between the two electron shells and is unique for the element. Hence, the characteristic X-rays and Auger electrons can be used for chemical analysis of the specimen [119]. The SEs are used for image formation in scanning electron microscopy (SEM), showing the topology of the specimen surface. In addition to the SE, the elastically scattered *backscattered electrons (BSE)* are used for imaging in SEM.

All inelastic interactions described above lead to a a loss in energy of the incoming electron that interacted with the specimen. Such electrons are referred to as *inelastically scattered electrons* and their energy loss can be measured by electron energy loss spectroscopy (EELS) and can be used for chemical analysis of the specimen.

For TEM, the *elastically scattered electrons* are the most relevant and are used for imaging and diffraction experiments, which will be described in the Section 3.1.1. Being a wave phenomenon, electron scattering can be divided into *coherent* and *incoherent* scattering, referring to scattering where the phase of the electron wave is preserved or not, respectively. The inelastic scattering is almost always incoherent, while the elastic scattering typically becomes more incoherent at higher scattering angles [116].

3.1.1 Transmission electron microscopy

Fig. 3.2 shows the key components of a TEM, which comprise the electron gun, electrostatic lenses to focus the electrons both above and below the specimen and apertures to control which electrons contribute to the final image. In addition, the beam is controlled by deflection and scan coils, which are omitted for simplicity in the figure. Note that several more components and lenses might be included in the instrument, but for clarity, only the main components are included in the figure. The electrons are generated by the electron gun and accelerated at typically 80-300 kV to relativistic speeds through an accelerating field. The electrons travel down the TEM column and are controlled by several electrostatic lenses, apertures and deflector coils. The TEM consists of three essential components: The *illumination system*, *objective system* and *imaging system* [116]. The illumination system, consisting of the electron gun and condenser lenses, takes the electrons and transfers them onto the specimen either as a broad or focused beam. The first condenser lens (C1) demagnifies the electron source and controls the brightness of the beam and which region of the sample is illuminated. C1 also affects the probe size on the specimen [120]. It is the second condenser lens (C2) along with the condenser aperture, which is inserted under the condenser lenses, that controls the *convergence angle*, α, of the beam.

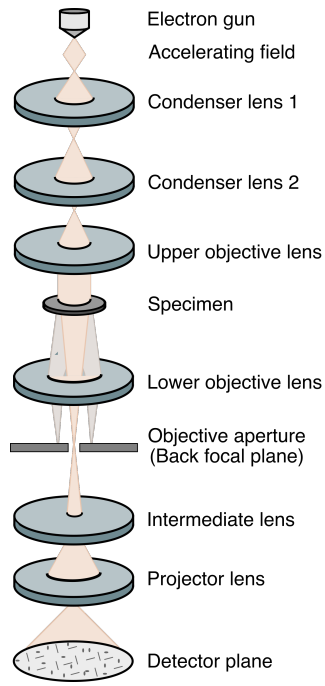

Figure 3.2: Schematic of the key components in a TEM. Adapted from [119].

The objective system consists of objective lenses, and the objective aperture. The specimen is situated between the upper and lower pole-pieces of the objective lens and it needs to be electron transparent, i.e. thin enough for electrons to be transmitted. This varies from material to material, but as a rule of thumb, the specimen typically needs to be thinner than 100 nm at an operation voltage of 200 kV [116, 119].

Following the electron-specimen interactions, some electrons have changed their direction. For crystalline specimens, this occurs through *diffraction*, which will be discussed in detail in Section 3.2. The electrons scattered to the same angle will converge in the *back focal plane* of the objective lens. The objective lens focuses the transmitted electrons to form a *diffraction pattern* in its back focal plane and an image in its image plane.

The intermediate lens of the imaging system controls what mode the instrument is operated in. The object plane of the intermediate lens can be adjusted to coincide with the image or back focal plane of the objective lens. Hence, the TEM can be operated in either imaging or diffraction mode. Typically, the instrument is equipped with several detectors. Today, the most common detectors for imaging and diffraction are *charge-coupled device (CCD)* cameras. One major drawback of such detectors is that they are coupled to a scintillator that converts the electrons to visible light phonons before converting these to electrical signals. This reduces the *detective quantum efficiency (DQE)* of the detector, a quantity that affects the detection efficiency and signal-to-noise ratio of the images [121]. In the recent years, so-called *direct electron detectors* have become commercially available. These detectors cound the individiual events, leading to a higher DQE as compared to the CCD cameras [121, 122].

Above, the TEM hardware was briefly described. In order to be useful, the collected signal needs to be understood. The intensity variations in diffraction patterns are discussed in Section 3.2. The contrast in TEM images is dependent on the geometry of the electron illumination, the electron scattering and which electrons one allows to contribute to the image. In *conventional transmission electron microscopy (CTEM)*, the illumination onto the specimen is parallel. The apertures control which electrons contribute to the image and two different imaging modes are available in CTEM. In *bright-field (BF) imaging*, the objective aperture is placed such that only the central beam contributes to the image. Thus, only the unscattered electrons contribute to the image. Hence, regions that scatter actively will have fewer electrons and therefore a darker contrast [119]. This is known as *diffraction contrast*. The other imaging mode is facilitated by placing the objective aperture such that the central beam does not contribute to the image. This is known as *dark-field (DF) imaging* and in such images, the regions in the image that scatter more will appear brighter as compared to the regions that scatter less. This imaging mode facilitates a high contrast, but the signal is weak and hence a longer exposure time is needed as compared to BF imaging. Regions with increased thickness and mass will also increase the electron scattering, this is known as *mass-thickness contrast* [119].

In diffraction mode in CTEM, the selected area aperture, situated in the image plane of the objective lens, limits the region generating the diffraction pattern. This is known as *selected area electron diffraction (SAED)*. Detailed analysis of diffraction patterns can determine the crystallography of the region of the sample generating the diffraction pattern, including lattice type, point group, lattice parameter, phase orientation relationships, presence of clusters/precipitates and more. Diffraction theory and different diffraction modes will be the focus in the Sections 3.2 and 3.3.

3.1.2 Scanning transmission electron microscopy

In the previous section, a static, parallel beam is used. Such imaging modes are typically referred to as CTEM to differentiate it from techniques using a convergent probe. In *scanning transmission electron microscopy (STEM)*, a convergent probe, formed by C1, C2 and the condenser aperture (Fig. 3.2) is incident on the specimen. The probe is scanned in a raster pattern over a region of interest using scanning coils situated above the specimen. On each scan position, the electron probe propagates through the specimen. Since the electron probe is convergent, the diffraction pattern is a *convergent beam electron diffraction (CBED)* pattern, containing disks instead of the spots characteristic for a SAED pattern. If the convergence angle, α, is large enough, the disks will partially overlap. The coherent, partial overlap of the diffraction disks is a requirement for resolving a given crystal spacing in atomically resolved STEM images [123]. A probe that is of the size of the atomic spacing of the crystal to be resolved is another necessity for atomic resolved imaging with STEM.

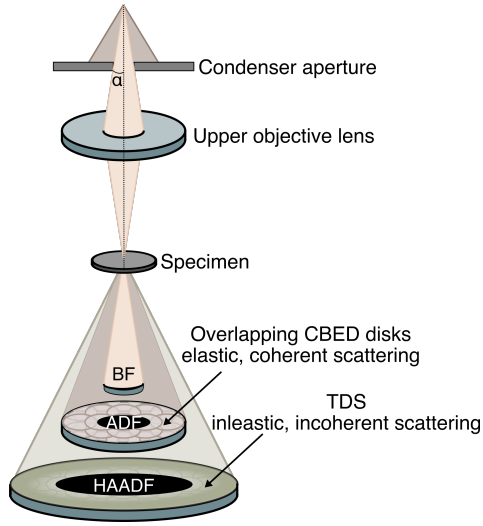

Figure 3.3: Schematic of the key components in a STEM. Inspired by Fig 3.1 in Ref. [123].

It is common for the TEM instruments to be equipped with scanning coils enabling the acquisition of STEM and TEM images on the same instrument. Fig. 3.3 shows the key components and typical detector configurations for STEM. The condenser aperture is inserted to control the convergence angle, α. The probe is formed by the upper pole-piece of the objective lens. It is the electron probe size that is decisive for the resolution in STEM. The width of the electron probe increases with increasing electron wavelength and decreasing α. This is known as the *diffraction limit*. Only in the case that $\alpha \to \infty$ or $\lambda \to 0$, is the electron probe point-like [123].

As mentioned in Section 3.1.1, the magnetic lenses of the TEM are imperfect due to considerable aberrations. The lens aberrations cause the electrons to be spread out over some region of space rather than to a focused point. Several aberrations exist, but the spherical aberration, C_s, is the most important aberration of the objective lens. For small convergence angles, the diffraction limit is the factor limiting the probe size, while for larger α, the spherical aberration becomes the limiting factor. Hence, balancing the diffraction limit and the spherical aberration is key to form a sufficiently small electron probe to facilitate atomically resolved STEM [123]. The defocus should be set so that the spherical aberration is minimised. Aberration correction for STEM was developed to cancel out the positive C_s from the objective lens by fitting the microscope with extra lenses. This development enabled characterisation at length scales not previously attainable and the 2020 Kavli prize in nanoscience was awarded to Harald Rose, Maximilian Haider, Knut Urban and Ondrej L. Krivanek for their contributions to construction of aberration corrected lenses which ultimately enabled sub-ångstrøm imaging and chemical analysis. For a full introduction to aberrations and probe size limiting factors for STEM, the reader is referred to Ref. [123].

Typically, a set of detectors is situated in the back focal plane of the objective lens, allowing the recording of multiple signals simultaneously. Due to the high *depth of focus* in TEM, the detectors can be placed above each other in the back focal plane. The contrast in STEM images is dependent on the position and size of the detector. A detector recording the signal from the direct beam produces a *BF-STEM* image. Annular detectors also exist, enabling the simultaneous acquisition of BF- and *annular dark-field (ADF)-STEM* images. The size and angular extent of the detector are described by the *inner*- and *outer collection angles*. For BF-STEM, the inner collection angle is 0 mrad, while the outer collection angle is typically less than 10 mrad [116]. If the inner collection angle is increased to around 50 mrad, one typically describe the resulting image as a HAADF-STEM image. The images resulting from using inner collection angles between the BF-STEM- and HAADF-STEM inner collection angles are typically referred to as ADF-STEM images. As the inner collection angle is increased, the collected signal is increasingly incoherent, yielding more directly interpretable images [124].

By increasing the inner collection angle, the coherent elastic scattering is reduced and *thermal diffuse scattering (TDS)* becomes the dominant contribution to a signal collected by a large, annular detector. TDS is inelastic scattering where the incident electrons excite thermal vibrations of atoms in the specimen and are scattered in a diffuse manner. The resultant signal is essentially incoherent. High-angle electron is dominated by Rutherford scattering and the contrast in HAADF-STEM images approaches Z^2, which is the Z dependency of pure Rutherford scattering [123, 125]. Hence, light elements appear dark, while heavy elements appear bright in a HAADF-STEM image. HAADF-STEM is often referred to as *Z-contrast imaging* due to its atomic number dependence. For aluminium oriented in the [001]Al zone axis, the criteria for lattice imaging is a probe size smaller than 2.025 Å. As mentioned, the state-of-the-art instruments, equipped with C_s correctors, can resolve spacings below 1 Å. It is thus straightforward for an adequate microscopist to resolve the aluminium lattice in this orientation. The crystal structure of many precipitate phases in Al alloys has been solved by using HAADF-STEM in the recent years [12, 19]. This technique is employed in Papers I-V to investigate the structure of both GP zones and precipitates.

3.2 Electron diffraction theory

From Section 3.1, it became clear that understanding electron diffraction is essential for interpreting the contrast in images obtained in CTEM and STEM. In this section, electron diffraction theory under the *kinematical approximation* will be presented. In contrast to *dynamical diffraction theory*, we assume single, elastic scattering events. In addition, the scattering is assumed to be coherent. This is a crude simplification for electron scattering in TEM, since for a typical specimen thickness, the strong electron-matter interaction leads to multiple scattering. The occurrence of multiple scattering increases with increasing specimen thickness and only diffraction from sufficiently thin specimens ($t < 10$ nm) can be considered kinematical. The kinematical approximation is however useful in defining important quantities in diffraction, such as atomic scattering and crystal structure factors and for applications where the positions of the diffracted beams is the major consideration. The diffracted intensities in a 2-beam condition will be derived under the assumption that the amplitude of the scattered wave is much less than the amplitude of the incident wave. This approximation is known as the *Born approximation*. At the end of this section, the diffracted intensities in a 2-beam case from dynamical theory will briefly be presented and compared to the result obtained from the kinematical theory. The last section considers simulations of electron images and diffraction patterns.

3.2.1 Reciprocal lattice

The *reciprocal lattice* represents the Fourier transform of the *Bravais lattice* of the crystal. A Bravais lattice is described by:

$$\vec{R} = u\vec{a_1} + v\vec{a_2} + w\vec{a_3}, \tag{3.3}$$

where u, v and w are integers and $\vec{a_1}$, $\vec{a_2}$ and $\vec{a_3}$ are the primitive vectors. The Miller indices of a crystallographic plane are denoted (hkl). The interplanar spacing between crystallographic planes is denoted d_{hkl} and is for a cubic crystal given by:

$$d_{hkl} = \frac{a}{h^2 + k^2 + l^2}, \tag{3.4}$$

where a is the lattice parameter of the crystal. The *reciprocal lattice vector*, $\vec{g}_{hkl}$, is given by:

$$\vec{g}_{hkl} = h\vec{a_1}^* + k\vec{a_2}^* + l\vec{a_3}^*, \tag{3.5}$$

where $\vec{a_1}^*$, $\vec{a_2}^*$ and $\vec{a_3}^*$ are the primitive vectors of the reciprocal lattice and are given by $\vec{a_i}^* \cdot \vec{a_j} = 2\pi\delta_{ij}$. A SAED pattern can be seen as the two-dimensional projection of the reciprocal crystal lattice. The diffraction spots correspond to the individual crystallographic planes (hkl) that satisfy the diffraction conditions. The reciprocal lattice is hence a useful concept for understanding diffraction.

3.2.2 Conditions for diffraction

An incident electron wave with wave vector $\vec{k}_0$ with $|\vec{k}_0| = 1/\lambda$ is scattered by the lattice planes of a crystal if the wavelength λ is comparable to the atomic spacings, d_{hkl}. This is illustrated in Fig. 3.4a. If the scattered waves from successive planes are in phase, constructive interference occurs. This is fulfilled if the path length difference, $2d_{hkl}\sin\theta_B$ is equal to an integer number, n, of wavelengths [117]:

$$2d_{hkl}\sin\theta_B = n\lambda. \tag{3.6}$$

This is known as *Bragg's law*. The particular angle θ_B satisfying the above equation is known as the *Bragg angle*.

An alternative way of formulating the conditions for diffraction is known as the *Laue condition*. This condition is illustrated in Fig. 3.4b and states that at the Bragg condition, in reciprocal terms, we have:

$$\Delta\vec{k} = \vec{k} - \vec{k}_0 = \vec{g}_{hkl}. \tag{3.7}$$

In this form, Bragg's law and the Laue condition are equivalent. For elastic scattering, we have that $|\vec{k}_0| = |\vec{k}|$. The Laue condition is particularly useful for constructing the *Ewald sphere*. The radius of the Ewald sphere is $|\vec{k}| = 1/\lambda$. According to this formulation, only reciprocal lattice points that lie on the surface of the Ewald sphere fulfill the Laue condition and hence

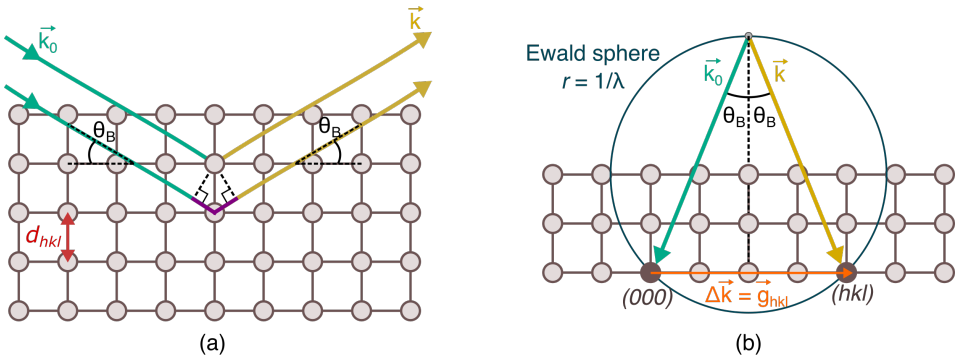

Figure 3.4: a: Schematic showing Bragg diffraction by a set of lattice plane for an incident plane wave $\vec{k}_0$ at the Bragg angle θ_B. b: Schematic of the Laue condition and Ewald sphere construction. a and b are inspired by Figures 3.1 and 3.5 in Ref. [117], respectively. Note that in electron diffraction experiments, λ is small, yielding a large Ewald sphere radius.

only such reciprocal lattice points contribute to diffraction. Due to the small wavelength λ of the electron waves in TEM, the radius of the Ewald sphere is much larger than the distance between the reciprocal lattice points and hence many reflections are typically visible in zone axis electron diffraction patterns.

According to the Laue condition in Eq. 3.7, no diffraction spots should be visible in a diffraction pattern if the electron beam is exactly parallel to any zone axis. However, in zone axis electron diffraction patterns, many diffraction spots are visible. Hence, there is intensity in the diffracted beams even though the Bragg condition is not exactly satisfied. Due to the geometry of the TEM specimen, i.e. the specimen thickness being much smaller than the lateral dimensions, the reciprocal lattice points will extend as rods with their major axis perpendicular to the specimen thickness. These rods are called *reciprocal lattice rods*, or *relrods* for short [118]. This is illustrated in Fig. 3.5, where the reciprocal lattice points are substituted with relrods. The relrods intersect the Ewald sphere in the zeroth-order Laue zone (ZOLZ), first-order Laue zone (FOLZ), second-order Laue zone (SOLZ) and higher-order Laue zones (HOLZ). Laue zones are defined as the reciprocal lattice planes perpendicular to the direction of the incident beam, as depicted in the figure. HOLZ is the umbrella term for all Laue zones above the ZOLZ.

The actual intensity of a diffracted beam is dependent on the deviation from the Bragg condition. This quantity is known as the excitation error, $\vec{s}$ and it is defined as the distance between the reciprocal lattice point and the Ewald sphere along the major axis of the relrod. When Bragg's law is accurately satisfied, $\vec{s} = 0$. The sign convention for s is shown in Fig. 3.5: s is positive if the reciprocal lattice point lie inside the Ewald sphere and negative outside.

3.2.3 Kinematic diffraction intensities

Bragg's law (Eq. 3.6) and the Laue condition (Eq. 3.7) say something about which Bragg angle θ_B and which reciprocal lattice point give rise to diffraction, respectively. They do not say anything about the intensity of the diffracted beams. We will now derive an expression for the intensity of a diffracted beam under the 2-beam condition for crystalline materials. I.e. we only consider the direct beam and one diffracted beam and lattices that can be described by a translational vector as in Eq. 3.3.

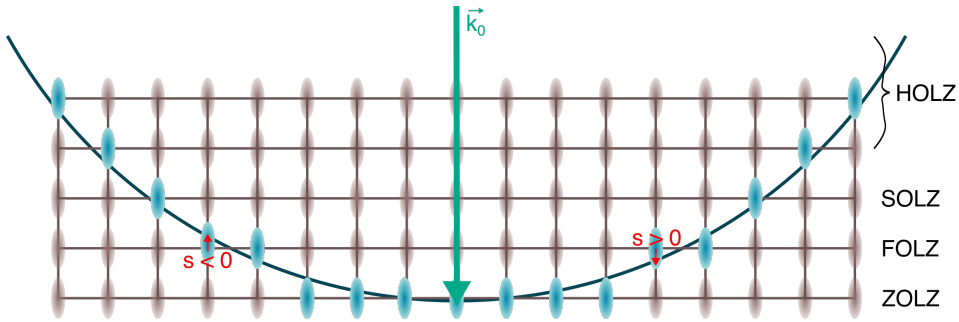

Figure 3.5: Schematic of the Laue condition taking the excitation error $\vec{s}$ into account. The reciprocal lattice points are replaced with relrods due to the geometry of the TEM specimen. The distance from the center of the relrod to the Ewald sphere is s. The Ewald sphere intersects relrods in the ZOLZ, FOLZ, SOLZ and HOLZ. Adapted from Fig. 1 in Ref. [126].

The intensity of a diffracted beam is proportional to the amplitude of the scattered wave squared, $|F(\Delta\vec{k})|^2$. A defect-free crystal can be explained as [*crystal structure*] = [*lattice*] $\circledast$ [*basis*]. The *lattice* is the Bravais lattice of the crystal, while the *basis* is the arrangement of atoms associated with each lattice point. $F(\Delta\vec{k})$ can be described as the Fourier transform of the crystal structure. Following the convolution theorem, which states that the Fourier transform of a convolution of two functions is the point-wise product of their Fourier transform, we obtain the following expression for the amplitude of the scattered wave [127]:

$$F(\Delta\vec{k}) = F_{basis}(\Delta\vec{k})F_{lattice}(\Delta\vec{k}) = F_{hkl}F_{lattice}(\Delta\vec{k}), \tag{3.8}$$

where $F_{basis}(\Delta\vec{k})$ is the scattering amplitude of the basis, known as the *structure factor* F_{hkl} and $F_{lattice}(\Delta\vec{k})$ is known as the *lattice amplitude* or *shape factor* and depends on the external shape of the crystal [127, 128]. For very large crystals the shape factor intensity can be approximated as a set of delta functions centered at the values of $\Delta\vec{k}$ where $\Delta\vec{k} = \vec{g}_{hkl}$. $\Delta\vec{k}$ is defined in Eq. 3.7 and has a magnitude of $2\sin\theta_B/\lambda$ for elastic scattering. Firstly, we will consider the F_{hkl} and its dependencies, before introducing an expression for the shape factor. The structure factor F_{hkl} is given as [127]:

$$F_{hkl} = \sum_{j=1}^{N} f_j(\Delta k)e^{[-2\pi i(hx_j+ky_j+lz_j)]}. \tag{3.9}$$

The sum is over all atoms in the unit cell, x_j, y_j, z_j are the coordinates of the j-th atom and $f_j(\Delta k)$ is the *atomic scattering factor* of the j-th atom. $f_j(\Delta k)$ is a measure of the scattering amplitude of a wave by an isolated atom. It depends on the scattering and consequently on the type of radiation used. For electrons, it is defined as the Fourier transform of the atomic potential. For an atom with atomic number Z, the electron scattering factor $f(\Delta k)$ is related to the X-ray scattering factor f_x through the Mott-Bethe formula [129]:

$$f(\Delta k) = \frac{1}{2\pi^2 a_0}\frac{Z - f_x(\Delta k)}{\Delta k^2}, \tag{3.10}$$

where a_0 is the Bohr radius. f_x is the Fourier transform of the electron charge density. Since X-rays are scattered by the electron cloud of the atom, f_x increases with the atomic number Z. The atomic scattering factor for electrons is hence dependent on the wavelength λ and the scattering angle θ_B through Δk, and the atomic number Z. Consequently, the intensity $I \propto |F_{hkl}|^2$ is dependent on the type of atom through $f(\Delta k)$, the position of the atoms in the unit cell and the atomic planes of the crystal. For a thorough discussion on atomic scattering factor, the reader is referred to Ref. [127]. The structure factor F_{hkl} in Eq. 3.9 can be solved for a given lattice and gives rise to the so-called *extinction rules*. The extinction rules imply that according to the lattice type, only certain diffraction indices hkl are allowed. For e.g. the FCC lattice, only such hkl that either all are even or all odd are allowed, hence 200 is allowed and 110 is not.

Thermal scattering was neglected in the above treatment. The atoms in the crystal are not stationary, they participate in thermal motion related to the finite temperature of the material. This effectively leads to an increase of the space occupied by an atom and a displacement term $\vec{u}_n(t)$ must be added to the position of atom n at time t. This causes a decrease in the intensity of the Bragg peaks which is redistributed to appear as *thermal diffuse scattering* between the diffracted beams. This can be accounted for by adding a damping factor, e^{-W}, where W is known as the *Debye-Waller* factor, to the structure factor in Eq. 3.9 [130].

To derive an expression for the shape factor $F_{lattice}(\Delta\vec{k})$, the crystal is assumed to be a parallelepiped with edge lengths $L_i = M_i a_i, i =$ (1,2,3) parallel to the lattice parameters $\vec{a}_i$ defining the crystal structure. The shape factor under these assumptions is given as [127]:

$$F_{lattice}(\Delta\vec{k}) = \sum_{m}^{M_1}\sum_{n}^{M_2}\sum_{o}^{M_3} \exp\left[-2\pi i(\Delta\vec{k} + \vec{s}) \cdot \vec{r}_g\right], \tag{3.11}$$

where $\vec{r}_g$ is a translational vector, $\vec{r}_g = m\vec{a}_1 + n\vec{a}_2 + o\vec{a}_3$, describing the lattice and m, n, o are integers. It is the shape factor that will be altered by the deviation parameter $\vec{s}$, while the structure factor F_{hkl} is constant for varying $\vec{s}$ (Eq. 3.9). Due to the phase $2\pi i(\Delta_k + \vec{s})$ varying slowly as we move from one unit cell to another, the triple sum can be replaced by an integral over the crystal volume and the following expression is obtained:

$$F_{lattice} = \frac{\sin(\pi s_x L_1)}{\pi s_x a_1}\frac{\sin(\pi s_y L_2)}{\pi s_y a_2}\frac{\sin(\pi s_z L_3)}{\pi s_z a_3}. \tag{3.12}$$

In TEM, the specimens must be electron transparent, i.e. typically thinner than 100 nm. The specimen can hence be approximated as a thin plate of thickness t (=L_3) which is much less than its lateral dimensions, L_1 and L_2. The two terms in Eq. 3.12 involving L_1 and L_2 tend to approach δ functions for large values of L_1 and L_2 and the shape factor for TEM specimens approximated as thin plates can be described by [130]:

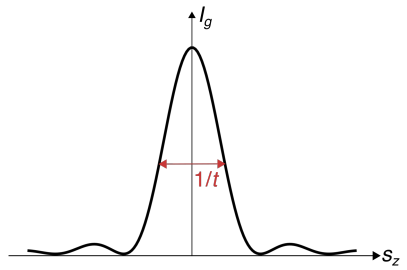

Figure 3.6: Intensity I_g as a function of the excitation error s_z.

$$F_{lattice} = \frac{L_1 L_2}{V_{cell}} \frac{\sin(\pi s_z t)}{\pi s_z} \delta(s_x)\delta(s_y), \tag{3.13}$$

where V_{cell} is the volume of the unit cell. The total intensity in the g'th diffracted beam from a crystal of thickness t will under the kinematical approximation be given as:

$$I_g(t) = \left(\frac{\pi}{\xi_g}\right)^2 \left(\frac{\sin(\pi t s_z)}{\pi s_z}\right)^2, \tag{3.14}$$

where ξ_g is the *extinction distance* and is given as $\pi V_{cell}/\lambda F_{hkl}$. The intensity I_g is shown as a function of s_z in Fig. 3.6. The full width at half maximum (FWHM) in reciprocal space is approximately $1/t$. This is the origin of the reciprocal lattice points extending to relrods of width $1/t$ in Fig. 3.5.

3.2.4 Limitations of the kinematical theory

As mentioned initially, the kinematical theory is only valid for very thin specimens where $I_g \ll 1$ and the decrease of the intensity in the direct beam can be neglected. From Eq. 3.14, the intensity of the diffracted beam I_g increases with t^2 when the Bragg's law is fulfilled, i.e. when $s_z = 0$. In such cases, the condition $I_g \ll 1$ is only valid for $t < \xi_g/10$. With typical extinction distances in the range of few hundred Å, $t < 10$ nm sets a threshold for the validity of the kinematical theory. We might expect the kinematical theory to be valid if $I_g \approx 0.1$. F_{111} for Al has been found to be approximately 8.87 e^-/atom [131], assuming a specimen thickness of 10 nm and s_z = 0, I_{111} is approximately 0.1. As a typical TEM specimen has a thickness of 40-100 nm, it is clear that the kinematical theory of diffraction does not hold for typical TEM experiments. For this, the dynamical theory of diffraction needs to be considered to appropriately calculate the diffracted intensities. However, for qualitative interpretation of diffracted intensities and image contrast, the kinematic theory is an adequate first approximation.

Furthermore, we have assumed that only one Bragg reflection is excited, i.e. a two-beam case. In electron diffraction experiments, most often a larger of numbers of reflections is considered. This is related to the large radius of the Ewald sphere, see Fig. 3.5, having the consequence that many relrods intersect the Ewald sphere in a zone axis orientation. Instead of an intensity redistribution between the direct and one diffracted beam, it is between the direct and many different beams. The n-beam case reduces the validity of the kinematical theory to even smaller thicknesses, since multiple intensities I_g can reduce the intensity of the direct beam even more [127].

In deriving Eq. 3.14, only elastic scattering was considered. This is a simplification, since the electrons also undergo inelastic scattering during their interaction with the specimen. The inelastic scattering is often accounted for by adding an imaginary term to the potential $iV'(\vec{r})$ to represent absorption [130]. The magnitude of $V'(\vec{r})$ is typically less than or equal to one-tenth of the real part of the potential $V(\vec{r})$. Inelastic scattering causes the incident electrons to be scattered angularly out of the Bragg-reflected beams. In the kinematical theory, inelastic scattering is not of interest. However, the inelastic signal itself can be of value when analysed separately, for example for chemical analysis by energy-dispersive X-ray spectroscopy (EDS) or EELS [128].

3.2.5 Brief note on dynamical theory

In the above treatment, the kinematical theory of diffraction was introduced. It became clear that the dynamical diffraction theory was necessary to appropriately calculate the intensity distribution of the diffracted beams for real specimens. Obtaining expressions for the diffracted intensities using dynamical theory involves solving the Schrödinger equation for the wavefunction $\Psi(\vec{r})$ of the fast electrons. This becomes more complex as we increase the number of diffracted beams. Now, we will briefly consider the main results from the dynamical theory under the two-beam approximation.

This theory shows that in the general case. i.e. neglecting absorption, the direct and diffracted beam intensities, $I_0(t)$ and $I_g(t)$, may be shown to be [130]:

$$I_0(t) = I - I_g(t) \tag{3.15}$$

$$I_g(t) = \left(\frac{\pi}{\xi_g}\right)^2 \left(\frac{\sin(\pi t s'_z)}{\pi s'_z}\right)^2, \tag{3.16}$$

where

$$s'_z = \left(s_z^2 + \xi_g^{-2}\right)^{1/2}. \tag{3.17}$$

The form of Eq. 3.16 is similar to the result obtained from the kinematical theory in Eq. 3.14. The difference is however important, since in most electron diffraction experiments, only small deviations from the Bragg condition, s, is considered and s' is thus significantly different from s. The intensities diffracted at the Bragg condition, $s = 0$, is zero for $t = n\xi_g$ (n an integer) and there are thicknesses $t = (n + 1/2)\xi_g$ where the intensity is completely concentrated in the Bragg reflections. This is the reason why ξ_g is called the extinction distance. This means that the electron intensity oscillates between the direct and the Bragg reflected beams as a function of t. This is known as *pendellösung* of the dynamical theory describing the interaction between the direct and diffracted beam. If $s' \approx s$, the diffracted beam is very weak and the kinematical approximation may be useful under such conditions.

To summarise, kinematical theory describes the intensity distribution in coherent electron diffraction and is often adequate for qualitative analysis of diffracted intensities. For more quantitative interpretations using variations in diffraction maxima, the dynamic theory is needed. The electron-matter interaction is strong and the kinematical theory breaks for typical specimen thicknesses studied in TEM. This comes at the expense of more complex calculations as the dynamical n-beam case must normally be treated numerically. Different approaches exist and the multislice approach will be introduced in the next section, in regards to simulating electron diffraction patterns. Dynamical simulations are computationally heavy and hence it has been of interest to develop new electron diffraction techniques in which the diffracted intensities are more similar to the ones predicted by the kinematical theory. One such development is *precession electron diffraction*, which averages the diffracted intensity over a cone of incident beam directions. This is the basis for Section 3.3.

3.2.6 Electron diffraction simulations

When doing electron diffraction experiments, one often needs to simulate electron diffraction patterns or images for different phases and orientations. Different approaches exist and in the following we will consider the approaches used in this thesis: a kinematical approach and an approach for solving the n-beam condition for dynamical theory, namely *multislice simulations*.

Kinematical simulations

One approach for simulating electron diffraction patterns in terms of the kinematical theory is to consider which reciprocal lattice points intersect the Ewald sphere (Fig. 3.4b) and can be summarised as follows:

1. Calculate the reciprocal lattice of the structure. Find all reciprocal points within a sphere with radius *reciprocal radius*. This will determine the field of view in reciprocal space.
2. Determine which reciprocal lattice points g_{hkl} (corresponding to lattice plane (hkl)) intersect the Ewald sphere given a maximum excitation error s_{max}. s_{max} is the length of the relrods.
3. The intensity of each reflection is proportional to the modulus square of the structure factor $I_{hkl} \propto F_{hkl}F^*_{hkl}$ (F_{hkl} is given in Eq. 3.9).
4. Only diffracted intensities over a certain threshold will contribute to the simulated diffraction pattern.

Diffsims [132], a sublibrary of pyxem, enables the simulations of electron diffraction patterns by the approach described above. The atomic scattering factors $f(\Delta k)$ (Eq. 3.10) are determined based on either Lobato *et al.* [129] or the *International tables of crystallography, Vol. C* [133]. Different *shape factor models* are implemented to account for the contribution of the shape factor $F_{lattice}(\Delta\vec{k})$ (Eq. 3.12) to the diffracted intensities.

Multislice simulations

The multislice method is schematically visualised in Fig. 3.7. An initial specimen model is approximated by thin slices with Δz spacings perpendicular to the direction of the incoming electron wave ψ_0 [134]. The electron wave is alternately transmitted through a slice and propagates to the next slice. This can be expressed mathematically by:

$$\psi_{n+1}(x,y) = t_n(x,y)\left[p_n(x,y,\Delta z_n \circledast \psi_n(x,y)\right], \tag{3.18}$$

where the wave function at the top of each slice is labeled $\psi_n(x,y)$ and the propagator and transmission functions for each slice are labeled $t_n(x,y)$ and $p_n(x,y,\Delta z_n)$, respectively. The initial wave function $\psi_0(x,y)$ is a plane wave in CTEM and the probe wave function in STEM. Each slice is thin enough to be interpreted as a weak phase object, i.e. the atomic potentials $V(\vec{r})$ slightly modify the phase of the electrons as they pass through the specimen, while the amplitude is constant [134].

Given a description of the potential $V(\vec{r})$ inside the specimen, the electron wave function can be calculated at any depth z inside the specimen by repeated application of Eq. 3.18. The

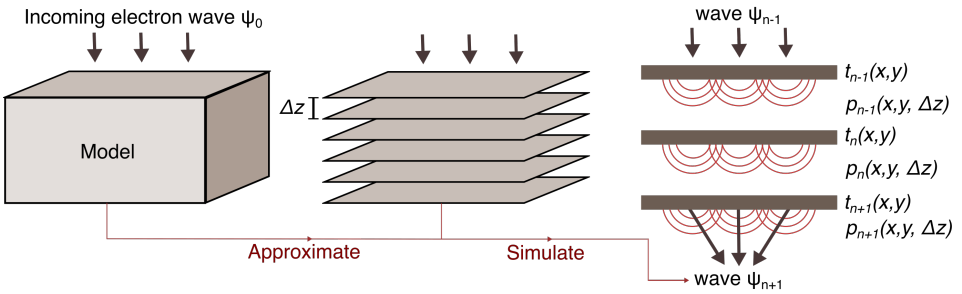

Figure 3.7: Schematic showing the principle of the multislice method. An initial model is approximated by thin slices and the electron wave is alternately transmitted (t) through a slice and propagates (p) to the next slice. Adapted from Ref. [134].

transmission function $t(x, y)$ can be associated with a phase grating approximation and the propagator function $p(x, y, \Delta z)$ can be associated with the Fresnel (near zone) diffraction over a distance Δz.

The convolution in Eq. 3.18 is computationally ineffective. This is overcome by solving the problem in Fourier space. Hence, the model needs to be periodic and sampled on a grid of size $N_x \times N_y = 2^n \times 2^n$. Typically, a bandwidth of 2/3 is also applied to avoid aliasing [134]. The resolution of the simulations is determined by the size of the model. Given a model with dimensions L_x and L_y in the x and y dimensions, the dimension of each pixel in reciprocal space is $\Delta k_x = 1/L_x$ and $\Delta k_y = 1/L_y$.

As mentioned in Section 3.1.2, thermal diffuse scattering is important for image contrast in HAADF-STEM. This is typically accounted for in multislice simulations by taking the average of multiple simulations, where each simulation is a result of a slightly different atomic configuration of the model. This is known as the *frozen phonon approximation*, where one assumes that the speed of electrons is much higher compared to the thermal vibration velocity of the vibrating atoms. By randomly shifting the atoms by a certain amount, limited by the Debye-Waller factors, between each multislice simulation, the thermal diffuse scattering is accounted for.

A variety of software packages exists for multislice simulations, examples include the MULTEM software developed by Lobato and Dyck [135] and μSTEM, developed by Allen *et al.* [136].

Whether a kinematical or dynamical simulation is required is dependent on the problem to be solved. If one is only interested in the positions (k_x, k_y) of the diffracted beams, a kinematical simulation might be sufficient. If however one is interested in the intensities, a dynamical approach is needed. For simulations of HAADF-STEM images, a dynamical approach is required, since the thermal diffuse scattering is neglected in the kinematical theory.

3.3 Scanning precession electron diffraction

Electron diffraction experiments allow insight into the crystal structure of the material and the microstructure the material exhibits. Stationary diffraction patterns can be captured, either by using a parallel or convergent beam with micrometer to nanometer diameter. In the former, the collected diffraction pattern will be from an extended region of the sample, determined by

the selected area aperture, as discussed in Section 3.1.1. Such patterns have poor spatial resolution and can be challenging to interpret in the presence of multiple microstructural features giving rise to distinct Bragg peaks, e.g. when multiple precipitates or clusters are present. In *nanobeam diffraction (NBD)*, the diffraction pattern is acquired from a nanometer region of the specimen. This is accomplished by converging the electron beam onto the sample using a small condenser aperture. In this mode, the Bragg peaks will appear as disks corresponding to the convergence angle, α, of the electron beam. This way of collecting data is particular useful for crystallographic analysis of precipitates or clusters since it enables the acquisition of diffraction pattern from single precipitates. In CBED, the convergence angle is larger and the probed region smaller than in NBD and the intensities inside the disks are often complex and can only be described by the dynamical diffraction theory.

In addition to collecting stationary diffraction patterns, the scanning coils also enable the acquisition of 4D-STEM datasets [18]. In 4D-STEM, 2D diffraction patterns are collected over a 2D grid of probe positions. This way of collecting data is particular useful for obtaining statistics of relative phase fractions in multi-phase materials. Even though STEM has existed since the middle of the 20th century, large scale 4D-STEM experiments were enabled only in the recent years through the development of fast detectors and cheap computer storage [137]. Typical experiments require the storage and analysis of datasets of several gigabytes. Clearly, analyses are driven by computational methods for interpreting the data. Data analysis of such datasets will be the topic of Section 3.4. 4D-STEM can be classified by how the specimen is illuminated, i.e. by the probe size and convergence angle α.

A subclass of 4D-STEM is *scanning precession electron diffraction (SPED)*. In PED, the static probe is replaced with a dynamic hollow cone of illumination, precessing the Ewald sphere through the volume of reciprocal space. Below the specimen, the beam is de-precessed to obtain a static pattern exhibiting the original diffraction pattern geometry [137–139]. The net effect is equivalent to precessing the sample about a fixed beam parallel to the optic axis. The key components in PED are shown in Fig. 3.8. The inner angle of the hollow cone is $\phi - \alpha$, while outer angle is $\phi + \alpha$, where ϕ is the *precession angle* which typically is less than 0.1-3° depending the application. SPED is enabled by scanning the hollow cone probe over the specimen and collecting the resulting PED pattern at each probe position. The probe size is typically a nanobeam probe with diameter $\approx$ 1 nm, yielding small disks in the diffraction pattern. The diameter of the probe is affected by the precession, since precession involves tilting the beam away from the optic axis of the probe forming lens. The spherical aberration of this lens causes the probe diameter to increase [139, 140].

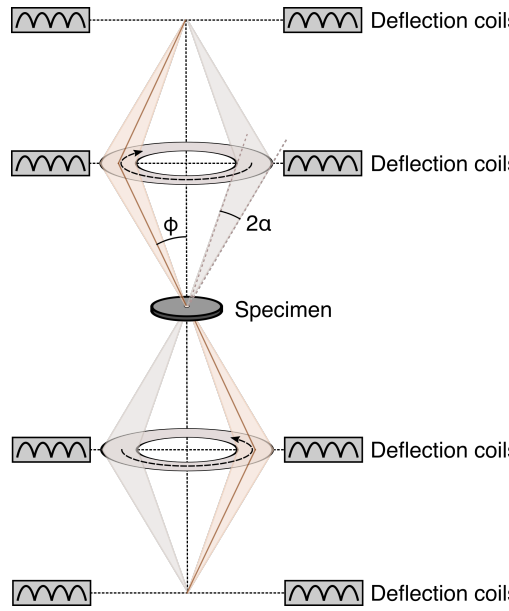

Figure 3.8: Schematic ray diagram for precession electron diffraction. Inspired by Fig. 1 in Ref. [138].

The incoming beam is tilted ϕ degrees off the optical axis by the deflector coils and subsequently rotated at incremental steps above the specimens. Hence, a zone axis PED pattern is collected by integrating multiple off-axis probe positions. This influence the diffracted intensities. Firstly, more Bragg peaks are excited and one probes further into reciprocal space as compared to NBD, hence more reflections are visible in the ZOLZ and HOLZ. This is schematically illustrated in Fig. 3.9. Moreover, since less beams are simultaneously excited, the final pattern contributions from the dynamic diffraction seem reduced [141]. The intensity within each diffracted disc is integrated over a range of angles, effectively averaging out the complex intensity variations stemming from dynamical effects [139] and intensity variations due to thickness variations and bending are strongly reduced. PED patterns are often referred to as 'kinematical like' due that the diffracted intensities in PED patterns and kinematic electron diffraction simulations are more similar as compared to unprecessed patterns [117, 138].

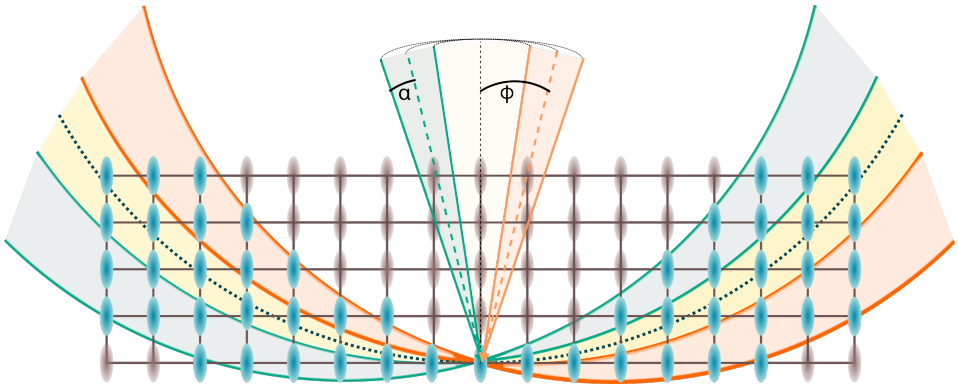

Figure 3.9: Schematic showing the effect of precession on the Ewald sphere construction. An incoming beam with convergence angle α is precessed around the optical axis at a precession angle ϕ. The precessing causes the excitation of more relrods as compared to a stationary beam. Adapted from Fig. 3.12 in Ref. [142].

3.4 Scanning precession electron diffraction data analysis

As a typical SPED dataset comprises > 100000 diffraction patterns, it is obvious that conventional image analysis is insufficient in investigating the data. Hence, *big data* approaches are typically the preferred analysis tools. In this section we will introduce various approaches for studying SPED datasets, with emphasis on the tools used in this thesis. Most of the analysis was done using *pyxem* [143], an open-source python library for multi-dimensional diffraction microscopy. pyxem is an extension of the hyperspy [144] library for multi-dimensional data analysis and defines diffraction specific signal classes. The dataset constitutes a *navigation space* (x, y) where each pixel has an associated *signal space* (k_x, k_y). Unless otherwise stated, pyxem was used for the analysis.

3.4.1 Virtual imaging

The simplest analysis of SPED data involves *virtual imaging* [18, 137]. This is realised by placing 'virtual' apertures in the diffraction patterns at each probe position and integrate the intensity within the aperture, similar to placing the objective aperture into the back focal plane of the objective lens when doing BF- and DF imaging introduced in Section 3.1.1. In compar-

ison to conventional imaging however, one has full flexibility in choosing the size and geometry of the apertures when doing virtual imaging. This is exemplified in Fig. 3.10 where five circular, virtual apertures are placed in the SPED data stack. The pattern corresponding to the maximum of each pixel in reciprocal space is shown in Fig. 3.10, the virtual apertures used to create the virtual images in Fig. 3.10b-f are indicated. Fig. 3.10b corresponds to a virtual bright-field (VBF) image. The virtual dark-field (VDF) images in Fig. 3.10 demonstrate how the virtual apertures can be employed to highlight certain precipitates in real space. This dataset is used in Paper IV.

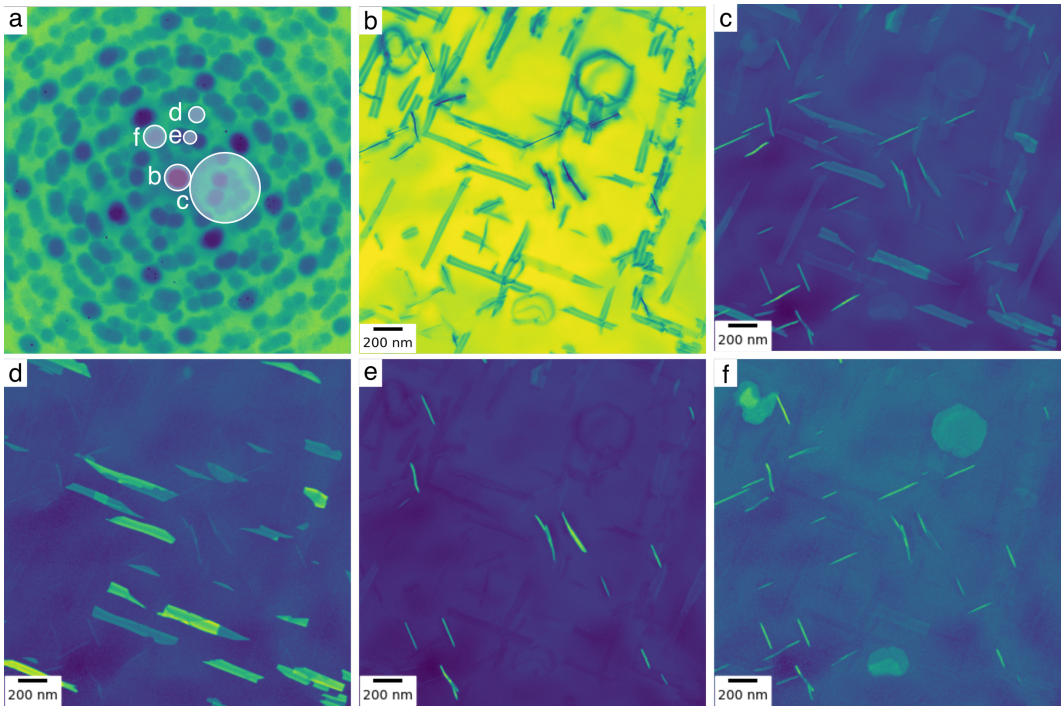

Figure 3.10: Demonstration of virtual imaging. In a, the maximum pattern is shown and virtual apertures corresponding to the virtual images in b-f are indicated.

3.4.2 Machine learning

Broadly speaking, machine learning aims at recognizing patterns in data, one example being image recognition [145]. The learning aspect usually involves minimizing a function, often referred to as the *cost function* or *loss function*, which is an estimate on how well the model is performing. The algorithms run iteratively until a local, or preferably global minima, of the cost function is reached. Machine learning is typically divided into *supervised learning* and *unsupervised learning*, referring to whether the training requires labeled data or not, respectively.

In general, we have a set of n samples containing some data, $\mathbf{X}$, that we want to predict. The data of interest in this thesis is a set of $n = N_{xy}$ diffraction patterns, with N_{xy} being the pixels in real space, i.e. the number of probe positions in the dataset. Let us denote one diffraction pattern as $DP_\mu \in \mathbb{R}^{N_{k_x k_y}}$, where $\mu = 1, .., N_{xy}$. $N_{k_x k_y}$ are the number of pixels reciprocal space,

i.e. the size of the detector for the raw dataset. In supervised learning, each diffraction pattern is given a label $y_\mu \in \mathbb{R}^d$, most commonly $d = 1$. A typical task for supervised learning is *classification*, which is a predictive modeling problem where a label is predicted for a given input data DP_μ. In phase mapping, the label is which phase the diffraction pattern DP_μ corresponds to.

In unsupervised learning, we have the same type of input data, but no labels are available. One of the most basic tools of unsupervised learning is methods based on low-rank decomposition of the observed data matrix **X** into two components. Low-rank refers to the fact that the decomposed data has reduced rank as compared to the input data [145].

In the following we will consider the unsupervised learning technique *non-negative matrix factorisation (NMF)* and the supervised learning approach *artificial neural network (ANN)*, specifically in terms of classification. In this thesis, tensorflow [146] was used to implement the ANN.

Non-negative matrix factorisation

The underlying principle of NMF is to decompose the dataset **X** into two new datasets **A** and **B** such that [147, 148]:

$$\mathbf{X} \approx \mathbf{AB}, \tag{3.19}$$

where $\mathbf{X} \in \mathbb{R}_+^{N_{xy} \times N_{k_x k_y}}$, $\mathbf{A} \in \mathbb{R}_+^{L \times N_{xy}}$ and $\mathbf{B} \in \mathbb{R}_+^{N_{k_x k_y} \times L}$. $\mathbb{R}_+$ is the set of all non-negative real numbers. L is the number of components the input data will be decomposed into. In most cases, NMF can be viewed as a dimensionality reduction with $L \ll N_{k_x k_y}$ and $L \ll N_{xy}$ [148]. The approximation of **X** by Eq. 3.19 is achieved by finding **A** and **B** that minimise a cost function, usually the *Frobenius norm* $||\mathbf{X} - \mathbf{AB}||_F$, subject to $\mathbf{A} \geq 0$ and $\mathbf{B} \geq 0$. NMF is hence done iteratively until a good approximation of **X** is found.

This is similar to other low-rank decomposition methods such as principal component analysis (PCA), the difference lies in the different constraints imposed on the component matrices [148]. NMF incorporates a non-negativity constraint, enhancing the interpretability of the data as compared to other linear matrix decomposition approaches allowing negative intensities in the decomposed datasets. This is especially advantageous when analysing SPED data, since $I_0 \geq 0$ and $I_g \geq 0$ (Eq. 3.16).

Upon performing NMF in hyperspy, the SPED data is reshaped into a 2D signal matrix $\mathbf{X} \in \mathbb{R}_+^{N_{xy} \times N_{k_x k_y}}$, where each row has a length of N_{xy} and each column of length $N_{k_x k_y}$ holds the PED patterns. The data **X** is decomposed into *factors* **B** and *loadings* **A**. Factor i, $i = 1, .., L$ has the same dimension as the input PED patterns, while loading i exhibits the same dimensionality as the scan region. Qualitatively, the factors resemble PED patterns and are often referred to as *component maps*, while the loadings describe the spatial intensity distribution of the corresponding factor. The *loading maps* indicate regions where the component maps are significant and resemble VDF images such as the images shown in Fig. 3.10d-f.

An important parameter to consider in NMF is the number of components L. In a multi-phase material, such as heat-treatable Al alloys consisting of N_{phases} phases, one could initially expect that $L = [1 + \sum_i i \cdot \text{OR}_i]$, where $i = 1, ..N_{\text{phases}}$ and OR_i is the number of orientation relationships for precipitate i with the matrix. The sum needs to be added with one to account

for the component describing pure Al. It is however often necessary with more components, due to varying deviation from Bragg's condition, due to e.g. variation in specimen tilt over the scanned region, significant deformation, strain and so on. Some approaches for choosing L include trial-and-error or estimation using *singular value decomposition (SVD)*, which is another matrix factorisation approach where the components are required to be orthogonal and ordered by variance. By plotting the variance against the component index, a *scree plot* is generated. Ideally, the scree plot should decrease rapidly, eventually becoming a slowly descending line. The point at which the plot becomes linear, often referred to as the *elbow*, is generally judged to be a good estimate of the dimensionality L of the data.

Although not strictly necessary, some preprocessing is often employed on the input data $\mathbf{X}$. For phase mapping of precipitates in heat-treatable Al alloys, one important preprocessing step is to create boolean masks containing disks with a given radius r at the center of each Al reflection in the PED pattern. The mask is superimposed on each diffraction pattern in the input data. The intensity of the diffracted beams stemming from Al is typically much higher than the intensity of the diffracted beams stemming from the precipitates. If one included the Al reflections in the NMF decomposition, the variations in the Al diffracted beams would most likely cause the required number of components L to describe the data to increase significantly. In phase mapping, we are only interested in recognising the diffraction patterns stemming from precipitates and hence masking out the Al reflections is a good approach to minimise L and hence the computational time, while at the same time improving the quality of the decomposition.

Artificial neural networks

The goal of a supervised ANN is to find a function f so that when a new sample x_{new} is presented without its label, then the output of $f(x_{new})$ approximates the label well [145]. The dataset $\{x_\mu, y_\mu\}$ is called the training set. Typically, the training set is split into a training set used to learn the function and a test set to monitor the performance. During the training, a set of parameters, called the *weights* $w \in \mathbb{R}$ and *biases*, $b \in \mathbb{R}$, are adjusted to minimise the cost function, $\mathcal{C}(w,b)$. For reasons that will become clear, the number of trainable parameters can be huge, often in the order of 10^6. The algorithms commonly employed to minimise the cost function are based on gradient descent with respect to the weights w. The weights and biases are iteratively adjusted in the direction of the gradient of the cost function [145]:

$$w^{t+1} = w^t - \gamma \nabla_w \mathcal{C}(w,b) \tag{3.20}$$

$$b^{t+1} = b^t - \gamma \frac{\partial \mathcal{C}(w,b)}{\partial b}, \tag{3.21}$$

where γ is known as the learning rate. Gradient descent is computationally heavy if the number of training inputs is large, since the partial derivatives need to be calculated for each trainable parameter. A commonly applied variant of gradient descent is the *stochastic gradient descent (SGD)*, where the full cost function $\mathcal{C}(w,b)$ is replaced by the contribution of just a few, randomly chosen samples. This can significantly speed up the computation time.

A schematic of a typical ANN is shown in Fig. 3.11. An ANN is built up of artificial neurons, shown as circles in the figure. Each neuron in the input layer takes several inputs $x_1, x_2, ..$ and produces an output. The output is produced by applying an *activation function*, $F(z)$, $z = \sum_j w_j x_j - b$, where the bias b acts as a threshold for when a certain neuron is activated. In

fact, all the neurons in an ANN have an activation function related to it. Hence, each neuron is associated with a bias. The layers between the input- and output layer are known as *hidden layers* and are added in order for the ANN to learn non-linearity in the input data. The lines connecting the different layers are often referred to as *nodes*. Each node has an associated weight w. Increasing the number of neurons increases both the number of biases b and number of weights w, which are the trainable parameters, explaining why a typical ANN can have millions of trainable parameters [145].

Different activation functions exist, common ones include *sigmoid* ($\sigma(z)$), *hyperbolic tangent* ($\tanh(z)$) and *ReLU* ($R(z)$). Common for them all is that they are differentiable and non-linear. The non-linear behaviour allows our neural network to learn non-linear relationships in the data. Differentiability is important because it allows us to *backpropagate* the model's error when training to optimise the trainable parameters.

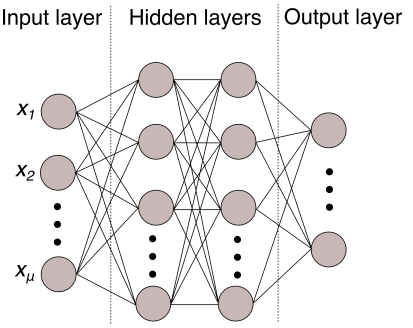

Figure 3.11: Schematic of a typical ANN consisting of one input layer, one hidden layer and one output layer.

The output layer predicts which label y_μ the input x_μ corresponds to. The activation function in this layer is typically different from the ones in the input- and hidden layer. For multiclass classification, i.e. in models with more than two labels, *softmax* is often the preferred function. Softmax outputs a vector of values that sums to 1 and can be interpreted as probabilities of class membership and is defined as $e^z / \sum e^z$.

It is the backpropagation that adjusts the weights in a network. Ultimately, this means computing the partial derivatives in Eqs. 3.20 and 3.21, $\nabla_w \mathcal{C}(w,b)$ and $\frac{\partial \mathcal{C}(w,b)}{\partial b}$. Backpropagation gives us a procedure to compute the error in the j^{th} neuron in the l^{th} layer, δ^l_j, and relate it to the partial derivatives in Eqs. 3.20 and 3.21. The weights and biases are updated accordingly starting backwards, hence the name backpropagation.

For SPED data, the goal of the ANN is to predict something from a certain PED pattern at a certain probe position. To facilitate supervised learning, we need labeled data. In general, we have two choices for creating the labels y_μ needed to generate a good training set $\{x_\mu, y_\mu\}$, (i): Label experimental data or (ii): build the training set by doing electron diffraction simulations. Typically, this involves labeling ten thousands of diffraction patterns. This is tedious if done manually, which might be the case if one chooses to train on experimental data. Experimental data could also be labeled by first performing an unsupervied learning approach such as NMF to reduce the dimensionality of the dataset. The diffracted intensities are heavily dependent on the experimental set-up, e.g. the thickness t of the sample, the excitation error s and the wavelength of the electrons λ via Eq. 3.16, but also the alignment of the microscope, precession angle ϕ and so on and so forth. To generate an adequate training set, one would have to label multiple datasets acquired on different samples and on different days to increase the variations in the input data. This challenge can be overcome by simulating the diffraction patterns instead, which can be less tedious depending on which simulation algorithm one chooses.

An alternative data analysis strategy to virtual imaging and machine learning is *template*

matching [149, 150], initially developed for orientation mapping. In this approach, a template library consisting of simulated diffraction patterns is compared with the experimental patterns. A correlation score is calculated and the experimental pattern is labeled according to the label of the simulated pattern with the highest score. Which data analysis strategy is needed to interpret the data is dependent on the data and the task. NMF has been proven to be a suitable tool for reducing the dimensionality of SPED datasets and yield interpretable component patterns [151]. Furthermore, NMF has been demonstrated to be well-equipped as a strategy for phase mapping of precipitates in Al alloys [20, 21] and was also employed in Paper II, IV, V and VI in this thesis. In Paper VI, NMF, template matching and ANN and a vector based approach for phase mapping of precipitates are compared in terms of accuracy and reproducibility.

Part II

Research

Chapter 4

Experimental

This chapter gives a an overview of the Al alloys studied and transmission electron microscopes used in this thesis. The first section lists the chemical compositions of the Al alloys, while the second lists the microscopes used.

Material selection in this thesis

In **Paper I**, an industrial 7046 alloy was used along with a high purity, lab-cast alloy named ZM42. The 7046 alloy was provided by Hydro Extrusions, while ZM42 was provided by University of Toyama. ZM42 was also studied in **Paper II**. A 7003 alloy provided by Benteler was studied in **Paper III**. **Papers IV-V** investigated various compositions of the so-called Toyama alloy, an alloy developed at University of Toyama for the company Yoshida Kōgyō Kabushiki-gaisha (YKK) with the intended use of zip fasteners. In **Paper VI**, an Al-Cu-Li alloy supplied by American Elements was used. Tab. 4.1 lists the composition of all the alloys studied in this thesis.

Table 4.1: Compositions of the alloys studied in this thesis in at.%. The papers in which they were used are also indicated.

Paper	Alloy	Zn	Mg	Si	Cu	Mn	Fe	Cr	Zr	Ti	Li
I	7046	2.980	1.420	0.080	-	-	0.080	-	0.040	-	-
I, II	ZM42	3.490	1.890	-	-	-	-	-	-	-	-
III	7003	2.430	0.840	0.090	-	-	0.110	-	0.050	0.010	-
IV	Toyama alloy-1	0.001	1.129	0.368	0.543	<0.001	0.034	0.001	-	0.011	-
V	Toyama alloy-2	<0.004	1.084	0.329	0.500	<0.005	0.034	<0.005	<0.003	<0.011	-
V	Toyama alloy-3	<0.004	1.051	0.329	0.500	<0.005	0.078	<0.005	<0.003	<0.011	-
VI	Al-Cu-Li	-	-	-	1.246	0.264	0.095	-	-	-	5.705

Microscopes used in this thesis

All of the TEM data presented in this thesis was collected using microscopes in the NORTEM facility [152] within the TEM Gemini Centre [153] at Norwegian university of science and technology (NTNU) in Trondheim. Three instruments were used: JEOL JEM 2100, JEOL JEM 2100F and JEOL JEM ARM200F. All three microscopes were operated at 200 kV. The JEOL JEM ARM200F has a cold field emission gun (FEG) with an energy spread of < 0.3 eV. The instrument is Cs-probe- and Cs-image corrected yielding a resolution of < 1 Å in the HAADF-STEM mode. This instrument was used to collect the atomically resolved HAADF-STEM images shown in **Papers I-V** and BF images and SAED patterns presented in **Paper I**. The JEOL JEM 2100F has a Schottky FEG with an energy spread of 0.7 eV and is equipped with a Gatan 2k UltraScan CCD and the Nanomegas ASTAR system enabling SPED. It is also equipped with a Medipix3 MerlinEM camera with a single 256x256 Si chip from Quantum detectors [154] enabling the possibility for SPED experiments on a direct electron detector. The SPED data

presented in **Paper II-III** and **Paper V-VI** was collected using the Medipix3 MerlinEM. In **Paper IV**, the SPED data was collected using an externally mounted Stingray camera, since this work was done prior to the installation of the direct electron detector. The JEOL JEM 2100 has a LaB6 filament and is equipped with a Gatan 2k Orius CCD camera and a Gatan imaging filter (GIF) system with a 2k CCD. The BF images and SAED patterns presented in **Paper IV-V** were collected using this instrument.

Chapter 5

Results

This chapter gives a short summary of the results presented in each paper included in Part III in this thesis. All manuscripts are focused on the study of GP zones and metastable precipitate phases formed in heat-treatable Al alloys after various thermomechanical treatments with the use of TEM. A majority of the papers were enabled by atomically resolved HAADF-STEM imaging to study the fine details of the atomic structure of GP zones and precipitates. SPED was also used as a characterisation tool in most of the papers, either to obtain statistics regarding the relative phase fraction of precipitates or to compare the experimental diffraction patterns with simulated ones from atomic models to increase the understanding of the atomic structure of the investigated phases. In this regard, the Paper VI is concerned with comparison between SPED data analysis approaches for phase mapping of precipitates in Al alloys.

Paper I — Atomic structure of solute clusters in Al-Zn-Mg alloys

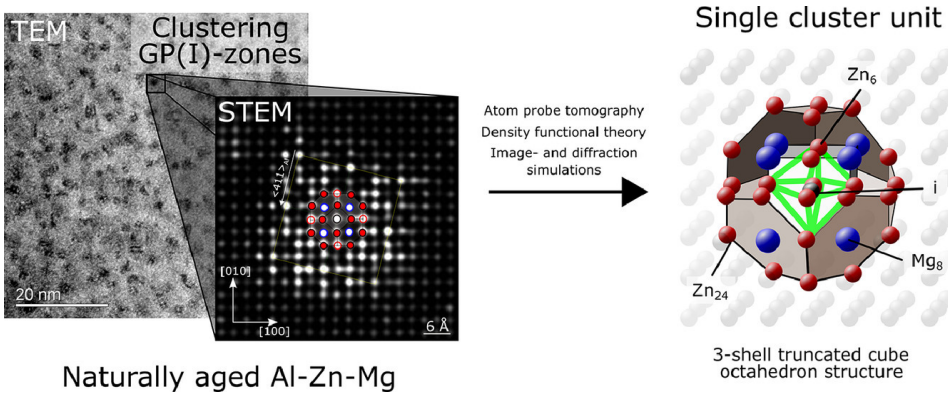

Figure 5.1: Graphical abstract for Paper I.

In this paper, we presented presumably the first atomically resolved HAADF-STEM images of the atomic structure of the GPI zones in the Al-Zn-Mg alloy system. Up until this publication, no adequate atomic models existed for this phase even though it had been known and studied for decades. Based on the obtained HAADF-STEM images, atomic models were prepared and refined by density functional theory (DFT). The atomic structure of the GPI zones was fundamentally different from previously proposed models deduced from analysis of SAED patterns from regions containing several GPI zones and possibly other phases [78]. GPI zones with the same structure and similar size were found in both the 7046 alloy naturally aged for seventeen years and the ZM42 alloy with NA for four days and AA at 120°C for 8 minutes.

It was demonstrated that the GPI zones are composed of a fundamental unit. A 3-shell truncated cube octahedron structure, termed TCO for simplicity, see Fig. 5.1, constituted the fundamental unit, which essentially is a partial substitution of Zn and Mg on the Al fcc cubic cell and its surrounding TCO shell. DFT calculations indicated that the octahedral position in the central column of the TCO could be occupied. The TCO unit connected along different directions to form larger zones. The most commonly observed configuration was TCOs connected exclusively along $\langle 411 \rangle_{\mathrm{Al}}$, a small portion of the TCOs was connected along both the $\langle 411 \rangle_{\mathrm{Al}}$ and $\langle 330 \rangle_{\mathrm{Al}}$ directions. Hence, the GPI zones exhibit variable long-range structure.

By comparing simulated HAADF-STEM images with experimental images, and simulated NBD patterns with fast Fourier transforms of the experimental images, a good correspondence was found between the atomic models and the images. Atom probe tomography (APT) also supported the results. No structural connection was found between the GPI zones and the η' precipitates, indicating that the GPI zones cannot transform into η' upon ageing. This paper provides new insight into the very early stages of precipitation hardening in Al-Zn-Mg alloys and was the basis for Paper II and Paper III.

Paper II — Studying GPI zones in Al-Zn-Mg alloys by 4D-STEM

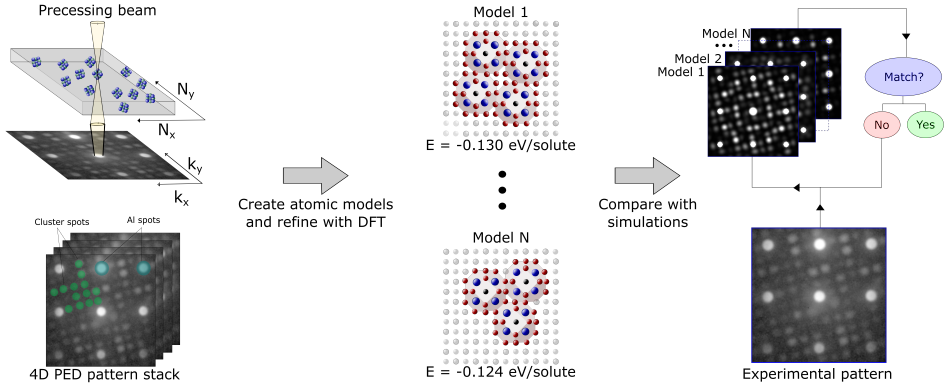

Figure 5.2: Graphical abstract for Paper II.

To further investigate the fine details of the atomic structure of the GPI zones, SPED was employed in Paper II to collect a large number of PED patterns from the zones and compare them with simulated NBD patterns of the atomic models. The alloy used was ZM42 in the same condition as in Paper I. Example PED patterns are shown in the graphical abstract in Fig. 5.2. TCOs connected purely along $\langle 411 \rangle_{\mathrm{Al}}$ and along both $\langle 411 \rangle_{\mathrm{Al}}$ and $\langle 330 \rangle_{\mathrm{Al}}$ were observed and their corresponding PED patterns were characteristic viewed along the unique $[001]_{\mathrm{GPI}}$ axis. Three unique PED patterns were observed of GPI zones oriented in orientations perpendicular to $[001]_{\mathrm{GPI}}$. Three configurations of the central column of the TCO gave simulated patterns matching the positions of the diffracted beams of the experimental patterns. The first one, being least energetically favourable according to DFT, corresponded to the TCO occupying the Al fcc lattice sites. In the second and most energetically favourable configuration, the central column of the TCO was displaced by 2.025 Å, so that the octahedral site was occupied. This is a 1D column defect in the Al lattice, first identified in the β'' phase in the Al-Mg-Si system [155]. In the last configuration, exhibiting intermediate formation enthalpy, the central column had 3/2 occupancy relative to Al, i.e. one extra solute is present in the central column for every second TCO.

This paper demonstrated the advantage of coupling HAADF-STEM with PED for investigating the crystal structure of small, ordered crystal phases embedded in a host material.

Paper III — The evolution of precipitates in an Al-Zn-Mg alloy

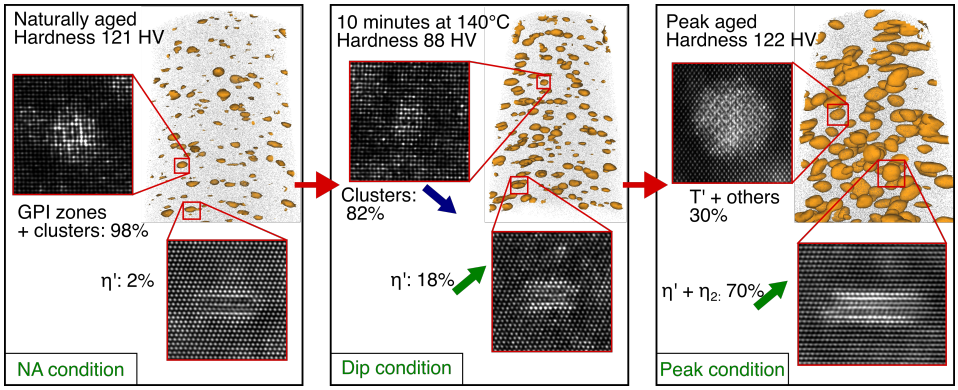

Figure 5.3: Graphical abstract for Paper III.

Paper III is concerned with the evolution of precipitates in Al-Zn-Mg alloys and the graphical abstract is shown in Fig. 5.3. A 7003 alloy naturally aged for one year was subjected to AA at 140°C for different times to investigate the evolution from GPI zones to hardening precipitates. The microstructures of the NA condition, after ten minutes of AA and at the peak aged condition were investigated by TEM and APT. The NA condition comprised a dense population of clusters and GPI zones coexisting with a small population of η' and had a hardness of 121 HV. After ten minutes AA, the hardness decreased to 88 HV, termed the 'dip' condition. The number densities of clusters in the two conditions were similar, but the Zn/Mg ratio decreased from 2 in the NA condition to 1.7 in the dip condition. The average size of the clusters was larger in the dip condition in comparison to the NA condition. HAADF-STEM imaging revealed that the clusters in the dip condition no longer exhibited the GPI zone atomic structure. At the same time, the occurrence of η' increased from 2% to 18%.

The lowering in hardness and increase in cluster size while still maintaining a similar number density of clusters in the dip condition as compared to the NA condition were attributed to a lower obstacle strength of the clusters/precipitates in the dip condition. The η' precipitates were much smaller and less developed as compared to the η' in the peak aged condition and hence have a lower obstacle strength. A measurable evolvement of clusters was also detected with APT. There were no indications that a phase transformation took place from GPI to η' and the decrease in hardness was attributed to a partial reversion of the GPI zones. This was supported by the incompatible atomic structures of the phases as found in Paper I.

At the peak aged condition, the size of the particles increased while the number density decreased. Based on HAADF-STEM, the most prominent precipitate at peak age was η' which co-existed with η_1, η_2 and T'. SPED confirmed these observations.

We believe these results to be a significant contribution to improving the understanding of early stage precipitation in Al-Zn-Mg alloys and are important for industrial heat treatment, where NA is always used.

Paper IV — The effect of heavy deformation on the precipitation in an Al-1.3Cu-1.0Mg-0.4Si wt.% alloy

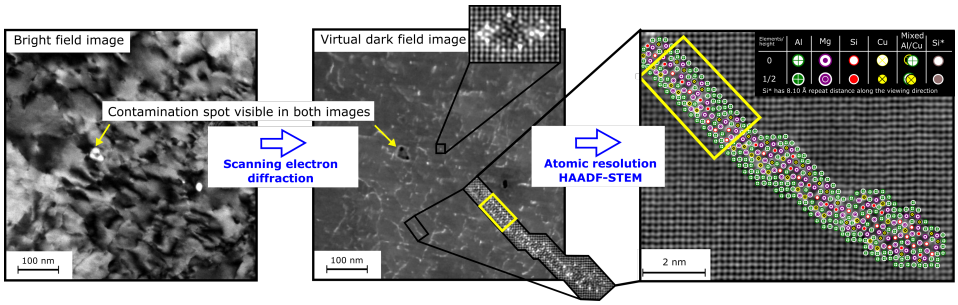

Figure 5.4: Graphical abstract for Paper IV.

In this work, Toyama alloy-1 was investigated after three different thermomechanical treatments: All three conditions underwent the same SHT and NA for 20 hours. Two of the samples were 80% deformed prior to AA, the difference was the order of NA and the pre-deformation: NA20ha underwent deformation after NA, while NA20hb underwent NA before deformation. The third condition, NA20hn, was the underformed condition. All three conditions were investigated in terms of hardness evolution during each processing step and HAADF-STEM. In addition, SPED was employed on the pre-deformed samples NA20ha and NA20hb to investigate the relative fractions of precipitate phases.

The undeformed condition NA20hn exhibited a homogeneous distribution of precipitates. Based on HAADF-STEM, two types of precipitates were present, namely the L phase from the Al-Mg-Si-Cu alloy system and structural units of GPB zones from the Al-Cu-Mg system.

The pre-deformed conditions consisted of the L phase nucleated away from the deformation induced defects. Furthermore, C and E phases and disordered precipitates were nucleated on the deformation induced defects. The E phase had previously been reported [156], but its crystal structure was solved in this paper, based on HAADF-STEM imaging coupled with DFT calculations.

A typical BF image of the microstructure after pre-deformation is shown in the graphical abstract in Fig. 5.4. The contrast from the dislocations were masking out the precipitates and such images were deemed inadequate to obtain quantitative information about the precipitate distribution. Hence, SPED datasets from the pre-deformed conditions were obtained. A VDF image from the same region as the BF image is shown in Fig. 5.4. Phase mapping of the precipitates was enabled by NMF and supported the findings by HAADF-STEM that the same type of precipitates was nucleated in the two conditions. The order of the NA and pre-deformation however influenced the relative fractions of C+E and L as a higher fraction of C+E was found in NA20ha as compared to NA20hb.

Paper V — The effect of small additions of Fe and heavy deformation on the precipitation in an Al-1.1Mg-0.5Cu-0.3Si at.% alloy

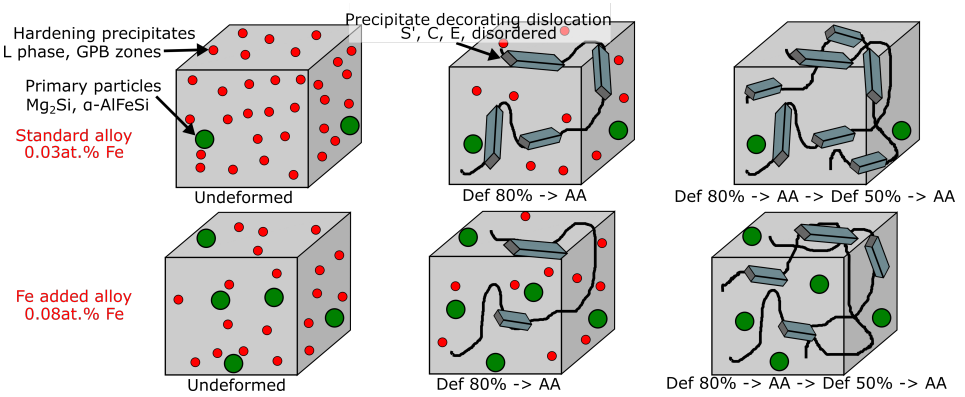

Figure 5.5: Graphical abstract for Paper V.

Paper V concerns investigates the effect of small additions of Fe on the precipitation in the Toyama alloy. Toyama alloy-2, referred to as the standard alloy, had a similar composition as Toyama alloy-1 studied in Paper IV, while Toyama alloy-3 had an addition of Fe. SEM was employed on the undeformed condition to quantify the distribution of primary particles. Both alloys had similar amounts of primary Mg_2Si particles, while the higher Fe level alloy produced roughly twice the number density and volume fraction of primary bcc α-AlFeSi particles. The higher content of α-AlFeSi particles in the Fe added alloy caused a reduction in the volume fraction of hardening precipitates.

The alloys underwent NA for 18 hours followed by a deformation of 80% and AA, termed Def1_AA1, followed by a second deformation of 50% and a short AA treatment, termed Def1,2_AA1,2. SPED was used as a characterisation tool for both conditions and the latter condition was in addition studied by HAADF-STEM. The main results are schematically shown in the graphical abstract in Fig. 5.5. Precipitate volume fractions could not be extracted, but it was assumed that the standard alloy had a higher volume fraction of precipitates compared to the Fe added alloy, since this was the scenario in the undeformed condition.

It was found that the standard alloy in condition Def1_AA1 had a more homogeneous distribution of precipitates as compared to the Fe added alloy, i.e. more precipitates were nucleated on the deformation induced defects in the Fe added alloy. The standard alloy exhibited a higher hardness increase during Def2, attributed to a higher presence of non-shearable precipitates in the Def1_AA1 condition, indicating that the overall volume fraction of precipitates was highest in the standard alloy. The precipitates nucleated heterogeneously were C- E- and S' in addition to disordered precipitates, while the L phase was nucleated in between the deformation induced defects.

The precipitates in the Def1,2_AA1,2 condition in both alloys were more disordered as compared to the Def1_AA1 condition, making quantification by SPED challenging. The precipitate types in this condition were the same as in Def1_AA1, but the PED patterns were in general less characteristic, hence a quantification based on SPED was deemed not feasible.

Paper VI — Scanning precession electron diffraction data analysis approaches for phase mapping of precipitates in aluminium alloys

In Paper VI, four different SPED data analysis approaches for phase mapping of precipitates in Al alloys were employed on a model dataset obtained from an Al-Cu-Li alloy with T1 and θ' precipitates. The data was obtained from the $\langle 001 \rangle_{\mathrm{Al}}$ zone axis. Due to different orientation relationships and morphologies, the precipitates were discernible in VDF images in this projection. Based on this, a ground truth image was created to estimate the accuracy of each phase mapping strategy.

The approaches included NMF, template matching, ANN and a vector based approach termed *vector analysis*. The phase maps are shown in Fig. 5.6a-d for NMF, vector analysis, template matching and ANN, respectively. The maps in Fig. 5.6e-h indicate the difference between the ground truth image and the phase maps in Fig. 5.6a-d, respectively. Enlarged regions of the phase maps are shown in Fig. 5.6i-l. The NMF, vector analysis and ANN yielded satisfactory results, with less than 2% of the pixels mislabeled. The template matching however, mislabeled over 10% of the pixels. Most of the mislabeled pixels in the template matching stemmed from regions with low diffracted intensities from the respective precipitate. Template matching was concluded to be an inadequate strategy for phase mapping when the dataset contained weak diffracted intensities.

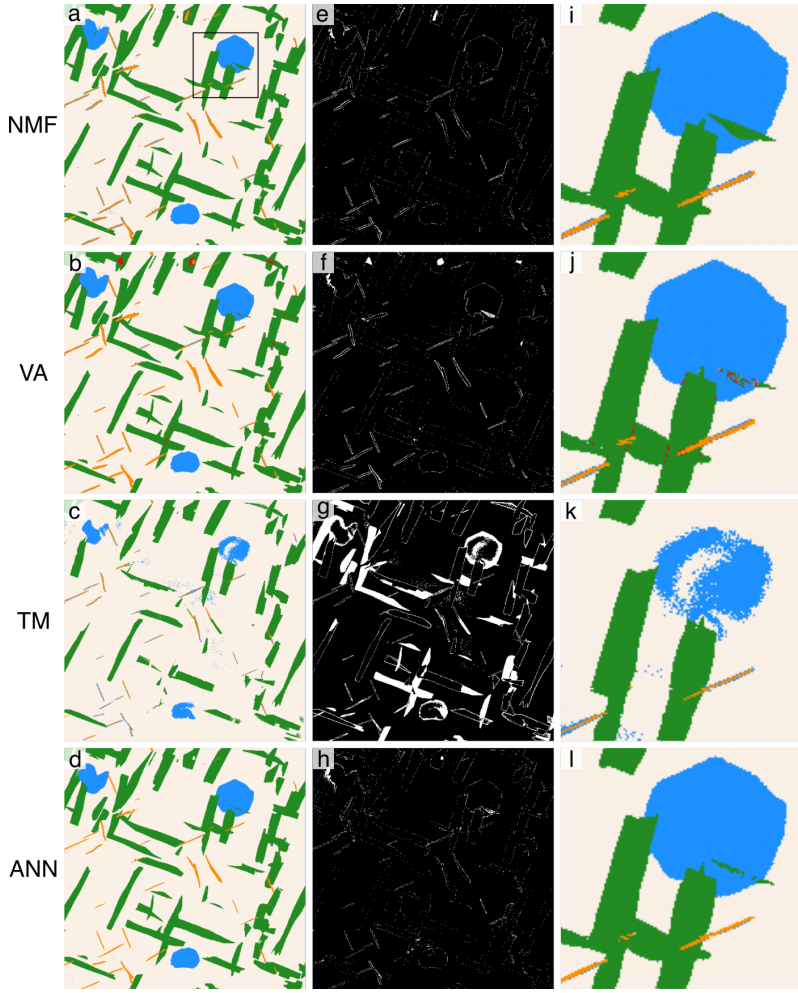

Figure 5.6: Resulting phase and difference maps based on NMF, vector analysis, template matching and ANN. **a**-**d**: Phase maps obtained from NMF, vector analysis, tempalte matching and ANN, respectively. **e**-**h**: Difference maps. **i**-**l**: Enlarged regions from the phase maps corresponding to the region marked by the black rectangle in **a**. The difference maps indicate the difference between the ground truth image and the phase map, white pixels are mislabeled.

Chapter 6

Discussion and outlook

6.1 GP zones and precipitation in Al-Zn-Mg alloys

The atomic structure of the GPI zones was solved in Paper I and found to be fundamentally different from the previous model proposed by Berg *et al.* [78]. Their model was deduced from SAED patterns from regions containing multiple GPI zones under the assumption that the positions of the diffracted beams in the SAED were identical to that of diffraction patterns from single GPI zones. It was shown in Paper I that the TCO units of the GPI zones connect along certain crystallographic directions in the Al lattice to form larger zones. In this regard, the diffraction pattern from the GPI zones depends on i) how they connect and ii) the configuration of the central column of the TCO. In Paper II this was proven rigorously, since SPED enabled the acquisition of PED patterns from single GPI zones. Five unique PED patterns stemming from the GPI zones were observed, the sum of all these contributes to a pattern similar to the SAED shown by Berg *et al.* [78].

In addition to GPI zones, GPII zones were also reported in the study by Berg *et al.* [78]. The GPII zones grow as thin plates on $\{111\}_{\mathrm{Al}}$ planes and have been reported in the following papers: [78, 157–159] among others. The earlier observations were either high resolution TEM images or indirect observations by SAED. To the author's knowledge, no HAADF-STEM images of good quality have been published showing GPII zones. Liu *et al.* [160] present HAADF-STEM images showing some diffuse contrast elongated along $\{111\}_{\mathrm{Al}}$ planes and attribute the contrast to stem from GPII zones. It is however not apparent, since the contrast is too diffuse to reveal atomic ordering and may stem from overlap between clusters along the viewing direction or overlap with Al. In this thesis, multiple Al-Zn-Mg alloys subjected to different heat treatments were investigated and GPII zones were never observed.

The GPI zones form at room temperature and up to their formation temperature, depending on the composition of the alloy [79]. The GPII zones however are often reported to form after quenching from temperatures above 450°C and AA at temperatures above 70°C [78]. In this thesis, it was of great interest to obtain HAADF-STEM of the GPII zones to investigate their atomic structure. In that regard, the 7003 alloy was heat treated in the following manner: SHT at 480°C for 30 minutes followed by an ice water quench. The AA was performed immediately after quench at 100°C for five hours. The microstructure consisted of GPI zones co-existing with η' precipitates, see HAADF-STEM images in Fig. 6.1a and b showing examples of an η' and a GPI zone, respectively. Unfortunately, no GPII zones were observed. The fact that the GPII zones were not observed in this thesis gives an indication that they are not a necessity for the precipitation in Al-Zn-Mg alloys since η' can nucleate directly from the SSSS and does not depend on a phase transformation from GPII zones. The previously observed GPII zones were defined from microstructures imaged on microscopes that were not aberration corrected and therefore did not have high enough resolution to resolve them. It might be the case that the observed GPII zones were a combination of GPI zones and different η' or η type of precipitates

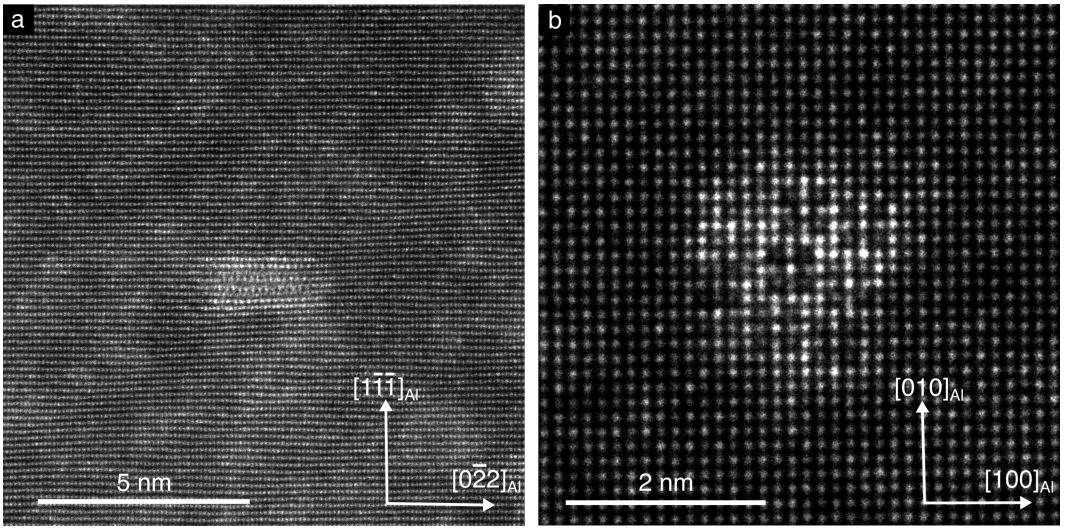

Figure 6.1: Precipitates in 7003 after a heat treatment considered likely to produce GPII zones: SHT for 30 minutes at 480°C, ice water quenchng and AA for five hours at 100°C. **a**: η' viewed along $\langle 211 \rangle_{Al}$. **b**: GPI zone viewed along $\langle 001 \rangle_{Al}$.

and that the GPII zones do not exist at all.

The GPI zones are however of great importance for the precipitation in Al-Zn-Mg alloys since they are the main phase forming during NA. They can also co-exist with η' from NA and up to AA temperatures under the GPI formation temperature. For the 7003 alloy studied in this thesis, the GPI formation temperature is above 100°C as evidenced in Fig. 6.1b, and the GPI dissolution temperature is below 140°C as evidenced in Paper III.

No structural similarities were found between the GPI zones and η' in Paper I, they also have different habit planes, suggesting that there is no phase transition between the two. Paper III supported this, since there were indications that the GPI zones dissolved upon AA at 140°C, releasing solute which could participate in the formation of η'. The simultaneous dissolution of GP zones and formation of η' are usually referred to as partial reversion in the literature [79]. Previous investigations of this phenomena relied on hardness measurements and positron annihilation lifetime spectroscopy [79, 161, 162]. In Paper III, we give direct evidence of the dissolution of GPI zones, since the clusters present in the dip condition no longer exhibited the characteristic atomic structure of the zones. In Paper III, a small population of η' co-existed with the GPI zones in the NA condition, indicating that the GPII zones are not a necessity for the nucleation of η'.

Typically, the microstructure of the peak aged condition in Al-Zn-Mg alloys is considered to consist of η' co-existing with the different η_{1-14}, c.f. Tab. 2.5. The most frequently observed orientation relationships of η include η_1, η_2 and η_4 [77, 103]. In Paper III, η', η_1 and η_2 were observed to co-exist with the T′ phase [108]. This phase is often overseen in the Al-Zn-Mg alloys, although recently the interest of the T′ phase has elevated. This can be correlated with cross-over alloying attracting attention of the metallurgical community, wherein a "crossover" between different alloy classes is created [163]. The idea is to add alloying elements such as

Cu and/or Zn to non-heat treatable Al-Mg alloys so that the resulting alloy exhibits the good formability of Al-Mg alloys combined with the age hardening potential from Al-Zn-Mg alloys. In crossover alloys, Mg is the major alloying element, as opposed to in traditional Al-Zn-Mg alloys, where Zn is the major alloying element [4, 163]. In these alloys, the T′ phase is the main hardening phase [106, 108, 112, 163].

The crystal structure of the T′ phase is assumed to be similar to that of the equilibrium T-$Mg_{32}(Al,Zn)_{49}$ [108]. The exact crystal structure is however not known. This is ongoing work at the TEM Gemini centre, NTNU, since we have observed structural similarities between the T′ phase and the Z phase in Al-Mg-Cu-Ag alloys [164, 165].

Evidently, there are questions still to be answered regarding the precipitation in Al-Zn-Mg alloys. These include the crystal structure of GPII zones and the T′ phase. The samples used in the work by Berg *et al.* [78] in the early 2000s still exist and it is of interest to investigate these samples by the means of modern TEM, including atomically resolved HAADF-STEM and SPED. Moreover, as a part of ongoing work, the crystal structure of the T′ phase and the Z phase will be compared. Correct atomic models of precipitates are often of interest since they are important in modelling of mechanical properties such as strength in Al alloys. The GPII zones in this regard can be considered a curiosity since it is uncertain whether they exist. The η' however must start from somewhere, so the GPII zones may be an illusive version of η' with fewer layers existing only briefly before they thicken. The crystal structure of the T′ phase might be considered more important, especially with the emergence of cross-over alloying.

6.2 Pre-deformation and its effect on precipitation in the Cu-rich 6xxx alloys

Many products of heat-treatable Al alloys are subjected to different forms of deformation prior to AA, often referred to as pre-deformation. The pre-deformation affects the precipitation since the introduced dislocations provide heterogeneous nucleation sites that may change the precipitation kinetics and the precipitation sequence [166]. This was studied in Paper IV and Paper V: The undeformed material consisted of homogeneously distributed L phases co-existing with structural units of GPB zones. The pre-deformed material exhibited a more heterogeneous precipitation, where L phases were nucleated homogeneously away from the deformation induced defects and C, E, S' and disordered phases were decorating the dislocation lines.

Although the E phase had previously been reported by Teichmann *et al.* [156], the atomic structure of the phase was not deduced in their work. The crystal structure of this phase was solved in Paper IV. The E phase is considered to be an important phase in pre-deformed conditions for both Al-Mg-Si and Al-Mg-Si-Cu alloys, since it is exclusively observed nucleated in the vicinity of deformation induced defects, such as dislocations. Hence, this structure may be important for the material properties of pre-deformed Al-Mg-Si(-Cu) alloys.

In both Paper IV and Paper V, the relative fraction of homogeneous precipitation, i.e. nucleation away from the deformation induced defects, and heterogeneous precipitation, i.e. nucleation in the vicinity of the deformation induced defects, was estimated based on phase mapping enabled by SPED. This relative fraction is an important property for pre-deformed materials, since the homogeneous precipitation contributes more to the hardness in comparison to the heterogeneous precipitation. The amount of solute available for precipitation was

found to have a measurable effect on the relative fraction. In Paper IV, it was found that in the condition where the pre-deformation was done before the NA, the clustering was impeded attributed to the dislocations acting as vacancy sinks, effectively decreasing the kinetics during NA. This is in accordance with previous studies [167, 168]. When the pre-deformation was performed after NA, a higher amount of the solutes was locked in the NA clusters. This caused a more heterogeneous precipitation in this condition as opposed to when the NA was performed after deformation, since more solutes were available for precipitation in the latter condition. In Paper V, less solute was available for precipitation in the Fe added alloy as compared to the standard alloy. Hence, the precipitation was more heterogeneous in the Fe added alloy. At a certain solute level, the dislocations might be saturated with solutes/precipitates. Additional solutes above this level stay in solid solution or nucleate precipitates homogeneously. It is concluded that the relative ratio of heterogeneous to homogeneous precipitation in pre-deformed materials is dependent on the solutes available for precipitation.

Pre-deformation was shown to be an effective processing step to reduce the detrimental effect of both NA and Fe additions. Both these are considered important in the metallurgy community. NA is often unavoidable during production of heat-treatable Al alloys since the delivery of semi-finished products mostly occurs after quenching to enable forming processes at low strength prior to the final AA treatment [169]. Strategies to reduce the detrimental effect of NA often includes controlling the density of free vacancies. The idea is that upon decreasing the amount of free vacancies, the kinetics during NA will be lowered and diffusion-assisted nucleation of clusters will be lowered. Pre-deformation is often considered an effective way of reducing the free vacancy concentration, since the introduced dislocations act as fast diffusion paths for the vacancies [167, 168, 170, 171]. A drawback of utilising pre-deformation to reduce the detrimental effect of NA is that the introduced dislocations also affect other important mechanical properties such as the ductility, which is typically reduced upon pre-deformation [172]. Other strategies for controlling NA include pre-ageing treatments [173, 174] and additions of trace elements trapping vacancies during NA, such as Sn [169].

The pre-deformation level was high in both Paper IV and Paper V and it was shown that with such high deformation levels, the precipitates are no longer the main contributor to hardness. Rather, the dislocation density is assumed to be the largest contributor to strength. The Toyama alloy is intended to replace brass in YKK's zipper fastener products and the different thermomechanical treatments utilised in Paper IV and Paper V were employed to mimic the different thermomechanical steps of the zip fastener products.

6.3 Studying GP zones and precipitates by scanning precession electron diffraction

In this thesis, a majority of the results are based on observations of GP zones and precipitates by SPED, often in conjunction with HAADF-STEM observations. This section is dedicated to discussing the advantage of using SPED as a characterisation technique, along with a discussion on the data analysis tools compared in Paper VI.

SPED was employed to study the GPI zones in Paper II and aided in refinement of the atomic models of the GPI zones deduced from HAADF-STEM images in Paper I. This was enabled by the installation of a MerlinEM direct electron detector provided by Quantum Detectors at the JEOL 2100F at TEM Gemini centre, Trondheim. Prior to installation, effort was made to obtain adequate signal from the GPI zones using SPED with an externally mounted CCD cam-

era, but the signal-to-noise ratio was too poor. Since the GPI zones are spherical particles with a diameter of 1-3 nm, the signal from the zones is low compared to the signal from the surrounding Al, due TEM specimens used for these experiments typically had thicknesses of 30-50 nm. Evidently, the direct electron detectors enable studies of microstructural features not previously attainable due to its high DQE. The scanning of SPED is favourable to study small particles, since it might be challenging to do static PED from single particles of very small sizes embedded in a host material.

The study in Paper II was possible due to the ordering of the GPI zones and their orientation relationships with the aluminium fcc lattice. Their tetragonal structure also enabled the acquisition of more than one GPI zone axis along only one Al zone axis, i.e. PED patterns were collected from both the unique $[001]_{GPI}$ zone axis and directions perpendicular to this unique axis. Since the GPI zones are seemingly not atomically resolvable along the directions perpendicular to $[001]_{GPI}$, SPED aided in attaining 3D information about the atomic structure, revealing that the octahedral site of the central column in the fundamental TCO unit of the GPI zones is sometimes occupied. This was hypothesised in Paper I, since the HAADF-STEM images of the GPI zones along $[001]_{GPI}$ indicated that the atoms surrounding the central column were slightly pushed out as compared to the fcc lattice positions, which was supported by DFT calculations. In Paper II, direct evidence of the occupancy of the octahedral site of the central column was presented. In that regards, SPED is a technique suitable in complementing structural investigations by HAADF-STEM. The SPED workflow presented in Paper II is considered to be useful for other material systems where ordered, small particles are embedded in a host matrix.

SPED was also employed in Paper III to investigate the precipitates in the peak aged condition of alloy 7003. Particularly, it was of interest to obtain PED patterns from the T′ phase. This is part of an ongoing study, and the PED patterns from T′ will be compared to that of the Z phase in Al-Cu-Mg-Ag alloys [164, 165]. Since the Z phase is considered to have a cube-in-cube orientation relationship, the PED patterns must be collected from more than one Al zone axis. Diffraction is in this case considered superior to HAADF-STEM since it is simpler to compare PED patterns with numerical algorithms as opposed to images. Also, many precipitates are scanned at once with SPED, yielding better statistics. Precession also decreases the intensity variations caused by bending, thickness variations, stage tilt, position of the precipitate in the specimen, which can cause large variations in intensity in HAADF-STEM images.

SPED is considered to be a robust technique to study precipitation in heat-treatable Al alloys [20, 21]. This was the motivation to employ SPED to study the heavy pre-deformed conditions of the Toyama alloys in Paper IV and Paper V. SPED proved to be uttermost useful to study such conditions, since the high density of dislocations obscures the contrast from the precipitates in BF images. It also yields better statistics as compared to HAADF-STEM imaging [175]. SPED enabled the estimation of the relative fraction of heterogeneous to homogeneous precipitation, which is an important property of pre-deformed materials. In principle, this fraction could also be deduced from DF images obtained by centering the objective aperture such that only the precipitates contribute to the resulting image. One would have to rely on thresholding to obtain a binary image and then separate the connecting pixels making up one precipitate based on morphology. This is however challenging, since the background in the images might vary and hence thresholding is not always straight-forward. SPED is advantageous, since one obtains information from both reciprocal space and real space.

The precipitate statistics obtained in Paper IV and Paper V relied on NMF as data analysis

tool. The NMF components are reproducible if the routine is properly initialised and converges [176, 177]. To enable phase mapping however, each component pattern needs to be labeled according to which precipitate phase it stems from. Historically, this has been done by manual inspection of the component patterns [175]. This introduces bias into the routine, since it is up to the user to label the component patterns. Moreover, a drawback of NMF in this regards is that the underlying pixels in real space, i.e. in the loading maps, are not unique to one component pattern. Hence, a certain pixel x_i, y_i might have a considerable intensity in the loading maps from several phases. Thresholding is employed to force a one-to-one relation between the loading maps and component maps, ensuring that a pixel x_i, y_i can only stem from one phase. This is typically done by summing the loading maps for all the component patterns from one phase and then thresholding the resulting summed loading map. The loading maps are subsequently compared for overlapping pixels. The thresholding is user dependent and the routine is considered not reproducible due to the employment of the user specific threshold. This was the main motivation for Paper VI, since the subjectivity of the NMF based phase mapping routine is considered a major drawback.

The data analysis approaches compared in Paper VI included NMF, vector analysis, template matching and ANN. Of these, NMF, vector analysis and ANN exhibited satisfactory accuracy, mislabeling less than 2% of the pixels. Template matching on the other hand, mislabeled over 10% of the pixels, mostly in regions where the diffracted intensities from the precipitate phases were weak. The vector analysis relied on peak finding to find the positions of the diffraction spots in the PED patterns. The peaks were used to obtain two-dimensional vectors k_x, k_y that were compared to reference vectors calculated from the precipitate phases. This drastically improves the speed of the calculation as compared to template matching, since it is less computational heavy to compare 2D vectors as compared to full images. This approach requires little pre-processing and hence is considered objective.

Template matching was enabled by using the implementation in pyxem [178], using the kinematical theory to simulate the diffraction patterns as explained in Section 3.2.6. The accuracy of the template matching could be increased by applying certain pre-processing steps, such as background subtraction. This is often considered a necessity in template matching [178]. The risk of doing this however is that weak diffracted intensities might be removed. This is especially critical in phase mapping of embedded particles, since if the weak diffracted intensities are removed, the region will be mislabeled as the host material. The background subtraction is also subjective, since the parameters of the background subtraction must be chosen by the user.

The ANN approach relied on kinematical diffraction pattern simulations to create the training data. The creation of training data and the implementation of the ANN are both user dependent. The creation of training data is considered to be the most tedious step of this approach, since many parameters need to be adjusted to properly account for the variations in the diffracted intensities in the experimental data. Once the ANN is properly trained, the resulting phase maps are however reproducible. This strategy is considered to be very useful in cases where many datasets need to be classified. Upon classifying only one dataset however, the vector analysis or NMF approach might be more suitable, since obtaining a properly trained ANN can be tedious.

In this work, a special case of phase mapping was considered, since the precipitates have well-defined orientation relationships with the Al fcc lattice. This is considered advantageous for the NMF approach. NMF is useful in cases where there are few unique diffraction patterns so

that the dimensionality of the data can be reduced. For phase mapping of particles with more random orientations, vector analysis, template matching and ANNs are considered more suitable than NMF.

Evidently, SPED is considered to be useful for many different characterisation tasks. It is however also important to consider its limitations. Firstly, both the acquisition and data analysis can be time-consuming. This is especially true if the data analysis tools have not been implemented yet. Luckily, there exists several open-source softwares for the analysis of 4D-STEM data, including pyxem and hyperspy, which this thesis has relied heavily on. Secondly, large amounts of data is typically obtained and special computer resources are often needed to analyse the data. Nevertheless, it is evident that electron diffraction techniques combined with scanning and precession and new detectors offer a variety of opportunities for new applications within materials science and it is expected that developments of the 4D-STEM techniques give large impacts.

Chapter 7

Conclusions

This thesis focused on microstructural investigations of GP zones and precipitation in a range of heat-treatable Al alloys by advanced TEM. A majority of the results relied on atomically resolved HAADF-STEM and SPED. Three main topics were studied: (i) GPI zones in Al-Zn-Mg alloys and their influence on precipitates forming during AA, (ii): The effect of heavy pre-deformation and NA on the precipitation in an Al-Cu-Mg-Si alloy and (iii): Data analysis strategies for phase mapping of precipitates in heat-treatable Al alloys. In the following, the main results from each topic are briefly summarised:

(i) The atomic structure of the GPI zones in Al-Zn-Mg alloys were solved based on HAADF-STEM images and the atomic models were further refined by comparing PED patterns with simulated patterns. Upon AA, the GPI zones undergo partial reversion by a simultaneous dissolution of the zones accompanied by the formation of η'.

(ii) Deformation prior to AA changes the precipitate kinetics and the precipitation sequence in Al-Cu-Mg-Si alloys. The relative fraction of homogeneous precipitation, i.e. precipitation away from the deformation induced defects, and heterogeneous precipitation, i.e. precipitation in the vicinity of the deformation induced defects, is dependent on the solute available for precipitation. A larger amount of free solutes in the material increases the homogeneous precipitation.

(iii) SPED is proven to be a useful characterisation technique for investigating the crystal structure of both GP zones and precipitates in heat-treatable Al alloys and is complementary to HAADF-STEM in deducing atomic models. SPED also enables phase mapping of precipitates, both in deformed and undeformed materials. Different data analysis approaches for phase mapping by SPED exist and it is case dependent which technique is most suitable for a given task. For metastable precipitates embedded in Al, NMF, vector analysis and ANN work best out of the approaches investigated in this work.

Bibliography

[1] M. Själander, M. Jahre, G. Tufte and N. Reissmann, *EPIC: An Energy-Efficient, High-Performance GPGPU Computing Research Infrastructure*, 2019.

[2] R. Lumley, *Fundamentals of aluminium metallurgy: Production, processing and applications*. 2011.

[3] G. E. Totten and S. D. MacKenzie, *Handbook of Aluminum: Vol 1: Physical metallurgy and processes*. CRC Press, 2003.

[4] D. Raabe, C. C. Tasan and E. A. Olivetti, "Strategies for improving the sustainability of structural metals," *Nature*, vol. 575, no. 7781, pp. 64–74, Nov. 2019. DOI: 10.1038/s41586-019-1702-5.

[5] A. Poznak, D. Freiberg and P. Sanders, "Automotive Wrought Aluminium Alloys," in *Fundamentals of Aluminium Metallurgy*, Woodhead Publishing, 2018, pp. 333–386. DOI: 10.1016/B978-0-08-102063-0.00010-2.

[6] I. J. Polmear, *Light Alloys*. Elsevier Ltd, 2005. DOI: 10.1016/B978-0-7506-6371-7.X5000-2.

[7] E. Hornbogen, "Hundred years of precipitation hardening," *Journal of Light Metals*, vol. 1, no. 2, pp. 127–132, May 2001. DOI: 10.1016/S1471-5317(01)00006-2.

[8] P. D. Merica, R. G. Waltenburg and H. Scott, "The heat treatment of duralumin," *Bull. Am. Inst. Min. Metall. Eng.*, vol. 16, p. 271, 1919.

[9] A. Guinier, "Structure of age-hardened aluminium-copper alloys," *Nature*, vol. 142, no. 3595, pp. 569–570, 1938. DOI: 10.1038/142569b0.

[10] G. Preston, " LXXIV. The diffraction of X-rays by an age-hardening alloy of aluminium and copper. The structure of an intermediate phase," *The London, Edinburgh, and Dublin Philosophical Magazine and Journal of Science*, vol. 26, no. 178, pp. 855–871, Nov. 1938. DOI: 10.1080/14786443808562177.

[11] A. Kelly and R. B. Nicholson, "Precipitation hardening," *Progress in Materials Science*, vol. 10, pp. 151–391, Jan. 1963. DOI: 10.1016/0079-6425(63)90010-0.

[12] S. J. Andersen, C. D. Marioara, J. Friis, S. Wenner and R. Holmestad, "Precipitates in aluminium alloys," *Advances in Physics: X*, vol. 3, no. 1, p. 1 479 984, Jan. 2018. DOI: 10.1080/23746149.2018.1479984.

[13] P. Dumitraschkewitz, S. S. Gerstl, L. T. Stephenson, P. J. Uggowitzer and S. Pogatscher, "Clustering in Age-Hardenable Aluminum Alloys," *Advanced Engineering Materials*, vol. 20, no. 10, p. 1 800 255, Oct. 2018. DOI: 10.1002/ADEM.201800255.

[14] C. Liu, Z. Feng, P. Ma *et al.*, "Reversion of natural ageing and restoration of quick bake-hardening response in Al-Zn-Mg-Cu alloy," *Journal of Materials Science & Technology*, vol. 95, pp. 88–94, Dec. 2021. DOI: 10.1016/J.JMST.2021.03.070.

[15] S. Pogatscher, H. Antrekowitsch, H. Leitner, T. Ebner and P. J. Uggowitzer, "Mechanisms controlling the artificial aging of Al–Mg–Si Alloys," *Acta Materialia*, vol. 59, no. 9, pp. 3352–3363, May 2011. DOI: 10.1016/J.ACTAMAT.2011.02.010.

[16] N. Tanaka, "Present status and future prospects of spherical aberration corrected TEM/STEM for study of nanomaterials," *Science and technology of advanced materials*, vol. 9, no. 1, pp. 14 111–14 122, Mar. 2008. DOI: 10.1088/1468-6996/9/1/014111.

[17] P. Hartel, H. Rose and C. Dinges, "Conditions and reasons for incoherent imaging in STEM," *Ultramicroscopy*, vol. 63, no. 2, pp. 93–114, Jun. 1996. DOI: 10.1016/0304-3991(96)00020-4.

[18] C. Ophus, *Four-Dimensional Scanning Transmission Electron Microscopy (4D-STEM): From Scanning Nanodiffraction to Ptychography and Beyond*, 2019. DOI: 10.1017/S1431927619000497.

[19] T. Saito, E. A. Mørtsell, S. Wenner *et al.*, "Atomic Structures of Precipitates in Al–Mg–Si Alloys with Small Additions of Other Elements," *Advanced Engineering Materials*, vol. 20, no. 7, p. 1 800 125, Jul. 2018. DOI: 10.1002/ADEM.201800125.

[20] J. K. Sunde, C. D. Marioara, A. T. van Helvoort and R. Holmestad, "The evolution of precipitate crystal structures in an Al-Mg-Si(-Cu) alloy studied by a combined HAADF-STEM and SPED approach," *Materials Characterization*, vol. 142, pp. 458–469, May 2018. DOI: 10.1016/j.matchar.2018.05.031.

[21] J. K. Sunde, S. Wenner and R. Holmestad, "In situ heating TEM observations of evolving nanoscale Al–Mg–Si–Cu precipitates," *Journal of Microscopy*, vol. 279, no. 3, pp. 143–147, Sep. 2020. DOI: 10.1111/JMI.12845.

[22] J. Akkola, "AllDesign project description," Tech. Rep., 2018.

[23] J. Davis, *Alloying: understanding the basics-Light Metals and Alloys*. 2001, pp. 192–203.

[24] P. N. H. Nakashima, *The Crystallography of Aluminum and its Alloys*, G. E. Totten, T. Murat and O. Kessler, Eds. CRC Press, 2020. DOI: 10.1201/9781351045636-140000245.

[25] P. A. Rometsch, Y. Zhang and S. Knight, "Heat treatment of 7xxx series aluminium alloys - Some recent developments," *Transactions of Nonferrous Metals Society of China*, vol. 24, no. 7, pp. 2003–2017, Jul. 2014. DOI: 10.1016/S1003-6326(14)63306-9.

[26] G. Gottstein, *Physical Foundations of Materials Science*. Springer Berlin Heidelberg, 2004. DOI: 10.1007/978-3-662-09291-0.

[27] B. Rinderer, "The Metallurgy of Homogenisation," *Materials Science Forum*, vol. 693, pp. 264–275, 2011. DOI: 10.4028/WWW.SCIENTIFIC.NET/MSF.693.264.

[28] S. R. Claves, D. L. Elias and W. Z. Misiolek, "Analysis of the intermetallic phase transformation occurring during homogenization of 6xxx aluminium alloys," *Materials Science Forum*, vol. 396-402, pp. 667–674, 2002. DOI: 10.4028/www.scientific.net/MSF.396-402.667.

[29] E. Hornbogen, "Hundred years of precipitation hardening," *Journal of Light Metals*, vol. 1, no. 2, pp. 127–132, May 2001. DOI: 10.1016/S1471-5317(01)00006-2.

[30] A. Wilm, "Physikalisch-metallurgische Untersuchungen über magnesiumhaltige Aluminiumlegierungen," *Metallurgie*, vol. 8, no. 2, pp. 225–227, 1911.

[31] O. R. Myhr, O. Grong and S. J. Andersen, "Modelling of the age hardening behaviour of Al–Mg–Si alloys," *Acta Materialia*, vol. 49, no. 1, pp. 65–75, Jan. 2001. DOI: 10.1016/S1359-6454(00)00301-3.

[32] O. R. Myhr, Grong and C. Schäfer, "An Extended Age-Hardening Model for Al-Mg-Si Alloys Incorporating the Room-Temperature Storage and Cold Deformation Process Stages," *Metallurgical and Materials Transactions A: Physical Metallurgy and Materials Science*, vol. 46, no. 12, pp. 6018–6039, Oct. 2015. DOI: 10.1007/s11661-015-3175-y.

[33] T. Gladman, "Precipitation hardening in metals," *Materials science and technology*, vol. 15, no. 1, pp. 30–36, 1999. DOI: 10.1179/026708399773002782.

[34] A. Deschamps and Y. Brechet, "Influence of predeformation and agEing of an Al–Zn–Mg alloy—II. Modeling of precipitation kinetics and yield stress," *Acta Materialia*, vol. 47, no. 1, pp. 293–305, Dec. 1998. DOI: 10.1016/S1359-6454(98)00296-1.

[35] S. C. Wang and M. J. Starink, "Precipitates and intermetallic phases in precipitation hardening Al–Cu–Mg–(Li) based alloys," *International Materials Review*, vol. 50, no. 4, pp. 193–215, Aug. 2005. DOI: 10.1179/174328005X14357.

[36] Y. A. Bagaryatsky, "Structural changes on aging Al-Cu-Mg alloys," *Doklady Akademii S.S.S.R*, vol. 87, p. 397, 1952.

[37] S. P. Ringer, T. Sakurai and I. J. Polmear, "Origins of hardening in aged Al-Cu-Mg-(Ag) alloys," *Acta Materialia*, vol. 45, no. 9, pp. 3731–3744, Sep. 1997. DOI: 10.1016/S1359-6454(97)00039-6.

[38] S. P. Ringer, K. Hono, T. Sakurai and I. J. Polmear, "Cluster hardening in an aged Al-Cu-Mg alloy," *Scripta Materialia*, vol. 36, no. 5, pp. 517–521, Mar. 1997. DOI: 10.1016/S1359-6462(96)00415-0.

[39] L. Kovarik, S. A. Court, H. L. Fraser and M. J. Mills, "GPB zones and composite GPB/GPBII zones in Al–Cu–Mg alloys," *Acta Materialia*, vol. 56, no. 17, pp. 4804–4815, Oct. 2008. DOI: 10.1016/J.ACTAMAT.2008.05.042.

[40] L. Kovarik and M. J. Mills, "Structural relationship between one-dimensional crystals of Guinier–Preston–Bagaryatsky zones in Al–Cu–Mg alloys," *Scripta Materialia*, vol. 64, no. 11, pp. 999–1002, Jun. 2011. DOI: 10.1016/J.SCRIPTAMAT.2011.01.033.

[41] M. J. Styles, C. R. Hutchinson, Y. Chen, A. Deschamps and T. J. Bastow, "The coexistence of two S (Al2CuMg) phases in Al–Cu–Mg alloys," *Acta Materialia*, vol. 60, no. 20, pp. 6940–6951, Dec. 2012. DOI: 10.1016/J.ACTAMAT.2012.08.044.

[42] G. B. Winkelman, K. Raviprasad and B. C. Muddle, "Orientation relationships and lattice matching for the S phase in Al–Cu–Mg alloys," *Acta Materialia*, vol. 55, no. 9, pp. 3213–3228, May 2007. DOI: 10.1016/J.ACTAMAT.2007.01.011.

[43] H. Perlitz and A. Westgren, "The crystal structure of Al2CuMg," *Kemi, mineralogi och geologi*, vol. 16B, no. 1, 1943.

[44] S. C. Wang, M. J. Starink and N. Gao, "Precipitation hardening in Al–Cu–Mg alloys revisited," *Scripta Materialia*, vol. 54, no. 2, pp. 287–291, Jan. 2006. DOI: 10.1016/J.SCRIPTAMAT.2005.09.010.

[45] A. Meetsma, J. L. De Boer and S. Van Smaalen, "Refinement of the crystal structure of tetragonal Al2Cu," *Journal of Solid State Chemistry*, vol. 83, no. 2, pp. 370–372, Dec. 1989. DOI: 10.1016/0022-4596(89)90188-6.

[46] J. M. Silcock, T. J. Heal and H. K. Hardy, "Structural ageing characteristics of binary aluminium-copper alloys," *Journal of the Institute of Metals*, vol. 82, 1953.

[47] C. Dwyer, M. Weyland, L. Y. Chang and B. C. Muddle, "Combined electron beam imaging and ab initio modeling of T1 precipitates in Al–Li–Cu alloys," *Applied Physics Letters*, vol. 98, no. 20, p. 201 909, May 2011. DOI: 10.1063/1.3590171.

[48] S. J. Andersen, C. D. Marioara, R. Vissers *et al.*, "The Dual Nature of Precipitates in Al-Mg-Si Alloys," *Materials Science Forum*, vol. 638-642, pp. 390–395, 2010. DOI: 10.4028/WWW.SCIENTIFIC.NET/MSF.638-642.390.

[49] C. D. Marioara, S. J. Andersen, J. Jansen and H. W. Zandbergen, "Atomic model for GP-zones in a 6082 Al–Mg–Si system," *Acta Materialia*, vol. 49, no. 2, pp. 321–328, Jan. 2001. DOI: 10.1016/S1359-6454(00)00302-5.

[50] H. W. Zandbergen, S. J. Andersen and J. Jansen, "Structure determination of Mg5Si6:particles in Al by dynamic electron diffraction studies," *Science*, vol. 277, no. 5330, pp. 1221–1225, Aug. 1997. DOI: 10.1126/science.277.5330.1221.

[51] H. S. Hasting, A. G. Frøseth, S. J. Andersen *et al.*, "Composition of β precipitates in Al–Mg–Si alloys by atom probe tomography and first principles calculations," *Journal of Applied Physics*, vol. 106, no. 12, p. 123 527, Dec. 2009. DOI: 10.1063/1.3269714.

[52] C. Cayron and P. A. Buffat, "Transmission electron microscopy study of the β phase (Al–Mg–Si alloys) and QC phase (Al–Cu–Mg–Si alloys): ordering mechanism and crystallographic structure," *Acta Materialia*, vol. 48, no. 10, pp. 2639–2653, Jun. 2000. DOI: 10.1016/S1359-6454(00)00057-4.

[53] R. Vissers, M. A. van Huis, J. Jansen *et al.*, "The crystal structure of the β phase in Al–Mg–Si alloys," *Acta Materialia*, vol. 55, no. 11, pp. 3815–3823, Jun. 2007. DOI: 10.1016/J.ACTAMAT.2007.02.032.

[54] S. J. Andersen, C. D. Marioara, R. Vissers, A. Frøseth and H. W. Zandbergen, "The structural relation between precipitates in Al–Mg–Si alloys, the Al-matrix and diamond silicon, with emphasis on the trigonal phase U1-MgAl2Si2," *Materials Science and Engineering: A*, vol. 444, no. 1-2, pp. 157–169, Jan. 2007. DOI: 10.1016/J.MSEA.2006.08.084.

[55] S. J. Andersen, C. D. Marioara, A Frøseth, R Vissers and H. W. Zandbergen, "Crystal structure of the orthorhombic U2-Al4Mg4Si4 precipitate in the Al–Mg–Si alloy system and its relation to the β and β phases," *Materials Science and Engineering: A*, vol. 390, no. 1, pp. 127–138, 2005. DOI: 10.1016/j.msea.2004.09.019.

[56] R. Vissers, C. D. Marioara, S. J. Andersen and R. Holmestad, "Crystal Structure Determination of the B' Phase in Al-Mg-Si Alloys by Combining Quantitative Electron Diffraction and Ab Initio Calculations," in *ICAA11*, 2008, pp. 1263–1269.

[57] H. Chen, J. Lu, Y. Kong *et al.*, "Atomic scale investigation of the crystal structure and interfaces of the B precipitate in Al-Mg-Si alloys," *Acta Materialia*, vol. 185, pp. 193–203, Feb. 2020. DOI: 10.1016/J.ACTAMAT.2019.11.059.

[58] M. H. Jacobs, "The structure of the metastable precipitates formed during ageing of an Al-Mg-Si alloy," *The Philosophical Magazine: A Journal of Theoretical Experimental and Applied Physics*, vol. 26, no. 1, pp. 1–13, 1972. DOI: 10.1080/14786437208221015.

[59] Y. Weng, Z. Jia, L. Ding *et al.*, "The multiple orientation relationships and morphology of β' phase in Al-Mg-Si-Cu alloy," *Journal of Alloys and Compounds*, vol. 767, pp. 81–89, Oct. 2018. DOI: 10.1016/J.JALLCOM.2018.07.077.

[60] W. Yang, M. Wang, R. Zhang, Q. Zhang and X. Sheng, "The diffraction patterns from β precipitates in 12 orientations in Al–Mg–Si alloy," *Scripta Materialia*, vol. 62, no. 9, pp. 705–708, May 2010. DOI: 10.1016/J.SCRIPTAMAT.2010.01.039.

[61] C. Cayron, L. Sagalowicz, L. Sagalowicz and P. A. Buffat, "Structural phase transition in Al-Cu-Mg-Si alloys by transmission electron microscopy study on an Al-4 wt% Cu-1 wt% Mg-Ag alloy reinforced by SiC particles," *Philosophical Magazine A*, vol. 79, no. 11, pp. 2833–2851, 1999. DOI: 10.1080/01418619908212027.

[62] D. J. Chakrabarti and D. E. Laughlin, "Phase relations and precipitation in Al–Mg–Si alloys with Cu additions," *Progress in Materials Science*, vol. 49, no. 3-4, pp. 389–410, Jan. 2004. DOI: 10.1016/S0079-6425(03)00031-8.

[63] C. D. Marioara, S. J. Andersen, T. N. Stene *et al.*, "The effect of Cu on precipitation in Al-Mg-Si alloys," *Philosophical Magazine*, vol. 87, no. 23, pp. 3385–3413, 2007. DOI: 10.1080/14786430701287377.

[64] M. Torsæter, W. Lefebvre, C. D. Marioara *et al.*, "Study of intergrown L and Q precipitates in Al–Mg–Si–Cu alloys," *Scripta Materialia*, vol. 64, no. 9, pp. 817–820, May 2011. DOI: 10.1016/J.SCRIPTAMAT.2011.01.008.

[65] C. D. Marioara, S. J. Andersen, J. Røyset *et al.*, "Improving thermal stability in Cu-containing Al-Mg-Si alloys by precipitate optimization," *Metallurgical and Materials Transactions A*, vol. 45, no. 7, pp. 2938–2949, Mar. 2014. DOI: 10.1007/s11661-014-2250-0.

[66] Z. Jia, L. Ding, L. Cao *et al.*, "The Influence of Composition on the Clustering and Precipitation Behavior of Al-Mg-Si-Cu Alloys," *Metallurgical and Materials Transactions A*, vol. 48, no. 1, pp. 459–473, Jan. 2017. DOI: 10.1007/s11661-016-3850-7.

[67] K. Buchanan, K. Colas, J. Ribis, A. Lopez and J. Garnier, "Analysis of the metastable precipitates in peak-hardness aged Al-Mg-Si(-Cu) alloys with differing Si contents," *Acta Materialia*, vol. 132, pp. 209–221, Jun. 2017. DOI: 10.1016/J.ACTAMAT.2017.04.037.

[68] L. Ding, Z. Jia, Y. Weng *et al.*, "The morphology and orientation relationship variations of Q phase in Al–Mg–Si–Cu alloy," *Materials Characterization*, vol. 118, pp. 279–283, Aug. 2016. DOI: 10.1016/J.MATCHAR.2016.06.005.

[69] W. Yang, M. Wang, X. Sheng, Q. Zhang and L. Huang, "Precipitate characteristics and selected area diffraction patterns of the β and Q precipitates in Al–Mg–Si–Cu alloys," *Philosophical Magazine Letters*, vol. 91, no. 2, pp. 150–160, Feb. 2011. DOI: 10.1080/09500839.2010.541165.

[70] C. D. Marioara, J. Nakamura, K. Matsuda *et al.*, "HAADF-STEM study of β-type precipitates in an over-aged Al–Mg–Si–Ag alloy," *Philosophical Magazine*, vol. 92, no. 9, pp. 1149–1158, Mar. 2012. DOI: 10.1080/14786435.2011.642319.

[71] M. Torster, F. J. Ehlers, C. D. Marioara, S. J. Andersen and R. Holmestad, "Applying precipitate-host lattice coherency for compositional determination of precipitates in Al-Mg-Si-Cu alloys," *Philosophical Magazine*, vol. 92, no. 31, pp. 3833–3856, Nov. 2012. DOI: 10.1080/14786435.2012.693214.

[72] T. Saito, C. D. Marioara, S. J. Andersen, W. Lefebvre and R. Holmestad, "Aberration-corrected HAADF-STEM investigations of precipitate structures in Al-Mg-Si alloys with low Cu additions," *Philosophical Magazine*, vol. 94, no. 5, pp. 520–531, Feb. 2014. DOI: 10.1080/14786435.2013.857051.

[73] K. Matsuda, S. Ikeno, T. Sato and Y. Uetani, "Metastable phases in an Al-Mg-Si alloy containing copper," *Metallurgical and Materials Transactions A 2001 32:6*, vol. 32, no. 6, pp. 1293–1299, 2001. DOI: 10.1007/S11661-001-0219-2.

[74] C. Wolverton, "Crystal structure and stability of complex precipitate phases in Al–Cu–Mg–(Si) and Al–Zn–Mg alloys," *Acta Materialia*, vol. 49, no. 16, pp. 3129–3142, Sep. 2001. DOI: 10.1016/S1359-6454(01)00229-4.

[75] C. S. Chang, I. Wieler, N. Wanderka and J. Banhart, "Positive effect of natural pre-ageing on precipitation hardening in Al–0.44 at% Mg–0.38 at% Si alloy," *Ultramicroscopy*, vol. 109, no. 5, pp. 585–592, Apr. 2009. DOI: 10.1016/J.ULTRAMIC.2008.12.002.

[76] S. Pogatscher, H. Antrekowitsch, T. Ebner and P. J. Uggowitzer, "The Role of Co-Clusters in the Artificial Aging of AA6061 and AA6060," *Light Metals 2012*, pp. 415–420, Jan. 2012. DOI: 10.1007/978-3-319-48179-1{_}70.

[77] A. Lervik, C. D. Marioara, M. Kadanik *et al.*, "Precipitation in an extruded AA7003 aluminium alloy: Observations of 6xxx-type hardening phases," *Materials & Design*, vol. 186, p. 108 204, Jan. 2020. DOI: 10.1016/J.MATDES.2019.108204.

[78] L. K. Berg, J. Gjønnes, V. Hansen *et al.*, "GP-zones in Al-Zn-Mg alloys and their role in artificial aging," *Acta Materialia*, vol. 49, no. 17, pp. 3443–3451, 2001. DOI: 10.1016/S1359-6454(01)00251-8.

[79] H. Löffler, I. Kovács and J. Lendvai, "Decomposition processes in Al-Zn-Mg alloys," *Journal of Materials Science*, vol. 18, no. 8, pp. 2215–2240, Aug. 1983. DOI: 10.1007/BF00541825.

[80] J. Lendvai, "Precipitation and Strengthening in Aluminium Alloys," in *Aluminium Alloys - ICAA5*, vol. 217-222, Trans Tech Publications Ltd, 1996, pp. 43–56. DOI: 10.4028/WWW.SCIENTIFIC.NET/MSF.217-222.43.

[81] A. Lervik, E. Thronsen, J. Friis *et al.*, "Atomic structure of solute clusters in Al–Zn–Mg alloys," *Acta Materialia*, vol. 205, p. 116 574, Feb. 2021. DOI: 10.1016/j.actamat.2020.116574.

[82] K. Watanabe, K. Matsuda, S. Ikeno, T. Yoshida and S. Murakami, "TEM Observation of Precipitate Structures in Al-Zn-Mg Alloys with Additions of Cu/Ag," *Materials Science Forum*, vol. 794-796, pp. 985–987, 2014. DOI: 10.4028/WWW.SCIENTIFIC.NET/MSF.794-796.985.

[83] G. W. Lorimer and R. B. Nicholson, "Further results on the nucleation of precipitates in the Al-Zn-Mg system," *Acta Metallurgica*, vol. 14, no. 8, pp. 1009–1013, Aug. 1966. DOI: 10.1016/0001-6160(66)90229-X.

[84] J. H. Auld and S. Mck. Cousland, "The transition phase η in Al-Zn-Mg alloys," *Scripta Metallurgica*, vol. 5, no. 9, pp. 765–769, Sep. 1971. DOI: 10.1016/0036-9748(71)90160-8.

[85] J. H. Auld and S. M. Cousland, "On the structure of the M' phase in Al–Zn–Mg alloys," *Journal of applied crystallography*, vol. 18, no. 1, pp. 47–48, Feb. 1985. DOI: 10.1107/S002188988500975X.

[86] X. Z. Li, V. Hansen, J. GjØnnes and L. R. Wallenberg, "HREM study and structure modeling of the η phase, the hardening precipitates in commercial Al–Zn–Mg alloys," *Acta Materialia*, vol. 47, no. 9, pp. 2651–2659, Jul. 1999. DOI: 10.1016/S1359-6454(99)00138-X.

[87] A. Kverneland, V. Hansen, R. Vincent, K. Gjønnes and J. Gjønnes, "Structure analysis of embedded nano-sized particles by precession electron diffraction. η-precipitate in an Al–Zn–Mg alloy as example," *Ultramicroscopy*, vol. 106, no. 6, pp. 492–502, Apr. 2006. DOI: 10.1016/J.ULTRAMIC.2006.01.009.

[88] H. P. Degischer, W. Lacom, A. Zahra and C. Y. Zahra, "Decomposition Processes in an Al-5% Zn-1% Mg Alloy. Part II: Electronmicroscopy investigations," *Zeitschrift für Metallkunde*, vol. 71, no. 4, pp. 231–238, Apr. 1980. DOI: 10.1515/IJMR-1980-710405/MACHINEREADABLECITATION/RIS.

[89] A. Bendo, K. Matsuda, S. Lee *et al.*, "Atomic scale HAADF-STEM study of η and η_1 phases in peak-aged Al–Zn–Mg alloys," *Journal of Materials Science*, vol. 53, no. 6, pp. 4598–4611, Mar. 2018. DOI: 10.1007/s10853-017-1873-0.

[90] H. Schmalzried and V. Gerold, "Röntgenographische Untersuchungen über die Aushärtung einer Aluminium-Magnesium-Zink-Legierung," *Zeitschrift für Metallkunde*, vol. 49, no. 6, pp. 291–301, Jun. 1958. DOI: 10.1515/IJMR-1958-490603.

[91] J. D. Embury and R. B. Nicholson, "The nucleation of precipitates: The system Al-Zn-Mg," *Acta Metallurgica*, vol. 13, no. 4, pp. 403–417, Apr. 1965. DOI: 10.1016/0001-6160(65)90067-2.

[92] P. A. Thackery, "The nature and morphology of precipitate in aluminium-zinc-magnesium alloys," *Journal of the Institute of Metals*, vol. 96, no. 8, pp. 228–235, 1968.

[93] J. Gjønnes and C. J. Simensen, "An electron microscope investigation of the microstructure in an aluminium-zinc-magnesium alloy," *Acta Metallurgica*, vol. 18, no. 8, pp. 881–890, Aug. 1970. DOI: 10.1016/0001-6160(70)90016-7.

[94] L. F. Mondolfo, N. A. Gjostein and D. W. Levinson, "Structural Changes During the Aging in An Al-Mg-Zn Alloy," *JOM*, vol. 8, no. 10, pp. 1378–1385, Jan. 1956. DOI: 10.1007/BF03377889.

[95] Y. Y. Li, L. Kovarik, P. J. Phillips *et al.*, "High-resolution characterization of the precipitation behavior of an Al–Zn–Mg–Cu alloy," *Philosophical Magazine Letters*, vol. 92, no. 4, pp. 166–178, Apr. 2012. DOI: 10.1080/09500839.2011.652682.

[96] C. D. Marioara, W. Lefebvre, S. J. Andersen and J. Friis, "Atomic structure of hardening precipitates in an Al-Mg-Zn-Cu alloy determined by HAADF-STEM and first-principles calculations: Relation to η-MgZn2," *Journal of Materials Science*, vol. 48, no. 10, pp. 3638–3651, 2013. DOI: 10.1007/s10853-013-7158-3.

[97] J. Z. Liu, J. H. Chen, D. W. Yuan *et al.*, "Fine precipitation scenarios of AlZnMg(Cu) alloys revealed by advanced atomic-resolution electron microscopy study Part I: Structure determination of the precipitates in AlZnMg(Cu) alloys," *Materials Characterization*, vol. 99, pp. 277–286, Jan. 2015. DOI: 10.1016/J.MATCHAR.2014.11.028.

[98] J. Z. Liu, J. H. Chen, Z. R. Liu and C. L. Wu, "Fine precipitation scenarios of AlZnMg(Cu) alloys revealed by advanced atomic-resolution electron microscopy study Part II: Fine precipitation scenarios in AlZnMg(Cu) alloys," *Materials Characterization*, vol. 99, pp. 142–149, Jan. 2015. DOI: 10.1016/J.MATCHAR.2014.11.027.

[99] A. Bendo, K. Matsuda, K. Nishimura *et al.*, "The possible transition mechanism for the meta-stable phase in the 7xxx aluminium," *Materials Science and Technology*, vol. 36, no. 15, pp. 1621–1627, Oct. 2020. DOI: 10.1080/02670836.2020.1821323.

[100] T.-F. Chung, Y.-L. Yang, M. Shiojiri *et al.*, "An atomic scale structural investigation of nanometre-sized η precipitates in the 7050 aluminium alloy," *Acta Materialia*, vol. 174, pp. 351–368, Aug. 2019. DOI: 10.1016/J.ACTAMAT.2019.05.041.

[101] T. F. Chung, Y. L. Yang, C. L. Tai *et al.*, "HR-STEM investigation of atomic lattice defects in different types of η precipitates in creep-age forming Al–Zn–Mg–Cu aluminium alloy," *Materials Science and Engineering: A*, vol. 815, p. 141 213, May 2021. DOI: 10.1016/J.MSEA.2021.141213.

[102] N. Ryum, "Precipiation kinetics in an Al-Zn-Mg alloy," *Zeitschrift für Metallkunde*, vol. 66, no. 6, pp. 338–343, Jun. 1975. DOI: 10.1515/IJMR-1975-660603/MACHINEREADABLECITATION/RIS.

[103] A. Bendo, K. Matsuda, A. Lervik *et al.*, "An unreported precipitate orientation relationship in Al-Zn-Mg based alloys," *Materials Characterization*, vol. 158, p. 109 958, Dec. 2019. DOI: 10.1016/J.MATCHAR.2019.109958.

[104] B. Cheng, X. Zhao, Y. Zhang *et al.*, "Co-segregation of Mg and Zn atoms at the planar η1-precipitate/Al matrix interface in an aged Al–Zn–Mg alloy," *Scripta Materialia*, vol. 185, pp. 51–55, Aug. 2020. DOI: 10.1016/J.SCRIPTAMAT.2020.04.004.

[105] Y. Komura and K. Tokunaga, "Structural studies of stacking variants in Mg-base Friauf–Laves phases," *Acta Crystallographica Section B*, vol. 36, no. 7, pp. 1548–1554, Jul. 1980. DOI: 10.1107/S0567740880006565.

[106] G. Bergman, J. Waugh, L. Pauling and IUCr, "The crystal structure of the metallic phase Mg32(Al, Zn)49," *Acta Crystallographica*, vol. 10, no. 4, pp. 254–259, Apr. 1957. DOI: 10.1107/S0365110X57000808.

[107] J. H. Auld and S. M. Causland, "The metastable T phase in Al-Zn-Mg and Al-Ag-Mg alloys," *Metal Science*, vol. 10, no. 12, 1976.

[108] A. Bigot, P. Auger, S. Chambreland, D. Blavette and A. Reeves, "Atomic Scale Imaging and Analysis of T' Precipitates in Al-Mg-Zn Alloys," *Microscopy Microanalysis Microstructures*, vol. 8, no. 2, pp. 103–113, Apr. 1997. DOI: 10.1051/MMM:1997109.

[109] S. Hou, P. Liu, D. Zhang, J. Zhang and L. Zhuang, "Precipitation hardening behavior and microstructure evolution of Al–5.1 Mg–0.15Cu alloy with 3.0Zn (wt%) addition," *Journal of Materials Science*, vol. 53, no. 5, pp. 3846–3861, Mar. 2018. DOI: 10.1007/s10853-017-1811-1.

[110] S. Hou, D. Zhang, Q. Ding, J. Zhang and L. Zhuang, "Solute clustering and precipitation of Al-5.1Mg-0.15Cu-xZn alloy," *Materials Science and Engineering: A*, vol. 759, pp. 465–478, Jun. 2019. DOI: 10.1016/J.MSEA.2019.05.066.

[111] H. P. Tang, Q. D. Wang, C. Luo *et al.*, "Effects of aging treatment on the precipitation behaviors and mechanical properties of Al-5.0Mg-3.0Zn-1.0Cu cast alloys," *Journal of Alloys and Compounds*, vol. 842, p. 155 707, Nov. 2020. DOI: 10.1016/J.JALLCOM.2020.155707.

[112] L. Stemper, M. A. Tunes, P. Dumitraschkewitz *et al.*, "Giant hardening response in AlMgZn(Cu) alloys," *Acta Materialia*, vol. 206, p. 116 617, Mar. 2021. DOI: 10.1016/J.ACTAMAT.2020.116617.

[113] Y. Zou, X. Wu, S. Tang *et al.*, "Co-precipitation of T and η phase in Al-Zn-Mg-Cu alloys," *Materials Characterization*, vol. 169, p. 110 610, Nov. 2020. DOI: 10.1016/J.MATCHAR.2020.110610.

[114] Y. Zou, X. Wu, S. Tang *et al.*, "Correlation between bulk and precipitate composition in Al-Zn-Mg-Cu alloys," *Philosophical Magazine Letters*, vol. 102, no. 2, pp. 41–52, 2022. DOI: 10.1080/09500839.2021.1998690.

[115] ——, "Investigation on microstructure and mechanical properties of Al-Zn-Mg-Cu alloys with various Zn/Mg ratios," *Journal of Materials Science & Technology*, vol. 85, pp. 106–117, Sep. 2021. DOI: 10.1016/J.JMST.2020.12.045.

[116] D. B. Williams and C. B. Carter, *Transmission electron microscopy: A textbook for materials science*, 2nd ed. Springer Science & Business Media, 2009. DOI: 10.1007/978-0-387-76501-3.

[117] J. M. Zuo and J. C. Spence, *Advanced transmission electron microscopy: Imaging and diffraction in nanoscience*, 1st ed. Springer, 2017. DOI: 10.1007/978-1-4939-6607-3.

[118] M. D. Graef, *Introduction to Conventional Transmission Electron Microscopy*, 1st ed. Cambridge University Press, 2003. DOI: 10.1017/CBO9780511615092.

[119] B. J. Inkson, "Scanning electron microscopy (SEM) and transmission electron microscopy (TEM) for materials characterization," in *Materials Characterization Using Nondestructive Evaluation (NDE) Methods*, Woodhead Publishing, 2016, pp. 17–43. DOI: 10.1016/B978-0-08-100040-3.00002-X.

[120] L. E. Franken, K. Grünewald, E. J. Boekema *et al.*, "A Technical Introduction to Transmission Electron Microscopy for Soft-Matter: Imaging, Possibilities, Choices, and Technical Developments," *Small*, vol. 16, no. 14, p. 1 906 198, Apr. 2020. DOI: 10.1002/SMLL.201906198.

[121] G. McMullan, D. M. Cattermole, S. Chen *et al.*, "Electron imaging with Medipix2 hybrid pixel detector," *Ultramicroscopy*, vol. 107, no. 4-5, pp. 401–413, Apr. 2007. DOI: 10.1016/J.ULTRAMIC.2006.10.005.

[122] A. R. Faruqi and G. McMullan, "Direct imaging detectors for electron microscopy," *Nuclear Instruments and Methods in Physics Research Section A: Accelerators, Spectrometers, Detectors and Associated Equipment*, vol. 878, pp. 180–190, Jan. 2018. DOI: 10.1016/J.NIMA.2017.07.037.

[123] R. Erni, *Aberration-Corrected imaging in transmission electron microscopy: An Introduction*. Imperial College Press, 2010. DOI: 10.1142/p703.

[124] P. D. Nellist and S. J. Pennycook, "Incoherent imaging using dynamically scattered coherent electrons," *Ultramicroscopy*, vol. 78, no. 1-4, pp. 111–124, Jun. 1999. DOI: 10.1016/S0304-3991(99)00017-0.

[125] S. J. Pennycook and D. E. Jesson, "High-resolution Z-contrast imaging of crystals," *Ultramicroscopy*, vol. 37, no. 1-4, pp. 14–38, Aug. 1991. DOI: 10.1016/0304-3991(91)90004-P.

[126] A. C. Gaillot, V. A. Drits, D. R. Veblen and B. Lanson, "Polytype and polymorph identification of finely divided aluminous dioctahedral mica individual crystals with SAED. Kinematical and dynamical electron diffraction," *Physics and Chemistry of Minerals*, vol. 38, no. 6, pp. 435–448, Feb. 2011. DOI: 10.1007/s00269-011-0417-4.

[127] H. Kohl and L. Reimer, *Transmission Electron Microscopy*, ser. Springer Series in Optical Sciences. New York, NY: Springer New York, 2008, vol. 36. DOI: 10.1007/978-0-387-40093-8.

[128] B. Fultz and J. Howe, *Transmission Electron Microscopy and Diffractometry of Materials*, ser. Graduate Texts in Physics. Berlin, Heidelberg: Springer Berlin Heidelberg, 2013. DOI: 10.1007/978-3-642-29761-8.

[129] I. Lobato and D. Van Dyck, "An accurate parameterization for scattering factors, electron densities and electrostatic potentials for neutral atoms that obey all physical constraints," *Acta Crystallographica Section A*, vol. 70, no. 6, pp. 636–649, Oct. 2014. DOI: 10.1107/S205327331401643X.

[130] C. J. Humphreys, "The scattering of fast electrons by crystals," *Reports on Progress in Physics*, vol. 42, no. 11, p. 1825, Nov. 1979. DOI: 10.1088/0034-4885/42/11/002.

[131] P. N. H. Nakashima, "The crystallography of aluminium and its alloys," in *Encyclopedia of aluminum and its alloys*, G. E. Totten, M. Tiryakioğlu and O. Kessler, Eds., CRC Press, 2018, pp. 488–586.

[132] D. Johnstone, P. Crout, H. W. Ånes *et al.*, *pyxem/diffsims: diffsims 0.5.0*, 2022. DOI: 10.5281/ZENODO.6603007.

[133] C. Colliex, J. M. Cowley, S. L. Dudarev *et al.*, "Electron diffraction," in *International Tables for Crystallography*, E. Prince, Ed., Springer, Dordrecht, 2006, pp. 259–429. DOI: 10.1107/9780955360206000593.

[134] E. J. Kirkland, *Advanced computing in electron microscopy: Second edition*. Springer US, 2010, pp. 1–289. DOI: 10.1007/978-1-4419-6533-2.

[135] I. Lobato and D. Van Dyck, "MULTEM: A new multislice program to perform accurate and fast electron diffraction and imaging simulations using Graphics Processing Units with CUDA," *Ultramicroscopy*, vol. 156, pp. 9–17, Sep. 2015. DOI: 10.1016/J.ULTRAMIC.2015.04.016.

[136] L. J. Allen, A. J. D'Alfonso and S. D. Findlay, "Modelling the inelastic scattering of fast electrons," *Ultramicroscopy*, vol. 151, pp. 11–22, Apr. 2015. DOI: 10.1016/j.ultramic.2014.10.011.

[137] A. S. Eggeman, "Scanning transmission electron diffraction methods," *Acta Crystallographica Section B*, vol. 75, no. 4, pp. 475–484, Aug. 2019. DOI: 10.1107/S2052520619006723.

[138] P. A. Midgley and A. S. Eggeman, *Precession electron diffraction - A topical review*, 2015. DOI: 10.1107/S2052252514022283.

[139] R. Vincent and P. A. Midgley, "Double conical beam-rocking system for measurement of integrated electron diffraction intensities," *Ultramicroscopy*, vol. 53, no. 3, pp. 271–282, Mar. 1994. DOI: 10.1016/0304-3991(94)90039-6.

[140] A. S. Eggeman and P. A. Midgley, "Precession Electron Diffraction," in *Advances in Imaging and Electron Physics*, P. W. Hawkes, Ed., vol. 170, Elsevier, 2012, pp. 1–63. DOI: 10.1016/B978-0-12-394396-5.00001-4.

[141] P. Oleynikov, S. Hovmöller and X. D. Zou, "Precession electron diffraction: Observed and calculated intensities," *Ultramicroscopy*, vol. 107, no. 6-7, pp. 523–533, Jun. 2007. DOI: 10.1016/J.ULTRAMIC.2006.04.032.

[142] T. Bergh, "Electron microscopy of intermetallic phases in aluminium-steel joints," Ph.D. dissertation, NTNU, 2021.

[143] D. Johnstone, P. Crout, M. Nord *et al.*, *pyxem/pyxem: pyxem 0.14.1*, 2022. DOI: 10.5281/ZENODO.6505200.

[144] F. d. l. Peña, E. Prestat, V. T. Fauske *et al.*, *hyperspy/hyperspy: Release v1.7.0*, 2022. DOI: 10.5281/ZENODO.6492919.

[145] G. Carleo, I. Cirac, K. Cranmer *et al.*, "Machine learning and the physical sciences," *Reviews of Modern Physics*, vol. 91, no. 4, p. 045 002, Dec. 2019. DOI: https://doi.org/10.1103/RevModPhys.91.045002.

[146] Tensorflow Developers, *TensorFlow*, 2022. DOI: 10.5281/ZENODO.6454633.

[147] M. Shiga and S. Muto, "High spatial resolution hyperspectral imaging with machine-learning techniques," in *Nanoinformatics*, I. Tanaka, Ed., Springer Singapore, 2018, pp. 179–203. DOI: https://doi.org/10.1007/978-981-10-7617-6{_}9.

[148] Y. X. Wang and Y. J. Zhang, "Nonnegative matrix factorization: A comprehensive review," *IEEE Transactions on Knowledge and Data Engineering*, vol. 25, no. 6, pp. 1336–1353, Jun. 2013. DOI: 10.1109/TKDE.2012.51.

[149] E. F. Rauch and L. Dupuy, "Rapid spot diffraction patterns idendification through template matching," *Archives of metallurgy and materials*, vol. 50, no. 1, pp. 87–99, 2005.

[150] E. F. Rauch and M. Véron, "Automated crystal orientation and phase mapping in TEM," *Materials Characterization*, vol. 98, pp. 1–9, Dec. 2014. DOI: 10.1016/J.MATCHAR.2014.08.010.

[151] B. H. Martineau, D. N. Johnstone, A. T. van Helvoort, P. A. Midgley and A. S. Eggeman, "Unsupervised machine learning applied to scanning precession electron diffraction data," *Advanced Structural and Chemical Imaging*, vol. 5, no. 1, pp. 1–14, Mar. 2019. DOI: 10.1186/s40679-019-0063-3.

[152] *NORTEM – The Norwegian Centre for Transmission Electron Microscopy*, https://nortem.no/, 2022.

[153] *TEM Gemini Centre - NTNU*, https://www.ntnu.edu/temgemini, 2022.

[154] J. A. Mir, R. Clough, R. MacInnes *et al.*, "Characterisation of the Medipix3 detector for 60 and 80 keV electrons," *Ultramicroscopy*, vol. 182, pp. 44–53, Nov. 2017. DOI: 10.1016/j.ultramic.2017.06.010.

[155] M. A. Van Huis, M. H. Sluiter, J. H. Chen and H. W. Zandbergen, "Concurrent substitutional and displacive phase transformations in Al-Mg-Si nanoclusters," *Physical Review B - Condensed Matter and Materials Physics*, vol. 76, no. 17, p. 174 113, Nov. 2007. DOI: 10.1103/PhysRevB.76.174113.

[156] K. Teichmann, C. Marioara, S. Andersen *et al.*, "HRTEM study of the effect of deformation on the early precipitation behaviour in an AA6060 Al–Mg–Si alloy," *Philosophical Magazine*, vol. 91, no. 28, pp. 3744–3754, Oct. 2011. DOI: 10.1080/14786435.2011.593577.

[157] X. J. Jiang, B. Noble, B. Holme, G. Waterloo and J. Tafto, "Differential scanning calorimetry and electron diffraction investigation on low-temperature aging in Al-Zn-Mg alloys," *Metallurgical and Materials Transactions A 2000 31:2*, vol. 31, no. 2, pp. 339–348, 2000. DOI: 10.1007/S11661-000-0269-X.

[158] V. Hansen, O. B. Karlsen, Y. Langsrud and J. Gjønnes, "Precipitates, zones and transitions during aging of Al - Zn - Mg - Zr 7000 series alloy," *Materials Science and Technology*, vol. 20, no. 2, pp. 185–193, 2004. DOI: 10.1179/026708304225010424.

[159] Z. Li, B. Xiong, Y. Zhang *et al.*, "Investigation of microstructural evolution and mechanical properties during two-step ageing treatment at 115 and 160 °C in an Al–Zn–Mg–Cu alloy pre-stretched thick plate," *Materials Characterization*, vol. 59, no. 3, pp. 278–282, Mar. 2008. DOI: 10.1016/J.MATCHAR.2007.01.006.

[160] J. Liu, R. Hu, J. Zheng *et al.*, "Formation of solute nanostructures in an Al–Zn–Mg alloy during long-term natural aging," *Journal of Alloys and Compounds*, vol. 821, p. 153 572, Apr. 2020. DOI: 10.1016/J.JALLCOM.2019.153572.

[161] R. Ferragut, A. Somoza and A. Tolley, "Microstructural evolution of 7012 alloy during the early stages of artificial ageing," *Acta Materialia*, vol. 47, no. 17, pp. 4355–4364, Nov. 1999. DOI: 10.1016/S1359-6454(99)00315-8.

[162] R. Ferragut, A. Somoza, A. Tolley and I. Torriani, "Precipitation kinetics in Al–Zn–Mg commercial alloys," *Journal of Materials Processing Technology*, vol. 141, no. 1, pp. 35–40, Oct. 2003. DOI: 10.1016/S0924-0136(02)01044-0.

[163] L. Stemper, M. A. Tunes, R. Tosone, P. J. Uggowitzer and S. Pogatscher, "On the potential of aluminum crossover alloys," *Progress in Materials Science*, vol. 124, p. 100 873, Feb. 2022. DOI: 10.1016/J.PMATSCI.2021.100873.

[164] H. Deep Chopra, B. C. Muddle and I. J. Polmear, "The structure of primary strengthening precipitates in an Al-1.5wt% Cu-4.0wt% Mg-0.5wt% Ag alloy," *Philo*, vol. 73, no. 6, pp. 351–358, 1996. DOI: 10.1080/095008396180623.

[165] M. Mihara, C. D. Marioara, S. J. Andersen *et al.*, "Precipitation in an Al–Mg–Cu alloy and the effect of a low amount of Ag," *Materials Science and Engineering: A*, vol. 658, pp. 91–98, Mar. 2016. DOI: 10.1016/J.MSEA.2016.01.087.

[166] K. Teichmann, C. D. Marioara, S. J. Andersen and K. Marthinsen, "The effect of preaging deformation on the precipitation behavior of an Al-Mg-Si alloy," *Metallurgical and Materials Transactions A: Physical Metallurgy and Materials Science*, vol. 43, no. 11, pp. 4006–4014, Nov. 2012. DOI: 10.1007/s11661-012-1235-0.

[167] S. Jin, T. Ngai, L. Li *et al.*, "Aging Response and Precipitation Behavior after 5% Pre-Deformation of an Al-Mg-Si-Cu Alloy," *Materials*, vol. 11, no. 8, p. 1422, Aug. 2018. DOI: 10.3390/MA11081422.

[168] D. Yin, Q. Xiao, Y. Chen *et al.*, "Effect of natural ageing and pre-straining on the hardening behaviour and microstructural response during artificial ageing of an Al–Mg–Si–Cu alloy," *Materials & Design*, vol. 95, pp. 329–339, Apr. 2016. DOI: 10.1016/J.MATDES.2016.01.119.

[169] M. Werinos, H. Antrekowitsch, T. Ebner *et al.*, "Design strategy for controlled natural aging in Al–Mg–Si alloys," *Acta Materialia*, vol. 118, pp. 296–305, Oct. 2016. DOI: 10.1016/J.ACTAMAT.2016.07.048.

[170] S. Jin, T. Ngai, L. Li *et al.*, "Influence of natural aging and pre-treatment on the precipitation and age-hardening behavior of Al-1.0Mg-0.65Si-0.24Cu alloy," *Journal of Alloys and Compounds*, vol. 742, pp. 852–859, Apr. 2018. DOI: 10.1016/J.JALLCOM.2017.10.005.

[171] T. Masuda, Y. Takaki, T. Sakurai and S. Hirosawa, "Combined Effect of Pre-Straining and Pre-Aging on Bake-Hardening Behavior of an Al-0.6 mass%Mg-1.0 mass%Si Alloy," *Materials Transactions*, vol. 51, no. 2, pp. 325–332, Feb. 2010. DOI: 10.2320/MATERTRANS.L-M2009831.

[172] M. Kolar, K. O. Pedersen, S. Gulbrandsen-Dahl and K. Marthinsen, "Combined effect of deformation and artificial aging on mechanical properties of Al–Mg–Si Alloy," *Transactions of Nonferrous Metals Society of China*, vol. 22, no. 8, pp. 1824–1830, Aug. 2012. DOI: 10.1016/S1003-6326(11)61393-9.

[173] Y. Aruga, M. Kozuka, Y. Takaki and T. Sato, "Effects of natural aging after pre-aging on clustering and bake-hardening behavior in an Al–Mg–Si alloy," *Scripta Materialia*, vol. 116, pp. 82–86, Apr. 2016. DOI: 10.1016/J.SCRIPTAMAT.2016.01.019.

[174] M. Murayama and K. Hono, "Pre-precipitate clusters and precipitation processes in Al–Mg–Si alloys," *Acta Materialia*, vol. 47, no. 5, pp. 1537–1548, Mar. 1999. DOI: 10.1016/S1359-6454(99)00033-6.

[175] J. K. Sunde, "The Effect of Elevated Temperatures on Precipitation in Aluminium Alloys – An Advanced Transmission Electron Microscopy Study," Ph.D. dissertation, NTNU, 2020.

[176] C. Boutsidis and E. Gallopoulos, "SVD based initialization: A head start for nonnegative matrix factorization," *Pattern Recognition*, vol. 41, no. 4, pp. 1350–1362, Apr. 2008. DOI: 10.1016/J.PATCOG.2007.09.010.

[177] F. Esposito, "A Review on Initialization Methods for Nonnegative Matrix Factorization: Towards Omics Data Experiments," *Mathematics*, vol. 9, no. 9, p. 1006, Apr. 2021. DOI: 10.3390/MATH9091006.

[178] N. Cautaerts, P. Crout, H. W. Ånes *et al.*, "Free, flexible and fast: Orientation mapping using the multi-core and GPU-accelerated template matching capabilities in the Python-based open source 4D-STEM analysis toolbox Pyxem," *Ultramicroscopy*, vol. 237, p. 113 517, Jul. 2022. DOI: 10.1016/J.ULTRAMIC.2022.113517.

Part III

Papers

Chapter 8

Publications

Paper I

Atomic structure of solute clusters in Al-Zn-Mg alloys

A. Lervik, E. Thronsen, J. Friis, C. D. Marioara, S. Wenner, A. Bendo, K. Matsuda, R. Holmestad, S. J. Andersen

Acta Materialia (2021) **205** 116574

Author contributions

A. Lervik conducted all STEM experiments and wrote the initial draft. E. Thronsen assisted significantly in writing the initial draft and conducted the diffraction and image simulations. J. Friis prepared the models and conducted the DFT calculations. S. Wenner conducted the ATP measurements. S. J. Andersen analysed the STEM data, deduced the structure of the clusters and assisted in writing the draft. A. Bendo and K. Matsuda suggested the study and provided the lab cast alloy. C. D. Marioara analysed the STEM data and commented on the initial draft. R. Holmestad and S.J. Andersen supervised the study. All authors commented on the final manuscript.

Acta Materialia 205 (2021) 116574

Contents lists available at ScienceDirect

Acta Materialia

journal homepage: www.elsevier.com/locate/actamat

Atomic structure of solute clusters in Al–Zn–Mg alloys

A. Lervik[a], E. Thronsen[a], J. Friis[a,b], C.D. Marioara[b], S. Wenner[a,b], A. Bendo[c], K. Matsuda[c], R. Holmestad[a,*], S.J. Andersen[b]

[a] Department of Physics, Norwegian University of Science and Technology (NTNU), Trondheim N-7491, Norway
[b] SINTEF Industry, Trondheim, N-7465, Norway
[c] Graduate School of Science and Engineering, University of Toyama, 3190 Gofuku, Toyama 930-8555, Japan

ARTICLE INFO

Article history:
Received 31 August 2020
Revised 12 December 2020
Accepted 13 December 2020
Available online 17 December 2020

Keywords:
Aluminium alloys
Transmission electron microscopy (TEM)
Natural ageing
Atom probe tomography (APT)
Density functional theory (DFT)

ABSTRACT

Scanning transmission electron microscopy imaging of Al–Zn–Mg alloys has provided new information on the atomic structures of solute rich clusters forming from a supersaturated solid solution at low temperatures. A unique unit of high Zn/Mg ratio is the fundamental cluster building block. The unit is essentially a partial substitution by Mg and Zn on the cubic aluminium cell and its surrounding truncated cube octahedral shell. A simple set of principles based on Frank–Kasper structures describes how the basic units arrange with respect to each other to form larger clusters. Density functional theory calculations, atom probe tomography and simulated diffraction patterns support the proposed atomic models. The results provide new insight into the very early stages of age-hardening in aluminium alloys.

1. Introduction

The age-hardenable Al–Zn–Mg (7xxx) alloys are important in the transportation industry, due to properties such as good formability and high strength-to-weight ratio [1,2]. Prior to hardening, a high temperature solution heat treatment (SHT) is required to dissolve the solute atoms, followed by a quench to room temperature leading to a supersaturated, metastable solid solution consisting of solute elements and vacancies. By keeping the material at room temperature, the hardness will gradually increase [3]. This effect is called 'natural ageing (NA)' and is caused by solute atoms aggregating to clusters on the face centered cubic (fcc) aluminium lattice. The solute clusters act as small obstacles for dislocation movements during plastic deformation and contribute to strength.

Clusters with periodic ordering are referred to as 'Guinier–Preston (GP) zones', after their discoverers in 1938 [4,5]. In Al–Zn–Mg alloys, two types of GP-zones have been suggested: GP(I) related to solute rich clusters [6–10], and GP(II) related to vacancy rich clusters [6–12]. Earlier studies have suggested that both play key roles during the subsequent artificial ageing (AA) stage (120–200 °C), especially in initiating the formation of the coherent, hardening precipitate structure η' ($MgZn_2$) [6,13–18]. GP(I) zones have been found to exist even after longer ageing times [6,9,19,20]. The GP(II) zones are suggested as possible precursors of the metastable η' precipitate [6,9]. However, the transformation from clusters to precipitates are not understood [12].

This work focuses on the structure of the solute rich GP(I) clusters formed at low temperature, previously reported in studies using transmission electron microscopy (TEM) [8,21–23], X-ray diffraction (XRD) [11,24–26] and positron annihilation spectroscopy (PAS) [11,27]. Up till now, a simple anti-phase ordering of solute has been proposed based on diffraction patterns acquired from large regions [8]. This work shows that the ordering is of a fundamentally different kind, and uncovers the atomic structure of the GP(I) zones with support from experimental techniques, simulations and calculations.

2. Material and methods

2.1. Materials

The data in this work has been obtained from two Al–Zn–Mg alloys. An industrial alloy (in at.%: 0.08% Fe, 1.42% Mg, 0.08% Si, 2.98% Zn and 0.04% Zr), labelled Alloy #1, was air cooled after extrusion and left naturally ageing for 17 years. A high purity lab-cast alloy (in at.%: 1.89% Mg and 3.49% Zn), labelled Alloy #2, was SHT at 475 °C for 1 h before it was quenched into water and left for NA. A group of samples were directly artificially aged at 150 °C, while some were artificially aged at 120 °C after 4 days of NA. The Vickers hardness (HV0.1) curve for Alloy #2 obtained during natural ageing reaches a hardness of ~ 110 after ~ 10 days. This does not

* Corresponding author.
E-mail address: Randi.Holmestad@ntnu.no (R. Holmestad).

https://doi.org/10.1016/j.actamat.2020.116574

increase significantly with further natural ageing times. A similar hardness value is obtained after 4 days natural ageing and 8 min artificial ageing at 120 °C. Hardness curves are shown in Supplementary Fig. 1. Alloy #1 naturally aged for 17 years had a hardness value of 107 ± 11.

2.2. Transmission electron microscopy

TEM specimens were prepared by grinding bulk samples with SiC abrasive paper to ~ 60 µm foil thickness, punched into 3 mm discs and thereafter electropolished with a Struers TenuPol-5 machine using an electrolyte mixture of 1/3 HNO_3 and 2/3 C_3CH_3OH at temperatures between −30 and −20 °C and an applied potential of 20 V. High-resolution high-angle annular dark field (HAADF)-scanning transmission electron microscopy (STEM) images were acquired using an image- and probe Cs-corrected JEOL ARM200CF operated at 200 kV with convergence semi-angle and inner collector angle 28 mrad and 48 mrad, respectively. Smart Align (HREM research) was used in the acquisition, which involves acquiring a stack of successive low-dose images and afterwards aligning them to correct both rigid- and non-rigid scan distortions [28].

2.3. Atom probe tomography

Samples for atom probe tomography (APT) were prepared according to the conventional focused ion beam (FIB) lift-out method [29], using a FEI Helios G2 dual-beam instrument. The tips were oriented along the [001] direction and sharpened to apex diameters of <50 nm, finishing with a 5 kV Ga^+ ion beam. APT was performed with a Cameca LEAP 5000XS in voltage pulse mode, with the sample cooled to 50 K. A volume of 20 million atoms was evaporated with a pulse fraction of 25%, a pulse rate of 500 kHz, and 0.3% of the pulses leading to a detected atom. A detection efficiency of 77% was assumed in the data reconstruction. Poles and lattice spacings in the [001] directions were visible, allowing a fit of the image compression factor and field factor to obtain the correct scaling in all directions. The maximum separation algorithm was used [30], with clusters defined by 3rd nearest neighbor solutes being closer than $d_{max} = 0.53$ nm and the minimum size of clusters being $N_{min} = 80$ atoms. This maximizes the ratio of real to random identified clusters. Enveloping and erosion of 0.53 nm were used to define the cluster-matrix interface and improve composition quantification [30]. The cluster radius was estimated using the radius of gyration in the (non-aberrated) z direction multiplied by a shape factor. Since the chemical composition is averaged over a large number of small clusters, the statistical deviation is expected to be large and is used as an error estimate. Expected measurement errors include detection efficiency errors (the average error is roughly 1% in compositional fraction), uneven chemical distributions due to crystallographic poles, as well as background events. All these are random errors and are reflected in the statistically determined error.

2.4. Density functional theory

The density functional theory (DFT) calculations of the formation enthalpies for the structures were performed at 0 K with the Vienna Ab initio Simulation Package (VASP) [31,32], using the Perdew–Burke–Ernzerhof (PBE) gradient approximation [33]. A gamma-centred k-point mesh was used in all calculations with a plane wave energy cut-off above 400 eV and a maximal k-point distance of 0.18 $Å^{-1}$. The Methfessel–Paxton method [34] of 1st order was applied for atomic position relaxations with maximum force of 0.001 eV/Å and a smearing factor of 0.2. For accurate energies, all relaxations were followed by a static calculation using the tetrahedron method with Bloch corrections. The formation enthalpies for the different configurations were calculated as

$$\Delta H = E - \sum_i E_{X_i}, \tag{1}$$

where E is the total energy of the configuration in question and i is an index running over all atoms in the structure. E_X is the energy of one element X, embedded in the matrix ($X = \mathrm{Al, Mg, Zn}$). For consistency E_X is calculated from bulk Al supercells of the same size as the configuration in question with a single Al substituted with X [14];

$$E_X = E_{XAl_{N-1}} - \frac{N-1}{N} E_{Al_N}, \tag{2}$$

where N is the number of atoms in the supercell.

2.5. Diffraction pattern and image simulations

The nanobeam diffraction (NBD) patterns were simulated using the μSTEM simulation software in the position-averaged convergent beam electron diffraction (PACBED) mode [35]. Calculations were carried out on a 512 × 512 pixel mesh grid with 10 layers of Al unit cells surrounding the cluster model on each lateral side forming a supercell with dimensions approximately 97 × 97 Å to avoid wrap-around errors due to the Al-cluster interface. The probe forming aperture was set to 0.75 mrad to avoid overlap of the diffraction spots. The model was periodic in the z-direction and the simulations were carried out over a TEM sample thickness interval of 12–700 Å. For the HAADF-STEM image simulations, the MULTEM simulation software was used [36]. Calculations were carried out on a 1024 × 1024 pixel mesh grid using a supercell with lateral dimensions of approximately 40 × 40 Å and a thickness of approximately 405 Å. The convergence angle was set to 27.78 mrad and the inner and outer collection angles were 48 mrad and 206 mrad, respectively.

3. Results and discussion

3.1. Microstructure overview

Conventional bright field (BF)-TEM imaging along the [001] Al direction showed high densities of small (1–2 nm) clusters uniformly distributed within the Al matrix, as Fig. 1**a** demonstrates for Alloy #1. Fig. 1**b** shows the corresponding selected area diffraction pattern (SADP). Two types of diffraction spots appear between the Al reflections. The sharp diffraction spots (red circles) on the {100} and {110} positions in Fig. 1**b** originate from larger Al_3Zr dispersoids [37,38]. The diffuse spots (yellow triangles) originate from clusters and are a result of high densities combined with the different crystallographically equivalent orientations the clusters can have with the aluminium, while the spread in intensity is due to their small physical size. These spots have previously been associated with GP(I) zones [8–10,21,22,37,39–42]. Fig. 1**c** shows a HAADF-STEM image of clusters and Fig. 1**d** shows the corresponding fast Fourier transform (FFT). It has strong resemblance with the SADP in Fig. 1**b**. The diffuse, high-intensity spots at the {110} positions in Fig. 1**d** are artefacts caused by the TEM sample preparation (cf. Supplementary Information) and should not be confused with the clear diffraction from the Al_3Zr dispersoids (Fig. 1**b**). After 2 weeks and after 8 months natural ageing, as well as for 8 min ageing at 120 °C, Alloy #2 exhibits the same diffuse diffraction spots as Alloy #1 (Fig. 1) with only slight variations in intensities. This is shown in Supplementary Fig. 2.

3.2. Cluster statistics and composition by atom probe tomography

Fig. 2**a** shows the solute Mg and Zn atoms inside the defined clusters in an evaporated APT needle of Alloy #1 after 17 years

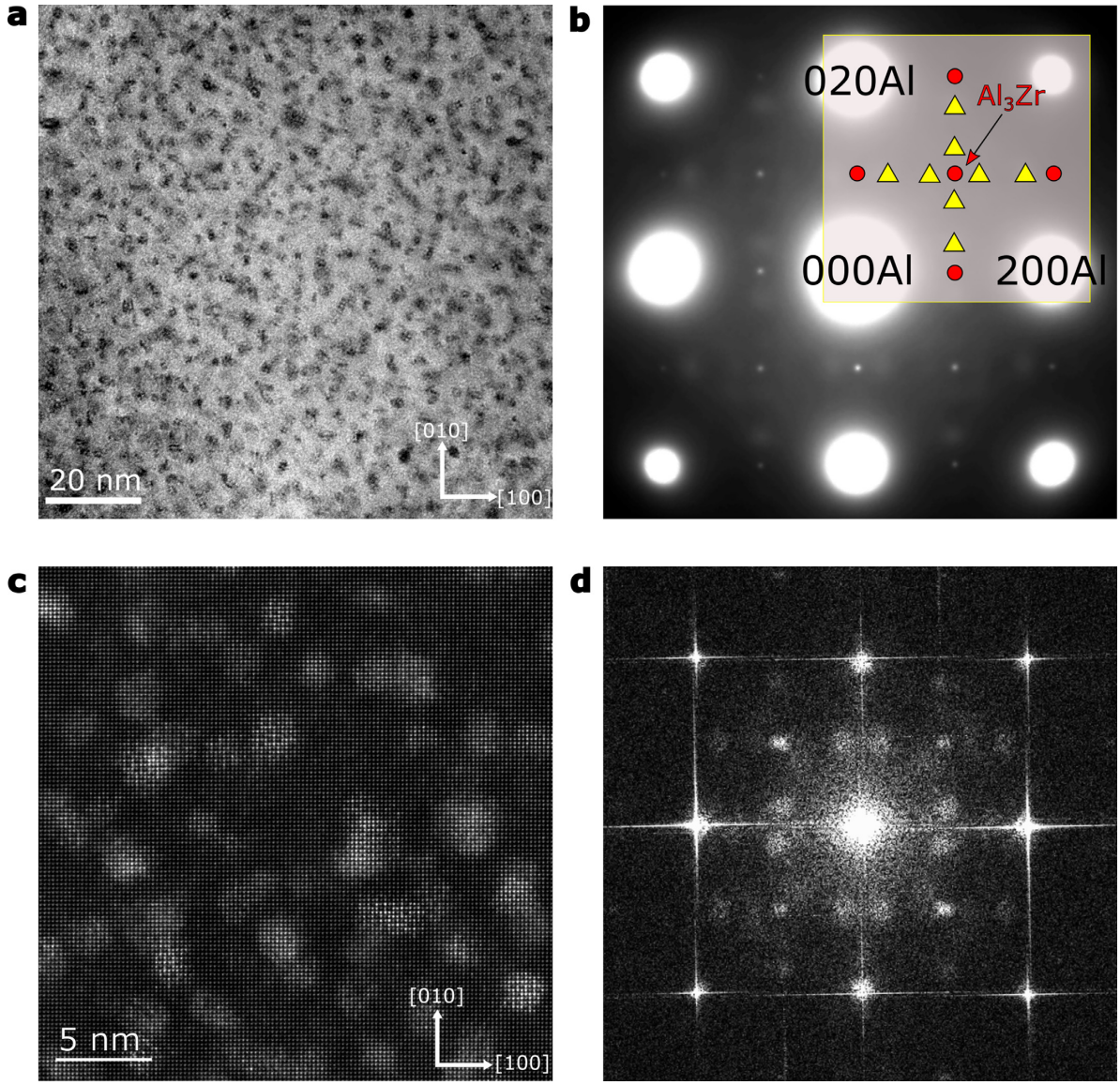

Fig. 1. Alloy #1 after 17 years of natural ageing, oriented along the [001] direction. **a**, BF-TEM image showing a high density of solute clusters (dark contrast). **b**, SADP with diffraction spots of Al_3Zr dispersoids and GP(I) zones, marked by circles and triangles, respectively. **c**, HAADF-STEM image clearly indicating ordering of solute on the fcc lattice. **d**, fast Fourier transform of **c** where the intensity in the forbidden {110} positions are due to a surface layer artefact.

natural ageing. As expected, dense co-clustering of Mg and Zn atoms is present. The composition of clusters as a function of the number of atoms within a cluster is shown in Fig. 2**b**. Clusters smaller than about 3 nm have a slightly lower level of Mg and Zn than the larger clusters. This is most likely an artifact of the evaporation field difference between clusters and the matrix, giving a local magnification effect [43]. The mean cluster radius is 1.90 nm, and the Zn/Mg ratio, which is shown as a function of the cluster diameter in Fig. 2**c**, has an average of 1.75. The average composition of clusters with a radius larger than 3 nm is 74.7 ± 0.2% Al, 16.8 ± 0.1% Zn, 8.5 ± 0.1% Mg (at.%). The measured Zn/Mg ratio is slightly higher than values reported in other APT studies [23,37,39,44–46]. However, these studies are not directly comparable as the alloys have different compositions and heat-treatments. Differences in natural ageing times can also affect the cluster composition [23]. In Cu-containing alloys, the ratio may be lower since Cu tends to substitute Zn positions [14,44]. The high amount of Al measured in the clusters is in agreement with other studies [37,44,46]. In the regions between the clusters, the Al matrix was found to contain 1.12 and 0.35 at.% Zn and Mg, respectively. The APT dataset gave an average nearest neighbour separation of 4.8 ± 0.9 nm and number density of clusters as approximately 3.35×10^{24} m^{-3}. The obtained values for mean size and number density are in correspondence with other studies using small-angle X-ray scattering (SAXS) [11,26,47].

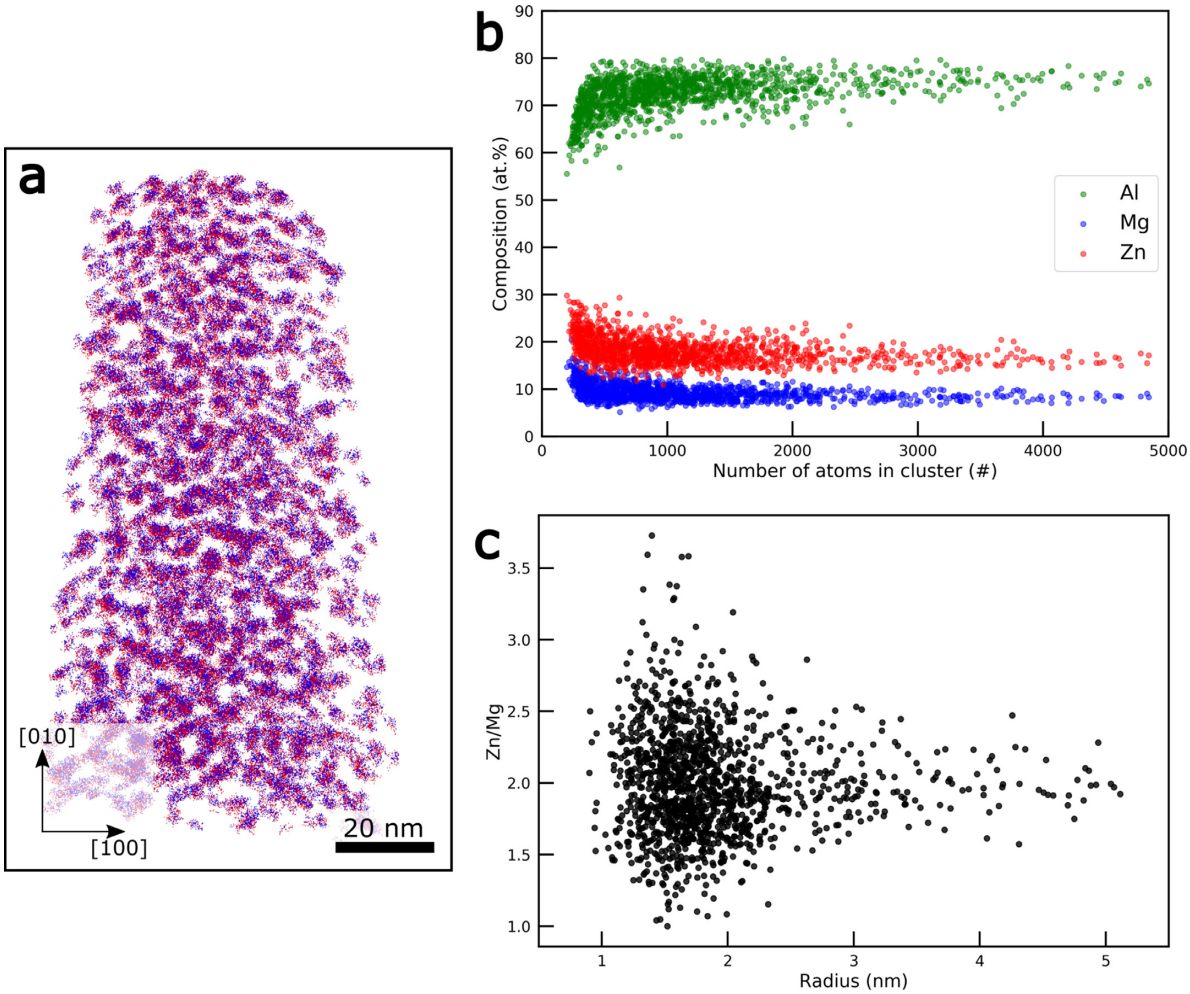

Fig. 2. **a**, Elemental map of solute atoms Mg (blue) and Zn (red) of clusters in Alloy #1 after 17 years NA, measured by atom probe tomography. **b**, composition of clusters shown against the number of atoms in each cluster. **c**, Zn/Mg ratio versus radius of the cluster. (For interpretation of the references to colour in this figure legend, the reader is referred to the web version of this article.)

3.3. Cluster units and their stacking principles

Both APT (Fig. 2**a**) and HAADF-STEM (Fig. 1**c**) indicate that the clusters are equiaxed. Along a ⟨100⟩ direction, approximately 1/3 of the non-overlapped clusters exhibits a clear atomic structure. Fig. 3**a** and **c** show two representative clusters. Based on the intensities and interatomic distances, suggested atomic motifs of Fig. 3**a** and **c** are given in **b** and **d**, respectively. Blue and red circles correspond to Al lattice columns with Mg and Zn substitutions, respectively. It can be seen that the atoms belonging to the cluster mostly adapt the Al lattice positions. The analysis demonstrates that the clusters may be simplified in terms of one single unit. This unit is identified by a unique high-intensity column situated at the centre where two rows of 5 bright columns along the lateral ⟨100⟩ Al directions intersect. This column is labelled as the 'Interstitial site' in Fig. 3. Together with the observation that the nearest four Zn columns of the centre are pushed slightly away (approximately 13%) from the ideal Al lattice, this indicates that the centre of the unit contains an interstitial atom relative to the fcc Al.

In the HAADF-STEM images along the [001] zone axis, the cluster unit has 4-fold symmetry. The solute arrangement compatible with these observations is a three-shell structure in the fcc lattice, centred on an Al cube with a possible interstitial. The inner shell is an octahedron formed by the six faces. The second shell is formed by the eight cube corners. The third shell is a truncated cube octahedron (TCO) of the 24 positions around the cube. Intensities in the images suggest that the shells have ideal compositions Zn_6, Mg_8 and Zn_{24}, respectively, with a common interstitial centre 'i'. This is illustrated in Fig. 3**e** and **f**. This cluster unit spans two Al-periods (8.1 Å). Thus, along the [001] direction the stacking is abbreviated by '[002]'. The TCO has six square and eight hexagonal faces, coinciding with the {100} and {111} Al planes, respectively, as shown in Fig. 3**e**. The 24 vertices are given by permutations of the lattice vector $\frac{1}{2}\langle 120\rangle$ from the centre of the cube.

Individual clusters show variations in structure, as in Fig. 3**a** and **c**. However, they can always be explained in terms of the described TCO unit stacked according to three principles: [002], ⟨411⟩ and ⟨330⟩. The two last concerns the lateral plane, both with an

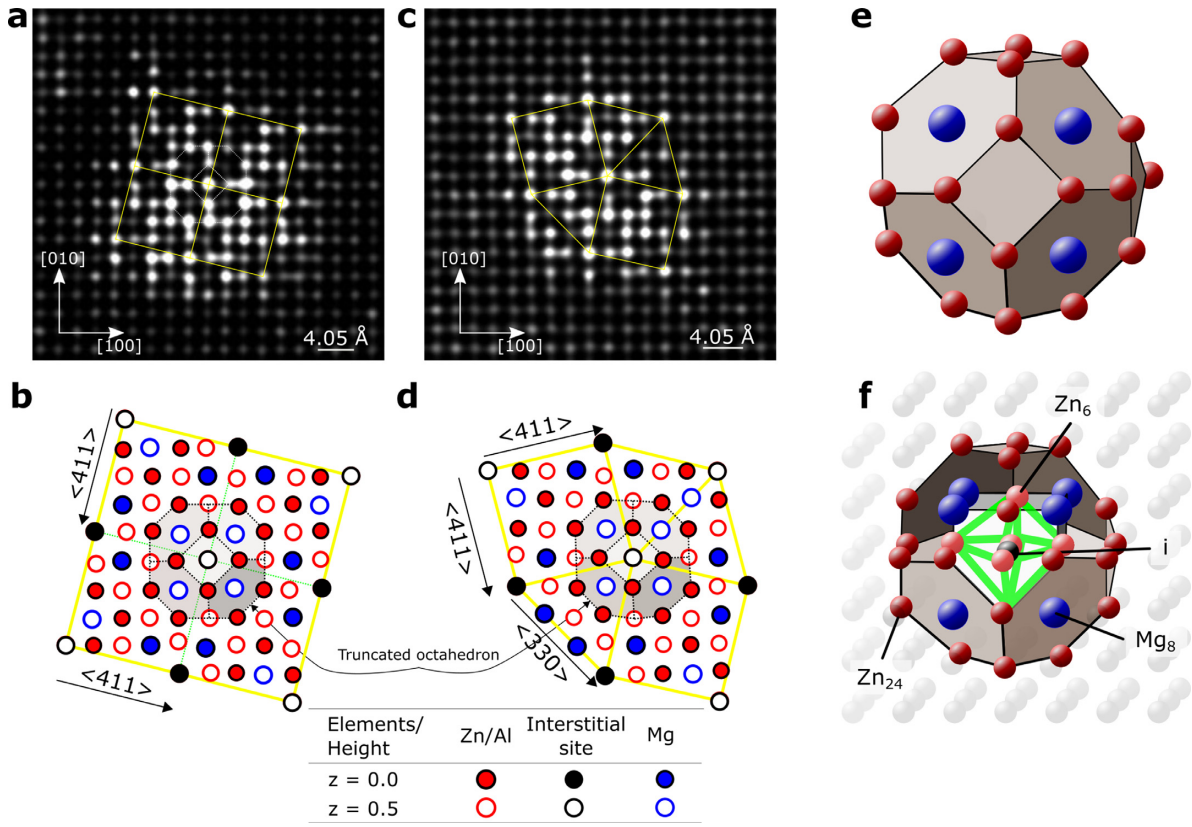

Fig. 3. a, c, Filtered HAADF-STEM images of two clusters. **b, d**, Suggested atomic column maps of **a** and **c**, showing the connection principles ($\langle 411\rangle$, $\langle 330\rangle$) between unit centres, denoted 'Interstital site'. **e**, TCO-shell with Zn on all vertices and Mg on corners. **f**, interior view of a cluster unit embedded in Al with an interstitial 'i'.

inter-distance of 8.59 Å as shown in Fig. 3, where the yellow lines connect the distinct 'Interstitial site' centres of the units. Experimental observations suggest that the most common lateral connection is $\langle 411\rangle$. In Fig. 3**a** and **b** four units arrange in a $\langle 411\rangle$ connected square. This is repeated in the viewing direction by the [002] connection. Fig. 3**a** and **c** show that the lateral connections form a pattern of squares and triangles, which is a σ-type Frank–Kasper ordering [48–50].

3.4. Density functional theory calculations

In order to elucidate the suggested structure, DFT calculations of cluster units embedded in $4 \times 4 \times 4$ Al cells (256 atoms) were conducted. We describe the unit by the nomenclature '$iZ_xM_yZ_z$', referring to the four constituents: an interstitial and three polyhedra (cf. Fig. 3**f**). The lower-case letter 'i' (= a, z or m) indicates an interstitial centre (Al, Zn or Mg, respectively). If no interstitial is present, the character is omitted. Z_x ($x = 0, \ldots, 6$) indicates the number of Zn atoms on the cube faces, M_y ($y = 0, 8$) are the Mg atoms on the cube corners and Z_z ($z = 0, \ldots, 24$) is the number of Zn on the TCO shell. The maximum number of solute atoms in the cluster unit is 39 including the interstitial. Fig. 4 shows formation enthalpy versus pressure for a range of configurations of cluster units (cf. Supplementary Tables 1 and 2).

The DFT calculations show that the cluster units prefer high Zn/Mg ratios and the two Zn-containing shells filled by only Zn. Fig. 4 shows that a fully occupied TCO ($Z_z, z = 24$) is stabilising, providing structures with 9 of the 11 lowest energies with Zn/Mg ratios above 3. Having both Zn shells fully occupied gives the best energies, which can be seen by considering the Mg-free series: $Z_0M_0Z_{12} \rightarrow Z_0M_0Z_{24} \rightarrow Z_6M_0Z_{24}$. This also shows that pressure falls with increased Zn concentration. Pressure represents the misfit volume compared to a supercell only containing Al but is not directly linked to energy: an interstitial ($zZ_6M_0Z_{24}$) improves pressure, but gives more unfavourable formation enthalpy. An interstitial Zn in $Z_0M_0Z_{12}$ ($zZ_6M_0Z_{12}$) is directly unfavourable. Thus, an interstitial is preferred for a Mg-cube (Mg_8) and one filled polyhedron (Z_6 or Zn_{24}), but preferably both.

$Z_6M_0Z_0$ and $zZ_6M_0Z_0$ show that Zn on the faces of an Al cell is more favorable than remaining in arbitrary solid solution, but that an interstitial is unlikely. With Mg on corners ($Z_6M_8Z_0$) the cluster energy improves significantly and an interstitial ($zZ_6M_8Z_0$) becomes favorable. This indicates that the interstitials are consequences of the TCO and not nucleation points. With an interstitial in $Z_6M_8Z_{24}$, three configurations of $iZ_6M_8Z_{24}$ are obtained with similar and overall lowest formation enthalpies. Despite a higher Zn/Mg ratio, $zZ_3M_8Z_{24}$ and $zZ_6M_8Z_{12}$ have comparable formation enthalpies. The reason is likely due to lower symmetry, as the inner octahedron Z_3 conserves only one (3-fold) symmetry axis.

3.5. Stacking of cluster units

Having established that the three most energetically favourable cluster units are of type $iZ_6M_8Z_{24}$, they were subsequently used to investigate the stability of larger clusters. The two stacking

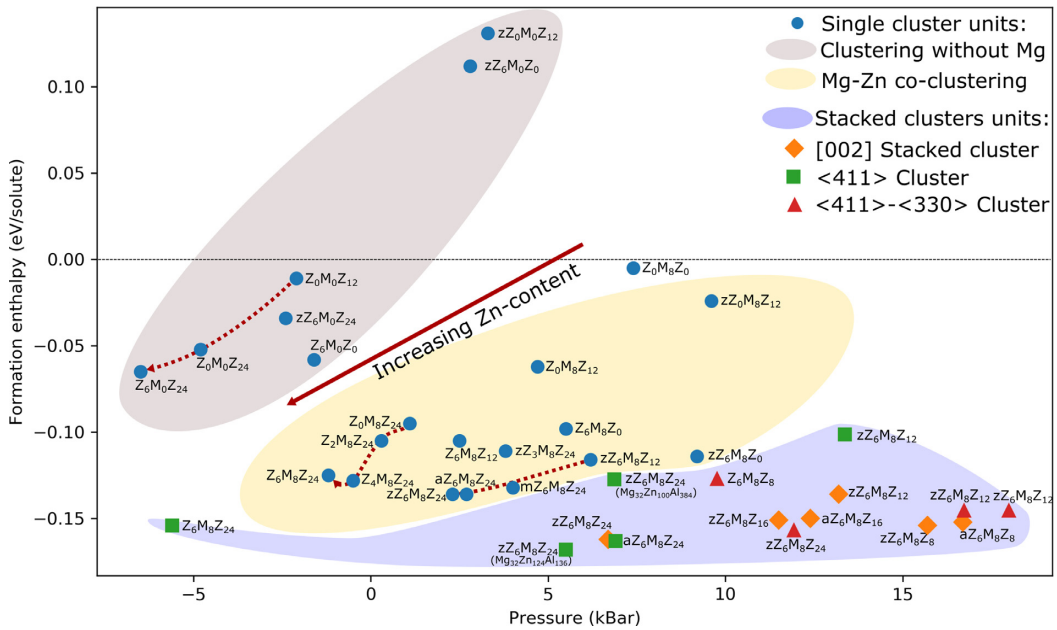

Fig. 4. DFT calculated formation enthalpy versus pressure for cluster structures with different Al, Zn, and Mg content embedded in aluminium matrix. Compositions refer to net content in single cluster units after stacking. Results demonstrate an advantage of high Zn content in the clusters. (Cf. Supplementary Tables 1 and 2 for detailed explanation of the structures.)

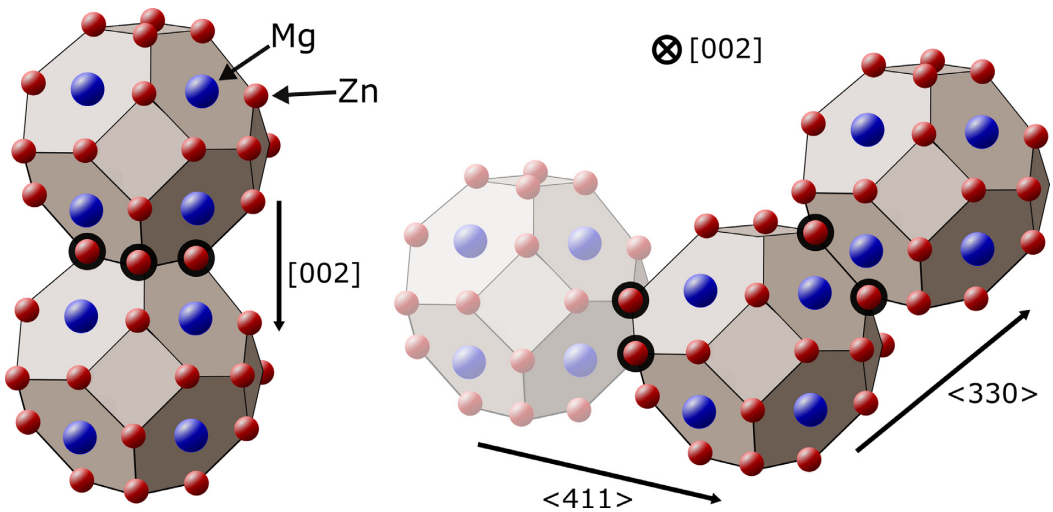

Fig. 5. Schematic illustration of the TCO unit stacking principles [002], ⟨330⟩ and ⟨411⟩ observed in the clusters. Note that the stacking causes certain atoms to be shared: two TCOs share 4, 2 and 2 positions, respectively, lowering the overall Zn/Mg ratio as compared to one TCO unit embedded in an Al matrix alone. The shared atoms are emphasised with black circles in the figure.

principles most frequently observed, [002] and ⟨411⟩, were used for the models, as shown in Fig. 5. A cluster of four units with ⟨411⟩ connections is shown in Fig. 6**a**. Two calculation supercells, $4 \times 4 \times 2$ and $6 \times 6 \times 2$ Al cells, were used for the [002] and the ⟨411⟩ stacked clusters, respectively. The calculations were done with Zn both fully and semi-occupied in the TCO shells. The results are marked by diamonds in Fig. 4 and labelled '[002] Stacked clusters' and '⟨411⟩ Cluster'. Based on the calculations, it can be concluded that clusters stacked along [002] are more energetically favourable than single cluster units embedded in the Al matrix. Moreover, by connecting the [002] stacked clusters in a ⟨411⟩ manner the lowest formation enthalpies are obtained for models containing an interstitial, which is in accordance with the analysis of HAADF-STEM images presented in Fig. 3.

The Zn/Mg ratio in the APT measurements was seen to approach 2 for larger clusters. In an infinite string of [002] connected units every unit shares 8 atomic positions. Thus, for the Zn completed cluster with Zn interstitial ($zZ_6M_8Z_{24}$), the number of Zn in the outer shell (Z_y) is reduced to 20, which results in an overall composition Mg_8Zn_{27}. The sharing of atoms due to

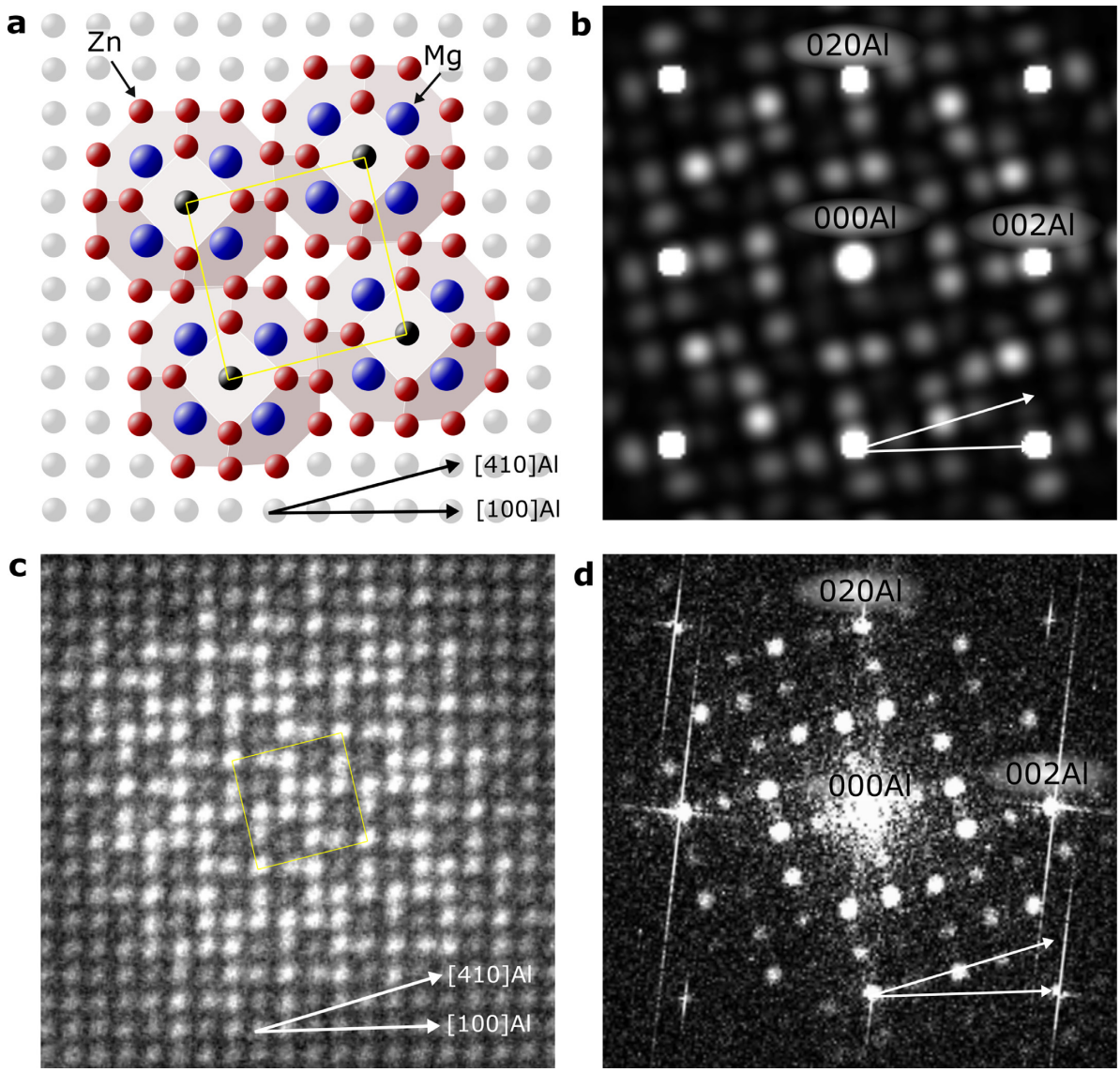

Fig. 6. **a**, [001] projection of $zZ_6M_8Z_{24}$ cluster units connected in a ⟨411⟩ square embedded in Al. **b**, Simulated NBD pattern of **a. c**, HAADF-STEM of a cluster in Alloy #2. **d**, FFT of **c**. The intensities of the simulated diffraction pattern in **b** match the intensities found in the corresponding FFT in **d**.

stacking is emphasised in Fig. 5 by black circles. Connecting four $zZ_6M_8Z_{24}$ units in a ⟨411⟩ square, means that for each unit 4 TCO positions are edge-shared. Therefore, the cluster $zZ_6M_8Z_{24}$ in an infinite stack of rings shares 12 atoms with neighbours and 'reduces' to $zZ_6M_8Z_{18}$ (Mg_8Zn_{25}). This Zn/Mg ratio (3.1) is still high compared to APT measurements. Although the calculations showed that single clusters prefer high Zn/Mg ratios, this suggests that the TCO and/or inner octahedron contain Al. HAADF-STEM image simulations (Supplementary Fig. 4.) support this: the intensity of the atomic columns belonging to the TCO and octahedron varies in the real images, whereas in the simulated image the intensity is constant due to constant amount of Zn in each column. Our models overestimate the Zn content as the atomic columns in the cluster-matrix interface in the simulations are consistently brighter than in the experimental images. Phases taking Frank–Kasper structures are known to have flexible compositions [50]. The APT data and simulated HAADF-STEM images suggest that the Zn shells contain substantial amounts of Al. Thus, we suggest that the TCO clusters start out with full shells and higher Zn/Mg ratios. The availability of Zn may be reduced during growth, meaning that the outer TCO shell may have a higher fraction of Al, as is supported by the DFT calculations and APT measurements.

In addition, some clusters were found to connect along the ⟨330⟩ directions, as exemplified in Fig. 3c. Models following this connection principle are marked as '⟨411⟩ – ⟨330⟩ Clusters' in Fig. 4 and the models consist of three single cluster units with one ⟨330⟩ connection and two ⟨411⟩ connections. For this stacking, the most favourable cluster is $zZ_6M_8Z_{24}$, again demonstrating that a

high Zn/Mg ratio is preferred. Furthermore, the higher pressure of the ⟨411⟩ – ⟨330⟩ clusters compared to their ⟨411⟩ counterparts, suggests that they are less favourable. This is in accordance with our experimental observations.

3.6. Diffraction from a single cluster

The contribution from a single cluster to the weak SADP diffraction spots (cf. Fig. 1**b**), was investigated. Using the ⟨411⟩ connected $zZ_6M_8Z_{24}$ cluster with the lowest formation enthalpy, as shown embedded in the Al matrix in Fig. 6**a**, NBD patterns were simulated. A simulated NBD pattern for sample thickness, $t = 40$ Å, is given in Fig. 6**b**. Montages of diffraction patterns ranging from 4 to 320 monolayers (0.8 to 64 nm) are shown in Supplementary Figs. 5 and 6. NBD patterns were also simulated for clusters positioned at different heights within the TEM sample (Supplementary Fig. 7). In Fig. 6**c**, a 'Smart Aligned' [28] HAADF-STEM image of a ⟨411⟩ connected cluster is shown, acquired in Alloy #2 after 400 min artificial ageing (cf. Supplementary Fig. 1). By comparing the FFT of Fig. 6**c** and**d** with the simulated NBD pattern in Fig. 6**b**, a strong correlation, both in position and intensity is evident. Note that, although Alloy #2 has been artificially aged, clusters are still present. This is in accordance with previous studies [6,9,19,20,46].

The lower cluster symmetry along [001] relative to Al, is obvious in Fig. 6**a**. The cluster belongs to space group P41 (#76), with a 4-fold screw axis, which projects to a pure rotational axis. It means that the cluster, as well as the diffraction pattern, will reverse the rotation as viewed from the other side. By taking the average from the two orientations, the resultant diffraction pattern is similar to the SADP in Fig. 1**b**. This is shown in Supplementary Fig. 8.

3.7. Transformations

The hardening precipitates in the 7xxx system and the equilibrium phase $MgZn_2$ have similar structures [14,16], facilitating transformation to the latter. This work finds no structural similarities between the GP(I) clusters and the precipitates. The clusters can be nucleation sites for the precipitates, but are likely to dissolve once hardening precipitates are established to fuel further precipitate growth. Thus, a low formation enthalpy associated with a cluster may delay, rather than assist precipitation. Future work will investigate how effective the different clusters are in forming the hardening phases. Better control of clustering has potential benefits for improving mechanical properties. It should be noted that an interstitial in the TCO produces a vacancy in the surrounding matrix, which could make the cluster more costly to produce. In the calculations this is not accounted for. It has been suggested before that some form of Mg clustering surrounding a vacancy is crucial in the earliest stages [6,11]. The calculations indicate a pathway: (1) Six Zn atoms occupies the centers of the Al cell, (2) eight Mg atoms replace the corners, (3) an interstitial is produced by a jump from a side to the cell center and (4) The side center is replaced by another Zn atom, and produces a vacancy that may be trapped or escape into the matrix.

3.8. Relation to quasi-crystalline phases

The 7xxx alloy system is known for phases related to quasicrystals (QC) [51]. The complex R-$(Al,Zn)_{49}Mg_{32}$ phase [52] is a so-called 1/1 approximant of the QC (cf. [53–55]) in addition to being a Frank–Kasper phase [50]. We therefore compared the molecular unit of R with the clusters. Both are shell-structures, but were found to differ fundamentally, both compositionally and structurally. It cannot be ruled out that the TCO relates to the QC, such as through a complex sharing, but this was beyond the scope of the current work.

4. Conclusion

To conclude, we have derived the structure of the clusters forming during natural ageing in Al–Zn–Mg alloys. They are solute orderings on the fcc aluminium and essentially Frank–Kasper σ-type structures. The orderings have been explained as stackings in terms of a near spherical solute-ordered unit. The unit is a three-layered shell structure around an Al unit cell, which can take up an interstitial during build-up: an octahedron formed by the six side centres, a cube with Mg on the eight corners and the immediate truncated cube octahedral shell with 24 atomic positions. The octahedron and the outer TCO shell are partially or fully occupied by Zn, while the interstitial can take all three species. The interstitial was found to be a product of the cluster rather than a nucleation point. Three stacking principles are sufficient to explain how the cluster unit builds larger clusters, which are all Frank–Kasper structures. The partial occupancy of Zn yields a range of different compositions with favourable energies, which is typical for Frank–Kasper orderings. We expect our result to be significant in further understanding and optimisation of age-hardening in aluminium alloys.

Author contribution

A.L., A.B., K.M., R.H. and S.J.A. conceived, designed and supervised the research. A.L. conducted the (S)TEM experiments. S.W. conducted the APT measurements and analysis. J.F. prepared the models and conducted the DFT modelling. E.T. conducted the image and diffraction simulations. S.J.A. and C.D.M. analysed the data and deduced the structure. A.L. and E.T. prepared the figures. A.L., E.T. and S.J.A wrote the manuscript with input from all the authors.

Data availability

The data used to produce this work is openly available from the Zenodo data archive repository at: https://doi.org/10.5281/zenodo.3988972.

Declaration of Competing Interest

The authors declare that they have no known competing financial interests or personal relationships that could have appeared to influence the work reported in this paper.

Acknowledgements

This work was supported by the The Research Council of Norway (NFR) through the projects 'FICAL' (NFR: 247598) (A.L. & R.H.), support by the industrial partners Hydro, Gränges, Benteler Automotive Raufoss AS and Steertec Raufoss, and 'SumAl' (NFR: 294933) (J.F., C.D.M., S.W., R.H. & S.J.A.), supported by Hydro, Benteler Automotive Raufoss AS and Neuman Aluminium. E.T. and R.H. are supported by the NTNU Digital Transformation initiative 'Alldesign'. The international collaboration was made possible through INTPART (NFR: 249698). The (S)TEM work was conducted on the NORTEM (NFR: 197405) infrastructure at the TEM Gemini Centre, Trondheim, Norway. The DFT calculations were performed on resources provided by UNINETT Sigma2 - the National Infrastructure for High Performance Computing and Data Storage in Norway (NN8068K). K.M. and A.B. acknowledge the Japan Science and Technology Agency (JST) under Collaborative Research Based on Industrial Demand "Heterogeneous Structure Control: Towards Innovative Development of Metallic Structural Materials".

Supplementary material

Supplementary material associated with this article can be found, in the online version, at doi:10.1016/j.actamat.2020.116574.

References

[1] O. Jensrud, High strength aluminium alloys extrusions-A review of the thermo-mechanical-process in high performance profile manufacturing, Key Eng. Mater. 491 (2011) 11–18. 10.4028/www.scientific.net/KEM.491.11

[2] T. Dursun, C. Soutis, Recent developments in advanced aircraft aluminium alloys, Mater. Des. 56 (2014) 862–871, doi:10.1016/j.matdes.2013.12.002.

[3] E. Hornbogen, Hundred years of precipitation hardening, J. Light Metals 1 (2) (2001) 127–132, doi:10.1016/S1471-5317(01)00006-2.

[4] A. Guinier, Structure of age-hardened aluminium-copper alloys, Nature 142 (3595) (1938) 569–570, doi:10.1038/142569b0.

[5] G. Preston, LXXIV. The diffraction of X-rays by an age-hardening alloy of aluminium and copper. The structure of an intermediate phase, Lond. Edinb. Dublin Philos. Mag. J. Sci. 26 (178) (1938) 855–871, doi:10.1080/14786443808562177.

[6] H. Löffler, I. Kovács, J. Lendvai, Decomposition processes in Al–Zn–Mg alloys, J. Mater. Sci. 18 (1983) 2215–2240, doi:10.1007/BF00541825.

[7] G. Dlubek, R. Krause, O. Brümmer, F. Plazaola, Study of formation and reversion of Guinier–Preston zones in Al-4.5 at.%Zn-x at%Mg alloys by positrons, J. Mater. Sci. 21 (3) (1986) 853–858, doi:10.1007/BF01117364.

[8] L.K. Berg, J. Gjønnes, V. Hansen, X.Z. Li, M. Knutson-Wedel, G. Waterloo, D. Schryvers, L.R. Wallenberg, GP-zones in Al–Zn–Mg alloys and their role in artificial aging, Acta Mater. 49 (17) (2001) 3443–3451, doi:10.1016/S1359-6454(01)00251-8.

[9] V. Hansen, O.B. Karlsen, Y. Langsrud, J. Gjønnes, Precipitates, zones and transitions during aging of Al–Zn–Mg–Zr 7000 series alloy, Mater. Sci. Technol. 20 (2) (2004) 185–193, doi:10.1179/026708304225010424.

[10] J. Buha, R.N. Lumley, A.G. Crosky, Secondary ageing in an aluminium alloy 7050, Mater. Sci. Eng. 492 (1–2) (2008) 1–10, doi:10.1016/j.msea.2008.02.039.

[11] A. Dupasquier, R. Ferragut, M.M. Iglesias, M. Massazza, G. Riontino, P. Mengucci, G. Barucca, C.E. MacChi, A. Somoza, Hardening nanostructures in an AlZnMg alloy, Philos. Mag. 87 (22) (2007) 3297–3323, doi:10.1080/14786430701271959.

[12] T.-F. Chung, Y.-L. Yang, B.-M. Huang, Z. Shi, J. Lin, T. Ohmura, J.-R. Yang, Transmission electron microscopy investigation of separated nucleation and in-situ nucleation in AA7050 aluminium alloy, Acta Mater. 149 (2018) 377–387, doi:10.1016/j.actamat.2018.02.045.

[13] J. Gjønnes, C.J. Simensen, An electron microscope investigation of the microstructure in an aluminium-zinc-magnesium alloy, Acta Metall. 18 (8) (1970) 881–890, doi:10.1016/0001-6160(70)90016-7.

[14] C.D. Marioara, W. Lefebvre, S.J. Andersen, J. Friis, Atomic structure of hardening precipitates in an Al-Mg-Zn-Cu alloy determined by HAADF-STEM and first-principles calculations: Relation to η-MgZn2, J. Mater. Sci. 48 (10) (2013) 3638–3651, doi:10.1007/s10853-013-7158-3.

[15] A. Bendo, K. Matsuda, S. Lee, K. Nishimura, N. Nunomura, H. Toda, M. Yamaguchi, T. Tsuru, K. Hirayama, K. Shimizu, H. Gao, K. Ebihara, M. Itakura, T. Yoshida, S. Murakami, Atomic scale HAADF-STEM study of η' and η_1 phases in peak-aged Al-Zn-Mg alloys, J. Mater. Sci. 53 (6) (2018) 4598–4611, doi:10.1007/s10853-017-1873-0.

[16] A. Lervik, C. Marioara, M. Kadanik, J. Walmsley, B. Milkereit, R. Holmestad, Precipitation in an extruded AA7003 aluminium alloy: Observations of 6xxx-type hardening phases, Mater. Des. 186 (2020) 108204, doi:10.1016/j.matdes.2019.108204.

[17] T.-F. Chung, Y.-L. Yang, M. Shiojiri, C.-N. Hsiao, W.-C. Li, C.-S. Tsao, Z. Shi, J. Lin, J.-R. Yang, An atomic scale structural investigation of nanometre-sized η precipitates in the 7050 aluminium alloy, Acta Mater. 174 (2019) 351–368, doi:10.1016/j.actamat.2019.05.041.

[18] A. Bendo, T. Maeda, K. Matsuda, A. Lervik, R. Holmestad, C.D. Marioara, K. Nishimura, N. Nunomura, H. Toda, M. Yamaguchi, K.-i. Ikeda, T. Homma, Characterisation of structural similarities of precipitates in Mg–Zn and Al–Zn–Mg alloys systems, Philos. Mag. 99 (21) (2019) 2619–2635, doi:10.1080/14786435.2019.1637032.

[19] H. Inoue, T. Sato, Y. Kojima, T. Takahashi, The temperature limit for GP zone formation in an Al–Zn–Mg alloy, Metall. Mater. Trans. A 12 (8) (1981) 1429–1434, doi:10.1007/BF02643687.

[20] C.K. Akuata, C. Altenbach, C. Schnatterer, P. Suwanpinij, C. Saiyasombat, D. Zander, Age hardening response of AA7108A investigated by means of Synchrotron-based X-ray Absorption Spectroscopy (XAS) measurements, Mater. Sci. Eng. 747 (September 2018) (2019) 42–52, doi:10.1016/j.msea.2019.01.052.

[21] X.J. Jiang, J. Taftø, B. Noble, B. Holme, G. Waterloo, Differential scanning calorimetry and electron diffraction investigation on low-temperature aging in Al–Zn–Mg alloys, Metall. Mater. Trans. A 31 (2) (2000) 339–348, doi:10.1007/s11661-000-0269-x.

[22] W. Sun, Y. Zhu, R. Marceau, L. Wang, Q. Zhang, X. Gao, C. Hutchinson, Precipitation strengthening of aluminum alloys by room-temperature cyclic plasticity, Science 363 (6430) (2019) 972–975, doi:10.1126/science.aav7086.

[23] J. Liu, R. Hu, Y. Zhang, D. Zhigang, W. Liu, Y. Zhu, G. Sha, Formation of solute nanostructures in an Al–Zn–Mg alloy during long-term natural aging, J. Alloys Compd. 821 (2019) 153572, doi:10.1016/j.jallcom.2019.153572.

[24] A. Deschamps, Y. Bréchet, F. Livet, Influence of copper addition on precipitation kinetics and hardening in Al–Zn–Mg alloy, Mater. Sci. Technol. 15 (9) (1999) 993–1000, doi:10.1179/026708399101506832.

[25] A. Deschamps, M. Niewczas, F. Bley, Y. Brechet, J.D. Embury, L.L. Sinq, F. Livet, J.P. Simon, Low-temperature dynamic precipitation in a supersaturated Al–Zn–Mg alloy and related strain hardening, Philos. Mag. A 79 (10) (1999) 2485–2504, doi:10.1080/01418619908214295.

[26] P. Schloth, J.N. Wagner, J.L. Fife, A. Menzel, J.-M. Drezet, H. Van Swygenhoven, Early precipitation during cooling of an Al–Zn–Mg–Cualloy revealed by *in situ* small angle X-ray scattering, Appl. Phys. Lett. 105 (10) (2014) 101908, doi:10.1063/1.4894768.

[27] R. Ferragut, A. Somoza, A. Tolley, Microstructural evolution of 7012 alloy during the early stages of artificial ageing, Acta Mater. 47 (17) (1999) 4355–4364, doi:10.1016/S1359-6454(99)00315-8.

[28] L. Jones, H. Yang, T.J. Pennycook, M.S.J. Marshall, S. Van Aert, N.D. Browning, M.R. Castell, P.D. Nellist, Smart slign - a new tool for robust non-rigid registration of scanning microscope data, Adv. Struct. Chem. Imaging 1 (1) (2015) 8, doi:10.1186/s40679-015-0008-4.

[29] T.J. Prosa, D.J. Larson, Modern focused-ion-beam-based site-specific specimen preparation for atom probe tomography, Microsc. Microanal. 23 (2) (2017) 194–209, doi:10.1017/S1431927616012642.

[30] E.A. Jägle, P.-P. Choi, D. Raabe, The maximum separation cluster analysis algorithm for atom-probe tomography: parameter determination and accuracy, Microsc. Microanal. 20 (6) (2014) 1662–1671, doi:10.1017/S1431927614013294.

[31] G. Kresse, J. Hafner, Ab initio molecular dynamics for open-shell transition metals, Phys. Rev. B 48 (1993) 13115–13118, doi:10.1103/PhysRevB.48.13115.

[32] G. Kresse, D. Joubert, From ultrasoft pseudopotentials to the projector augmented-wave method, Phys. Rev. B 59 (1999) 1758–1775, doi:10.1103/PhysRevB.59.1758.

[33] J.P. Perdew, K. Burke, M. Ernzerhof, Generalized gradient approximation made simple, Phys. Rev. Lett. 77 (1996) 3865–3868, doi:10.1103/PhysRevLett.77.3865.

[34] M. Methfessel, A.T. Paxton, High-precision sampling for Brillouin-zone integration in metals, Phys. Rev. B 40 (1989) 3616–3621, doi:10.1103/PhysRevB.40.3616.

[35] L.J. Allen, A.J. D'Alfonso, S.D. Findlay, Modelling the inelastic scattering of fast electrons, Ultramicroscopy 151 (2015) 11–22, doi:10.1016/j.ultramic.2014.10.011.

[36] I. Lobato, D.V. Dyck, MULTEM: a new multislice program to perform accurate and fast electron diffraction and imaging simulations using graphics processing units with CUDA, Ultramicroscopy 156 (2015) 9–17.

[37] K. Stiller, P.J. Warren, V. Hansen, J. Angenete, J. Gjønnes, Investigation of precipitation in an Al-Zn-Mg alloy after two-step ageing treatment at 100° and 150°C, Mater. Sci. Eng.: A 270 (1) (1999) 55–63, doi:10.1016/S0921-5093(99)00231-2.

[38] A. Cassell, J. Robson, C. Race, A. Eggeman, T. Hashimoto, M. Besel, Dispersoid composition in zirconium containing Al–Zn–Mg–Cu (AA7010) aluminium alloy, Acta Mater. 169 (2019) 135–146, doi:10.1016/j.actamat.2019.02.047.

[39] G. Sha, A. Cerezo, Early-stage precipitation in Al–Zn–Mg–Cu alloy (7050), Acta Mater. 52 (15) (2004) 4503–4516, doi:10.1016/j.actamat.2004.06.025.

[40] J. Chen, L. Zhen, S. Yang, W. Shao, S. Dai, Investigation of precipitation behavior and related hardening in AA 7055 aluminum alloy, Mater. Sci. Eng. 500 (1–2) (2009) 34–42, doi:10.1016/j.msea.2008.09.065.

[41] D. Liu, B. Xiong, F. Bian, Z. Li, X. Li, Y. Zhang, Q. Wang, G. Xie, F. Wang, H. Liu, Quantitative study of nanoscale precipitates in Al–Zn–Mg–Cu alloys with different chemical compositions, Mater. Sci. Eng. 639 (2015) 245–251, doi:10.1016/j.msea.2015.04.104.

[42] K. Matsuda, A. Kawai, K. Watanabe, S. Lee, C.D. Marioara, S. Wenner, K. Nishimura, T. Matsuzaki, N. Nunomura, T. Sato, R. Holmestad, S. Ikeno, Extra electron diffraction spots caused by fine precipitates formed at the early stage of aging in Al–Mg–X (X=Si, Ge, Zn)-Cu alloys, Mater. Trans. 58 (2) (2017) 167–175, doi:10.2464/jilm.67.186.

[43] T. Philippe, M. Gruber, F. Vurpillot, D. Blavette, Clustering and local magnification effects in atom probe tomography: a statistical approach, Microsc. Microanal. 16 (5) (2010) 643–648, doi:10.1017/S1431927610000449.

[44] K. Hono, N. Sano, T. Sakurai, Quantitative atom-probe analysis of some aluminum alloys, Surf. Sci. 266 (1) (1992) 350–357, doi:10.1016/0039-6028(92)91045-D.

[45] S.K. Maloney, K. Hono, I.J. Polmear, S.P. Ringer, The chemistry of precipitates in an aged Al-2.1Zn-1.7Mg at.% alloy, Scr. Mater. 41 (10) (1999) 1031–1038, doi:10.1016/S1359-6462(99)00253-5.

[46] Y.L. Wang, Y.Y. Song, H.C. Jiang, Z.M. Li, D. Zhang, L.J. Rong, Variation of nanoparticle fraction and compositions in two-stage double peaks aging precipitation of Al–Zn–Mg alloy, Nanoscale Res. Lett. 13 (2018) 131, doi:10.1186/s11671-018-2542-1.

[47] R.K. Gupta, A. Deschamps, M.K. Cavanaugh, S.P. Lynch, N. Birbilis, Relating the early evolution of microstructure with the electrochemical response and mechanical performance of a Cu-rich and Cu-lean 7xxx aluminum alloy, J. Electrochem. Soc. 159 (11) (2012) C492–C502, doi:10.1149/2.062211jes.

[48] F.C. Frank, J.S. Kasper, Complex alloy structures regarded as sphere packings. I. Definitions and basic principles, Acta Crystallogr. 11 (3) (1958) 184–190, doi:10.1107/S0365110X58000487.

[49] F.C. Frank, J.S. Kasper, Complex alloy structures regarded as sphere packings. II. Analysis and classification of representative structures, Acta Crystallogr. 12 (7) (1959) 483–499, doi:10.1107/S0365110X59001499.

[50] J.-M. Joubert, J.-C. Crivello, Non-stoichiometry and calphad modeling of Frank–Kasper phases, Appl. Sci. 2 (3) (2012) 669–681, doi:10.3390/app2030669.

[51] D. Shechtman, I. Blech, D. Gratias, J.W. Cahn, Metallic phase with long-range orientational order and no translational symmetry, Phys. Rev. Lett. 53 (1984) 1951–1953, doi:10.1103/PhysRevLett.53.1951.
[52] G. Bergman, J.L.T. Waugh, L. Pauling, The crystal structure of the metallic phase $Mg_{32}(Al,Zn)_{49}$, Acta Crystallogr. 10 (4) (1957) 254–259, doi:10.1107/S0365110X57000808.
[53] T. Takeuchi, U. Mizutani, Electronic structure, electron transport properties, and relative stability of icosahedral quasicrystals and their 1/1 and 2/1 approximants in the Al-Mg-Zn alloy system, Phys. Rev. B 52 (1995) 9300–9309, doi:10.1103/PhysRevB.52.9300.
[54] J. Hafner, M. Krajčí, Localized modes and topological frustration in rational approximants to quasicrystals, Phys. Rev. B 47 (1993) 1084–1087, doi:10.1103/PhysRevB.47.1084.
[55] M. Krajčí, J. Hafner, Structure and stability of quasicrystals: modulated tiling models, Phys. Rev. B 46 (1992) 10669–10685, doi:10.1103/PhysRevB.46.10669.

Supplementary material to:
Atomic structure of solute clusters in Al-Zn-Mg alloys

A. Lervik[a], E. Thronsen[a], J. Friis[a,b], C. D. Marioara[b], S. Wenner[a,b], A. Bendo[c], K. Matsuda[c], R. Holmestad[a,*], S. J. Andersen[b]

[a]*Department of Physics, Norwegian University of Science and Technology (NTNU), N-7491 Trondheim, Norway*
[b]*SINTEF Industry, N-7465, Trondheim, Norway*
[c]*Graduate School of Science and Engineering, University of Toyama, 3190 Gofuku, Toyama, 930-8555, Japan*

1. Supplementary hardness curves

The hardness curve for Alloy #2 after different ageing treatments is shown in Fig. 1. The alloy was either 1) artificially aged at 120 °C after 4 days of natural ageing where it was investigated in transmission electron microscopy (TEM) after 8 minutes ageing. 2) Directly artificially aged at 150 °C where it was studied in its peak hardness condition. 3) Naturally aged for two weeks and studied in TEM following 2 weeks natural ageing.

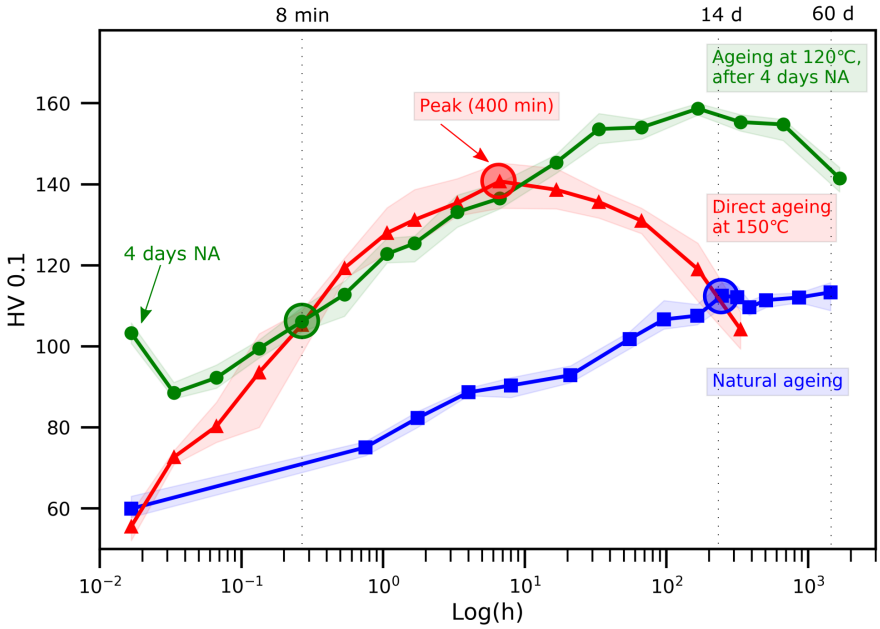

Figure 1: HV0.1 curves for Alloy #2 used in this study. TEM samples were prepared at the regions indicated by the shaded circles. The hardness is equal for 2 weeks natural ageing and after 8 minutes artificial ageing at 120 °C.

*Corresponding author at: Department of Physics, Norwegian University of Science and Technology (NTNU), N-7491 Trondheim, Norway
Email address: Randi.Holmestad@ntnu.no (R. Holmestad)

2. Supplementary TEM data

Additional high-angle annular dark field (HAADF)-scanning transmission electron microscopy (STEM) images, corresponding fast Fourier transform (FFT) and selected area diffraction pattern (SADP) of alloy #2 naturally aged for 2 weeks are shown in Figs. 2**a**, 2**b**, 2**c** and after 8 minutes artificial ageing at 120 °C in Figs. 2**d**, 2**e**, 2**f**.

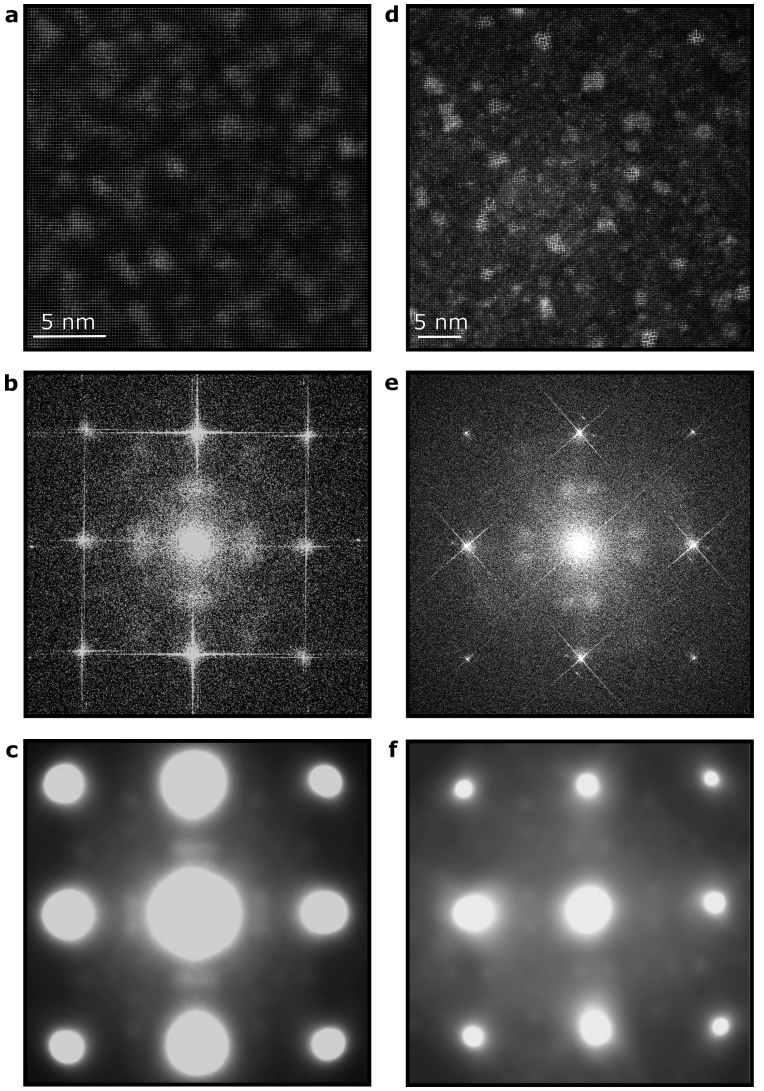

Figure 2: **a,b,c**, HAADF-STEM, corresponding FFT and a SADP for alloy #2 after 2 weeks natural ageing. **d,e,f**, Similar images for alloy #2 after 8 minutes ageing at 120 °C.

3. Supplementary surface layer

Fig. 3 shows the presence of a high Z-contrast layer of ~4 nm thickness close to the vacuum, but below the outermost aluminium oxide layer. Chemical analysis indicates the layer to be rich in Cu, with presence of both Al and O. A similar observation was reported by Weng et al. [1]. This layer covers the entire surface of the TEM specimen, resulting in the extra diffraction spots as shown in the FFT of the surface in Fig. 3. Further investigation of this layer is in progress [2]. This was only observed for Alloy #1 in this study, where the TEM specimens were prepared at NTNU (Trondheim, Norway). TEM specimens of Alloy #2 were prepared at Toyama University (Toyama, Japan). Similar Cu-rich layers has been observed in Al alloys using atom probe tomography (APT) [3].

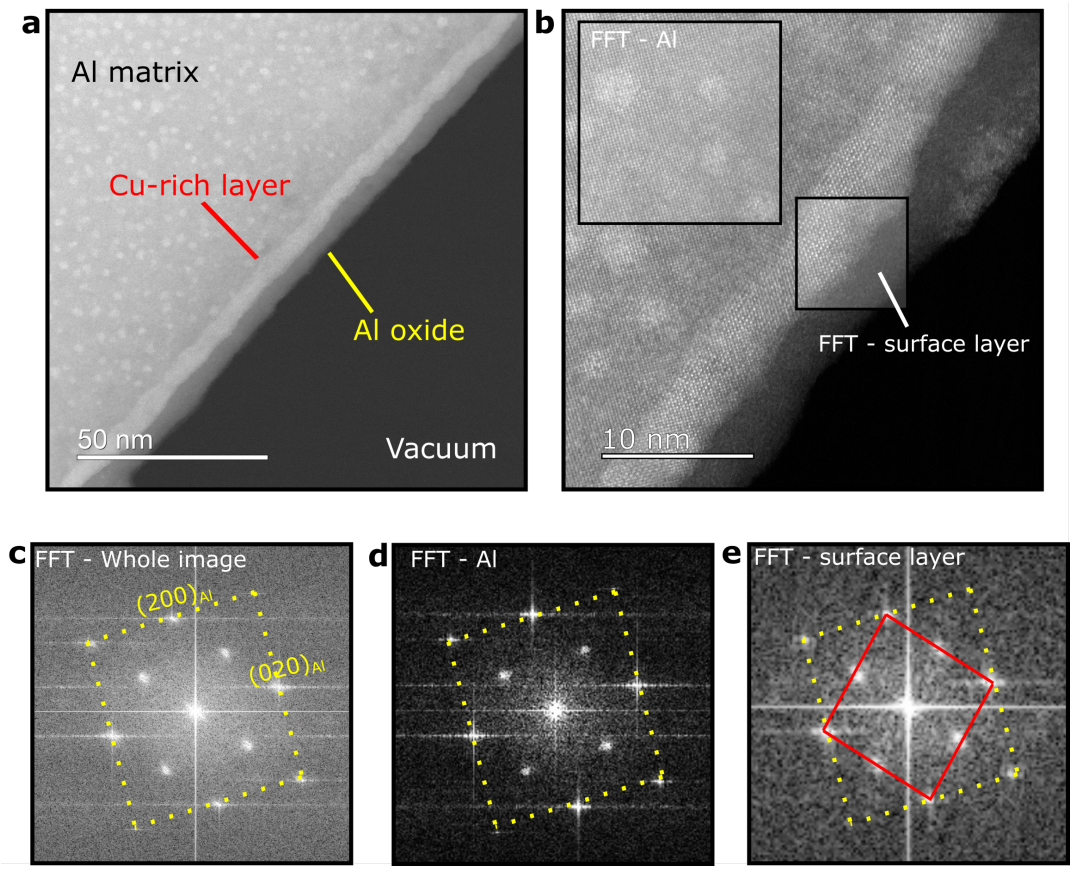

Figure 3: **a**, A HAADF-STEM image taken close to the edge of the specimen demonstrating an additional layer. **b**, high-resolution image of **a**. **c,d,e**, are FFT of the entire image **b** and from the two regions indicated in **b**.

4. Supplementary DFT data

The composition, formation enthalpy, pressure and Zn/Mg ratio for the density functional theory (DFT) calculations shown in Fig. 5 in the main text for single cluster units and stacked clusters are given in Tabs. 1 and 2, respectively.

Table 1: Cluster single unit $iZ_xM_yZ_z$ formation enthalpies and pressure in a 4×4×4 Al calculation cell. Sorted according to the lowest formation enthalpy per solute. See the main text and Fig. 3 for explanation of the cluster configurations.

Configuration/composition			Formation enthalpy [eV] per			Pressure	Ratio
No	Cluster	Calculation cell	total	atom	solute	kBar	Zn/Mg
1	$aZ_6M_8Z_{24}$	$Mg_8Zn_{30}Al_{219}$	-5.170	-0.020	-0.136	2.7	3.8
2	$zZ_6M_8Z_{24}$	$Mg_8Zn_{31}Al_{218}$	-5.284	-0.021	-0.136	2.3	3.9
3	$mZ_6M_8Z_{24}$	$Mg_9Zn_{30}Al_{218}$	-5.139	-0.020	-0.132	4.0	3.3
4	$Z_4M_8Z_{24}$	$Mg_8Zn_{28}Al_{220}$	-4.621	-0.018	-0.128	-0.5	3.5
5	$Z_6M_8Z_{24}$	$Mg_8Zn_{30}Al_{218}$	-4.731	-0.019	-0.125	-1.2	3.8
6	$zZ_6M_8Z_{12}$	$Mg_8Zn_{19}Al_{230}$	-3.120	-0.012	-0.116	6.2	2.4
7	$zZ_6M_8Z_0$	$Mg_8Zn_6Al_{242}$	-1.709	-0.007	-0.114	9.2	0.9
8	$zZ_3M_8Z_{24}$	$Mg_8Zn_{28}Al_{221}$	-3.981	-0.016	-0.111	3.8	3.5
9	$Z_6M_8Z_{12}$	$Mg_8Zn_{18}Al_{230}$	-2.731	-0.011	-0.105	2.5	2.3
10	$Z_2M_8Z_{24}$	$Mg_8Zn_{26}Al_{222}$	-3.562	-0.014	-0.105	0.3	3.3
11	$Z_6M_8Z_0$	$Mg_8Zn_6Al_{242}$	-1.368	-0.005	-0.098	5.5	0.8
12	$Z_0M_8Z_{24}$	$Mg_8Zn_{24}Al_{224}$	-3.024	-0.012	-0.095	1.1	3
13	$Z_6M_0Z_{24}$	$Zn_{30}Al_{226}$	-1.935	-0.008	-0.065	-6.5	3.8
14	$Z_0M_8Z_{12}$	$Mg_8Zn_{12}Al_{236}$	-1.232	-0.005	-0.062	4.7	1.5
15	$Z_6M_0Z_0$	Zn_6Al_{250}	-0.347	-0.001	-0.058	-1.6	-
16	$Z_0M_0Z_{24}$	$Zn_{24}Al_{232}$	-1.229	-0.005	-0.052	-4.8	-
17	$zZ_6M_0Z_{24}$	$Zn_{31}Al_{226}$	-1.057	-0.004	-0.034	-2.4	-
18	$zZ_0M_8Z_{12}$	$Mg_8Zn_{13}Al_{236}$	-0.508	-0.002	-0.024	9.6	1.6
19	$Z_0M_0Z_{12}$	$Zn_{12}Al_{244}$	-0.132	-0.001	-0.011	-2.1	-
20	$Z_0M_8Z_0$	Mg_8Al_{248}	-0.043	-0.000	-0.005	7.4	0
21	$zZ_6M_0Z_0$	Zn_7Al_{244}	0.781	0.003	0.112	2.8	-
22	$zZ_0M_0Z_{12}$	$Zn_{13}Al_{244}$	1.707	0.007	0.131	3.3	-

Table 2: Formation enthalpies and pressure of [002] connected $iZ_xM_8Z_y$. Confs. 1-6: single column of units (in 4×4×2 Al cells). Confs. 7-11: clusters stacked in ⟨411⟩ squares (in 6×6×2 and 8×8×2 Al cells for confs. 7-9 and confs. 10-11, respectively). Conf. 9: Interstitial by shifted column, normal occupancy. Confs. 12-14: cluster stacked in ⟨411⟩ connections (in 6×6×2 Al cells).

Configuration/unit/composition			Formation enthalpy [eV] per			Pressure	Ratio	Comments
No	Unit	Composition/shared	total	atom	solute	kBar	Zn/Mg	
1	$zZ_6M_8Z_{24}$	$Mg_8Zn_{27}Al_{94}$ / [002]	-5.681	-0.044	-0.162	6.7	3.4	-
2	$zZ_6M_8Z_8$	$Mg_8Zn_{11}Al_{110}$ / [002]	-2.916	-0.023	-0.154	15.7	1.4	-
3	$aZ_6M_8Z_8$	$Mg_8Zn_{10}Al_{111}$ / [002]	-2.740	-0.021	-0.152	16.7	1.3	-
4	$zZ_6M_8Z_{16}$	$Mg_8Zn_{19}Al_{102}$ / [002]	-4.065	-0.032	-0.151	11.5	2.1	-
5	$aZ_6M_8Z_{16}$	$Mg_8Zn_{18}Al_{103}$ / [002]	-3.903	-0.030	-0.150	12.4	2.3	-
6	$zZ_6M_8Z_{12}$	$Mg_8Zn_{17}Al_{104}$ / [002]	-3.394	-0.026	-0.136	13.2	2.4	-
7	$zZ_6M_8Z_{24}$	$Mg_{32}Zn_{124}Al_{136}$ / ⟨411⟩	-26.261	-0.090	-0.168	5.5	3.9	-
8	$aZ_6M_8Z_{24}$	$Mg_{32}Zn_{120}Al_{140}$ / ⟨411⟩	-24.721	-0.085	-0.163	6.9	3.8	-
9	$Z_6M_8Z_{24}$	$Mg_{32}Zn_{120}Al_{136}$ / ⟨411⟩	-23.444	-0.081	-0.154	-5.6	3.8	-
10	$zZ_6M_8Z_{24}$	$Mg_{32}Zn_{100}Al_{384}$ / ⟨411⟩	-16.812	-0.033	-0.127	6.870	3.1	Alternating Zn/Al in center columns
11	$zZ_6M_8Z_{12}$	$Mg_{32}Zn_{64}Al_{420}$ / ⟨411⟩	-9.737	-0.019	-0.101	13.370	2	Alternating Zn/Al in center columns
12	$zZ_6M_8Z_{24}$	$Mg_{24}Zn_{69}Al_{198}$ / ⟨411⟩-⟨330⟩	-14.596	-0.050	-0.157	11.930	2.9	-
13	$zZ_6M_8Z_{12}$	$Mg_{24}Zn_{49}Al_{218}$ / ⟨411⟩-⟨330⟩	-10.620	-0.04	-0.146	18.000	2	-
14	$zZ_6M_8Z_{12}$	$Mg_{24}Zn_{50}Al_{216}$ / ⟨411⟩-⟨330⟩	-10.907	-0.04	-0.145	16.730	2.1	Alternating Zn/vacancies in center columns

5. Supplementary simulated STEM images

In Fig. 4**a**, a simulated high-angle annular dark field scanning transmission electron microscopy (HAADF-STEM) image of the $zZ_6M_8Z_{24}$ model connected in a $\langle 411 \rangle$ manner is shown. Each corner in the square is the center of a single cluster unit. In **b**, an experimental HAADF-STEM image of a cluster connected in a $\langle 411 \rangle$ manner is shown. Note that in **a**, four cluster units are connected, indicated by yellow lines, whereas in **b**, nine cluster units are connected. Note that the cluster-matrix interface is not accounted for properly in the model. By comparing the top left square in **b** with the square in **a**, it is evident that the improper description of the interface in our models causes an overestimation of the Zn/Mg content.

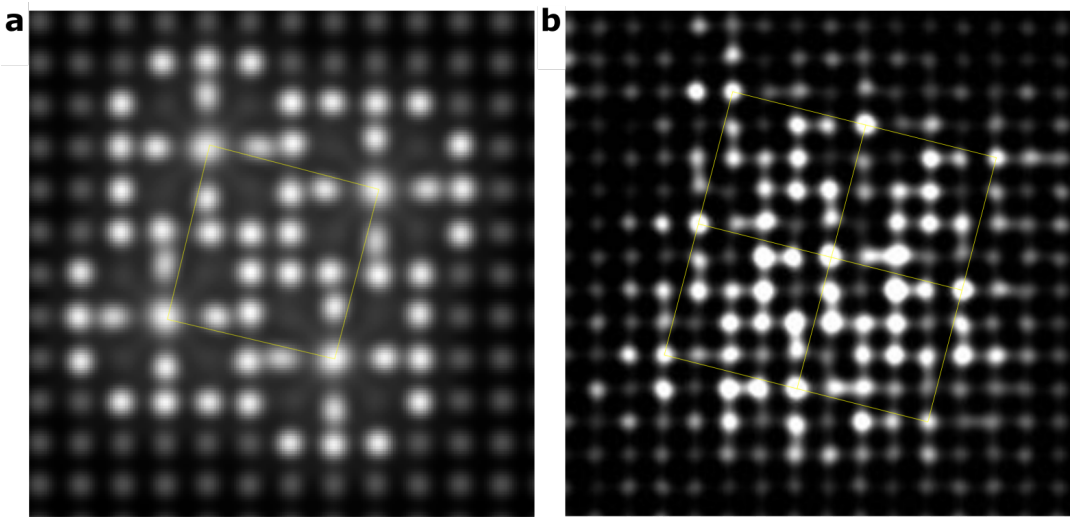

Figure 4: **a**, Simulated HAADF-STEM image of the model $zZ_6M_8Z_{24}$ connected in a $\langle 411 \rangle$ manner, i.e. configuration 8 in Tab. 2. **b**, Experimental HAADF-STEM image of a cluster connected in a $\langle 411 \rangle$ manner. Note that in the simulated image four cluster base units are connected, whereas the real image connects nine cluster units. This is indicated by the yellow lines.

6. Supplementary simulated nanobeam diffraction patterns

6.1. Model $zZ_6M_8Z_{24}$ connected in a $\langle 411 \rangle$ manner periodically through the whole thickness

Figs. 5 and 6 shows a montage of simulated nanobeam diffraction (NBD) patterns over a thickness intervals of t =8.09 Å to 323.60 Å and t =331.69 Å to 647.20 Å, respectively. The diffraction patterns are adjusted for contrast and brightness.

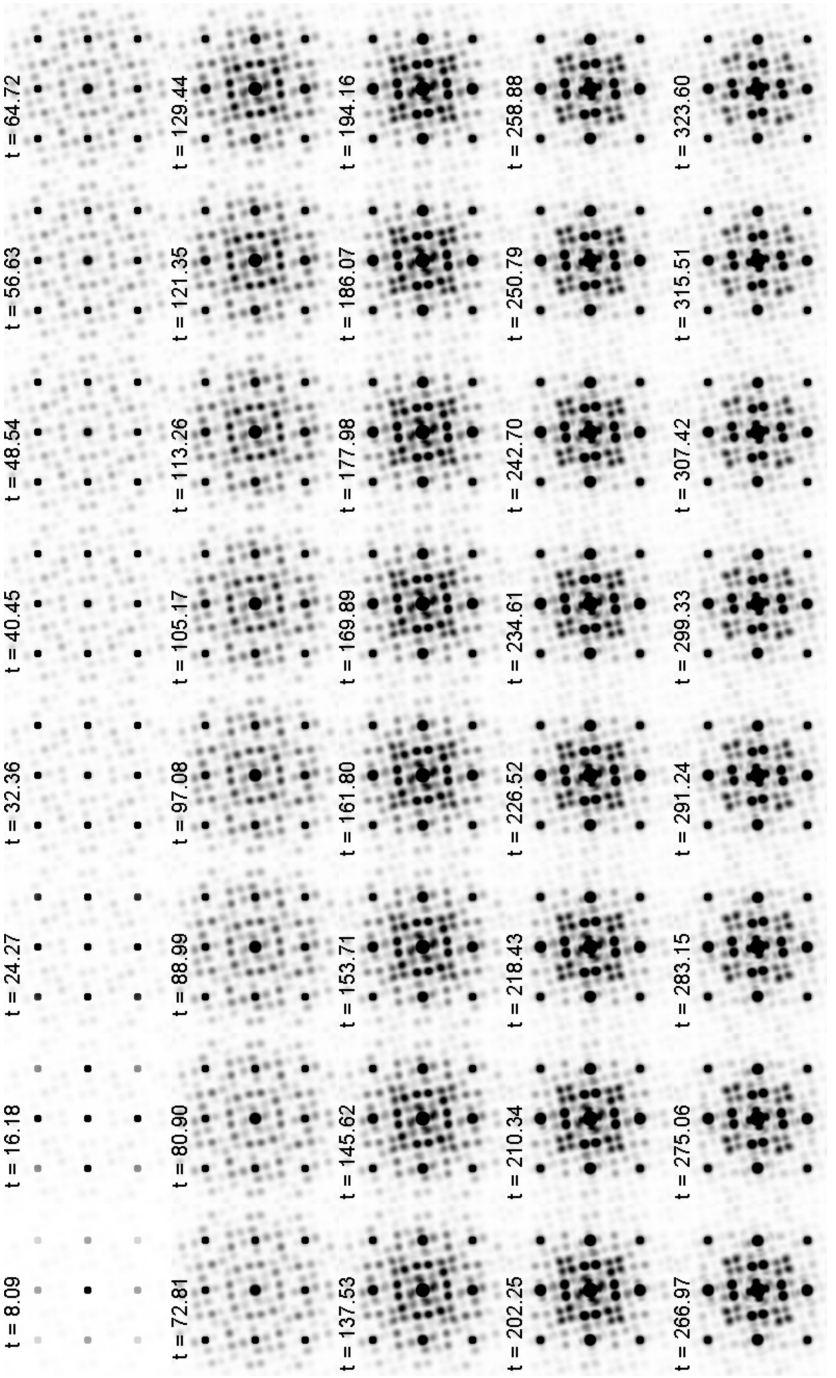

Figure 5: Montage of simulated NBD patterns over a thickness interval of t =8.09 Å to 323.60 Å.

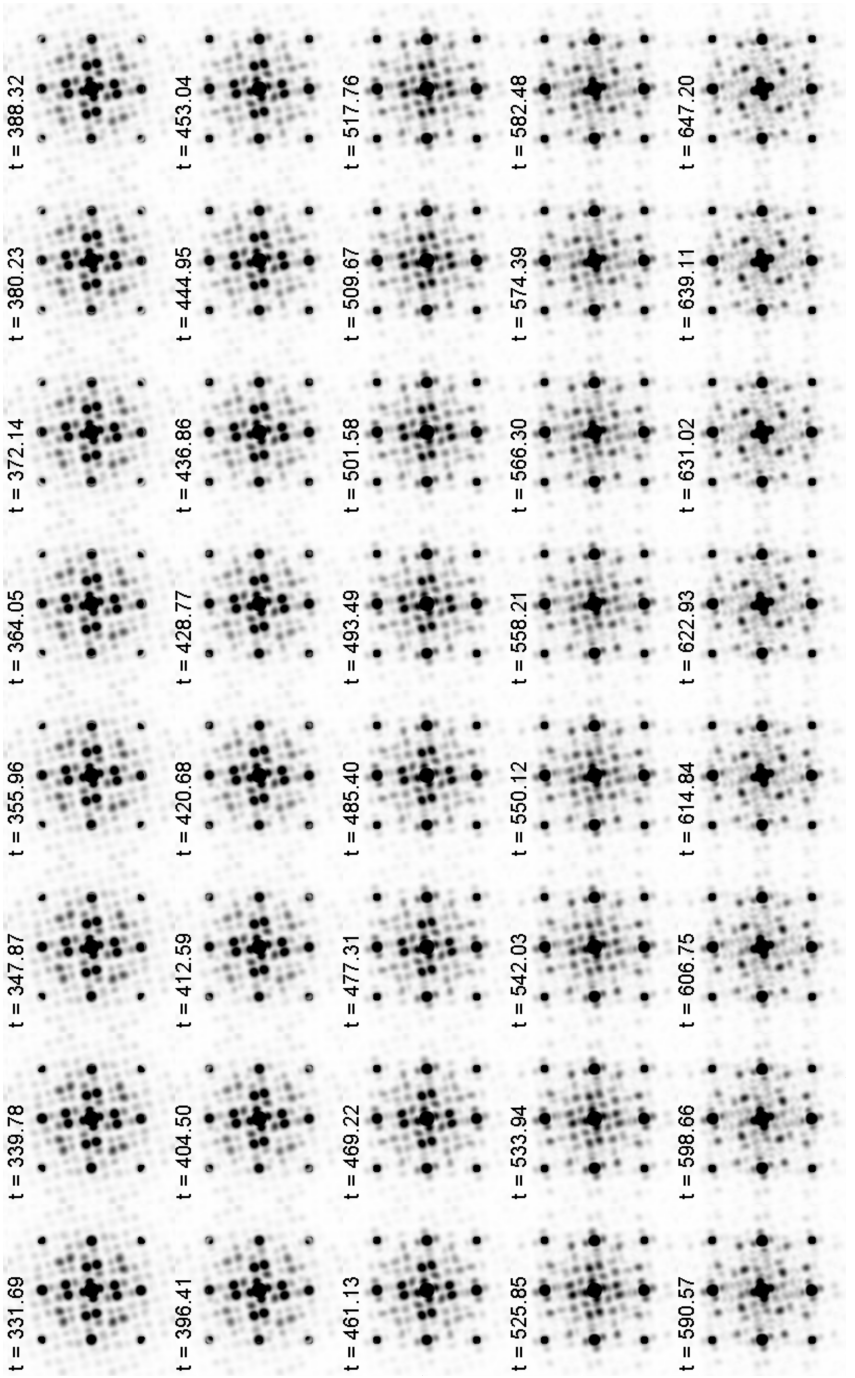

Figure 6: Montage of simulated NBD patterns over a thickness interval of t =331.69 Å to 647.20 Å.

6.2. Cluster embedded in the Al matrix

In addition to simulating the NBD pattern from a cluster model that was periodic through the thickness, a model where a cluster was embedded in the Al matrix was also simulated. The result is shown in Fig. 7. In **a**, the model $zZ_6M_8Z_{24}$ connected in a ⟨411⟩ manner periodically through the whole thickness extends through the sample with a periodicity of 8.09 Å as indicated. This is the same model as in Fig. 6 in the main text and Figs. 5 and 6 in this Supplementary text. The corresponding simulated NBD pattern is shown in 7**b** for t=40.45 Å. The model in **c** is not periodic in the z-direction: it shows the more realistic case where a cluster is embedded in the Al matrix with unit cells of Al both above and below the cluster. In this case, two unit cells of Al are placed above 5 unit cells of $zZ_6M_8Z_{24}$ connected in a ⟨411⟩ manner periodic through the whole thickness, while there are multiple layers of Al unit cells below to reach a total thickness of t=728 Å. The corresponding simulated NBD pattern is shown in 7**d** for t=728 Å. By comparing the two simulated diffraction patterns, it is evident that the same spots are present, but the dynamical effects are different in the two cases due to the difference in thickness.

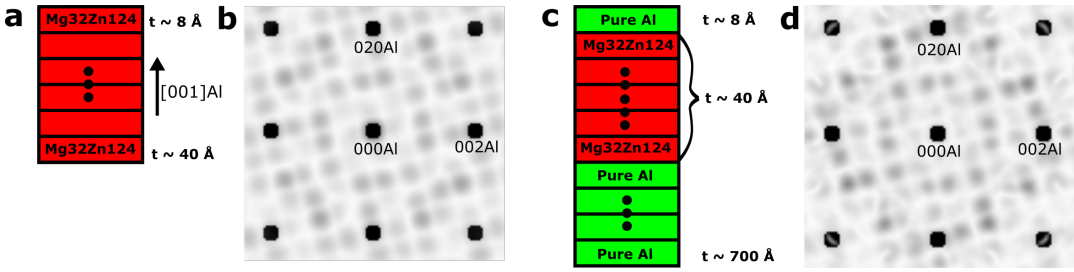

Figure 7: **a**, Model where $zZ_6M_8Z_{24}$ connected in a ⟨411⟩ manner extends periodically through the whole thickness. **b**, Simulated NBD pattern corresponding to the model in **a**. **c**, Model where $zZ_6M_8Z_{24}$ connected in a ⟨411⟩ manner is embedded in the Al matrix in the [001]Al-direction. **d**, Simulated NBD pattern corresponding to the model in **c**.

6.3. Average diffraction pattern

As discussed in the main text, there exists two possible orientations for the $zZ_6M_8Z_{24}$ connected in a $\langle 411 \rangle$ manner periodic through the whole thickness model. The two different orientations are equivalent to a flipping operation, thus the NBD pattern will also be flipped. By taking the average of simulated NBD patterns in the two possible orientations, the diffraction pattern will appear as in Fig. 8**a**. The experimental SADP in Fig. 8**b** is obtained from a region containing multiple clusters, i.e. it is an average diffraction pattern from multiple clusters. By comparing the average diffraction pattern in 8**a** with the experimental SADP pattern, it is evident that the same spots are visible, indicated by the opaque, green circles in **a** and **b**. Note: the forbidden 100 and 110 reflections in Fig. 8**b** are due to Al_3Zr dispersoids.

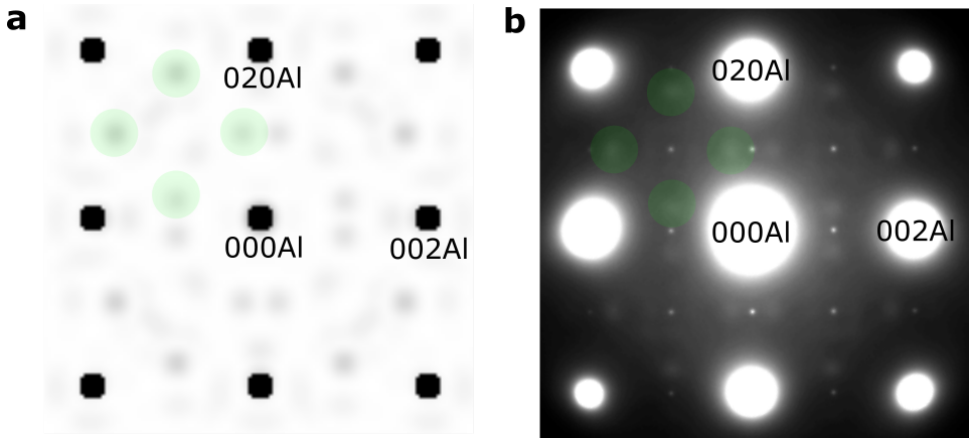

Figure 8: **a**, The average of two NBD patterns in the two possible orientations in the main text. **b**, SADP from a region containing multiple clusters and dispersoids.

References

[1] Z. Wang, K. Lv, J. K. Zheng, B. Chen, Atomic-scale characterization of interfaces between 2A70 aluminum alloy matrix and Cu-enriched layer after electropolishing, Materials Characterization 150 (2019) 150 – 154. doi:10.1016/j.matchar.2019.02.028.

[2] S. Wenner, A. Lervik, E. Thronsen, C. D. Marioara, S. Kubowicz, R. Holmestad, Copper enrichment on aluminium surfaces after electropolishing and its effect on electron imaging and diffraction (????). Submitted.

[3] F. Danoix, M. Miller, A. Bigot, Analysis conditions of an industrial Al–Mg–Si alloy by conventional and 3D atom probes, Ultramicroscopy 89 (2001) 177 – 188. doi:https://doi.org/10.1016/S0304-3991(01)00098-5.

Paper II

Studying GPI zones in Al-Zn-Mg alloys by 4D-STEM

E. Thronsen, J. Frafjord, J. Friis, C. D. Marioara, S. Wenner, A., S. J Andersen, R. Holmestad

Materials Characterization (2022) **185** 111675

Author contributions

E. Thronsen, C.D. Marioara, S.Wenner and R. Holmestad conceived, designed and supervised the research. E. Thronsen conducted the (S)TEM experiments. S.J. Andersen created the initial models. J. Frafjord and J. Friis prepared the models and conducted the DFT modelling. E. Thronsen conducted the diffraction simulations. E. Thronsen prepared the figures. E. Thronsen wrote the manuscript with input from all the authors.

Materials Characterization 185 (2022) 111675

Contents lists available at ScienceDirect

Materials Characterization

journal homepage: www.elsevier.com/locate/matchar

Studying GPI zones in Al-Zn-Mg alloys by 4D-STEM

E. Thronsen [a,*], J. Frafjord [a], J. Friis [a,b], C.D. Marioara [b], S. Wenner [a,b], S.J. Andersen [b], R. Holmestad [a]

[a] Department of Physics, Norwegian University of Science and Technology (NTNU), N-7491 Trondheim, Norway
[b] SINTEF Industry, N-7465 Trondheim, Norway

ARTICLE INFO

Keywords:
Aluminium alloys
Transmission electron microscopy (TEM)
Natural ageing
4D-STEM
Phase mapping
GP-zones

ABSTRACT

A new methodology has been developed to study the fine details of GP zones in age-hardenable aluminium alloys. It is complementary to atomic resolution high-angle annular dark-field scanning transmission electron microscopy imaging, and combines scanning precession electron diffraction with diffraction simulations. To evaluate the method, data was collected from an Al-Zn-Mg alloy in a condition with a dense distribution of GPI zones. Diffraction patterns were recorded in the ⟨001⟩Al orientation, capturing GPI zones in three projections: along the unique [001]GPI axis, and along the two other mutually orthogonal orientations. The GPI zones viewed along [001]GPI revealed how the truncated octahedron units of the GPI zones were connected in multi-unit GP zones, while the two orientations normal to [001]GPI highlight the internal structure. The stability of the atomic models developed based on the experimental results was verified by density functional theory calculations.

1. Introduction

Transmission electron microscopy (TEM) is a powerful and versatile tool for characterising materials on the nano scale. Its strength lies in its sub-nanometer resolution and the possibility of detecting multiple complementary signals simultaneously from the same region. With the advent of spherical aberration corrected TEMs, a more direct interpretation of atomic columns in an image is possible. This allows for studies of atomic details of extremely small particles and their interfaces with the host material. In this respect, atomically resolved high-angle annular dark field (HAADF)-scanning transmission electron microscopy (STEM) has proven very useful. The advantage of this technique is the incoherent nature of the image contrast, and an electron scattering power that increases monotonously with the atomic number of the imaged atomic column [1]. The advancement in the TEM field has had benefits for the understanding of hardening mechanisms in light alloys. For example, by combining *Z*-contrast atomic resolution HAADF-STEM and density functional theory (DFT) calculations, the crystal structure of key precipitates in a range of important age-hardenable Al alloys have been determined and verified [2,3].

The nano-sized precipitates are formed during what is normally the final processing step of age-hardenable aluminium alloys, known as artificial ageing (AA). The typical AA treatment in Al-Zn-Mg alloys is conducted at temperatures between 120°C and 200°C. The objective is to obtain a high number density of fine, semi-coherent precipitates which will optimize the dislocation pinning effect, maximising the hardness of the alloy. During ageing, the mobilities of solutes and vacancies are several factors higher than at room temperature (RT) and the hardness gradually increases as precipitates nucleate, grow and transform. The AA treatment is always preceded by the solution heat treatment (SHT) or other high-temperature processing, performed above the solvus line (typically 450°C for the Al-Zn-Mg system). Between SHT and AA, a fast cooling to RT is usually conducted, which creates a state of supersaturated solid solution (SSSS). In this state, most solutes are dissolved in the Al lattice, and the vacancy concentration may be several orders of magnitude higher than normal, depending on the quench rate. The state is unstable and if kept at RT, clusters form accompanied by a gradual increase in hardness [4,5]. This process is known as natural ageing (NA). When the clusters achieve periodic order in one or more spatial dimensions obtaining characteristic shapes (plates, spheres or needles) they are often referred to as Guinier-Preston (GP) zones after their discoverers in 1938 [6,7]. The clusters, GP zones and precipitates all influence the material properties. In the Al-Zn-Mg alloy system, two types of GP zones with different structure have been found to exist, namely the GPI- and GPII zones [8]. The current work contributes to expand the knowledge of the nature of the GPI zones.

Recently the crystal structure of the GPI zones forming during NA and the initial stage of AA were determined by a combination of HAADF-

* Corresponding author at: Department of Physics, Norwegian University of Science and Technology (NTNU), N-7491 Trondheim, Norway.
E-mail address: Elisabeth.thronsen@ntnu.no (E. Thronsen).

https://doi.org/10.1016/j.matchar.2021.111675
Received 14 September 2021; Received in revised form 23 November 2021; Accepted 9 December 2021
Available online 15 December 2021

STEM experiments/simulations and DFT calculations [9]. These GPI zones have been known and investigated for decades [8,10–13]. By taking advantage of the HAADF-STEM technique, the study showed that the GPI zones are built up by a single building block: Mg and Zn atoms order in the matrix on and around an fcc Al cell, forming a high symmetry shell-structure termed truncated cube octahedron (TCO). This is shown in Fig. 1a: The inner shell is an octahedron formed by the six faces centres, occupied by Zn atoms. The second shell is the eight Mg corners. The third shell is a TCO defined by 24 vertices, fcc positions immediately surrounding the cube, ideally occupied by Zn. In addition, the TCO may incorporate an interstitial site at the octahedral centre in the cell. This is emphasised by the dark centre atom in Fig. 1a. The unit was found to connect along three Al directions to form larger GPI zones: along ⟨001⟩, ⟨411⟩ and ⟨330⟩. The three different ways of connecting the TCOs are shown in Fig. 1b. The structure shows best contrast along its unique axis [001]GPI (left) where the TCOs share 4-fold faces, forming strings. The central column in a TCO string is special: It incorporates the main distinction from the fcc Al lattice as it can contain interstitials or vacancies. Along [001]GPI, the connection between two TCOs is denoted '[002]' to emphasise that the two tcos are separated by two Al-periods (8.1 Å). The lateral connections between TCOs in neighbour strings share edges (right hand side of Fig. 1b) and are termed '⟨411⟩' and '⟨330⟩'. Both measure 8.59 Å. The GPI zone with highest symmetry has TCO strings joined in ⟨411⟩ directions only, producing a 4-fold helix around [001]GPI. It has the tetragonal space group P41 (#76) [9] and will be termed '⟨411⟩ connected GPI zone'. Mixing of the lateral connection ⟨411⟩ and ⟨330⟩ in one zone is common, hence the individual GPI zones show variation in structure. These zones are referred to as '⟨330⟩-⟨411⟩ connected GPI zones'.

The HAADF-STEM approach is not always applicable for studying GP zones in age-hardenable Al alloys. The GP zones in Al-Zn-Mg and Al-Mg-Si alloy systems appear to be spherical with a diameter of 1-3 nm [14–17]. The regions investigated in electropolished TEM foils are typically up to 40 nm thick, implying a low GP zone/Al signal. In addition, zones overlap along the viewing direction. Alternative experimental techniques and complementary modelling are therefore needed. The Al-Zn-Mg alloy system has the advantage of exhibiting a strong *Z*-contrast due to the atomic numbers being 13, 30 and 12 respectively. This alloy system is therefore ideal for validating newly developed methods for studying GP zones in alloy systems where the Z-contrast is weaker.

With the new generations of cameras for TEM, direct electron detectors DED [18], together with a progress in computing power, 4D-STEM has gained recognition as a versatile and robust technique. In 4D-STEM, a convergent probe scans a 2D region of the specimen while recording the diffraction pattern for every probe position, creating a 4D dataset [19]. A subclass of 4D-STEM is scanning precession electron diffraction (SPED) [20]. For each real-space pixel, the beam is scanned at a constant angle, known as the precession angle, around the optical axis. The beam is de-scanned below the specimen. The net effect is equivalent to precession of the specimen around a stationary beam [21]. Recently, SPED was used to quantify the relative amount of different precipitate phases in Al alloys [22–24] and gave information about the crystallographic relationships of composite/intergrown precipitates [25]. The aim of the present work is to apply SPED to investigate the structure of the GPI zones and the role of the TCOs as fundamental building blocks in the GPI zones in the Al-Zn-Mg alloys. In combination with DFT calculations and diffraction pattern simulations, we explore a likely development path from the solid solution. One aim is to establish a general, robust methodology for studies of ordered clusters and GP zones in all age-hardenable Al alloys.

2. Material and methods

2.1. Material

A high purity lab-cast alloy with composition Al-3.49Zn-1.89 Mg (at. %) was used in this work. The alloy was prepared at University of Toyama. It was homogenized at 470°C for 24 h, extruded at 405°C and then cold-rolled into 0.3 mm thick sheets, being identical to what was used in a previous experiment [9]. The alloy underwent SHT at 475°C for 1 h before it was quenched in water and left at room temperature for 4 days. It was subsequently hardened by AA for 8 min at 120°C.

TEM specimens were prepared by mechanical grinding to ~60 μm thickness, from which 3 mm diameter discs were punched. The disks were electropolished with a Struers TenuPol-5 machine using an electrolyte mixture of 1/3 HNO_3 and 2/3 CH_3OH. The liquid was kept at −25°C±5°C and the applied voltage was 20 V.

2.2. Transmission electron microscopy

2.2.1. HAADF-STEM

An image- and probe corrected JEOL ARM200CF microscope operated at 200 kV was used to acquire the HAADF-STEM images and the selected area electron diffraction patterns (SADP). For the STEM acquisition, the convergence semi-angle was 27 mrad and the inner and outer collection semi-angles were 67 mrad and 155 mrad, respectively. The probe current was about 60 pA, which gives a good signal and sufficient spatial resolution. The HAADF-STEM images were filtered by performing a fast Fourier transform (FFT) and then applying a low-pass mask on the FFT of approximately 6.7 nm^{-1} before performing an inverse FFT.

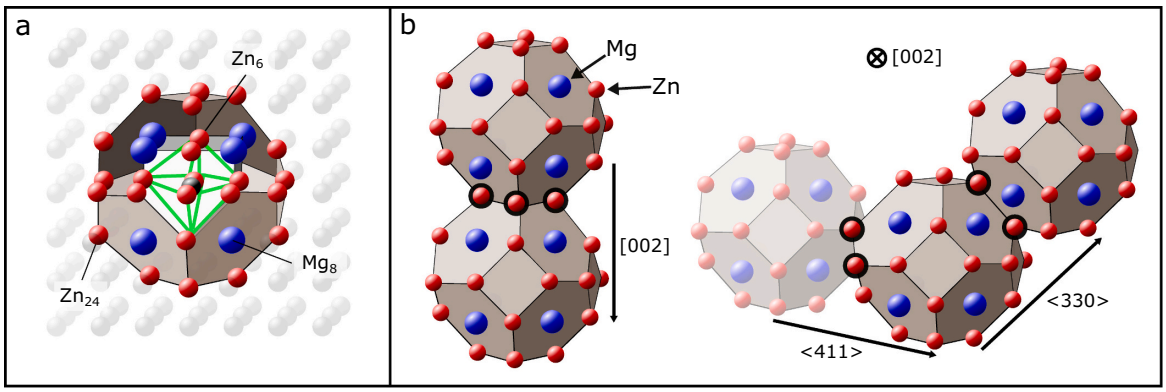

Fig. 1. a: Basic TCO molecular unit of the GPI zones. b: TCO connections in GPI zones. Left: two TCOs connected along [002] forming a TCO string. Right: Lateral sharing of TCO strings in ⟨411⟩ and ⟨330⟩ directions viewed along [001]GPI. Figure adapted from Ref. [9]. The black perimeter indicates shared atoms.

2.2.2. SPED acquisition and data analysis

A JEOL 2100F microscope operated at 200 kV was used in the experiments. The microscope was operated in nanobeam diffraction (NBD) mode, with a convergence angle of 1 mrad. The precession-angle and frequency was 0.3° (=5.2 mrad) and 100 Hz, respectively. The probe size was set to 0.5 nm, which is the smallest probe size available in the NBD mode with this instrument. Due to precession and aberrations, the actual probe size is larger, around 1–2 nm. The double-rocking probe was aligned according to the approach described by Barnard et al. [26] using the NanoMEGAS DigiSTAR control software. The SPED was performed using the NanoMEGAS P1000 scanner scan generator. The scan step size was set to 0.3 nm, and the scan regions were in the range of 100 × 100 - 300 × 300 pixels^2 corresponding to 30 × 30 - 100 × 100 nm^2. The 4D SPED datasets were recorded using a Medipix3 MerlinEM camera with a single 256 × 256 Si chip from Quantum detectors [27]. Diffraction patterns were recorded in 12 bit mode with an exposure time of 30–60 ms per pixel.

The SPED data was analysed using the open-source python libraries *hyperspy* [28] and *pyxem* [29]. The workflow is illustrated in Fig. 2. First, the 4D data matrix was acquired as described above. To inspect the data, virtual imaging was performed. By integrating the intensity of the diffraction patterns within a virtual aperture set in reciprocal space, a virtual dark-field (VDF) image was created. Binary masks were created both in the real- and reciprocal space using the python library *scikit-image* [30]. For the reciprocal-space mask, a blob-finding algorithm was used to locate the Al reflections in the average PED pattern of the entire data stack and subsequently masking out those reflections. The real-space mask was created in the following way: first the uneven background in the VDF image was accounted for using a rolling ball correction [31]. Next, the remaining background was subtracted by filtering regional maxima before a white tophat procedure was applied on the output image [32]. Finally, the binary VDF was created using a suitable intensity threshold. Each connected region in the binary VDF was assigned to an individual GP zone, and the PED patterns belonging to each zone was averaged to minimize the pattern noise. The result is a simplified dataset, with unchanged Al matrix, but with each zone assigned to its average PED pattern. The unsupervised learning routine, non-negative matrix factorisation (NMF) [33], was performed on the original datasets to check the validity of the simplified datasets. During the NMF decomposition, the Al reflections were masked out using the reciprocal space mask. The NMF routine decomposes the dataset into component maps, resembling diffraction patterns, and loading maps, resembling VDF images, showing where each particular component is important. By trial-and-error, a total of 5–10 components were deemed sufficient for each dataset. For etailed descriptions of NMF of SPED data confer Ref. [34]. An example of phase mapping can be found in Ref. [23].

To enhance the contrast between the diffraction spots and the background, which also makes the intensity distribution of the experimental patterns comparable to their simulated representations, the following pixel-by-pixel transformation was applied to the average PED patterns:

$$I_{\text{enhanced}} = 1 - e^{-I_{\text{initial}}/n}, \tag{1}$$

where I_{enhanced}, I_{initial} are the intensities in the enhanced and original image, respectively, while n is set to the typical maximum intensity in a GP zone diffraction spot. A value of 30 was used here.

2.3. Density functional theory

The DFT calculations were performed using the Vienna Ab Initio Simulation Package (VASP) [35,36], with the projector augmented wave method [37,38]. The generalised gradient approximation by Perdew-Burke-Erzenhof was the applied functional. The energy cutoff was set to 400 eV for all calculations.

The atomic model of the ⟨411⟩-connected GPI zone is illustrated in Fig. 3. The cell spans 6x6x2 Al unit cells. The double period of the supercell compared to the fcc along the [001] direction allows the central column of the TCO to be 3/2 occupied as compared to fcc Al. The system was first relaxed in a fixed volume with a gamma sampling of 0.18 Å^{-1}, afterwards, a maximum distance of k-points was set to 0.08 Å^{-1} for the energy calculations. A higher k-point density was required for the smearing method.

The formation enthalpy was calculated by

$$\Delta H = E - \sum_X N_X E_X, \tag{2}$$

where E is the total energy of the simulation cell comprising the GP zone. The summation gives the energy contribution of the different elements

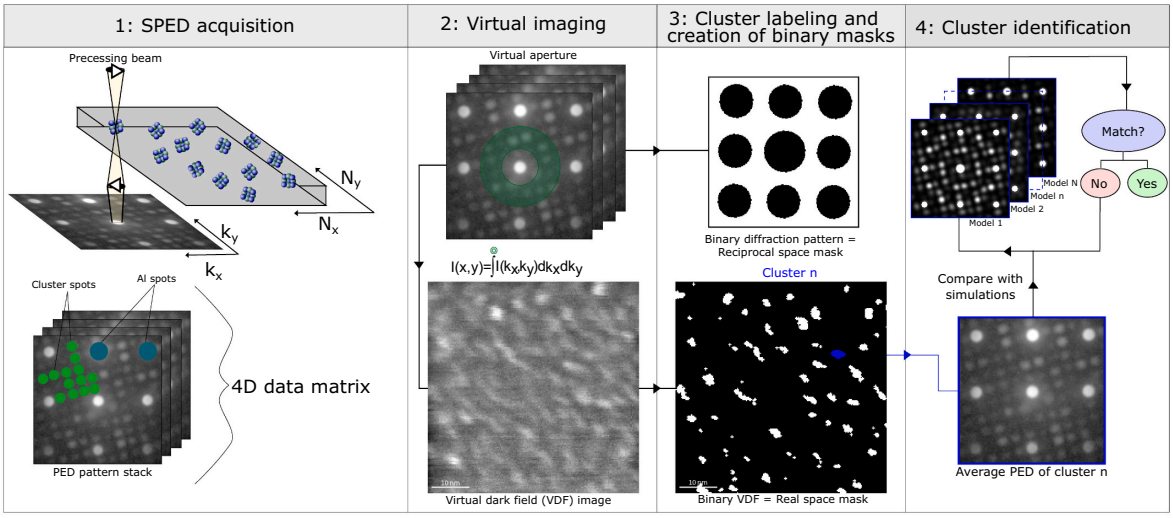

Fig. 2. Workflow of SPED experiments and data analysis showing the acquisition, the principle of virtual imaging, GP zone labelling, creation of binary masks and GP zone identification.

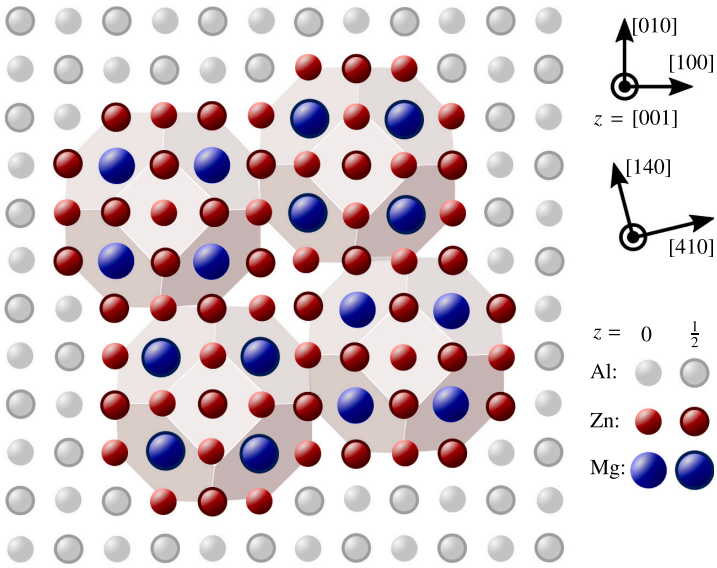

Fig. 3. Atomic model comprising a ⟨411⟩-connected GPI zone elongated in the [001] direction. The supercell spans 6x6x2 Al unit cells.

as single solutes in the matrix. N_X is the number of solutes of type X. E_X is the cohesive energy of element X in the aluminium matrix, per atom, and is calculated from a bulk configuration. The energy cost of the vacancies produced were also considered, as will be elaborated in the discussion section.

2.4. Diffraction pattern simulations

The multislice software μSTEM [39] was used to simulate the diffraction patterns in the position-averaged convergent beam electron diffraction (PACBED) mode. By setting the probe forming aperture to 1 mrad, mimicking the experimental condition, the resulting pattern will be an NBD pattern. Calculations were performed on a 512 × 512 pixels mesh grid. To obtain satisfactory resolution and simultaneously avoid wrap-around errors, a large supercell with dimensions 129 × 129 Å^2 was used, with layers of 13 Al unit cells surrounding the GPI zone model on each lateral side. The simulations were performed for thicknesses between 4 Å and 400 Å. Unless otherwise stated, the simulated diffraction patterns presented in the article are from a thickness of 48 Å.

To simulate PED patterns, a beam tilt of 5.2 mrad (= 0.3°) was introduced while rocking the tilted beam around the optical axis with increments of 4 mrad, resulting in a total of 1572 azimuthal angles. The final pattern represents an average of all the patterns. This is more computationally expensive than simulating NBD patterns. Hence, all the patterns presented in the article are NBD patterns, while PED patterns were simulated to investigate the effect of the precession compared to unprecessed patterns and are included in the Supplementary.

3. Results and discussion

3.1. Microstructure overview

The HAADF-STEM image in Fig. 4a shows the microstructure of the alloy in the ⟨001⟩Al projection. The dense population of GP zones comprises both ⟨411⟩- and ⟨330⟩-⟨411⟩ connected GPI zones. Note how all the atomically resolved zones are viewed along the unique [001]GPI axis. Fig. 4b shows a selected area diffraction pattern (SADP) from a region and orientation similar to Fig. 4a. The diffuse spots associated with the GPI zones are marked with yellow and green disks. Fig. 4c shows the FFT of Fig. 4a, exhibiting a good correspondence with the

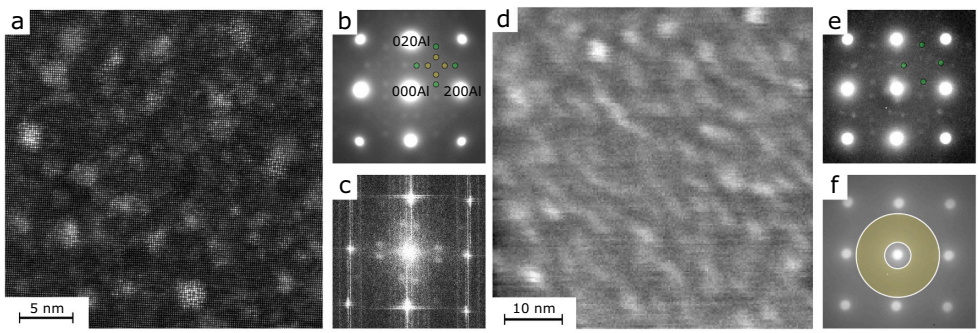

Fig. 4. a: HAADF-STEM showing a high density of GPI zones. b: SADP of a similar region as in a. c: fast Fourier transform of a. d: VDF image from a similar region as in a. e: Constructed pattern by maximum pixel values in the data stack. f: Average PED pattern illustrating the placement of the virtual aperture in the SPED data stack.

SADP in Fig. 4b. A VDF image from a 60 × 60 nm^2 region from one of the SPED datasets is shown in Fig. 4d. Fig. 4e is a constructed diffraction pattern with each pixel corresponding to its highest value in the 4D dataset. Fig. 4 f shows the average PED pattern from the same dataset, the overlay representing the virtual aperture. A bright pixel in the VDF image corresponds to a higher intensity within the virtual aperture in the corresponding PED pattern as compared to the rest of the diffraction patterns. Thus, higher intensity corresponds to solute ordering with longer periodicities than the basic Al period. The contrast in the VDF image appears stretched out because of stage drift during the acquisition.

The bright dots in the VDF image in Fig. 4d therefore indicate the presence of GPI zones or precipitates. Interestingly, there are no diffraction effects apart from the Al spots in the average PED patterns like Fig. 4f, while clear contributions from the GPI zones exist in the SADP, FFT and in the maximum patterns in Fig. 4b-c and e, respectively. This is understandable because the zones are small: The diameter of 1–3 nm [9] is small compared to the specimen thickness, which is the reason the GPI zone-to-Al signal is low. In the individual PED patterns, the intensity of the central disk is saturated, i.e. exceeding 4096 counts per detector pixel, while the Al diffracted disks have a typical count of 100–700. The GPI diffracted disks however, amount to 15–30 counts. In the PED patterns in the flat regions of the VDF image, the intensity between the Al diffracted spots is typically 6–15. The signal from the GPI zones is hence subdued by the background level in the average PED pattern in Fig. 4f.

3.2. Identification of unique PED patterns from GPI zones

Five PED patterns with unique diffraction effects were identified in the 4D data stack. To try to assess what type of structures gave rise to these PED patterns, NBD pattern simulations were performed based on different GPI models. The models are shown along [001]GPI, in column 1 in Fig. 5a-d. As mentioned, our previous work on the atomic structure of the GPI-zones indicated the presence of an interstitial position in the central column of the TCO strings [9]. Based on this, three models corresponding to four TCOs connected along the ⟨411⟩Al direction were set up. The difference between the models lies in the central column of the TCO: In the first model the solutes occupy the Al fcc lattice positions, hereby denoted 'fcc variant' and is shown in column 1 in Fig. 5a. Column 1 in Fig. 5b shows the 'defect variant', where the atoms of the central TCO column in a TCO string are displaced to the Al cell centres, i.e. the octahedral sites. This is a 1D column defect in the Al lattice, first identified in the β'' phase in the 6xxx system [40]. In the last ⟨411⟩ connected GPI zone model, the central column has 3/2 occupancy relative to Al, i.e. a fcc variant with every second octahedral site occupied. As opposed to the first two variants, the central columns have a period of 8.1 Å instead of 4.05 Å. This model is shown in column 1 in Fig. 5c and will in the following be denoted 'interstitial variant'. The extra solute in this configuration is delivered by the matrix, in exchange such columns can

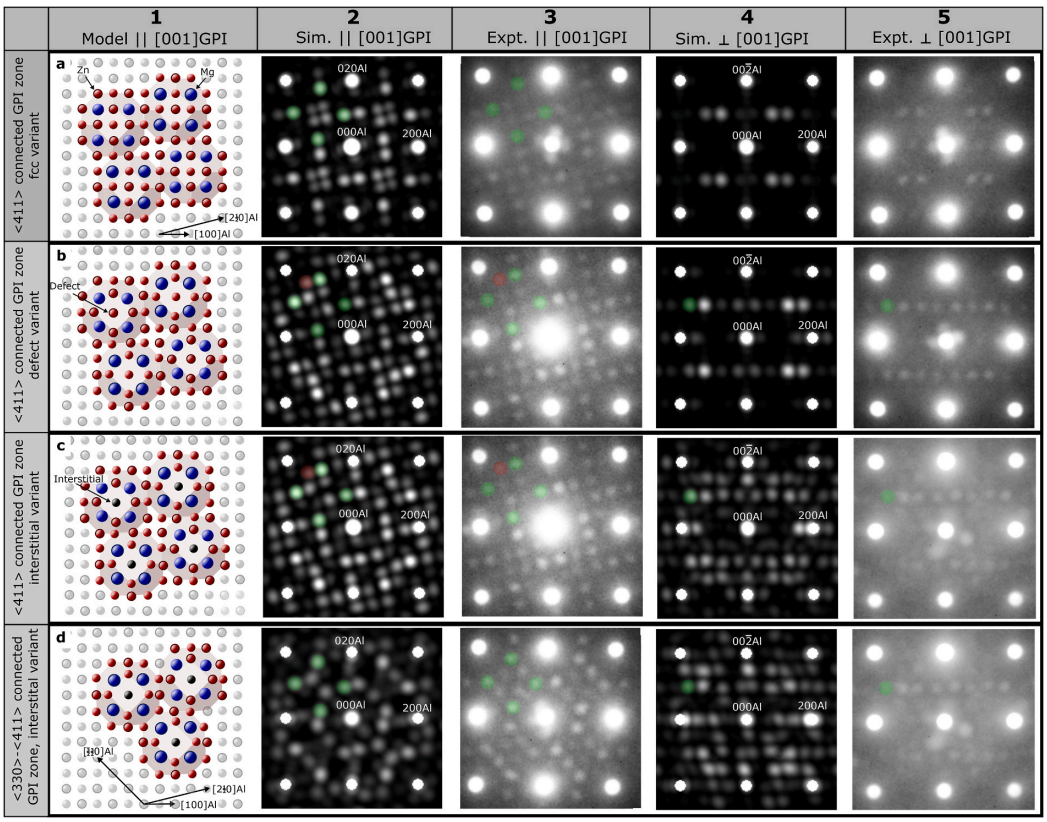

Fig. 5. GPI zone models and corresponding simulated NBD- and experimental PED patterns viewed parallel and normal to [001]GPI. Columns: (1) models along [001]GPI. (2,3) corresponding simulated patterns and selected experimental patterns, (4,5) simulated patterns and selected experimental patterns in one of the ⟨001⟩Al zone axes normal to [001]GPI. Rows: (a-c) ⟨411⟩ connected GPI zones with all solutes on fcc, with defected central column or with 3/2 occupancy in central columns, respectively, (d) ⟨330⟩-⟨411⟩ connected GPI zone with 3/2 occupancy in central columns. Note that all the simulations are NBD patterns, while the experimental patterns are PED patterns.

produce a vacancy every 8.1 Å. This is different from the defect variant, where the atoms of the central column are pushed into the octahedral site. In order to avoid too close spacing (2.025 Å) at the top and bottom of the GPI zone interfaces, a vacancy is locked, and by translation effectively split between the front and the end of the GPI zone.

The simulated NBD patterns corresponding to the three ⟨411⟩ connected variants along [001]GPI are shown in Fig. 5a-c, column 2. The reflections overlaid by green disks in the upper-left quadrant are of the same origin as the GPI reflections in the SADP in Fig. 4b. All three patterns inherit a 4-fold rotational axis. Visual comparison of selected diffraction spots shows that discrimination between the fcc variant and the two others is possible. For example, the reflections associated with the red disks in the patterns corresponding to the defect- and interstitial variants are absent for the fcc variant, indicating that such intensities are consequences of the interstitial ordering. The defect- and interstitial variants however, show strong similarity. Consequently, the diffraction patterns for these variants are indistinguishable in this projection. The experimental PED patterns in column 3 in Fig. 5a-c have a good correspondence with the simulated average NBD patterns. Note that in the experimental patterns, the reflections indicated by the red circles are faint, making it experimentally challenging to discriminate between the three variants in this orientation.

In addition to connecting purely along the ⟨411⟩Al directions, the TCO strings can also connect along the ⟨330⟩Al directions [9]. However, this was only observed by HAADF-STEM if the GPI zones also contained ⟨411⟩ connections. GPI zones structured this way will in the following be denoted ⟨330⟩-⟨411⟩ connected GPI zones. An example is shown in column 1 in Fig. 5d. The central column has 3/2 occupancy relative to Al, making this the interstitial variant of the ⟨330⟩-⟨411⟩ connected GPI zones. The corresponding simulated average NBD pattern is shown in column 2. The approximate 3-fold rotational symmetry of the inner reflections in the pattern makes it distinguishable from the 4-fold rotational symmetric patterns originating from the ⟨411⟩-connected GPI zones (cf. column 2 in Fig. 5a-c). The experimental PED pattern in column 3 in Fig. 5d has a good correspondence with the corresponding simulated pattern. Conclusively, the PED patterns from ⟨330⟩-⟨411⟩- and ⟨411⟩ connected GPI zones are distinguishable when viewed along [001]GPI. It is however more challenging to conclude whether the central column contains defects or interstitials.

Considering the tetragonal crystal structure of the GPI zones, NBD pattern simulations were also carried out along the directions normal to [001]GPI. The results are shown in column 4 in Fig. 5a-c for the ⟨411⟩-connected GPI zones. Column 5 in Fig. 5a-c shows experimental patterns with a strong resemblance with the simulated patterns in column 4. Thus, based on one 4D dataset only it is possible to extract information both along [001]GPI, showing how the TCO strings are connected, in addition to investigate the existence of point defects along the central column of the TCO. This is an important result, as proving the latter is challenging based on HAADF-STEM imaging alone since all the atomically resolved GPI zones imaged in the ⟨001⟩Al orientation are viewed along [001]GPI. The diffracted reflections originating from the GPI zones imaged along the direction normal to [001]GPI also contribute to the SADP in Fig. 4b, as illustrated by the green disks in column 5 in Fig. 5b-d. NBD simulations of the interstitial variant of the ⟨330⟩-⟨411⟩ connected GPI zones along the directions normal to [001]GPI were also carried out. The results are shown in column 4 of Fig. 5d. By comparing this pattern with the one in column 4 in Fig. 5c, it is concluded that the two different stackings of the TCO strings to form larger GPI zones are not possible to differentiate in reciprocal space in this orientation. The same experimental PED pattern as in column 5 in Fig. 5c is shown in Fig. 5d to illustrate the correspondence of this particular experimental pattern with both the simulations in column 4 in Fig. 5c-d. However, the two connections are distinguishable when the GPI zones are viewed along [001]GPI.

Similar NBD pattern simulations were also carried out for the ⟨330⟩-⟨411⟩ connected GPI zones with solutes on fcc and with defect. They are shown in Fig. 1 in the Supplementary. Similarly as for the ⟨411⟩ connected GPI zones, the simulated NBD patterns for the fcc variant are distinguishable from the defect- and interstitial variants, while the defect and interstitial variants are indistinguishable when viewed along [001]GPI. No experimental patterns could be identified as the fcc variant along [001]GPI. Along the directions normal to [001]GPI, the patterns are distinguishable and show some resemblance to the patterns from the corresponding ⟨411⟩ connected GPI variants. The differences are however less prominent than for the ⟨411⟩ connected GPI zones. Differentiating between the ⟨411⟩- and ⟨330⟩-⟨411⟩ connected GPI zones was not possible when the GPI zones were imaged normal to [001]GPI.

3.3. Investigating GP zones by SPED

The experimental PED patterns in Fig. 5 contain reflections with satisfactory correspondence with the simulated patterns of the different GPI zone models. In a 30 nm × 30 nm scan, typically 20 average PED patterns could be identified as originating from GPI zones. As mentioned above, viewing the GPI zones along [001]GPI allowed for separation between the ⟨411⟩- and ⟨330⟩-⟨411⟩ connected GPI zones, while viewing them along a direction normal to [001]GPI separated the fcc-, defect- and interstitial variants, amounting to a total of five categories. About 1/3 of the GPI zone diffraction patterns in any given scan could be matched with patterns of these five categories. The remaining GPI zone patterns could not be determined. The origin of such patterns is most likely overlapping GPI zones along the viewing direction, causing the corresponding PED pattern to be similar to the SADP in Fig. 4b. Overlap can be reduced by using a thin region of the TEM specimen. In our experience, a sample thickness of 20–40 nm is ideal. In thinner regions, the signal from the amorphous surface oxide layer tends to dominate.

In this work, a total of 39 patterns from 8 datasets were investigated and labelled manually to get an idea of the relative numbers of ⟨411⟩ connected GPI zones compared to ⟨330⟩-⟨411⟩ connected GPI zones. Fig. 6 shows one example, with the VDF image and the corresponding binary VDF image in Fig. 6a-b, respectively. Fig. 6c1-c4 show average PED patterns extracted from the region in the binary VDF image with the corresponding colour. The pattern indicated with turquoise (Fig. 6c1) corresponds to the ⟨411⟩ connected GPI zones. The patterns marked by yellow (Fig. 6c2) and orange (Fig. 6c3) correspond to GPI zones viewed normal to [001]GPI, with intensities corresponding the fcc- and defect variant, respectively. The pattern associated with purple is similar to the SADP in Fig. 4b. In Fig. 6d1-g1 and Fig. 6d2-g2, the results from an NMF analysis of the dataset are presented. The top row (Fig. 6d1-g1) shows component maps, while the bottom row (Fig. 6d2-g2) shows loading maps. The composite component- and loading maps in Fig. 6d1-d2 are the sum of all components associated with GPI zones. The individual NMF components are shown in Fig. 6e1-g1 and Fig. 6e2-g2, using the same colour scheme as in Fig. 6c1-c3. By comparing the simplified dataset from the binary VDF image with the results from the NMF decomposition, it was observed that the loading maps of specific components from the NMF corresponded well to the simplified dataset. It is interesting to note that the set of inner reflections marked by yellow disks in Fig. 4b stem from the GPI zones viewed normal to [001]GPI, as evidenced in the composite component map in Fig. 6d1. The average PED pattern in Fig. 6c4 has more resemblance with the SADP in Fig. 4b than with any of the simulated patterns along [001]GPI. This indicated that this particular pattern is a mix of GPI zones in the three orientations, most probably due to overlap of multiple zones along the viewing direction. This complicates the analysis as the NMF categorises the overlapped GPI zones as ⟨411⟩ connected GPI zones, evidenced in Fig. 6e2. Thus, the NMF succeeds at separating the GPI zones viewed normal to [001]GPI, but fails at separating the ones viewed along [001]GPI if overlapping GPI zones are present. Care should therefore be taken if using NMF to extract information about the relative amounts of GPI zones along [001]GPI. In the following, results from the manual labelling of patterns from the binary VDF image will be discussed.

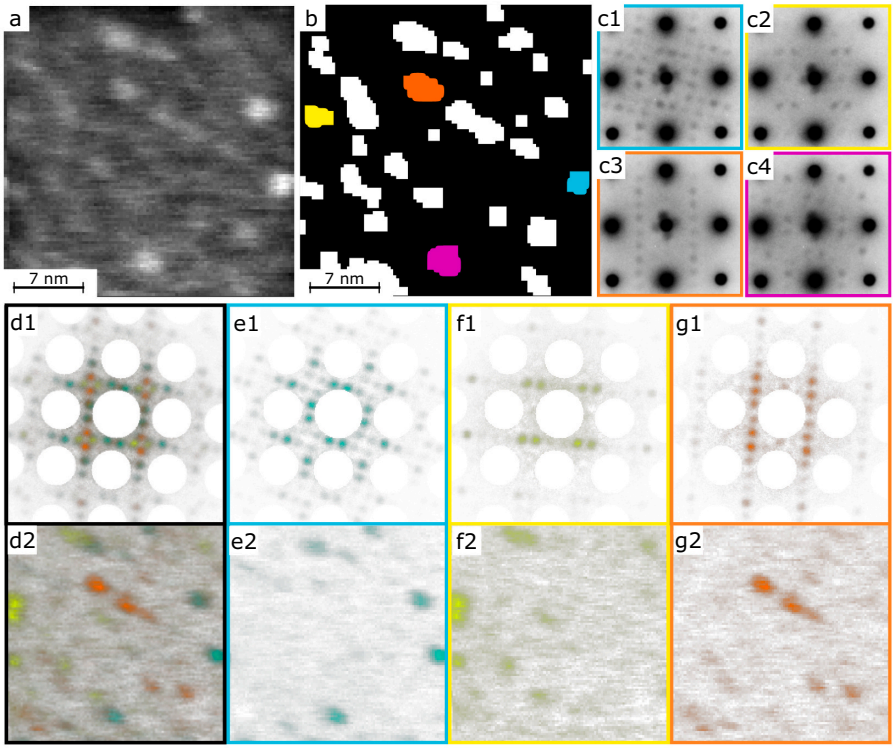

Fig. 6. One of the sped datasets investigated. a: VDF image. b: Binary VDF image. Colours indicate regions where the average PED patterns, seen in c1-c4, were extracted from. d1, d2: Composite component- and loading maps from all the NMF components associated with GPI zones. e1-g1: Component maps. e2-g2: Loading maps.

Out of 39 identifiable patterns, all the PED patterns viewed along [001]GPI were found to be ⟨411⟩ connected GPI zones except one, which was categorised as a ⟨330⟩-⟨411⟩ connected GPI zone. In one third (31%) of the GPI zones, [001]GPI was parallel to the viewing direction, the rest had [001]GPI normal to the viewing direction, c.f. column 4 and 5 in Fig. 5. This is reasonable, as [001]GPI has no preference for a specific ⟨001⟩Al direction. The diffracted intensity from a GPI zone was lowest in the direction normal to [001]GPI, making quantification harder. Although only 39 patterns were identifiable, the current HAADF-STEM experiments together with our previous work [9] support that the ⟨411⟩ connected GPI zones are more common than the ⟨330⟩-⟨411⟩ connected ones.

The simulated NBD patterns shown in Fig. 5 assume GPI zones of the same thickness as the Al along the ⟨001⟩ viewing direction. However, in reality the GPI zones are embedded in the Al matrix. This discrepancy between the models and reality hinders the extraction of quantitative information (such as GPI zone length/thickness) based on the intensities in the experimental patterns. Other factors also affect the intensity; these include the size of the GPI zones, their position inside the TEM sample, the thickness of the sample and the precession of the incoming beam. To investigate these effects, PED- and NBD patterns were simulated for two specimen thicknesses, as well as models having the GPI zone at the top or bottom surface. The results are shown in the Supplementary (Fig. 2). From the simulations, it is concluded that both specimen thickness and relative height of the GPI zone influence the intensity. Thus, only the position of the reflections, and not the relative intensities, should be used to identify the variant. Moreover, the precession affects the intensities of the unique reflections. It is observed that under certain circumstances, NBD yields a higher intensity in the reflections used for the profile plots in Supplementary Fig. 2, while under other circumstances, PED yields a higher intensity. Based on the simulations alone, one could conclude that it is ambiguous which operation mode is best fit for studying the GPI zones. However, the simulations are for a specific, ideal case. The experimental sample can incorporate artefacts from the sample preparation such as Cu-rich surface layers [41] or hydrocarbon contamination building up during TEM acquisition. Such layers affect the experimental diffraction patterns and are not accounted for in the simulations. The contamination can be lowered by decreasing the electron dose. However, in the case of studying GPI zones, a step size of 0.3 nm is needed to obtain sufficient resolution. In our experience, the precession improves the quality of the patterns by averaging out the signal from the contamination. The diffraction patterns also appear more even with precession, c.f. Supplementary Fig. 2.

3.4. Stability of the GPI zones

DFT calculations were performed to investigate the stability of the models in Fig. 5. The nomenclature is adapted from Ref. [9]: The models are denoted n-i$Z_6M_8Z_{24}$. The 'n' refers to either a pure ⟨411⟩ connected GPI zone or a ⟨330⟩-⟨411⟩ connected GPI zone, where we use '4' or '3', respectively. A lowercase 'i' or 'd' refers to interstitial or defect in the central column of the TCO, respectively. For the fcc variant, the character is omitted. The last part describes the atoms of the three shells in the TCO: 'Z6' indicates there are six Zn atoms at the faces of the inner cube, 'M8' refers to the eight Mg atoms at the corner of the cube and 'Z24' gives the number of Zn atoms in the 24 atom shell immediately outside the cube.

The results from the DFT calculations are shown in Table 1. The pure

Table 1
GPI zones formation enthalpies and pressure in a 6×6×2 Al calculation cell, as ranked by formation enthalpy per solute. See the main text for explanation of the GPI zone configurations.

Configuration/composition			Formation enthalpy [eV]			Pressure	Ratio
No	GPI zone	Composition	Total	Atom	Solute	[kbar]	Zn/Mg
1	4-d$Z_6M_8Z_{24}$	$Mg_{32}Zn_{120}$	−22.078	−0.077	−0.145	1.9	3.750
2	3-d$Z_6M_8Z_{24}$	$Mg_{24}Zn_{90}$	−15.838	−0.055	−0.139	2.2	3.750
3	4-$Z_6M_8Z_{24}$[a]	$Mg_{32}Zn_{120}$	−20.037	−0.070	−0.132	−5.6	3.750
4	4-i$Z_6M_8Z_{24}$[a]	$Mg_{32}Zn_{124}$	−20.258	−0.069	−0.130	5.5	3.875
5	3-$Z_6M_8Z_{24}$	$Mg_{24}Zn_{90}$	−14.500	−0.050	−0.127	−3.8	3.750
6	3-i$Z_6M_8Z_{24}$	$Mg_{24}Zn_{93}$	−14.468	−0.050	−0.124	5.0	3.875

[a] Same model as previously published in Ref. [9]

⟨411⟩ connected GPI zones are consistently more energetically favourable than the ⟨330⟩-⟨411⟩ connected ones. We believe a reason for this is that ⟨330⟩ connected units have all Mg atoms on the same {001}Al planes, increasing strain for every new connection. It is seen that the defect variants have the lowest formation enthalpy per solute, followed by the fcc and interstitial variants, respectively.

Every TCO incorporating an occupied octahedral site will result in a vacancy in the Al matrix. The energy of the vacancy is its cohesive energy. Naturally, this energy penalty will be lowered if the vacancy disappears into a nearby defect, such as a particle or grain boundary. In the results of Table 1, the strictest energy penalty is given to the interstitial variants, where the vacancy is assumed to be absorbed by the matrix. This was not considered in our previous work [9], which found the interstitial variants to be the most energetically favourable.

For both the ⟨411⟩- and ⟨330⟩-⟨411⟩ connected GPI zones, the DFT calculations find that the defect variant is energetically more favourable than the fcc variant. The SPED data gave indications that these configurations could co-exist. Based on this, we propose a transition from the fcc variant to the defect variant as shown in Fig. 7, where the formation enthalpy is plotted against pressure. For simplicity, the TCOs are shown without the outer Zn rich shell in the figure. Initially, all the solutes should occupy fcc lattice positions. To alleviate the pressure, the atoms of the central columns move 2.025 Å in the ⟨001⟩Al direction along [001]GPI. This creates the 1D column defect which is also found in β'' [40] in the Al-Mg-Si alloy system, and the new configuration obtains a significantly lower enthalpy.

Although the interstitial configuration appears less energetically favourable than the fcc- and defect variants, the SPED data indicated that some of the GPI zones contained 3/2 occupied central columns. By inspection of the experimental diffraction pattern of the defect- and interstitial variant in column 5 in Fig. 5b-c, respectively, it can be seen that there is a common row of reflections. The PED pattern from the interstitial variant exhibits an extra row of reflections compared to the common one, as evidenced in the simulations in column 4 in Fig. 5b-c. We note that in the experimental pattern of the interstitial variant in column 5 in Fig. 5c, the extra row of reflections is weaker than the common one. This could indicate that the interstitial variant does not exist in a 'pure state', but rather exists in GPI zones where the central column in a TCO string is a mixture of both defects and interstitials along [001]GPI.

4. Conclusion

In this work, a TEM-based methodology for studying GP zones with periodic structure embedded in the Al matrix has been developed. Data was collected from an Al-Zn-Mg alloy containing a dense population of GPI zones. Electron diffraction patterns from single GPI zones were successfully recorded by a direct electron detector with the TEM operated in the SPED mode. The GPI zones are spherical particles with a diameter of 1 to 3 nm embedded in the host Al matrix. The experimental diffraction patterns were compared with multi-slice simulations based on the previously proposed structures of the GPI zones. A good correspondence was found between the two. The technique allows 3D information to be obtained, since the resolution in reciprocal space is sufficient to extract information in ⟨001⟩Al zones, from individual GPI zones viewed both along their unique axis, [001]GPI, and the normal orientations, which is not possible from HAADF-STEM imaging alone. By taking advantage of this, it was found that the central column of the

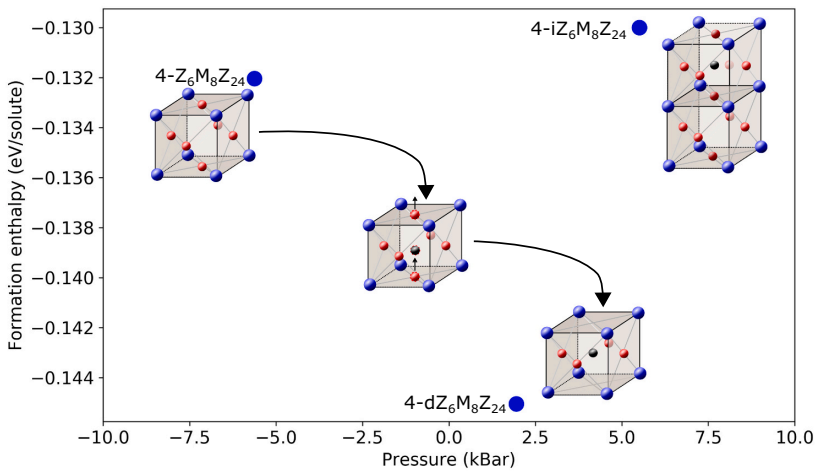

Fig. 7. Formation enthalpy given in eV/solute vs. pressure for the ⟨411⟩ connected GPI zones. In the schematics of the TCOs, the outer Zn rich layer is omitted for simplicity. (1) fcc variant, (2) defect variant and (3) shows the interstitial variant.

molecular building block of the GPI zones may be shifted one atomic plane compared to the Al fcc positions. This was supported by DFT calculations. The presented methodology is believed to be highly useful also for other material systems where small particles are embedded in a host material.

Author contribution

E.T., C.D., S.W. and R.H. conceived, designed and supervised the research. E.T. conducted the (S)TEM experiments. S.J.A. created the initial models. J.Fra. and J.Fri. prepared the models and conducted the DFT modelling. E.T. conducted the diffraction simulations. E.T. prepared the figures. E.T. wrote the manuscript with input from all the authors.

Data availability

The raw data and models used to reproduce the presented results are available in the Zenodo repository https://doi.org/10.5281/zenodo.5092880.

Declaration of Competing Interest

The authors declare that they have no known competing financial interests or personal relationships that could have appeared to influence the work reported in this paper.

Acknowledgements

This work was supported by the NTNU Digital Transformation initiative'Alldesign' (E.T., J.Fri. and R.H.) and The Research Council of Norway (NFR) through the project'SumAl' (NFR: 294933) (J.Fri., J.Fra., C.D.M., R.H. & S.J.A.), supported by Hydro, Benteler Automotive Raufoss AS and Neuman Aluminium. The (S)TEM work was conducted on the NORTEM (NFR: 197405) infrastructure at the TEM Gemini Centre, Trondheim, Norway. The DFT calculations were performed on resources provided by UNINETT Sigma2 - the National Infrastructure for High Performance Computing and Data Storage in Norway (NN8068K). We acknowledge A. Bendo and K. Matsuda at the University of Toyama for providing the alloy studied in this work. We acknowledge E. Christiansen and J. K. Sunde who wrote the initial code for analyzing the SPED data which has been further developed in this work.

Appendix A. Supplementary data

Supplementary data to this article can be found online at https://doi.org/10.1016/j.matchar.2021.111675.

References

[1] P. Hartel, H. Rose, C. Dinges, Conditions and reasons for incoherent imaging in STEM, Ultramicroscopy 63 (1996) 93–114, https://doi.org/10.1016/0304-3991(96)00020-4.
[2] S.J. Andersen, C.D. Marioara, J. Friis, S. Wenner, R. Holmestad, Precipitates in aluminium alloys, Adv. Phys. X 3 (2018) 1479984, https://doi.org/10.1080/23746149.2018.1479984.
[3] T. Saito, E.A. Mørtsell, S. Wenner, C.D. Marioara, S.J. Andersen, J. Friis, K. Matsuda, R. Holmestad, Atomic structures of precipitates in Al-Mg-Si alloys with small additions of other elements, Adv. Eng. Mater. 20 (2018) 1800125, https://doi.org/10.1002/adem.201800125.
[4] A. Wilm, Physikalisch-metallurgische Untersuchungen über magnesiumhaltige Aluminiumlegierungen, Metallurgie 8 (1911) 225–227.
[5] E. Hornbogen, Hundred years of precipitation hardening, J. Light. Met. 1 (2001) 127–132, https://doi.org/10.1016/S1471-5317(01)00006-2.
[6] A. Guinier, Structure of Age-Hardened Aluminium-Copper Alloys, 1938. URL, https://www.nature.com/articles/142569b0, https://doi.org/10.1038/142569b0.
[7] G. Preston, The diffraction of X-rays by an age-hardening alloy of aluminium and copper. The structure of an intermediate phase, Lond. Edinburgh Dublin Philos. Mag. J. Sci. 26 (1938) 855–871, https://doi.org/10.1080/14786443808562177.
[8] L.K. Berg, J. Gjøønnes, V. Hansen, X.Z. Li, M. Knutson-Wedel, G. Waterloo, D. Schryvers, L.R. Wallenberg, GP-zones in Al-Zn-Mg alloys and their role in artificial aging, Acta Mater. 49 (2001) 3443–3451, https://doi.org/10.1016/S1359-6454(01)00251-8.
[9] A. Lervik, E. Thronsen, J. Friis, C.D. Marioara, S. Wenner, A. Bendo, K. Matsuda, R. Holmestad, S.J. Andersen, Atomic structure of solute clusters in Al–Zn–mg alloys, Acta Mater. 205 (2021), 116574, https://doi.org/10.1016/j.actamat.2020.116574.
[10] H. Löffler, I. Kovács, J. Lendvai, Decomposition Processes in Al-Zn-Mg Alloys, 1983, https://doi.org/10.1007/BF00541825.
[11] G. Dlubek, R. Krause, O. Brümmer, F. Plazaola, Study of formation and reversion of Guinier-Preston zones in Al-4.5 at%Zn-x at%Mg alloys by positrons, J. Mater. Sci. 21 (1986) 853–858, https://doi.org/10.1007/BF01117364.
[12] V. Hansen, O.B. Karlsen, Y. Langsrud, J. Gjønnes, Precipitates, zones and transitions during aging of Al - Zn - Mg - Zr 7000 series alloy, Mater. Sci. Technol. 20 (2004) 185–193, https://doi.org/10.1179/026708304225010424.
[13] J. Buha, R.N. Lumley, A.G. Crosky, Secondary ageing in an aluminium alloy 7050, Mater. Sci. Eng. A 492 (2008) 1–10, https://doi.org/10.1016/j.msea.2008.02.039.
[14] M. Torsæter, H.S. Hasting, W. Lefebvre, C.D. Marioara, J.C. Walmsley, S. J. Andersen, R. Holmestad, The influence of composition and natural aging on clustering during preaging in Al-Mg-Si alloys, J. Appl. Phys. 108 (2010) 073527, https://doi.org/10.1063/1.3481090.
[15] Y. Aruga, M. Kozuka, Y. Takaki, T. Sato, Evaluation of solute clusters associated with bake-hardening response in isothermal aged Al-Mg-Si alloys using a three-dimensional atom probe, Metallurg. Mater. Trans. A: Phys. Metallurg. Mater. Sci. 45 (2014) 5906–5913, https://doi.org/10.1007/s11661-014-2548-y.
[16] H. Zhao, B. Gault, D. Ponge, D. Raabe, F. De Geuser, Parameter free quantitative analysis of atom probe data by correlation functions: application to the precipitation in Al-Zn-Mg-Cu, Scr. Mater. 154 (2018) 106–110, https://doi.org/10.1016/j.scriptamat.2018.05.024.
[17] G. Sha, A. Cerezo, Early-stage precipitation in Al-Zn-Mg-Cu alloy (7050), Acta Mater. 52 (2004) 4503–4516, https://doi.org/10.1016/j.actamat.2004.06.025.
[18] G. McMullan, A.R. Faruqi, R. Henderson, N. Guerrini, R. Turchetta, A. Jacobs, G. van Hoften, Experimental observation of the improvement in MTF from backthinning a CMOS direct electron detector, Ultramicroscopy 109 (2009) 1144–1147, https://doi.org/10.1016/j.ultramic.2009.05.005.
[19] C. Ophus, Four-Dimensional Scanning Transmission Electron Microscopy (4D-STEM): From Scanning Nanodiffraction to Ptychography and Beyond, 2019, https://doi.org/10.1017/S1431927619000497.
[20] P.A. Midgley, A.S. Eggeman, Precession Electron Diffraction - A Topical Review, 2015, https://doi.org/10.1107/S2052252514022283.
[21] R. Vincent, P.A. Midgley, Double conical beam-rocking system for measurement of integrated electron diffraction intensities, Ultramicroscopy 53 (1994) 271–282, https://doi.org/10.1016/0304-3991(94)90039-6.
[22] J.K. Sunde, S. Wenner Paulsen, R. Holmestad, Precipitate statistics in an Al-Mg-Si-Cu alloy from scanning precession electron diffraction data, in: Journal of Physics: Conference Series vol. 902, Institute of Physics Publishing, 2017, p. 12022, https://doi.org/10.1088/1742-6596/902/1/012022.
[23] J.K. Sunde, C.D. Marioara, A.T.J. van Helvoort, R. Holmestad, The evolution of precipitate crystal structures in an Al-Mg-Si(-Cu) alloy studied by a combined HAADF-STEM and SPED approach, Mater. Charact. 142 (2018) 458–469, https://doi.org/10.1016/j.matchar.2018.05.031.
[24] J.K. Sunde, C.D. Marioara, R. Holmestad, The effect of low Cu additions on precipitate crystal structures in overaged Al-Mg-Si(-Cu) alloys, Mater. Charact. 160 (2020), 110087, https://doi.org/10.1016/j.matchar.2019.110087.
[25] J.K. Sunde, D.N. Johnstone, S. Wenner, A.T. van Helvoort, P.A. Midgley, R. Holmestad, Crystallographic relationships of T-/S-phase aggregates in an Al–Cu–Mg–Ag alloy, Acta Mater. 166 (2019) 587–596, https://doi.org/10.1016/j.actamat.2018.12.036.
[26] J.S. Barnard, D.N. Johnstone, P.A. Midgley, High-resolution scanning precession electron diffraction: alignment and spatial resolution, Ultramicroscopy 174 (2017) 79–88, https://doi.org/10.1016/j.ultramic.2016.12.018.
[27] J.A. Mir, R. Clough, R. MacInnes, C. Gough, R. Plackett, I. Shipsey, H. Sawada, I. MacLaren, R. Ballabriga, D. Maneuski, V. O'Shea, D. McGrouther, A.I. Kirkland, Characterisation of the Medipix3 detector for 60 and 80 keV electrons, Ultramicroscopy 182 (2017) 44–53, https://doi.org/10.1016/j.ultramic.2017.06.010.
[28] F.D.L. Peña, E. Prestat, V.T. Fauske, P. Burdet, T. Furnival, P. Jokubauskas, M. Nord, T. Ostasevicius, J. Lähnemann, K.E. MacArthur, D.N. Johnstone, M. Sarahan, J. Taillon, T. Aarholt, Pquinn-Dls, V. Migunov, A. Eljarrat, J. Caron, T. Poon, S. Mazzucco, B. Martineau, S. Somnath, T. Slater, C. Francis, M. Walls Actions-User, N. Tappy, N. Cautaerts, F. Winkler, G. Donval, hyperspy/hyperspy: Release v1.6.3, 2021, https://doi.org/10.5281/ZENODO.4923970.
[29] D.N. Johnstone, P. Crout, M. Nord, J. Laulainen, S. Høgås, B. Martineau EirikOpheim, C. Francis, T. Bergh, E. Prestat, S. Smeets, S. Collins Andrew-rossl, I. Hjorth, T. Furnival Mohsen, D. Jannis, N. Cautaerts, E. Jacobsen, T. Poon AndrewHerzing, H.W. Anes, J. Morzy, S. Huang, T. Doherty Phillipcrout, T. Ostasevicius Affaniqbal, R. Tovey Mvonlany, pyxem/pyxem: pyxem 0.13.1, 2021. URL.
[30] S. van der Walt, J.L. Schönberger, J. Nunez-Iglesias, F. Boulogne, J.D. Warner, N. Yager, E. Gouillart, T. Yu, The scikit-image contributors, scikit-image: image processing in Python, PeerJ 2 (2014), e453, https://doi.org/10.7717/peerj.453.
[31] S.R. Sternberg, Biomedical image processing, Computer 16 (1983) 22–34, https://doi.org/10.1109/MC.1983.1654163.
[32] A.C. Bovik, The Essential Guide to Image Processing, Elsevier Inc., 2009, https://doi.org/10.1016/B978-0-12-374457-9.X0001-7.
[33] D.D. Lee, H.S. Seung, Learning the parts of objects by non-negative matrix factorization, Nature 401 (1999) 788–791. URL.

[34] B.H. Martineau, D.N. Johnstone, A.T. van Helvoort, P.A. Midgley, A.S. Eggeman, Unsupervised machine learning applied to scanning precession electron diffraction data, Adv. Struct. Chem. Imaging 5 (2019) 1–14, https://doi.org/10.1186/s40679-019-0063-3.
[35] G. Kresse, J. Hafner, Ab initio molecular dynamics for liquid metals, Phys. Rev. B 47 (1993) 558–561, https://doi.org/10.1103/PhysRevB.47.558.
[36] G. Kresse, J. Furthmüller, Efficient iterative schemes for ab initio total-energy calculations using a plane-wave basis set, Phys. Rev. B - Condens. Matter Mater. Phys. 54 (1996) 11169–11186, https://doi.org/10.1103/PhysRevB.54.11169.
[37] P.E. Blöchl, Projector augmented-wave method, Phys. Rev. B 50 (1994) 17953–17979, https://doi.org/10.1103/PhysRevB.50.17953.
[38] G. Kresse, D. Joubert, From ultrasoft pseudopotentials to the projector augmented-wave method, Phys. Rev. B - Condens. Matter Mater. Phys. 59 (1999) 1758–1775, https://doi.org/10.1103/PhysRevB.59.1758.
[39] L.J. Allen, A.J. D'Alfonso, S.D. Findlay, Modelling the inelastic scattering of fast electrons, Ultramicroscopy 151 (2015) 11–22, https://doi.org/10.1016/j.ultramic.2014.10.011.
[40] M.A. Van Huis, M.H. Sluiter, J.H. Chen, H.W. Zandbergen, Concurrent substitutional and displacive phase transformations in Al-Mg-Si nanoclusters, Phys. Rev. B - Condens. Matter Mater. Phys. 76 (2007) 174113, https://doi.org/10.1103/PhysRevB.76.174113.
[41] S. Wenner, A. Lervik, E. Thronsen, C.D. Marioara, S. Kubowicz, R. Holmestad, Copper enrichment on aluminium surfaces after electropolishing and its effect on electron imaging and diffraction, Mater. Charact. 172 (2021), 110846, https://doi.org/10.1016/j.matchar.2020. 110846.

Supplementary material to: Studying GPI zones in Al-Zn-Mg alloys by 4D-STEM

E. Thronsen[a,*], J. Frafjord[a], J. Friis[a,b], C. D. Marioara[b], S. J. Andersen[b], R. Holmestad[a]

[a] *Department of Physics, Norwegian University of Science and Technology (NTNU), N-7491 Trondheim, Norway*
[b] *SINTEF Industry, N-7465, Trondheim, Norway*

[*] Corresponding author at: Department of Physics, Norwegian University of Science and Technology (NTNU), N-7491 Trondheim, Norway
Email address: Elisabeth.Thronsen@ntnu.no (E. Thronsen)

1. Supplementary simulated nanobeam diffraction patterns

Models and corresponding simulated nanobeam diffraction (NBD) patterns of GPI zones along ⟨001⟩Al directions are shown in Fig. 1a-c for the fcc-, defect- and interstitial model for the ⟨330⟩-⟨411⟩ connected GPI zones, respectively.

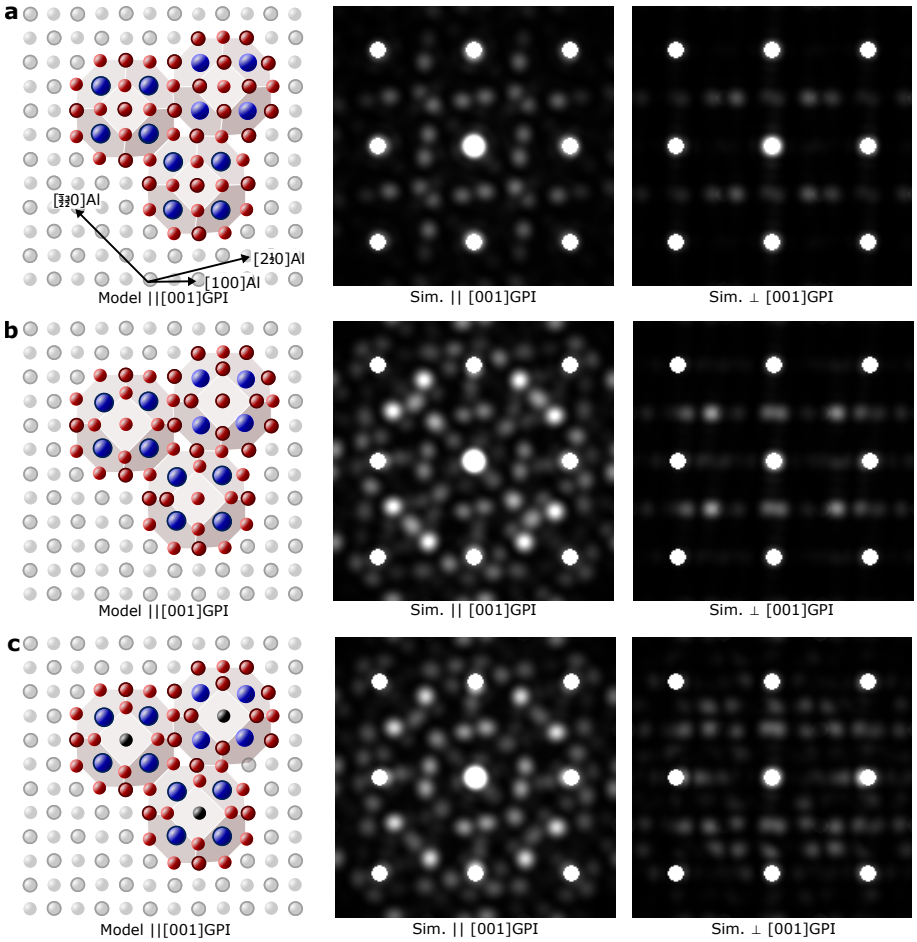

Figure 1: Models and corresponding simulated NBD patterns along and normal to [001]GPI for different ⟨330⟩-⟨411⟩ connected GPI zones. a: Fcc variant. b: Defect variant. c: Interstitial variant.

2. Supplementary simulated precession electron diffraction patterns

Fig. 2 shows simulated NBD and PED patterns along [001]GPI containing GPI zones placed at different heights in 30 and 40 nm thick slabs of Al. Six truncated cube octahedron (TCO)s define the zone extension in this direction, i.e. the zones have a thickness of 4.86 nm. The simulations show the GPI zones placed either at the top or bottom in the slab. The model used was the interstitial variant of the ⟨411⟩ connected GPI zone. The Al reflections are masked out from the simulated patterns to enhance the contrast from the GPI zones. To enable a better quantitative comparison of the simulations, line scan intensity profiles (red line in the top left image in Fig. 2) were extracted as shown in the right hand side of the figure. The two profile plots are for the GPI zone placed at the top (upper plot) and bottom (lower plot) of the Al slab,

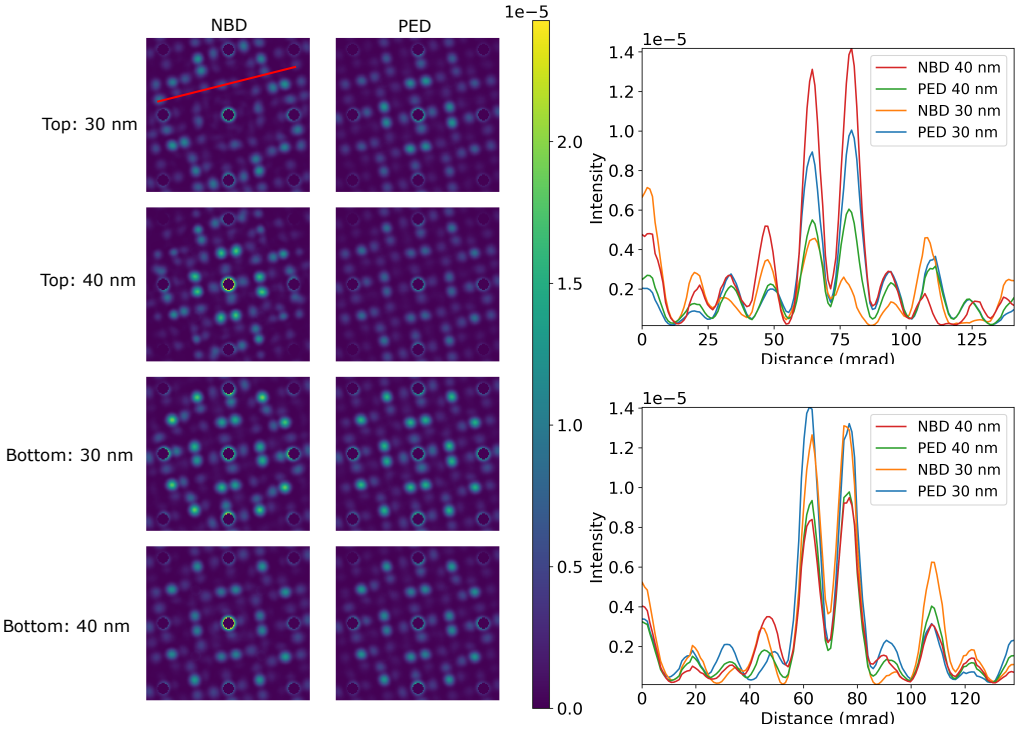

Figure 2: Simulated NBD- and PED patterns of the interstitial model of the ⟨411⟩ connected GPI zones viewed along [001]GPI placed at different heights in the Al matrix along the viewing direction for two different TEM specimen thicknesses: 30 nm or 40 nm. The red line indicates the path of the scan for generating the intensity profile plots on the right hand side. The colourbar shows the intensity distributions in the 'viridis' colormap used for the diffraction pattern simulations.

Paper III

The evolution of precipitates in an Al-Zn-Mg alloy

E. Thronsen, S. Shah, C. Hatzoglou, C.D. Marioara, S. Wenner, S.J. Andersen, B. Holmedal, R. Holmestad

To be submitted

Author contributions

E. Thronsen and S. Shah initiated the study. E. Thronsen did the (S)TEM experiments and subsequent data analysis. S. Shah did the APT experiments. S. Shah and C. Hatzoglou analysed the APT data. E. Thronsen and S. Shah wrote the initial draft. C. D. Marioara, S. Wenner, S. J. Andersen, B. Holmedal and R. Holmestad supervised the research. All authors commented on the final manuscript.

Paper IV

The effect of heavy deformation on the precipitation in an Al-1.3Cu-1.0Mg-0.4Si wt.% alloy

E. Thronsen, C. D.Marioara, J. K. Sunde, K. Minakuchi, T. Katsumi, I. Erga, S. J. Andersen, J. Friis, K. Marthinsen, K. Matsuda, R. Holmestad

Materials & Design (2020) **186** 108203

Author contributions

E. Thronsen did the SPED work and basic TEM imaging. J. K. Sunde assisted E. Thronsen in obtaining and analyzing the SPED data. C. D. Marioara did the STEM experiments. S. J. Andersen prepared the initial models. J. Friis did the DFT calculations. I. Erga and E. Thronsen measured the hardness. K. Minakuchi, T. Katsumi and K. Matsuda suggested the study and provided the material. K. Minakuchi, T. Katsumi, K. Matsuda, R. Holmestad and K. Marthinsen supervised the research. E. Thronsen wrote the manuscript with input from all co-authors.

Materials and Design 186 (2020) 108203

Contents lists available at ScienceDirect

Materials and Design

journal homepage: www.elsevier.com/locate/matdes

The effect of heavy deformation on the precipitation in an Al-1.3Cu-1.0Mg-0.4Si wt.% alloy

Elisabeth Thronsen[a,*], Calin D. Marioara[b], Jonas K. Sunde[a], Kazuhiro Minakuchi[c], Tetsuya Katsumi[c], Iven Erga[d], Sigmund J. Andersen[b], Jesper Friis[b], Knut Marthinsen[d], Kenji Matsuda[e], Randi Holmestad[a]

[a]Department of Physics, Norwegian University of Science and Technology, Høgskoleringen 5, N-7491, Trondheim, Norway
[b]Materials and Nanotechnology Department, SINTEF Industry, Høgskoleringen 5, Trondheim, N-7465, Norway
[c]Machinery and Engineering Group, YKK Corporation, 200, Yoshida, Kurobe, Toyama, 938-8601, Japan
[d]Department of Materials Science and Engineering, Norwegian University of Science and Technology, Alfred Getz Vei 2, N-7491, Trondheim, Norway
[e]Graduate School of Science and Engineering for Research, University of Toyama, Toyama, 930-8555, Japan

HIGHLIGHTS

- An advanced TEM for detailed characterisation of precipitates in pre-deformed materials is presented.
- The effect of natural ageing and pre-deformation on precipitation in terms of type and distribution is investigated.
- The crystal structure of a previously reported phase in pre-deformed Al-Mg-Si(-Cu) alloys is presented.

GRAPHICAL ABSTRACT

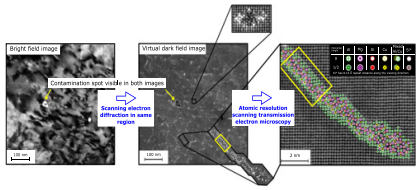

ARTICLE INFO

Article history:
Received 4 July 2019
Received in revised form 26 August 2019
Accepted 10 September 2019
Available online 24 October 2019

Keywords:
Al-Mg-Si-Cu alloys
Natural ageing
Pre-deformation
Precipitation
Scanning precession electron diffraction
High angle annular dark-field scanning transmission electron microscopy

ABSTRACT

This work has investigated the effect of the combination of natural ageing and 80% pre-deformation after solution heat treatment on precipitation during subsequent artificial ageing in an Al-1.3Cu-1.0Mg-0.4Si wt.% alloy. It was found that a combined use of atomic resolution aberration corrected high-angle annular dark-field scanning transmission electron microscopy and scanning precession electron diffraction enabled a detailed characterisation of precipitates in heavy pre-deformed materials. The dominant phase in the undeformed condition was the L phase. L was also found to be nucleated in the undistorted regions of the Al matrix in the pre-deformed conditions. Two phases with high aspect ratios were nucleated on dislocations: The C phase and a previously reported phase, which we named here the 'E phase'. The crystal structure of E was solved experimentally as monoclinic with core composition $Mg_6Al_2Si_2Cu_4$, supported by density functional theory calculations. It was determined that the order of pre-deformation and natural ageing had an influence on the relative fractions of the aforementioned phases formed during artificial ageing. An increased fraction of C+E relative to L was found in the condition where the pre-deformation was applied after natural ageing as compared to the condition where the pre-deformation was applied before natural ageing.

1. Introduction

Al-Mg-Si(-Cu) alloys are a class of materials with an increased use in the construction and automotive industries due to a combination

* Corresponding author.
E-mail address: elisabeth.thronsen@ntnu.no (E. Thronsen).

https://doi.org/10.1016/j.matdes.2019.108203

of desired properties such as light weight, high strength and good corrosion resistance. Their manufacturing consists of a succession of thermo-mechanical steps including casting, homogenisation, extrusion or rolling, solution heat treatment (SHT) and artificial aging (AA). The role of homogenisation is to reduce chemical segregation of the cast, and to produce dispersoidal AlSi(Mn,Fe) particles that will control grain size during the subsequent high temperature processing [1,2]. A solid solution is formed during SHT at temperatures above the solvus line of the system (>500 °C), consisting of a uniform dispersion of Mg, Si and Cu solute atoms substituting the Al positions in the FCC lattice, together with a high density of vacancies. This becomes super-saturated by rapid cooling, and constitutes the starting point of the AA, usually conducted at temperatures between 150°C and 200°C. During this process the solute atoms diffuse with the help of vacancies and form high numbers of nano-sized, metastable precipitates, which significantly affect the final properties of the material [3,4]. It is interesting to notice that with only 1 to 2 at.% added Mg, Si and Cu solute, the material can triple its strength during AA. The strength arises from the interaction between the dislocations and precipitates, since the precipitates effectively hinder the movement of dislocations in the matrix. The metastable precipitates have crystalline structures and form with different types, compositions, volume densities and size distributions, depending on the thermo-mechanical treatment of a given alloy. Therefore, the processing of the alloy is very important for the final properties.

In the Al-Mg-Si(-Cu) system, all the metastable phases have one main coherency direction with the Al matrix, along ⟨100⟩Al. In these directions the precipitates retain the FCC Al atomic arrangement, having atoms on two planes ($z = 0$ and $z = 0.203$ nm) with 0.405 nm repeat distance. Therefore, they grow with needle/rod/lath/plate morphologies along such directions and are viewed as projected atomic columns in cross-section in ⟨100⟩Al orientations. The precipitate development during AA from the super saturated solid solution (SSSS) and until the equilibrium phase forms is given as a precipitation sequence, which for the Al-Mg-Si-Cu system is [4]:

SSSS → solute clusters → GP zones →
β'', L → $\beta'_{(Cu)}$, L, S, C, Q′ → Q (Stable).

Solute clusters and Guinier-Preston (GP) zones are solute aggregates ordered on the FCC Al matrix positions. β'' is the main phase that forms in peak hardness conditions in the Al-Mg-Si alloys [3,5]. The phase has also been observed in Cu-added alloys, but here other Cu-containing precipitates such as L, S, C and Q′ become dominant with prolonged heating [4]. Cu is added to many Al-Mg-Si alloys because it improves hardness and thermal stability [4,6]. Analysis of the metastable precipitate crystal structures led to the realisation that they must be based on a similar sub-lattice with projected near-hexagonal symmetry of around 0.4 nm when viewed in cross-section [7]. It was later demonstrated that the sub-lattice is defined by Si atomic columns, and all the other atomic columns (Mg, Al, Cu) are located in-between [4,8]. This was called the 'Si-network'. It can take two different orientations in respect to the Al matrix. One orientation is defined by the Si network being aligned with ⟨310⟩Al, ⟨110⟩Al, ⟨510⟩Al and in the other the network is aligned with ⟨100⟩Al. The former is the most common and is present in all metastable precipitates in the Al-Mg-Si system, and in the S, β'_{Cu}, Q′ phases in the Al-Mg-Si-Cu system. The latter has only been found in the Cu-added alloys, in the L and C phases [4,9]. In the Al-Mg-Si-Cu system the Q′ phase is the metastable version of the equilibrium Q phase, being isostructural with it. It grows as laths with cross-section elongation along ⟨510⟩Al [4]. The C phase grows as a plate, with elongations along two ⟨100⟩Al directions [4,10]. β'_{Cu} is isostructural with the β'_{Ag} phase, with Cu replacing Ag in the structure, and is different from the β' phase in the Cu-free system [9,11]. The Q/Q′, C and β'_{Cu} phases are the only periodic structures so far reported in the Al-Mg-Si-Cu system. One characteristic of the Cu-added alloys is the formation of disordered structures which can be characterised by different orderings on the Si-network. It is common to observe several local ordered configurations of known phases in the same needle or lath, producing hybrid structures. In this respect the L phase is disordered and can contain local Q′ and/ or C phase parts, while S is also disordered and can contain Q′ and/ or β'_{Cu} parts [4]. In peak hardness conditions of such alloys it is also very common to observe hybrid precipitates containing β''/Q′/β'_{Cu} parts [12,13].

Another important milestone in the Al-Mg-Si(-Cu) system is the discovery of a set of construction rules for most precipitates, which arise from a line defect in the Al matrix [14]. According to these rules, every Al atom has 12 near neighbours, every Mg atom has 15 and every Si has 9. Interestingly, in precipitates Cu has 9 near neighbours as Si, and can take two different configurations, with columns in-between the Si network columns, or replacing 1/3 of the Si on the network. The former configuration is present in the Q′ and C phase, and the latter in the β'_{Cu} phase [9].

It has been shown that there are two processing steps that, introduced individually or in combination between SHT and AA, have an important influence on the subsequent precipitate development during AA and consequently on mechanical properties. These are storage at room temperature (RT) also known as natural ageing (NA), and pre-deformation. NA is important because the SSSS is unstable at RT. During this time atomic diffusion is taking place, leading to the formation of solute orderings and atomic clusters, with the effect of hardness increase and electrical conductivity decrease. For dense alloys with (Mg + Si >1 wt.%), the NA clusters have been found to have a negative effect on the precipitation of the hardening phases during the subsequent AA, causing a delay in precipitation and sometimes a reduction in the final hardness compared to when NA is avoided [15,16]. It has been found that the negative effect of natural ageing decreases with increasing Cu concentrations [17,18]. During AA treatment of a pre-deformed material, the dislocations act as heterogeneous nucleation sites for the precipitates. The deformation has a strong effect on the precipitation behaviour: The precipitate type, their microstructure and the local distribution are altered. It has been shown that in the distorted regions of the Al matrix, i.e. areas consisting of crystallographic defects associated with deformation like dislocations and subgrains, ' string-like' precipitates, along with smaller, elongated precipitate types and precipitates associated with over-ageing nucleate [19-22]. The faster coarsening of the precipitates nucleated on dislocations may be due to dislocations acting as short-circuit diffusion path for solutes during AA. Moreover, the introduction of dislocations prior to NA has been found to impede NA clustering [23,24]. The dislocations are believed to act as sinks for the quenched-in vacancies, thus suppressing the formation of NA clusters.

In addition to the conventional applications, novel usages are emerging for the Al-Mg-Si-Cu alloys. In the present work, a new Al-1.3Cu-1.0Mg-0.4Si wt.% intended for the zip fastener industry has been developed. The alloy's composition is listed in Table 1. The manufacturing process of these alloys consists of casting, homogenisation, extrusion, solution heat treatment (SHT), drawing, SHT and cold rolling corresponding to 80% deformation before the final artificial ageing (AA), see Fig. 1. A period of NA can be introduced before or after the cold rolling, which may affect the subsequent AA response. Given these facts, the main objectives of this work is to characterise the precipitates that form during AA in the heavily deformed materials, and to understand the effect of NA in connection to pre-deformation. Vickers hardness is measured at each processing step after the SHT, and hardness development is connected to precipitate microstructure. The microstructure of the alloy is investigated by the use of transmission electron microscopy (TEM). TEM is a powerful technique in visualising the precipitate distribution

Table 1
The measured composition of the alloy investigated in the present work.

	Cu	Mg	Si	Fe	Ti	B	Zn	Mn	Cr	Zr
wt.%	1.27	1.01	0.38	0.069	0.019	0.004	0.003	0.001	<0.001	<0.001

through conventional techniques, such as bright-field (BF) or dark-field (DF) imaging using diffraction contrast, and the precipitate structure through more advanced techniques providing atomic resolution such as high-angle annular dark-field scanning TEM (HAADF-STEM). Studying precipitation in heavily pre-deformed materials by conventional techniques however, is challenging due to the contrast from dislocations masking out the precipitates.

Recently, scanning precession electron diffraction (SPED) has emerged as a promising technique in quantifying the precipitates in undeformed Al alloys [25,26]. By means of this technique, one may form virtual dark-field images using the 4D data set that comprised a 2D PED pattern in each pixel of a 2D scan area. The benefit of this technique is the acquisition of large data-sets that enable detailed statistical characterisation of microstructure, providing location, type and size for a large number of precipitates. In this study we will evaluate the applicability of SPED on heavily deformed Al alloys, as well as quantitatively explain the difference in deforming prior to- or after NA based on material hardness and precipitation.

2. Experimental procedure

2.1. Material and heat treatment

The alloy was cast, homogenised (505°C, 3 h), extruded and solution heat treated (505°C, 3 h) before drawing. Cylindrical bars (Ø 3.8 mm) were subjected to SHT at 505°C for 3 h and subsequently water quenched to room temperature. Three different conditions abbreviated 'NA20ha', 'NA20hb' and 'NA20hn' were investigated in the present work, see Fig. 1. For condition NA20ha, SHT was succeeded by NA for 20 h, followed by 80 % cold rolling and AA at 170°C for 3 h. NA20hb was cold rolled to 80 % immediately after SHT, followed by 20 h NA and subsequent AA at 170 °C for 3 h. NA20hn was exposed to 20 h NA followed by AA for 3 h at 170 °C without any deformation.

2.2. Vickers hardness tests

Prior to Vickers hardness tests, all samples were polished with a Saphir 330 equipped with grinding plates with grit sizes from 120 up to 4000 P. A Zwick/Roell ZHV30 indent machine equipped with JS-Tango controller unit was used for hardness measurements. For the undeformed and deformed samples, a total of 9 and 10 indentations were used per condition, respectively.

2.3. TEM sample preparation

TEM samples were prepared by first mechanically polishing the material down to 100 µm thickness using a Struers Rotopol-21. 3 mm diameter discs were then punched out normal to the drawing direction for the undeformed condition and normal to the rolling direction for the pre-deformed conditions. Subsequently, the samples were electropolished by using a Struers TenuPol-5 with an applied voltage of 20 V for the deformed samples and 14.6 V for the undeformed sample. The electrolyte was kept at a temperature of −25 ± 5°C and consisted of 1/3 nitric acid and 2/3 methanol. In order to reduce the risk of carbon contamination build-up under the data acquisition during SPED and HAADF-STEM investigations, the specimens were cleaned using a Fischione 1020 Plasma Cleaner before insertion into the TEM.

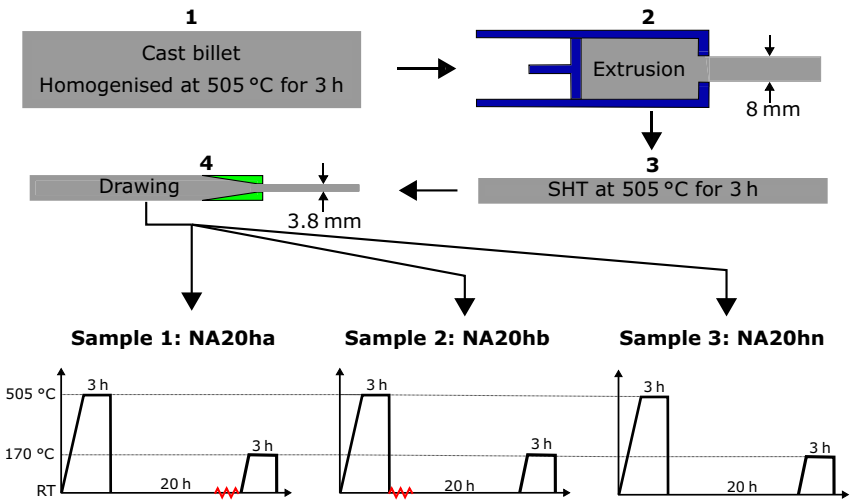

Fig. 1. The material processing prior to the as-received condition is shown in steps 1–4, along with the subsequent processing of the three different samples NA20ha, NA20hb and NA20hn. Both NA20ha and NA20hb were deformed by cold rolling to 0.76 mm, corresponding to 80% deformation.

2.4. TEM studies

A JEOL 2100F operated at high voltage of 200 kV and equipped with a NanoMEGAS ASTAR system was used to acquire the SPED scans. The PED patterns were collected by mounting an Allied Vision Stingray camera in the binocular stand outside the microscope column. While performing SPED, the instrument was operated in nanobeam diffraction mode using an unprecessed probe diameter of about 1.3 nm and semi-convergence angle $\alpha \approx 1$ mrad. The employed precession angle and corresponding precession frequency was kept at 1.0 ° and 100 Hz, respectively. The exposure time was set to 40 ms per pixel and the scan step size was 1.52 nm. The alignment of the precessing electron beam was done in accordance with the procedure reported by Barnard et al. [27]. In addition, the JEOL 2100F was used to acquire BF images.

The acquisition of the high resolution HAADF-STEM images was done in a double (image and probe) corrected JEOL ARM200F operated at 200 kV. The following parameters were used to obtain the images: 0.08 nm probe size, a semi convergence angle of 28 mrad, the inner and outer collection angles were 35 and 150 mrad, respectively. The inner collection angle is somewhat smaller than what is considered optimal for HAADF-STEM (50 mrad), but our experience is that the lower Z-contrast Mg-containing atomic columns are better resolved with this setting. When imaging in an ⟨100⟩ zone axis of Al, this technique provides atomic resolution of precipitates atomic columns along their main coherency direction with the Al matrix, having Z-contrast. Based on such images, the crystal structures of individual precipitates can be identified and presented as atomic overlays. The atomic overlay is made according to the construction rules for precipitates in the Al-Mg-Si(-Cu) system [14] mentioned in the introduction, which imply that in the overlay every Al atom is surrounded by four atoms of opposite height, every Mg by five and every Si and Cu by three.

Atomic resolution HAADF-STEM images in general have low signal-to-noise ratio. To improve clarity, all of the HAADF-STEM images shown in this paper are filtered using a circular bandpass mask applied on the respective fast fourier transform (FFT), and an inverse FFT (IFFT) was performed on the masked area, suppressing all features with separation shorter than 0.15 nm in real space. It should be noted that 0.15 nm is close to the minimum projected atomic column separation for precipitates in the Al-Mg-Si(-Cu) system viewed along their needle lengths.

2.5. Density functional theory calculations

The density functional theory (DFT) calculations were performed with the Vienna ab initio simulation package (VASP) [28,29] using the projector augmented wave method (PAW) within the PBE (Perdew-Burke-Ernzerhof) generalised gradient approximation [30]. The plane wave energy cutoff was 400 eV. For all calculations, gamma-centred k-points were used with a maximal k-point distances of 0.18 $Å^{-1}$ in each direction. The electronic accuracy for self-consistent loops was set at 10^{-6} eV. The atomic positions were relaxed to a maximum force of 0.001 ev $Å^{-1}$ between atoms, using 1st order Methfessel-Paxton for smearing of partial occupation and a smearing factor of 0.2. For accurate energies, a separate calculation was performed using the tetrahedron method with Blöchl correction for the smearing. The formation enthalpies were calculated according to Ref. [31] with solid solution reference energies E_x obtained from a 4×4×4 Al supercell with 255 Al atoms and a single solute atom X, X=Al, Mg, Si, Cu.

2.6. SPED data analysis

SPED involves rastering a precessing, nanometre-sized electron probe over an area of interest and recording the transmitted diffraction pattern at each probe position [27]. The net result is a 4D data set that comprised a 2D PED pattern at each position of a 2D area scan. The 4D SPED data sets were processed using the open-source Python library HyperSpy [32]. The source code used in the present work is developed by Sunde et al. and a thorough review can be found in [26]. A short summary is given here:

1. A *virtual aperture* is placed in the obtained PED pattern stack and the image intensity within the aperture is integrated. The value obtained is used to assign a colour-scale tone to the pattern's corresponding real-space position, resulting in the formation of a virtual dark-field (VDF) image after running through the full stack.
2. A real space *navigation mask* is created by masking out precipitate-free areas in the VDF.
3. A reciprocal space *signal mask* is created by masking out the Al reflections using a bulk Al PED pattern.
4. An unsupervised machine learning approach based on non-negative matrix factorisation (NMF) is applied to the SPED scan data highlighted by the constructed masks.

The NMF decomposition returned *component patterns* representing the data in reciprocal space, resembling PED patterns of specific features such as different precipitate types, in addition to the corresponding *loadings* at each pixel in real space. The *loading maps* indicate where the associated component patterns are significant and resemble simplified dark field images [33]. In theory, the number of components should equal the number of unique phases present multiplied by the number of allowed orientations. However, due to imperfections of the scans, such as bending across the strain area, imperfect masks, strain, a larger amount of components had to be included. By trial-and-error, a total number of 40 and 90 components for NA20ha and NA20hb, respectively, was found to adequately represent the features of interest in the SPED data.

Through comparison with the FFTs of previously obtained HAADF-STEM images, the component patterns were categorised. Components which did not match any of the FFTs were categorised as disordered, based on the HAADF-STEM images. Once identified, the real-space intensities of the components corresponding to the same precipitate were normalised and summed up. The net result yields a simplified and reconstructed description of the diffraction data, showing where each precipitate type is located in the scan area. Finally, precipitate phase fractions were estimated using a pixel-based calculation where the sum of pixels associated with one precipitate type was divided by the total number of pixels representing all the precipitate types.

Through comparison with the FFTs of previously obtained HAADF-STEM images, the component patterns were categorised. Components which did not match any of the FFTs were categorised as disordered, based on the HAADF-STEM images. Once identified, the real-space intensities of the components corresponding to the same precipitate were normalised and summed up. The net result yields a simplified and reconstructed description of the diffraction data, showing where each precipitate type is located in the scan area. Finally, precipitate phase fractions were estimated using a pixel-based calculation where the sum of pixels associated with one precipitate type was divided by the total number of pixels representing all the precipitate types.

A short summary is given here:

1. A *virtual aperture* is placed in the obtained PED pattern stack and the image intensity within the aperture is integrated. The value obtained is used to assign a colour-scale tone to the pattern's corresponding real-space position, resulting in the formation of a virtual dark-field (VDF) image after running through the full stack.

2. A real space *navigation mask* is created by masking out precipitate-free areas in the VDF.
3. A reciprocal space *signal mask* is created by masking out the Al reflections using a bulk Al PED pattern.
4. An unsupervised machine learning approach based on non-negative matrix factorisation (NMF) is applied to the SPED scan data highlighted by the constructed masks.

The NMF decomposition returned *component patterns* representing the data in reciprocal space, resembling PED patterns of specific features such as different precipitate types, in addition to the corresponding *loadings* at each pixel in real space. The *loading maps* indicate where the associated component patterns are significant and resemble simplified dark field images [33]. In theory, the number of components should equal the number of unique phases present multiplied by the number of allowed orientations. However, due to imperfections of the scans, such as bending across the strain area, imperfect masks, strain, a larger amount of components had to be included. By trial-and-error, a total number of 40 and 90 components for NA20ha and NA20hb, respectively, was found to adequately represent the features of interest in the SPED data.

Through comparison with the FFTs of previously obtained HAADF-STEM images, the component patterns were categorised. Components which did not match any of the FFTs were categorised as disordered, based on the HAADF-STEM images. Once identified, the real-space intensities of the components corresponding to the same precipitate were normalised and summed up. The net result yields a simplified and reconstructed description of the diffraction data, showing where each precipitate type is located in the scan area. Finally, precipitate phase fractions were estimated using a pixel-based calculation where the sum of pixels associated with one precipitate type was divided by the total number of pixels representing all the precipitate types.

3. Results and discussion

3.1. The influence of deformation and natural ageing on hardness evolution

The hardness response during NA for a sample deformed immediately after quenching from the SHT temperature and a undeformed sample is shown in Fig. 2a. The AA response for NA20ha, NA20hb and NA20hn at 170°C is shown in Fig. 2b, while Fig. 2c–e shows the hardness response during all processing steps after SHT for NA20ha, NA20hb and NA20hn, respectively, up until the conditions chosen for the TEM samples. In (a), the dashed, vertical line marks the point where the NA time is 20 h, while in (b) it indicates the condition of the samples prepared for TEM which corresponds to the maximum hardness of NA20hb, obtained after around 3 h. NA20ha reaches its maximum hardness after 6 h, while the undeformed sample, NA20hn, does not reach peak hardness after the maximum investigated time, 10 h. This suggests that the introduced dislocations enhance the precipitation kinetics, thereby shortening the AA time required to obtain the peak age condition.

The hardness response during NA is enhanced for the undeformed samples as compared to the pre-deformed samples, see Fig.2a, c and d. After 20 h the increase in hardness is 9 HV and 12 HV for the pre-deformed and undeformed samples, respectively. This is believed to be caused by reduced NA response in the pre-deformed samples due to vacancy annihilation at the dislocations [34,35]. The overall increase in hardness during NA of the pre-deformed sample throughout the measurement times is 10 HV, i.e. the hardness increase from 20 h NA time to five days NA time is only 1 HV, see Fig. 2a.

The pre-deformed samples obtain higher hardness than the undeformed sample for all measured AA times. By comparing Fig. 2c, d and e, it can be seen that the introduction of dislocations through the cold deformation prior to AA is responsible for the difference, and in the same time the contribution to hardness from precipitates is lower

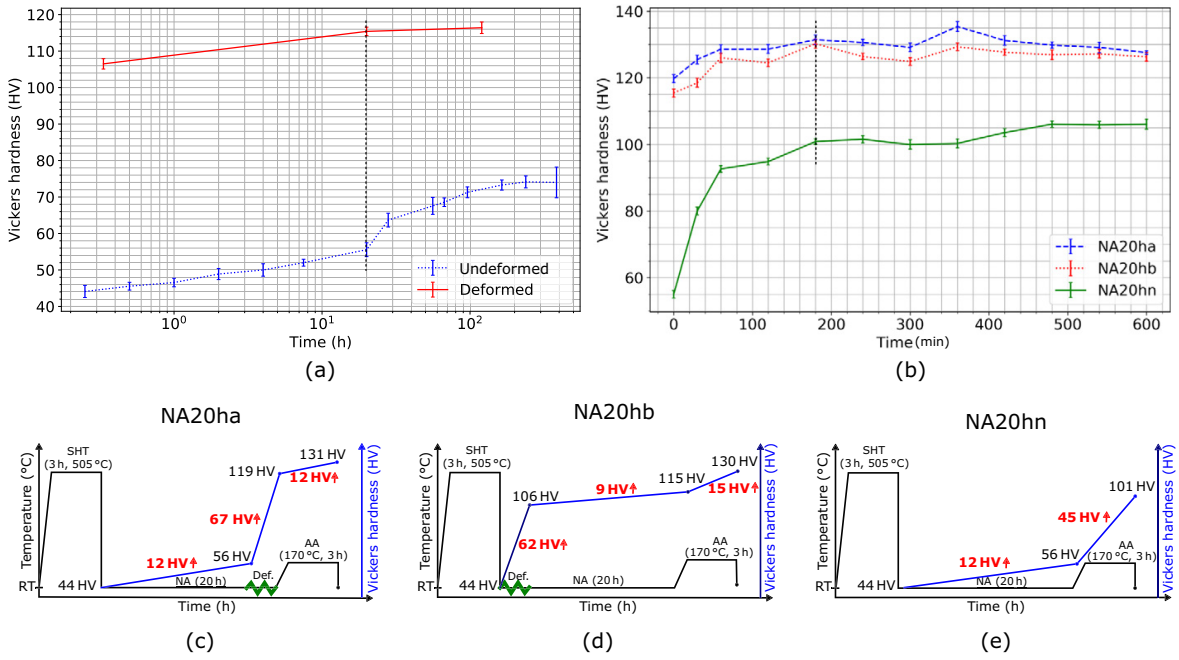

Fig. 2. In (a) the hardness evolution during NA for a pre-deformed and a undeformed sample is displayed. (b) Shows the AA response at 170 °C for the samples. It can be seen that NA20ha and NA20hb reach maximum hardness after 6 h and 3 h, respectively, while NA20hn does not reach peak age after 10 h. In (c), (d) and (e), the hardness increase associated with each processing step after solution heat treatment is shown for NA20ha, NA20hb and NA20hn, respectively.

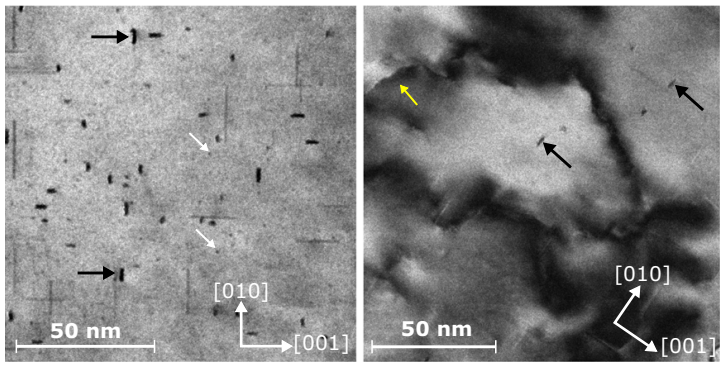

Fig. 3. (a) BF image showing the precipitate distribution in condition NA20hn. The black arrows indicate lath shaped precipitates with habit plane $\{100\}_{Al}$, while the white arrows indicate significantly smaller, rod shaped precipitates. (b) BF image showing the microstructure of one of the pre-deformed samples. The black arrows indicate precipitation in undistorted regions and the yellow arrow indicates a dislocation line.

in the pre-deformed conditions as compared to the undeformed. Moreover, pre-deformation after NA (NA20ha) gives a slightly harder sample after AA. For AA times exceeding 600 min the curves of the two pre-deformed samples are starting to coincide. This may suggest that a fraction of the precipitates in NA20ha are less thermally stable or that the dislocation density in this state is decreasing more rapidly than in NA20hb.

3.2. Precipitate distribution and microstructure of the undeformed sample

Fig. 3a and b shows BF images obtained in $\langle 100 \rangle_{Al}$ orientation for condition NA20hn and NA20ha. For the undeformed sample, the microstructure consists of two main types of precipitates, indicated by the white and black arrows. The precipitates indicated by the black arrows have habit plane $\{100\}_{Al}$ and are lath shaped, while the precipitates indicated by the white arrows are much smaller and are shaped as rods. In the pre-deformed sample (NA20ha), it is observed that precipitates are nucleated in the undistorted regions of the Al matrix, exemplified by the black arrows. The yellow arrow in (b) indicates the presence of a dislocation line. Due to the strong contrast from the dislocations in this and similar images, it is not possible to state if the dislocations are decorated by precipitates or not. Based on the results presented in the following subsections, precipitates are indeed found to decorate dislocations in the pre-deformed conditions. BF imaging was thus deemed unsuitable for visualising the precipitate distribution in the pre-deformed samples.

Fig. 4 shows an HAADF-STEM image of the precipitate microstructure for the undeformed sample. Based on such images, the lath shaped precipitates in Fig. 3a were found to be L phases. One example of the L phase is shown to the left in Fig. 4. The precipitates with very small cross-sections indicated by the white arrows in Fig. 3a were found to be structural units of GPB zones, indicated by white arrows in Fig. 4. GPB zones belong to the Al-Cu-Mg alloy system and are believed to form during the initial stages of AA [36,37].

3.3. Precipitate microstructure of the pre-deformed samples

The first part of the microstructure investigation of the pre-deformed samples involves analysis of precipitate crystal structures by HAADF-STEM. All images presented in the following are taken in a $\langle 100 \rangle_{Al}$ orientation. It is observed that precipitates nucleate in the distorted regions of the Al matrix, as well as in undistorted regions away from the dislocation network. Some regions of the images are atomically overlaid and the legend is presented in Fig. 5.

A representative selection of precipitates found in the pre-deformed conditions is shown in Fig. 6. The C phase was found to nucleate in the distorted regions of the Al matrix, one example is given in Fig. 6a through c, where three images of the same structure are shown. The numbered regions indicate distinguishable segments of the structure. Regions (1) and (4) indicate disordered parts of the structure. Region (2) indicates a segment of the structure nucleated in the C phase configuration. Likewise, the segment in region (5) is nucleated in the C phase configuration. However, whereas in region (2) the C phase is viewed along the $[001]_C$ direction, the segment in (5) is viewed along the $[010]_C$ direction. The C phase was first reported by Marioara et al. [4] and the structure was later solved by Torsæter et al. [10]. The crystal structure of this phase used in the atomic overlay in Fig. 5 is given in Table 2 and is derived from Ref. [10]. It is interesting to notice that peripheral alternating Si-Mg atoms in the C phase unit cell become Al (marked by white arrows) and constitute the $\{100\}_{Al}$ interface. The region in (3) consists of a periodic structure with habit plane $\{110\}_{Al}$ and 0.86 nm periodicity along $\langle 110 \rangle$Al. It is previously reported [21], but the structure has not been solved until now. We name it here the 'E phase', and discuss it in detail in the following subsection.

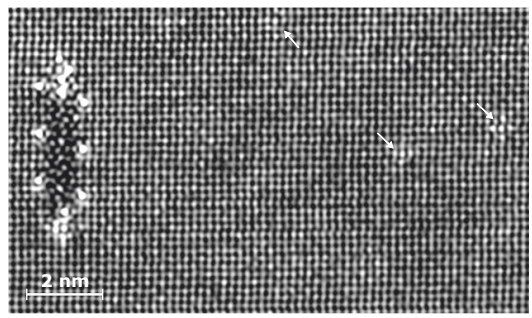

Fig. 4. HAADF-STEM image of NA20hn showing structural units of GPB zones indicated by white arrows, in addition to one example of the lath shaped L phase on the left hand side.

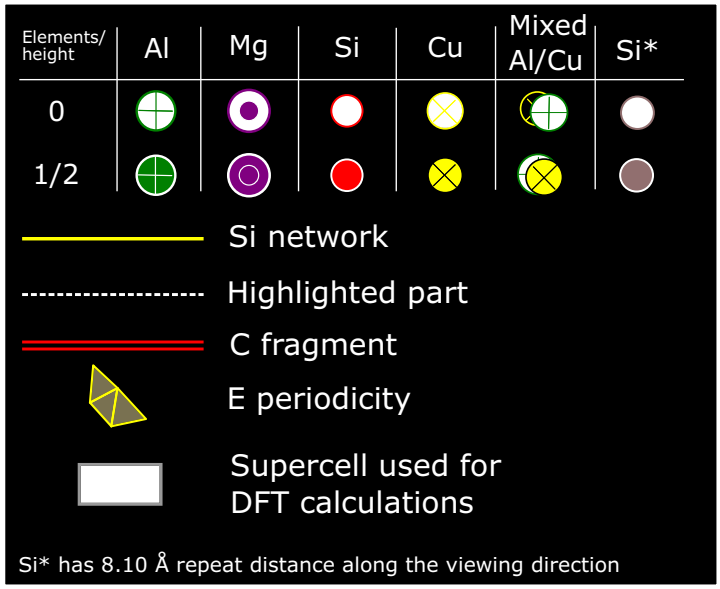

Fig. 5. Legend representing the overlays of HAADF-STEM images in the following subsections.

Precipitate structures like the one shown in Fig. 6a–c were found for both pre-deformed conditions, often consisting of two or more C phases connected by either disordered parts or short segments of the E phase. Furthermore, precipitates like the one imaged in (d) were also found to nucleate in the distorted regions of the Al matrix. The precipitates in Fig. 6a–d resembles the string-type reported in previous work on pre-deformed Al-Mg-Si alloys by Matsuda et al. [19,20] and more recently by Saito et al. [12,38], in the latter case for Al-Mg-Si-Cu alloys. The string-like precipitates like the one shown in (d) consists of segments of E type precipitates connected by disordered parts categorised as S phases. The precipitate in Fig. 6a–c may also be categorised as the string-type. This may imply that the C and E phases are ordered versions of the string-type. Discrete, disordered precipitates were also found to nucleate in the distorted regions of the Al matrix, one example is shown in (e) along with the corresponding FFT. The precipitate has habit plane $\{100\}_{Al}$, thus it can be categorised as an L phase. Discrete L precipitates nucleated in the distorted regions of the Al matrix were not found to be common based on the HAADF-STEM images, but were rather found to connect with or reside nearby larger structures.

As mentioned in the Introduction, there exist a nearly hexagonal sub-lattice known as the Si-network in all precipitate phases in the Al-Mg-Si(-Cu) system. The projected separation of the Si-network is $a \approx 0.4$ nm. Therefore, in FFT patterns it corresponds to spots having 2.89 nm^{-1} and 5 nm^{-1} spatial frequencies. These spots are easily identifiable, even in the case of disordered precipitates. In the FFTs presented in Fig. 6e–g, only spots corresponding to the 5 nm^{-1} spatial frequencies are connected by yellow lines.

Based on 53 and 69 HAADF-STEM images taken from the NA20ha and NA20hb conditions, respectively, it was concluded that the same precipitate types nucleate in the distorted regions of the Al matrix in both pre-deformed conditions. It is proposed that the underlying mechanisms governing the precipitation in such areas are independent of whether the deformation is applied prior to- or after NA.

Analysis of the 53 images obtained for NA20ha concluded that only one type of precipitate nucleates in the undistorted regions of the Al matrix: the L phase. One example is shown in Fig. 6f, along with the corresponding FFT. The L phase was found to nucleate in undistorted regions in NA20hb as well, however an additional category of precipitates was found here. One example is shown in Fig. 6 g, along with the corresponding FFT. The yellow lines indicate part of the Si-network. Such phases were disordered, but due to Cu incorporation and $\{130\}_{Al}$ habit plane, they can be categorised as the S phase [4].

3.4. Crystal structure of the E phase

As previously mentioned, the E phase was observed in both the NA20ha and NA20hb conditions. It has habit plane $\{110\}_{Al}$ and a periodicity of 0.86 nm along $\langle 110\rangle$Al. The E phase may be important for the material properties in pre-deformed Al-Mg-Si(-Cu) as it is seen to decorate dislocation lines and to connect more disordered precipitate-types along dislocation lines. The phase was first reported by Teichmann et al. [21] which studied the effect of 10% pre-deformation in an Al-Mg-Si alloy. However, the images recorded in that work were in high resolution TEM (HRTEM) mode with insufficient resolution to solve the structure. Fig. 7 shows an FFT filtered HAADF-STEM image of a precipitate with local arrangements of the E phase. The Z-contrast reveals a strong enrichment of Cu at the interfaces. The phase periodicity is indicated by the semi-transparent yellow areas.

As a first step in solving the crystal structure of the E phase, Fig. 7 was atomically overlaid based on the construction rules mentioned in the Introduction, the result is shown in Fig. 8a. The Si-network was found to be fragmented into three parts, indicated by the numbers. The longest segment exhibiting the E-phase periodicity is the lower part (no. 3). The Burger's vector $\vec{b}$ indicates the presence of a screw dislocation, believed to be the nucleation site of the precipitate. A supercell comprising Al and the core of the E phase was

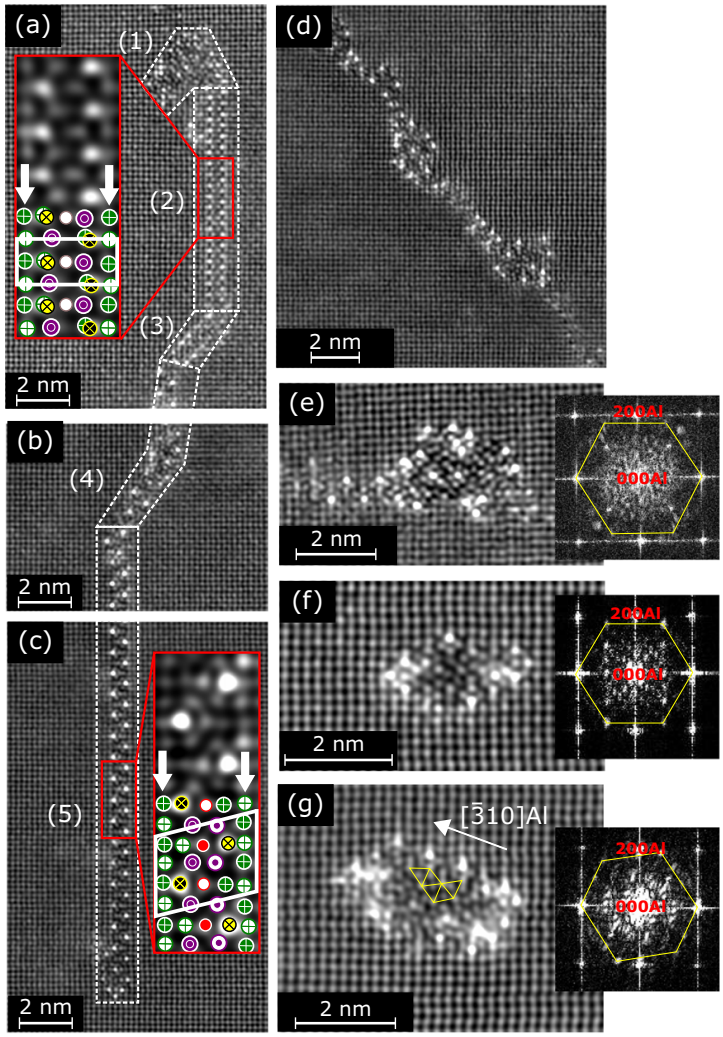

Fig. 6. FFT filtered HAADF-STEM images of different precipitate structures found in the pre-deformed samples. (a)–(c) Different part of the same precipitate. The regions enclosed by dotted lines represent different segments with different ordering in the precipitate. Parts of region (2) and (5), which show two different orientations of the C phase, are atomically overlaid and the unit cells are indicated by the white lines. (d) and (e) show two different types of precipitate nucleated in the distorted parts of the Al matrix. (f) and (g) are examples of precipitate nucleated in the undistorted parts of the Al matrix, categorised as L phase and S phase, respectively. The latter was only observed in NA20hb. In (e)–(g) the FFTs of the images are included.

extracted based on the image and is shown in (b). The black lines indicate the core of the precipitate. The supercell has dimensions $a = 24.34$Å$, b = 4.05$Å$, c = 8.59$Å, and all angles near 90°. However, the highest symmetry for the extracted atomic coordinates was $P2_1$ (space group 4) and thus we propose a monoclinic unit cell for the E phase.

Interestingly, structural similarities are found between the core of the E phase (b) and the core of the C phase (c). The interfacial atoms, denoted by (1) in both (b) and (c), differ: The Si atoms at the interface of the C phase are replaced by Cu atoms in the E phase. Moreover, the atoms within the core, denoted by (2), which in the C phase are Cu atoms, are replaced by Al atoms in the E phase. Some of the atoms are in addition shifted slightly in the E phase compared to the atoms' position in the C phase.

DFT calculations based on three different models of the E phase were employed. The first supercell, based on the experimental findings in this work has $Al_{38}Mg_6Si_2Cu_4$ composition and is shown in Fig. 8b. Based on the fact that the precipitate also has been reported in alloys without Cu, a Cu-free variant where the Cu atoms (denoted (1)) in Fig. 8b) at the interface were replaced by Si atoms, was also utilised. This variant has the composition $Al_{38}Mg_6Si_6$. Due to the observation of the similarities between the core of the E phase with the core of the C phase, a variant where the interfacial Cu atoms denoted (1) in Fig. 8b were replaced by Si atoms and the Al atoms denoted (2) in Fig. 8b were replaced by Cu atoms was also modelled. The latter has composition $Al_{36}Mg_6Si_6Cu_2$.

The results from the DFT calculations are shown in Table 3. According to the calculations, the model based on the experimental

Table 2
The atomic models for the C phase and the E phase. The space group of both phases is the monoclinic $P2_1$ (no. 4). The model for the C phase is derived from Ref. [10], while the model for the E phase is based on the DFT model exhibiting the lowest formation enthalpy (see Table 3).

C phase				E phase[1]		
$a_C = 10.32$ Å, $b_C = 4.05$ Å, $c_C = 8.10$ Å $\alpha_C = 90°$, $\beta_C = 100.9°$, $\gamma_C = 90°$				$a_E = 24.43$ Å, $b_E = 3.98$ Å, $c_E = 8.59$ Å $\alpha_E = 90°$, $\beta_E = 90°$, $\gamma_E = 90°$		
Atom	**x**	**y**	**z**	**x**	**y**	**z**
Al	–	–	–	0.148	0.250	0.085
Al	–	–	–	0.148	0.250	0.416
Al	–	–	–	0.147	0.250	0.750
Al	–	–	–	0.791	0.250	0.750
Al	–	–	–	0.793	0.250	0.418
Al	–	–	–	0.793	0.250	0.082
Al	–	–	–	0.266	0.250	0.085
Al	–	–	–	0.266	0.250	0.416
Al	–	–	–	0.263	0.250	0.750
Al	–	–	–	0.675	0.250	0.410
Al	–	–	–	0.675	0.250	0.089
Al	–	–	–	0.386	0.250	0.750
Al	–	–	–	0.443	0.250	0.250
Al	–	–	–	0.030	0.250	0.085
Al	–	–	–	0.030	0.250	0.416
Al	–	–	–	0.029	0.250	0.750
Al	–	–	–	0.089	0.750	0.583
Al	–	–	–	0.970	0.750	0.915
Al	–	–	–	0.970	0.750	0.584
Al	–	–	–	0.971	0.750	0.250
Al	–	–	–	0.911	0.250	0.750
Al	–	–	–	0.911	0.250	0.417
Al	0.680	0.500	0.810	0.911	0.250	0.082
Si	0.500	0.500	0.250	0.491	0.250	0.750
Si	0.830	0.500	0.080	–	–	–
Si	0.830	0.500	0.580	–	–	–
Mg	0.610	0.000	0.030	0.656	0.250	0.750
Mg	0.610	0.000	0.530	0.553	0.250	0.470
Mg	0.940	0.000	0.360	0.553	0.250	0.030
Mg	0.940	0.000	0.860	–	–	–
Cu	0.680	0.500	0.310	0.370	0.250	0.043
Cu	–	–	–	0.370	0.250	0.458

[1] The angles of the E phase is based on the DFT supercell. The unit cells angles may be approximately 90 degrees, but the atoms order in a $P2_1$ symmetry and no orthorombic space group was found for the precipitate phase.

observations, $Al_{38}Mg_6Si_2Cu_4$, is most energetically favourable, indicating that Cu must stabilise the Cu-free variant observed in the work of Teichmann et al. [21]. The refined fractional coordinates of the atomic sites in the energetically favourable model are shown in Table 2.

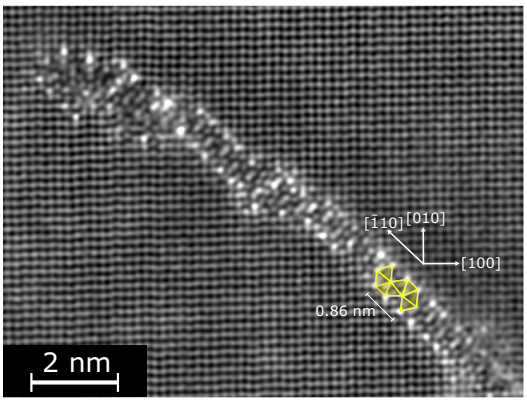

Fig. 7. FFT filtered HAADF-STEM image of one of the precipitate structures found in the pre-deformed samples. Parts of the precipitate contain the previously unsolved E phase. It has habit plane $\{110\}_{Al}$ and was observed to nucleate exclusively in the distorted regions of the Al matrix.

3.5. Phase mapping by SPED

Fig. 9 shows FFT filtered HAADF-STEM images of the main precipitates along with the corresponding FFTs and matched component patterns from the SPED data decomposition. This is the key information on which the phase decomposition and precipitate statistics extracted from the large SPED scans is based on. As indicated by the red, solid lines that connect the Cu atoms, the L phase in (a) contains a local C atomic configuration. Two orientations of the C phase are shown in (b) and (c) and their characteristic periodicity is highlighted. In (d), a segment of the E phase is shown. The Si-network is indicated by yellow lines in both the FFT patterns and identified component patterns. In the case of the FFTs and PED patterns, only spots corresponding to the 5 nm^{-1} spatial frequencies are connected by the yellow lines. Part of the Si-network is indicated in the images of the disordered L phase (a) and the E phase (d). As discussed earlier, a large part of the Si positions in the E phase is occupied by Cu. The structures presented in the figure are the ones exhibiting well-defined FFTs so that it is possible to identify the corresponding component patterns. Component patterns that did not correspond to any of the main phases were categorised as ' disordered', based on the HAADF-STEM images. Most of the precipitates categorised as disordered contained the Si-network.

Fig. 10 shows the results from the phase identification based on the SPED data for (a) NA20ha and (b) NA20hb. The VDF images are shown for both samples and the red rectangle indicates an area which is enlarged in the remaining images. All the bright spots and streaks correspond to precipitates. The HAADF-STEM investigation

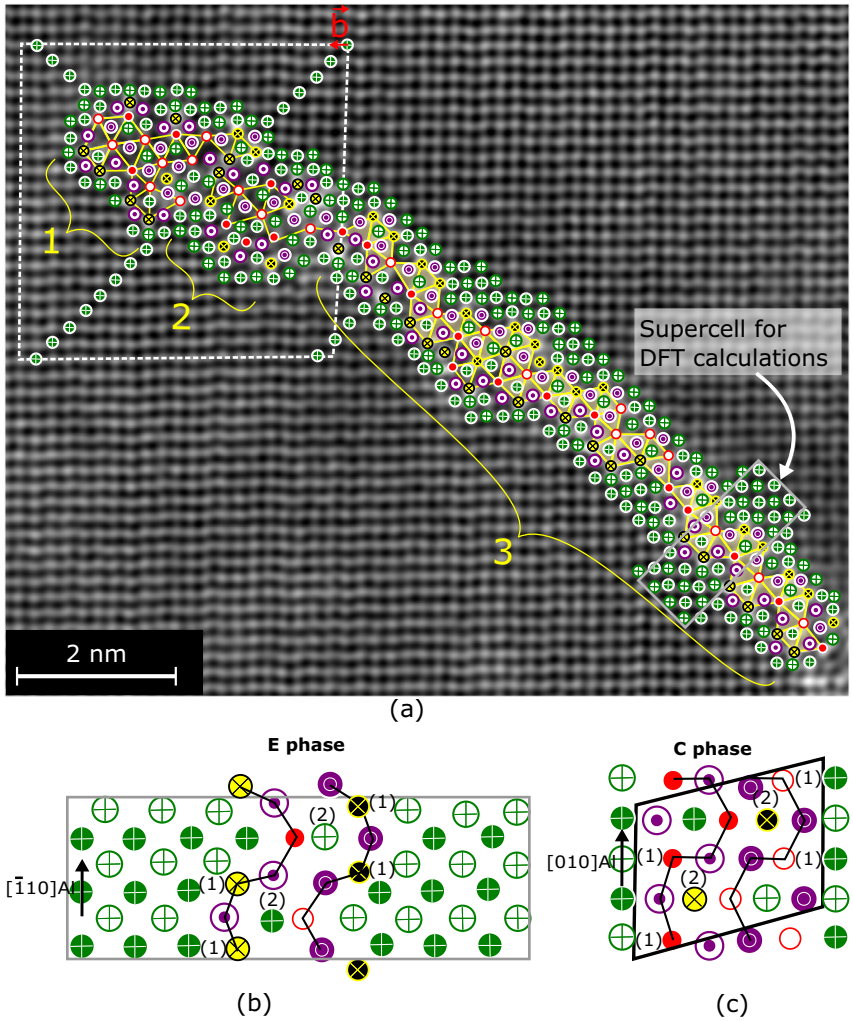

Fig. 8. (a) HAADF-STEM image with atomic overlay of the precipitate in Fig. 7. The legend is shown in Fig. 5. The Si-network is fragmented in three parts, as indicated by the numbers. The $\vec{b}$ indicates the presence of a Burger's vector. In (b), the supercell used for DFT calculations is shown. The black lines enclose the core of the E phase. In (c), the atomic model of the C phase based on the fractional coordinates in Table 3.1 is shown. The black parallelogram and black lines indicate the unit cell and the core of the C phase, respectively. The core of the E phase is derived from the core of the C phase rotated 45° from ⟨100⟩ to ⟨110⟩, with Si (1) atomic columns in C being occupied by Cu in E, and the Cu (2) columns in C being occupied by Al in E.

revealed that the precipitates nucleated independently of the dislocation networks were in the range of 2 nm to 6 nm in the main cross-sectional direction. Therefore, all the dots in the VDF images are assumed to correspond to precipitates nucleated homogeneously in the undistorted regions, while the more elongated spots and streaks in the VDF images are assumed to be associated with precipitates nucleated in distorted regions of the Al matrix. The images labelled 'L', 'C', 'E' and 'Disordered' correspond to the sum of the loading

Table 3
Results from DFT calculations on the E phase with three different structure models. The one with the lowest formation enthalpy, $Al_{38}Mg_6Si_2Cu_4$, corresponds to the experimentally observed phase in the present work.

Refined model	Formation enthalpy per atom (eV/atom)	Formation enthalpy/ volume (eV/Å^3)	Refined cell parameters (Å)			Core composition			
			a	*b*	*c*	Al	Mg	Si	Cu
$Al_{38}Mg_6Si_6$	−0.0567	−0.0033	24.400	3.987	8.753	2	6	6	–
$Al_{36}Mg_6Si_6Cu_2$	−0.0671	−0.0040	24.088	4.015	8.636	–	6	6	2
$Al_{38}Mg_6Si_2Cu_4$	−0.0701	−0.0042	24.426	3.980	8.590	2	6	2	4

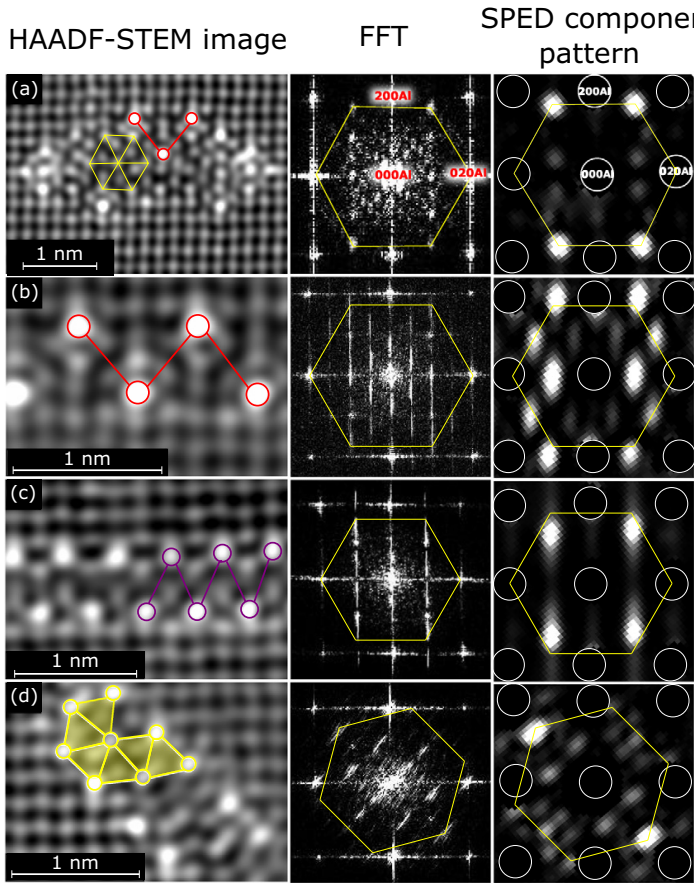

Fig. 9. FFT filtered HAADF-STEM images of the main precipitates types in the pre-deformed samples, the corresponding FFT and component patterns from the SPED data decomposition. The yellow lines indicate the Si-network. In (a), an example of the L phase is shown. The red lines indicate a local arrangement of C in the precipitate. (b) shows a segment of a C phase viewed along $[010]_C$ and the red lines connect Cu atomic columns indicating the 0.81 nm periodicity along $[001]_C$. In (c), a segment of a C phase viewed along $[001]_C$ is shown. The purple lines connect Cu-containing atomic columns, indicating the 0.41 nm periodicity along $[010]_C$. A segment of the E phase is displayed in (d). The component patterns are adjusted for brightness.

maps of the components associated with these phases. As mentioned earlier, some L type precipitates were also nucleated in the distorted regions of the Al matrix. These phases were categorised as disordered, in order to distinguish between heterogeneously and homogeneously nucleated L precipitates.

Note that even though some of the precipitates in the loading maps of the E and the C phase are dot-like, they may still be nucleated in the distorted regions of the Al matrix. As an example, consider the wall-like precipitate of Fig. 6a–c. Short segments of the E phase exist in this structure which will appear as dots in the loading maps. The images labelled ‘ Sum’ correspond to the sum of all loading maps used in the phase identification. By comparing the sum with the corresponding area in the VDF image, it is verified that most the precipitates viewed in the cross-sectional direction are included in the decomposition. The precipitates categorised as disordered in NA20ha are mostly found to be elongated. Based on this, it is believed that this category of precipitates is dominated by the ‘ string-like’ precipitates of Fig. 6d or larger L phases nucleated in distorted regions of the Al matrix. For NA20hb however, the disordered category mostly consists of more ‘ dot-like’ features and it is believed that this category is dominated by precipitates nucleated in the undistorted regions, like the S phase shown in Fig. 6g or the L phase (Fig. 6f).

It should be noted that although SPED has proven to be a powerful technique in visualising precipitates in heavily pre-deformed Al-alloys, the technique is currently limited by the detection system. This is especially true when studying samples with extremely small precipitates with the same habit planes and similar PED patterns, which results in a low signal-to-noise ratio limiting the NMF decomposition. As an example, consider Fig. 9, here the component of the L phase in (a) and the component of the C phase in (b) show some similar features. Due to the low signal-to-noise ratio, the NMF decomposition sometimes produced component patterns consisting of both the L phase and the C phase. This was partly overcome by reducing the number of NMF components so that the output components consisted of either dot-like features or more elongated features without any precipitate vanishing when comparing the sum of all components with the VDF. The HAADF-STEM images showed that the L phase often consisted of small segments of the C phase, which is causing some of the intensity spots in the loading maps of L to also be present in the loading maps of C.

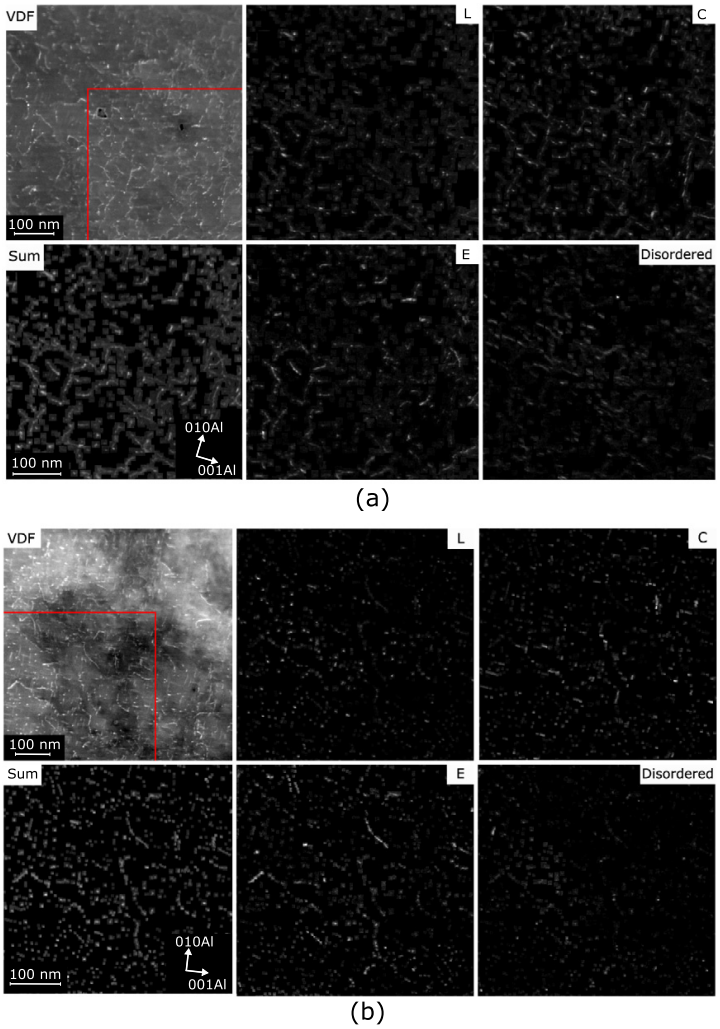

Fig. 10. SPED results including VDF images, loading maps for L, C, E and the disordered category, in addition to the sum of all loading maps used for the phase identification for (a) NA20ha and (b) NA20hb. The red rectangles indicate areas which are enlarged in the loading maps.

3.6. Precipitate fractions

In addition to visualisation of the precipitate distribution, the obtained PED stack was used to approximate the precipitate phase fractions for the two pre-deformed conditions. The estimation of these fractions was based on the approach described in Ref. [26]. The main assumption in this approximation is that the pixel (and hence area) fraction obtained for the different identified phases is similar to the volume fraction of the phases, i.e. $P_f \approx A_f \approx V_f$, where P_f, A_f and V_f denote the pixel-, area- and volume fractions, respectively. This approximation is only valid if the lengths of the different phases observed are nearly equal.

The estimated precipitate phase fractions are shown in the bar chart in Fig. 11. The results indicate that when deforming before NA, the ratio of nucleated L over C+E is larger than when deforming after NA. Based on the previous discussions, this suggests that by deforming after NA (NA20ha), the nucleation of precipitates is more heterogeneous compared to when deformation is conducted prior to NA (NA20hb).

Note that there is an uncertainty associated with the ratios presented in Fig. 11. Different masks in both reciprocal space and real space were tested, and the number of NMF components were varied to see how these factors altered the final precipitate phase fractions. The result showed that the relative ratios of the precipitate phase fractions varied with ±10%, but the conclusion remained unchanged: In NA20ha, the heterogeneous nucleation of precipitates dominated over the homogeneous nucleation of precipitates, and opposite for NA20hb. This conclusion was also supported by the HAADF-STEM images, which showed a larger number ratio of L over C+E in NA20hb than in NA20ha.

3.7. Evaluation of the effect of NA and pre-deformation

It was shown that the sample NA20hn had a precipitate distribution consisting of two main precipitate types: L phases and structural units of GPB-zones. Moreover, it was shown that the introduction of dislocations through cold rolling either before- or after NA caused additional precipitate-types to nucleate in the distorted regions of

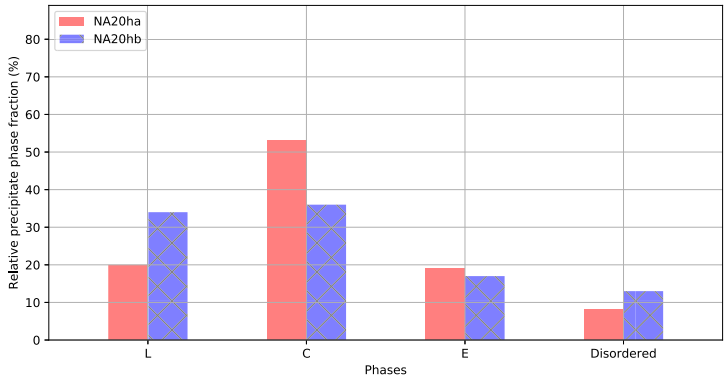

Fig. 11. Bar chart showing the results from the phase quantification by SPED.

the Al matrix. The relative fraction of precipitates nucleated in distorted regions and in undistorted regions were found to be different in the two pre-deformed samples NA20ha and NA20hb. The proposed evolution for NA20ha and NA20hb from SHT throughout the AA treatment is shown in Fig. 12. The schematic is based on the known detrimental effect of NA on the subsequent formation of precipitates during AA, and on the ability of dislocations to provide fast diffusion paths for vacancies and solute segregation leading to preferential precipitation during ageing. Note that the figure's key concepts are exaggerated for clarity and that we assume that the solute uptake in the precipitates are similar for the two conditions.

NA20ha is kept at RT immediately after SHT. The RT storage causes NA clusters to form by the diffusion of solutes using quenched-in vacancies. During the subsequent deformation, the introduced dislocations and NA clusters will interact. It is proposed that some of the NA clusters will dissolve, re-introducing solutes [39,40]. Immediately before the AA treatment, the microstructure therefore consists of NA clusters, solutes and dislocations. During the subsequent AA treatment, the clusters will delay the precipitation in the undistorted regions of the Al matrix, while the solutes will either migrate to the dislocation lines, nucleating heterogeneously as E, C or disordered structures in the distorted regions,

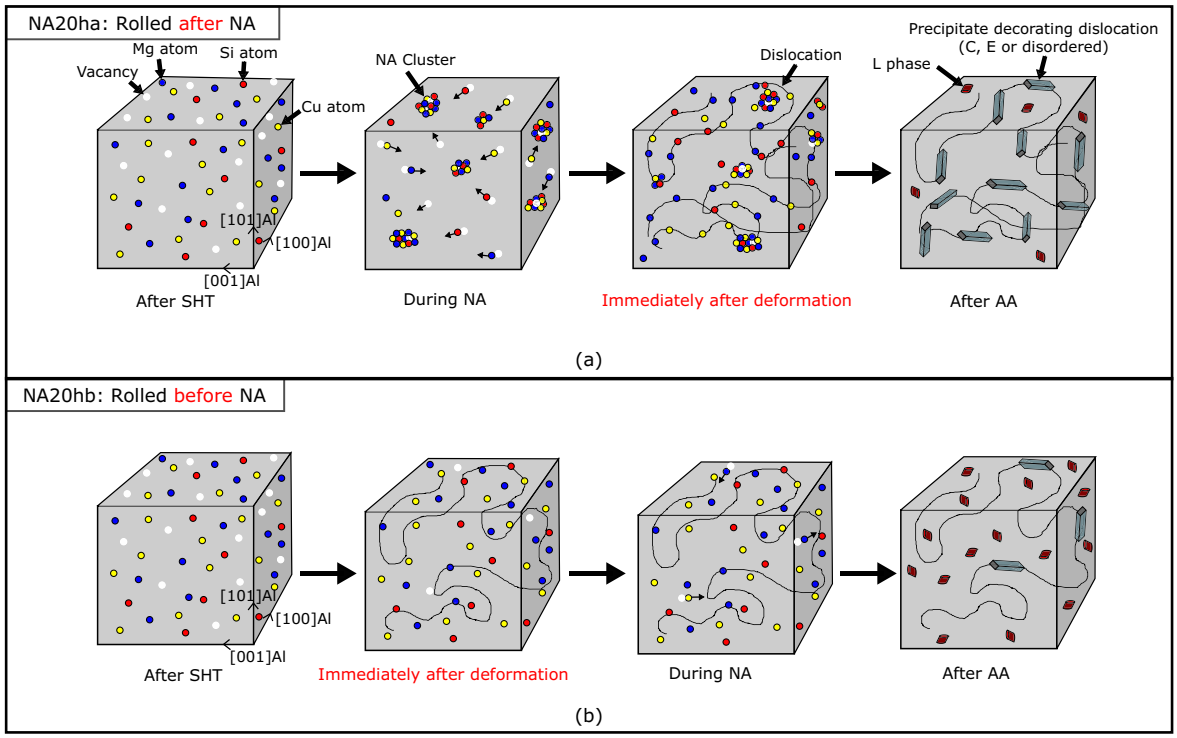

Fig. 12. The suggested microstructure evolution for (a) NA20ha and (b) NA20hb after solution heat treatment.

or nucleate homogeneously as the L phase in the undistorted areas.

NA20hb is deformed prior to NA. In this case, the dislocations are introduced into an environment consisting of a SSSS. During the deformation, a significant proportion of the vacancies will migrate to the dislocations and annihilate. The reduced concentration of vacancies reduces the diffusion of solutes during the subsequent room temperature storage, retaining a solid solution in the undistorted regions of the Al matrix and basically slowing down cluster formation as evidenced by the lower hardness increase during NA in this case, see Fig. 2d. This is believed to be causing the difference in the relative fraction of heterogeneous and homogeneous nucleation in the two samples: The density of NA clusters is lower in NA20hb than NA20ha during the initial stages of the AA treatment. In general, NA clusters forming in alloys with high solute content are associated with delaying the precipitation of hardening phases [41,42] and therefore the lower density of such clusters in NA20hb is causing the relative fraction of homogeneous precipitation to heterogeneous precipitation to be higher than in NA20ha.

It is interesting to note that no β'' precipitates are found in the three conditions investigated in the present work. Since the undeformed sample was found to contain mostly L phases and structural units of GPB-zones, it is believed that the high Cu-content is the reason for this. In a previous work, Marioara et al. [6] demonstrated that for Al-Mg-Si(-Cu) alloys, the L phase is associated with high thermal stability. This is confirmed in the present study, since the hardness of NA20hb, which contains a higher volume fraction of the L phase relative to C and E, decreases slower than the hardness of NA20ha during over-ageing, as seen in the HV-curve in Fig. 2b.

Moreover, it was found that the relative ratio of homogeneously nucleated precipitates to the heterogeneously nucleated precipitates was higher in the softest sample (NA20hb). In undeformed heat-treatable Al alloys, high hardness is associated with a homogeneous distribution of hardening phases. For pre-deformed samples, one has three main contributions to the hardness: both the homogeneously and the heterogeneously nucleated precipitates, in addition to the dislocation density. This work has shown that during a 10 h AA treatment, the NA20hb condition which contained the highest ratio of the hardening L phase to the coarser E- and C-phase after 3 h, was the softest, see Fig. 2b. Thus, precipitate hardening attributed to nucleation of the L phase is not the main hardening mechanism in the heavily pre-deformed samples. It was however shown that during the first three hours of the AA treatment, the hardness increase was most pronounced in NA20hb, see Fig. 2c–d. This is attributed to the higher ratio of the L phase to the coarser phases in this condition. It was also showed that the higher hardness of NA20ha was due to a higher hardness response both during NA and the cold deformation, see Fig. 2c–d. It is believed that the NA clusters present in NA20ha during the deformation is impeding dynamic recovery, making the hardness contribution from the cold working more pronounced in this sample than in NA20hb where the dislocations are introduced into an environment of solid solution.

4. Conclusions

The effect of 80% pre-deformation of an Al-Mg-Si-Cu alloy with high Cu content, applied either before or after a NA treatment for 20 h has been investigated in terms of hardness evolution and precipitate microstructure.

- It was demonstrated that HAADF-STEM in combination with SPED is a powerful tool to investigate precipitation in heavily deformed age-hardening materials.
- For the undeformed condition, two main precipitate types were identified: The L phase and structural units of GPB-zones.
- Three main precipitate types were identified in the deformed conditions, namely L, C and a new precipitate type, called 'E'. The L phase was observed to nucleate both as discrete precipitates on dislocation lines and in undistorted regions away from the dislocation network. C and E were only found at dislocations. C and L have $\{100\}_{Al}$ habit planes.
- The E phase is ordered and has $\{110\}_{Al}$ habit planes. A crystal structure for this phase was proposed here. This structure may be important for the material properties of pre-deformed Al-Mg-Si(-Cu) alloys.
- Deformation after NA enhances heterogeneous precipitation of C and E phases in distorted regions of the Al matrix. On the contrary, deformation applied before NA enhances precipitation of L phase in the undistorted regions. This condition has lower strength due to lower hardness response during NA and cold rolling, but better thermal stability attributed to the higher volume fraction of L phases.

CRediT authorship contribution statement

Elisabeth Thronsen: Conceptualization, Investigation, Data curation, Writing - original draft, Visualization. **Calin D. Marioara:** Conceptualization, Investigation, Writing - review & editing. **Jonas K. Sunde:** Software, Investigation, Writing - review & editing. **Kazuhiro Minakuchi:** Resources, Writing - review & editing, Supervision. **Tetsuya Katsumi:** Resources, Writing - review & editing, Supervision. **Iven Erga:** Investigation, Data curation. **Sigmund J. Andersen:** Formal analysis, Writing - review & editing. **Jesper Friis:** Investigation, Writing - review & editing. **Knut Marthinsen:** Supervision, Writing - review & editing. **Kenji Matsuda:** Resources, Supervision. **Randi Holmestad:** Supervision, Writing - review & editing.

Acknowledgments

The authors would like to acknowledge the Norwegian transmission electron microscopy infrastructure NORTEM (197405). The authors also acknowledge the INTPART project "Norwegian-Japanese Aluminium Alloy Research and Education Collaboration" (249698) funded by the Norwegian Research Council for establishing the collaborations to write this article.

Data availability

The raw/processed data required to reproduce these findings cannot be shared at this time as the data also forms part of an ongoing study.

References

[1] F.J. Humphreys, M. Hatherly, Control of recrystallization, Recrystallization and Related Annealing Phenomena, Elsevier, Oxford, 2004, pp. 469–476. https://doi.org/10.1016/B978-008044164-1/50019-0.
[2] L. Lodgaard, N. Ryum, Precipitation of dispersoids containing Mn and/or Cr in Al-Mg-Si alloys, Mater. Sci. Eng. A 283 (2000) 144–152. https://doi.org/10.1016/S0921-5093(00)00734-6.
[3] C.D. Marioara, S.J. Andersen, H.W. Zandbergen, R. Holmestad, The influence of alloy composition on precipitates of the Al-Mg-Si system, Met. Mater. Trans. A 36A (2005) 691–702. https://doi.org/10.1007/s11661-005-0185-1.
[4] C.D. Marioara, S.J. Andersen, T.N. Stene, H. Hasting, J. Walmsley, A.T.J.V. Helvoort, R. Holmestad, The effect of Cu on precipitation in Al-Mg-Si alloys, Philos. Mag. 87 (2007) 3385–3413. https://doi.org/10.1080/14786430701287377.
[5] H.S. Hasting, A.G. Frøseth, S.J. Andersen, R. Vissers, J.C. Walmsley, C.D. Marioara, F. Danoix, W. Lefebvre, R. Holmestad, Composition of β'' precipitates in Al-Mg-Si alloys by atom probe tomography and first principles calculations, J. Appl. Phys. 106 (123527). (2009) https://doi.org/10.1063/1.3269714.
[6] C.D. Marioara, S.J. Andersen, J. Røyset, O. Reiso, S. Gulbrandsen-Dahl, T. Nicolaisen, I. Opheim, J.F. Helgaker, R. Holmestad, Improving thermal stability in Cu-containing Al-Mg-Si alloys by precipitate optimization, Metall. Mater. Trans. A 45 (2014) 2938–2949. https://doi.org/10.1007/s11661-014-2250-0.

[7] C. Cayron, L. Sagalowicz, O. Beffort, P.A. Buffat, Structural phase transition in Al-Cu-Mg-Si alloys by transmission electron microscopy study on an Al-4 wt% Cu-1 wt% Mg-Ag alloy reinforced by SiC particles, Philos. Mag. A 79 (1999) 2833–2851. https://doi.org/10.1080/01418619908212027.

[8] S.J. Andersen, C.D. Marioara, R. Vissers, A. FrÃŷseth, H.W. Zandbergen, The structural relation between precipitates in Al-Mg-Si alloys, the Al-matrix and diamond silicon, with emphasis on the trigonal phase U1-MgAl2Si2, Mater. Sci. Eng., A 444 (2007) 157–169. https://doi.org/10.1016/j.msea.2006.08.084.

[9] T. Saito, E.A. Mørtsell, S. Wenner, C.D. Marioara, S.J. Andersen, J. Friis, K. Matsuda, R. Holmestad, Atomic structures of precipitates in Al-Mg-Si alloys with small additions of other elements, Adv. Eng. Mater. 20 (1800125). (2018) https://doi.org/10.1002/adem.201800125.

[10] M. Torsæter, F.J.H. Ehlers, C.D. Marioara, S.J. Andersen, R. Holmestad, Applying precipitate-host lattice coherency for compositional determination of precipitates in Al-Mg-Si-Cu alloys, Philos. Mag. 92 (2012) 3833–3856. https://doi.org/10.1080/14786435.2012.693214.

[11] C.D. Marioara, J. Nakamura, K. Matsuda, S.J. Andersen, R. Holmestad, T. Sato, T. Kawabata, S. Ikeno, HAADF-STEM study of β'-type precipitates in an over-aged Al-Mg-Si-Ag alloy, Philos. Mag. 92 (2012) 1149–1158. https://doi.org/10.1080/14786435.2011.642319.

[12] T. Saito, C.D. Marioara, S.J. Andersen, W. Lefebvre, R. Holmestad, Aberration-corrected HAADF-STEM investigations of precipitate structures in Al-Mg-Si alloys with low Cu additions, Philos. Mag. 94 (2014) 520–531. https://doi.org/10.1080/14786435.2013.857051.

[13] C.D. Marioara, A. Lervik, J. GrÃŷnvold, O. Lunder, S. Wenner, T. Furu, R. Holmestad, The correlation between intergranular corrosion resistance and copper content in the precipitate microstructure in an AA6005A alloy, Metall. Mater. Trans. A 49 (2018) 5146–5156. https://doi.org/10.1007/s11661-018-4789-7.

[14] S.J. Andersen, C.D. Marioara, J. Friis, R. Bjørge, Q. Du, I.G. Ringdalen, S. Wenner, E.A. Mørtsell, R. Holmestad, T. Saito, J. Røyset, O. Reiso, Directionality and column arrangement principles of precipitates in Al-Mg-Si-(Cu) and Al-Mg-Cu linked to line defect in Al, The 15th International Conference on Aluminium Alloys, Materials Science Forum, 877, Trans Tech Publications. 2017, pp. 461–470. https://doi.org/10.4028/www.scientific.net/MSF.877.461.

[15] A. Poznak, V. Thole, P. Sanders, The natural aging effect on hardenability in Al-Mg-Si: a complex interaction between composition and heat treatment parameters, Metals 8 (309). (2018) https://doi.org/10.3390/met8050309.

[16] S. Pogatscher, H. Antrekowitsch, T. Ebner, P.J. Uggowitzer, The Role of Co-Clusters in the Artificial Aging of AA6061 and AA6060, Springer International Publishing, Cham, 2016, 415–420. https://doi.org/10.1007/978-3-319-48179-1_70.

[17] M.W. Zandbergen, A. Cerezo, G.D.W. Smith, Study of precipitation in Al-Mg-Si alloys by atom probe tomography II. Influence of Cu additions, Acta Mater. 101 (2015) 149–158. https://doi.org/10.1016/j.actamat.2015.08.018.

[18] M. Werinos, H. Antrekowitsch, T. Ebner, R. Prillhofer, W.A. Curtin, P.J. Uggowitzer, S. Pogatscher, Design strategy for controlled natural aging in Al-Mg-Si alloys, Acta Mater. 118 (2016) 296–305. https://doi.org/10.1016/j.actamat.2016.07.048.

[19] K. Matsuda, S. Shimizu, H. Gamada, Y. Uetani, F. Shinagawa, S. Ikeno, Effect of deformation on the precipitates in Al-Mg_2Si alloys containing silicon in excess, J. Soc. Mater. Sci. Japan 48 (1999) 385–390. https://doi.org/10.2472/jsms.48.10.

[20] K. Matsuda, H. Gamada, Y. Uetani, S. Rengakuji, F. Shinagawa, S. Ikeno, Specific precipitates in Al-Mg_2Si alloys aged after deformation, J. Jpn. Inst. Met. 48 (1998) 471–475. https://doi.org/10.2464/jilm.48.471.

[21] K. Teichmann, C.D. Marioara, S.J. Andersen, K.O. Pedersen, S. Gulbrandsen-Dahl, M. Kolar, R. Holmestad, K. Marthinsen, HRTEM study of the effect of deformation on the early precipitation behaviour in an AA6060 Al-Mg-Si alloy, Philos. Mag. 91 (2011) 3744–3754. https://doi.org/10.1080/14786435.2011.593577.

[22] K. Teichmann, C.D. Marioara, S.J. Andersen, K. Marthinsen, The effect of preaging deformation on the precipitation behavior of an Al-Mg-Si alloy, Metall. Mater. Trans. A 43 (2012) 4006–4014. https://doi.org/10.1007/s11661-012-1235-0.

[23] S. Jin, T. Ngai, L. Li, S. Jia, T. Zhai, D. Ke, Aging response and precipitation behavior after 5% pre-deformation of an Al-Mg-Si-Cu alloy, Materials 11 (1422). (2018) https://doi.org/10.3390/ma11081422.

[24] D. Yin, Q. Xiao, Y. Chen, H. Liu, D. Yi, B. Wang, S. Pan, Effect of natural ageing and pre-straining on the hardening behaviour and microstructural response during artificial ageing of an Al-Mg-Si-Cu alloy, Mater. Des. 95 (2016) 329–339. https://doi.org/10.1016/j.matdes.2016.01.119.

[25] J.K. Sunde, Ø. Paulsen, S. Wenner, R. Holmestad, Precipitate statistics in an Al-Mg-Si-Cu alloy from scanning precession electron diffraction data, J. Phys. Conf. Ser. 902 (012022). (2017) https://doi.org/10.1088/1742-6596/902/1/012022.

[26] J.K. Sunde, C.D. Marioara, A.T.J. van Helvoort, R. Holmestad, The evolution of precipitate crystal structures in an Al-Mg-Si(-Cu) alloy studied by a combined HAADF-STEM and SPED approach, Mater. Charact. 142 (2018) 458–469. https://doi.org/10.1016/j.matchar.2018.05.031.

[27] J.S. Barnard, D.N. Johnstone, P.A. Midgley, High-resolution scanning precession electron diffraction: alignment and spatial resolution, Ultramicroscopy 1 (2017) 79–88. https://doi.org/10.1016/j.ultramic.2016.12.018.

[28] G. Kresse, J. Hafner, Ab initio molecular dynamics for liquid metals, Phys. Rev. B 47 (1993) 558–561. https://doi.org/10.1016/0022-3093(95)00355-X.

[29] G. Kresse, J. Furthmüller, Efficiency of ab-initio total energy calculations for metals and semiconductors using a plane-wave basis set, Comput. Mater. Sci. 6 (1996) 15–50. https://doi.org/10.1016/0927-0256(96)00008-0.

[30] J.P. Perdew, K. Burke, M. Ernzerhof, Generalized gradient approximation made simple, Phys. Rev. Lett. 77 (1996) 3865–3868. https://doi.org/10.1103/PhysRevLett.77.3865.

[31] C.D. Marioara, W. Lefebvre, S.J. Andersen, J. Friis, Atomic structure of hardening precipitates in an Al-Mg-Zn-Cu alloy determined by HAADF-STEM and first-principles calculations: relation to $\eta - MgZn_2$, J. Mater. Sci. 48 (3638). (2013) https://doi.org/10.1007/s10853-013-7158-3.

[32] F. de La Peña, V.T. Fauske, P. Burdet, E. Prestat, P. Jokubauskas, M. Nord, T. Ostasevicius, K.E. MacArthur, M. Sarahan, D.N. Johnstone, J. Taillon, A. Eljarrat, V. Migunov, J. Caron, T. Furnival, S. Mazzucco, T. Aarholt, M. Walls, T. Slater, F. Winkler, B. Martineau, G. Donval, R. McLeod, E.R. Hoglund, I. Alxneit, I. Hjorth, T. Henninen, L.F. Zagonel, A. Garmannslund, A. Skorikov, Hyperspy/Hyperspy V1.4.1, 2018. https://doi.org/10.5281/zenodo.1469364.

[33] A.S. Eggeman, R. Krakow, P.A. Midgley, Scanning precession electron tomography for three-dimensional nanoscale orientation imaging and crystallographic analysis, Nat. Commun. 6 (7267). (2015) https://doi.org/10.1038/ncomms8267.

[34] T. Masuda, Y. Takaki, T. Sakurai, S. Hirosawa, Combined effect of pre-straining and pre-aging on bake-hardening behavior of an Al-0.6 mass%Mg-1.0 mass%Si alloy, Mater. Trans. 51 (2010) 325–332. https://doi.org/10.2320/matertrans.L-M2009831.

[35] Y. Birol, Pre-straining to improve the bake hardening response of a twin-roll cast Al-Mg-Si alloy, Scr. Mater. 52 (2005) 169–173. https://doi.org/10.1016/j.scriptamat.2004.10.001.

[36] L. Kovarik, S.A. Court, H.L. Fraser, M.J. Mills, GPB zones and composite GPB/GPBII zones in Al-Cu-Mg alloys, Acta Mater. 56 (2008) 4804–4815. https://doi.org/10.1016/j.actamat.2008.05.042.

[37] M. Mihara, C.D. Marioara, S.J. Andersen, R. Holmestad, E. Kobayashi, T. Sato, Precipitation in an Al-Mg-Cu alloy and the effect of a low amount of Ag, Mater. Sci. Eng. A 658 (2016) 91–98. https://doi.org/10.1016/j.msea.2016.01.087.

[38] T. Saito, S. Muraishi, C.D. Marioara, S.J. Andersen, J. Røyset, R. Holmestad, The effects of low Cu additions and predeformation on the precipitation in a 6060 Al-Mg-Si alloy, Metall. Mater. Trans. A 44 (2013) 4124–4135. https://doi.org/10.1007/s11661-013-1754-3.

[39] Z. Wang, H. Li, F. Miao, B. Fang, R. Song, Z. Zheng, Improving the strength and ductility of Al-Mg-Si-Cu alloys by a novel thermo-mechanical treatment, Mater. Sci. Eng., A 607 (2014) 313–317. https://doi.org/10.1016/j.msea.2014.04.009.

[40] A. Serizawa, T. Sato, W.J. Poole, The characterization of dislocation-nanocluster interactions in Al-Mg-Si(-Cu/Ag) alloys, Philos. Mag. Lett. 90 (2010) 279–287. https://doi.org/10.1080/09500831003633231.

[41] C.D. Marioara, S.J. Andersen, J. Jansen, H.W. Zandbergen, The influence of temperature and storage time at RT on nucleation of the β'' phase in a 6082 Al-Mg-Si alloy, Acta Mater. 51 (2003) 789–796. https://doi.org/10.1016/S1359-6454(02)00470-6.

[42] F.A. Martinsen, F.J.H. Ehlers, M. Torsæter, R. Holmestad, Reversal of the negative natural aging effect in Al-Mg-Si alloys, Acta Mater. 60 (2012) 6091–6101. https://doi.org/10.1016/j.actamat.2012.07.047.

Paper V

The effect of small additions of Fe and heavy deformation on the precipitation in an Al-1.1Mg-0.5Cu-0.3Si at.% alloy

E. Thronsen, H. Mørkeseth, C.D. Marioara, K. Minakuchi, T. Katsumi, K. Marthinsen, K. Matsuda, R. Holmestad

Metallurgical and Materials Transactions A (2022) **In press**

Author contributions

E. Thronsen did the SPED acquisition and data analysis. C. D. Marioara did the STEM experiments. H. Mørkeseth did the SEM and basic TEM experiment. K. Minakuchi, T. Katsumi and K. Matsuda suggested the study and provided the material. E. Thronsen, K. Minakuchi, T. Katsumi, K. Matsuda, R. Holmestad and K. Marthinsen supervised the research. E. Thronsen wrote the manuscript with input from all co-authors.

The effect of small additions of Fe and heavy deformation on the precipitation in an Al-1.1Mg-0.5Cu-0.3Si at.% alloy

Elisabeth Thronsen[a,*], Hanne Mørkeseth[a], Calin D. Marioara[b], Kazuhiro Minakuchi[c], Tetsuya Katsumi[c], Knut Marthinsen[d], Kenji Matsuda[e], Randi Holmestad[a]

[a]*Department of Physics, Norwegian University of Science and Technology (NTNU), Høgskoleringen 5, Trondheim, N-7491, Norway*

[b]*Materials and Nanotechnology Department, SINTEF Industry, Høgskoleringen 5, Trondheim, N-7465, Norway*

[c]*Machinery and Engineering Group, YKK Corporation, 200, Yoshida, Kurobe, Toyama, 938-8601, Japan*

[d]*Department of Materials Science and Engineering, NTNU, Sem Sælands veg 14, Trondheim, N-7491, Norway*

[e]*Graduate School of Science and Engineering for Research, University of Toyama, Toyama, 930-8555, Japan*

**Corresponding author. Elisabeth.thronsen@ntnu.no*

Abstract

The effect of 0.03 and 0.08 at.% Fe additions on the formation of secondary phases in an Al-1.1Mg-0.5Cu-0.3Si at.% alloy was investigated. Following solution heat treatment and natural aging, the alloys were analyzed in an undeformed, artificially aged condition and in a two-step deformed condition consisting of 80% deformation, artificial aging, 50% deformation and a final, short artificial aging. Using electron microscopy, it was found that both alloys contained similar amounts of primary Mg_2Si particles, while the higher Fe level alloy produced roughly twice the number density and volume fraction of primary bcc α-AlFeSi particles. Lower volume fractions of hardening precipitates were measured in the high Fe level alloy, as attributed to the lower amount of Si available for precipitation. Using atomic resolution scanning transmission electron microscopy, a mix of L phases and structural elements of GPB zones was found in the undeformed conditions. In the deformed conditions, scanning precession electron diffraction revealed that the precipitates were nucleated both on and between deformation induced defects. The addition of Fe affected the relative ratio of these precipitates. Hardness measurements of conditions combining deformation and artificial aging were performed to investigate the hardening mechanisms at each processing step.

Keywords: Al-Mg-Si-Cu alloys; transmission electron microscopy; trace elements; heavy deformation; precipitation

1. Introduction

Age hardenable Al-Mg-Si-Cu alloys exhibit a rapid hardening upon artificial aging (AA) at elevated temperatures. The increase in hardness is attributed to the formation of metastable, nano-sized precipitates which are (semi-)coherent with the Al-matrix. The amount and types of precipitates that

form vary with the composition of the alloy and the thermomechanical treatment. The precipitation sequence in Al-Mg-Si-Cu alloys is normally given as [1]:

SSSS → solute clusters → GP zones → β'', L → β'_{Cu}, L, S, C, Q' → Q (Stable).

SSSS is the supersaturated solid solution which forms when the alloy is quenched from a solution heat treatment (SHT) at temperatures above the solvus line (> 500°C). For a thorough review of the different precipitate types and their characteristics, see our previous work [2–4]. All metastable precipitates in the Al-Mg-Si(-Cu) system are needle/rod/lath shaped with main elongation parallel to the <100>Al directions. They are structurally related through a common network of Si atomic columns along the precipitate lengths with a projected near hexagonal symmetry of 0.4 nm spacing [1,5,6]. Different precipitate types can be distinguished by the atoms' position on the Si-network and the orientation of the network relative to the Al matrix. For the L- and C phases, the network is aligned along <100>Al, while for the β'', $\beta'_{Cu,}$ S and Q', the network is aligned with <310>Al, <110>Al and <510>Al [1]. Al and Mg are always positioned in-between the Si-network columns, while Cu can either partly replace the Si columns (as in β'_{Cu}) [7] or be in-between them (as in Q' and C) [2]. Moreover, the crystal structures of these phases are governed by certain construction rules [8], which apply to the metastable precipitates in the Al-Mg-Cu and Al-Mg-Si(-Cu) systems. According to these rules, every Al atom has 12 nearest neighbors, every Mg atom has 15 and every Si or Cu has 9. This allows for atomic overlay of precipitates imaged in cross-section with the atomic-resolution high angle annular dark-field scanning transmission electron microscopy (HAADF-STEM) technique, because in projection every Al atom is surrounded by 4 atoms of opposite height, every Mg by 5 and every Si or Cu by 3.

Since all metastable phases in the precipitation sequence above have Mg/Si ratio ~ 1. For alloys with excess Mg (Mg/Si > 1), the amount of Si in an alloy will be the limiting factor for the precipitation. In addition to participating in precipitation, Si contributes to the formation of primary particles such as Mg_2Si and various AlFeSi intermetallic compounds during solidification of the cast aluminum ingot. To minimize solute segregations, a homogenization treatment is normally performed. During this process, the Mg_2Si particles may dissolve [9]. Fe has an almost negligible solubility in the Al matrix [10] and contributes mainly to the formation of non-soluble AlFeSi(Cu) particles during solidification. Thus, Fe is in general an unwanted element in Al alloys since such particles lower the material's ductility, in addition to lowering the hardening potential of the alloy as it leads to a reduced Si amount available for the formation of Al-Mg-Si(-Cu) hardening metastable phases. The needle- or plate like β-AlFeSi particles formed during solidification have been reported to transform to the more rounded body centered cubic (bcc) or simple cubic (sc) α-AlFeSi particles during homogenisation [11]. The bcc α-AlFeSi has composition close to $Al_{12}Fe_3Si$, while the β-AlFeSi composition is close to Al_5FeSi. The sc α-phase has a composition close to $Al_{13}Fe_3Si_{1.5}$ [12]. Even if Fe is unwanted in the alloy composition, it is usually hard to avoid since each processing step is a potential source for trace elements pick-up, such as Fe. For example, the bauxite itself contains Fe compounds [13]. The increasing trend of using post-consumed Al-scrap also has the consequence of introducing impurity elements, like Fe. Understanding how Fe influences the microstructure and the final properties during different thermomechanical treatments is therefore important for further development of Al alloys in a recycling context.

In our previous work [4], (scanning) transmission electron microscopy (S)TEM and hardness measurements were used to investigate an Al-1.3Cu-1.0Mg-0.4Si wt.% alloy to understand the effect of heavy pre-deformation on the material. We showed that a pre-deformation of 80% changed the precipitate types that formed during a subsequent AA. In the undeformed AA sample, the

microstructure consisted of L phases in addition to structural units of Guinier-Preston-Bagaryatsky (GPB) zones from the Al-Cu-Mg system [14,15]. For the pre-deformed and AA samples, the L phase nucleated in the undistorted regions of the Al-matrix away from dislocations, while the C phase, S' phase and a newly discovered E phase [4] nucleated on deformation induced defects together with more disordered structures. This work is a continuation of the previous study, with two main objectives. First, and most important, is to investigate the effect of small additions of Fe on precipitation in both undeformed and heavily deformed conditions. The second is to investigate the effect on precipitation when additional deformation and artificial ageing steps are introduced, in the sequence SHT -> natural aging (NA) -> first deformation (Def1) –> artificial aging (AA1) –> second deformation (Def2) –> second artificial aging (AA2). This thermomechanical treatment is scientifically interesting due to the presence of precipitates prior to the second deformation process. There are two main types of precipitate-dislocation interactions: shearing and bypassing. Whether the microstructure of the material consists of shearable or non-shearable precipitates strongly affects the final properties. A fine, homogeneous distribution of shearable precipitates is usually associated with peak hardness in age hardened materials, while non-shearable precipitates yield a higher work hardening potential. Precipitate type, size and morphology determine which of the two interactions dominate. Therefore, by investigating the characteristics of precipitates by scanning electron microscopy (SEM) and (S)TEM and the hardness evolution at each thermo-mechanical step, one can identify the processes taking place during the deformation.

2. Experimental procedure

Material and heat treatment

Table 1: Measured composition of the two alloys investigated in the present work in atomic percent. Weight percent is given in parenthesis.

Alloy	Cu	Mg	Si	Fe
Std	0.50 (1.17)	1.08 (0.97)	0.33 (0.34)	0.03 (0.07)
Fe	0.50 (1.17)	1.05 (0.94)	0.32 (0.34)	0.08 (0.16)

Two alloys were investigated in this work, one standard alloy (labelled as 'Std') and one with a small addition of Fe as compared to the standard (labelled as 'Fe'). The measured compositions of the alloys are shown in Table 1.

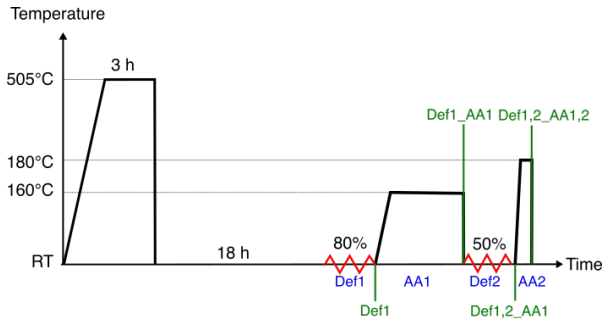

Figure 1: The thermomechanical treatments the alloys were subjected to: Different combinations of Def1, AA1, Def2 and AA2 were executed to study different effects in the alloys. The nomenclature for the different processing routes is highlighted by the green text.

The alloys were cast, homogenized (505°C, 3 h) and extruded to a round profile (Ø 2.85 mm). The profiles were subjected to SHT at 505°C for 3 h and quenched to room temperature before they underwent NA for 18 h. Subsequent to NA, the material underwent deformation Def1 (80% cold rolling) and artificial aging AA1 (160°C, 5 h), deformation Def2 (50% cold rolling) and AA2 (180°C, 10 min). The thermomechanical treatment is indicated in Figure 1. In certain experiments, some of these steps were left out. The nomenclature for the different conditions is: Alloy_Def1,2_AA1,2, where 'Alloy' can be either Std or Fe, indicating the standard- or Fe added alloy, respectively. E.g., Std_Def1,2_AA1,2 is the standard alloy subjected to the full thermomechanical treatment shown in Figure 1. An overview over the different conditions and the techniques used to investigate them is shown in Table 2. Both the Std- and Fe alloy were investigated for all conditions.

Table 2: The different conditions, explanation of their thermomechanical processing route and the techniques they were characterized by.

	Processing route	Hardness	TEM	SEM
AA1	AA1	x	x	x
Def1_AA1	Def1 → AA1	x	x	-
Def1,2_AA1,2	Def1 → AA1 → Def2 → AA2	x	x	-
Def1	Def1	x	-	-
Def1,2	Def1 → Def2	x	-	-
AA1,2	AA1 → AA2	x	-	-
Def1,2_AA1	Def1 → AA1 → Def2	x	-	-
Def1,2_AA2	Def1 → Def2 → AA2	x	-	-

Vickers hardness test

An Innovatest Nova 360 micro-macro Vickers & Brinell hardness tester was used for hardness measurements. The load was 1 kgf and 7 indents were used per condition to get statistically reliable average hardness values.

EM sample preparation

SEM sample preparation

The samples were embedded in epoxy resin and then ground and polished followed by an active oxide polishing to a mirror-like surface. To avoid charging effects in the SEM, the epoxy resin was covered using Al foil and carbon tape.

TEM sample preparation

The samples were first mechanically polished to a thickness of 100 µm using a Struers Rotopol-21 before punched out to Ø3 mm disks. For the undeformed conditions (Alloy_AA1), the disks were punched out along the extrusion direction, while samples for the deformed conditions (Alloy_Def1,2_AA1,2, Alloy_Def1_AA1) were punched out from the surface perpendicular to the rolling- and extrusion direction. The samples were subsequently electropolished using a Struers TenuPol-5 twin-jet with an applied voltage of 20 V. The electrolyte consisted of 1/3 nitric acid and 2/3 methanol and was kept at -25±5°C.

EM studies

SEM studies

Secondary electron (SE)- and backscattered electron (BSE) images and energy dispersive X-ray spectroscopy (EDS) data were acquired using a Zeiss Ultra 55 SEM equipped with an EDS detector from Bruker. The settings used for the different modes in the SEM investigations are shown in Table 3.

Table 3: Settings used for the SEM investigations.

Operation mode	**SE**	**BSE**	**EDS**
Acceleration voltage	20 kV	10-12 kV	10-20 kV
Working distance	10-25 mm	5-15 mm	5-10 mm
Current mode	High current	High current	High current
Aperture diameter	300 µm	120 µm	120/300 µm
Tilting angle	0	0	0

TEM studies

A JEOL 2100 operated at a high voltage of 200 kV equipped with a Gatan GIF 2002 was used to acquire selected area electron diffraction (SAED) patterns, bright-field (BF)- and dark-field (DF) images. The acquisition of HAADF-STEM images was done in a double (image and probe) corrected JEOL ARM200F operated at 200 kV. The following parameters were used to obtain the images: 0.08 nm probe size, a convergence semi-angle of 27 mrad, and inner- and outer collection semi-angles 35 and 150 mrad, respectively. Before imaging precipitates, the specimen was tilted to a [001]Al zone axis. All HAADF-STEM images shown in this paper are filtered using a circular bandpass mask applied on the respective fast Fourier transform (FFT), and an inverse FFT (IFFT) performed on the masked area, suppressing all features with separation shorter than 0.15 nm in real space.

For the scanning precession electron diffraction (SPED) experiments, a JEOL 2100F operated at 200 kV and equipped with a Medipix3 MerlinEM camera with a single 256x256 Si chip from Quantum detectors was used [16]. The instrument was operated in nanobeam electron diffraction mode using a convergence semi-angle of 1 mrad. The probe size was 1 nm, while the precession angle- and frequency was set to 8.7 mrad (=0.5°) and 100 Hz, respectively. The double-rocking probe was aligned according to the approach described by Barnard *et al.* [17] using the NanoMEGAS DigiSTAR control software. Diffraction patterns were recorded in the 12-bit mode of the Medipix3 detector using an exposure time of 40 ms. The step size was set to 1.3 nm and the scans comprised 400x400 pixels^2 (=520x520 nm^2)

EM data analysis

SEM data analysis

EDS data were analyzed with the Quantax Esprit software. Particles were analyzed using SE and BSE images. The image processing software Fiji [18] was utilized to analyze the SE images, while the BSE images were analyzed using a Python script [19]. Particle size, represented by the equivalent circle diameter (ECD), particle density and area fraction were obtained. For each sample, 10-12 images were analyzed, containing approximately 1300 particles.

TEM data analysis

Precipitate quantification

Average precipitate length and cross section were estimated based on BF images of the undeformed samples using the Fiji software. The number density and volume fractions were estimated using the approach given by Andersen [20]. Estimations were based on 15 BF images for each of the undeformed samples (Alloy_AA1) yielding approximately 1500 counted precipitates per sample. The lengths were measured for 200-300 precipitates, while a total of 120 cross sectional areas from each sample were measured. Sample thickness was estimated based on electron energy loss spectroscopy (EELS). By multiplying the number density with the average precipitate length and cross section, the precipitate volume fraction, *VF*, was estimated.

Solute balance calculations

The amount of solute locked up in each particle/precipitate type was calculated in the following way: The number of Al matrix atoms that would fit in the volume of a unit cell of a particle phase, N_{Al} was calculated. The number of solute atoms in one unit cell, N_{sol} is known from the chemical composition of the particle phase. Then, the solute fraction, *SF*, was calculated $SF = VF \cdot \frac{N_{sol}}{N_{Al}}$, where *VF* is the volume fraction of particles. The calculations were based on the compositions and lattice parameters in Table 4. The composition of the L phase is varying, and an average composition was estimated from the HAADF-STEM images. The L phase can be considered a disordered version of the C phase, thus the lattice parameters for C were used to calculate N_{Al} for L.

Table 4: Chemical composition and lattice parameter of the unit cell for the different phases used for estimating the solute balance.

Particle/precipitate	Composition	Unit cell lattice parameters	Reference
α-AlFeSi	$Al_{100}Fe_{24}Si_{14}$	Cubic, a = 1.256 nm	[21]
Mg_2Si	Mg_8Si_4	Cubic, a = 0.635 nm	[22]
L	$Al_{18.8}Si_{28.6}Mg_{36.9}Cu_{15.7}$[1]	Monoclinic, a=1.032 nm, b=0.405 nm, c=0.810 nm, β=100.9°[2]	[2]

Overlay of HAADF-STEM images

Two different approaches were used for the atomic overlay of HAADF-STEM images. Overlay was done based on the construction principles given by Andersen [8] and explained in the Introduction of the current work: A column with nearest neighbors in fourfold-like symmetry was assumed to be Al, in five-fold like symmetry Mg and in threefold-like symmetry Si or Cu. Further, Si and Cu were separated by the intensity: The Z-contrast of Cu (Z_{Cu} = 29) is much higher than that of Si (Z_{Si} = 14). Automatic overlay using the open-source software AutomAl6000 [23], based on the same principles, was used to analyze a large number of images in a shorter time than by manual overlay.

[1] Result from the present work
[2] C lattice parameter

SPED data analysis

The SPED data was processed using the open-source Python packages hyperspy [24], pyxem [25] and scikit-image [26]. To estimate the relative amounts of precipitates nucleated on dislocations to the ones nucleated in bulk the approach was as follows:

i. A virtual aperture was placed in the obtained PED pattern stack and the image intensity within the aperture was integrated. The resulting image is a virtual dark-field (VDF) image.
ii. The VDF images were background subtracted using a rolling ball correction [27], before they were thresholded using the triangle thresholding algorithm [28].
iii. Each connected region in the VDF image was classified as a precipitate and categorized as nucleated on or between dislocations depending on its extent and Feret diameter [29].

To obtain phase maps and estimate the relative fraction of precipitates, a non-negative matrix factorization (NMF) decomposition [30] was applied to the data. The approach is similar to the one presented in [4] and [31] but with some alterations. A short summary is given in the following:

i. Create masks in reciprocal space using blob-detection.
ii. Superimpose the reciprocal space mask on the dataset and do NMF.
iii. Manually label each NMF component into the following categories: C/L, S/E and disordered precipitates.
iv. Based on the VDF image classification of precipitates, separate the L phases in bulk from the C- and L phases on dislocations. Do the same for the disordered precipitates.
v. Calculate the area fraction of each of the five categories; C/L on dislocations, S/E on dislocations, disordered precipitates on dislocations, L in bulk and disordered in bulk, compared to the total area fraction of precipitates.

3. Results and discussions

Quantification of primary particles in the undeformed samples

Figure 2 shows the result from the SEM studies of primary particles in the Std- and Fe alloys in the AA1 condition. From the SEM BSE images in Figure 2a and b, it is clear that two types of primary particles exist in this condition for both alloys. The first type appears dark in the BSE images and has a round morphology. The second type appears bright and is smaller than the dark ones. EDS was done to determine the composition of both types of particles. In Figure 2c, a high magnification BSE image of Std_AA1 is shown. It is obtained normal to the extrusion direction and shows that the bright particles are aligned with the extrusion direction. Corresponding EDS maps for Si, Mg, Cu and Fe are shown in 2d-g, respectively, from the area marked by the white-line rectangle in 2c. One white particle is indicated by the red arrow, and one dark particle by the green arrow. It is evident that the dark particles in the BSE images consist of Mg and Si, while the bright particles consist of Si, Fe and Cu. Based on this, the dark particles were assumed to be Mg_2Si and the bright particles AlFeSi(Cu) intermetallic compounds. EDS analyses of the Mg and Si containing particles showed a varying Mg/Si ratio. In addition, some of the particles contained O. This is suspected to stem from dissolution of the Mg_2Si phase during polishing in water, which was done in preparation for both the SEM and the TEM specimens [32].

To further investigate the AlFeSi(Cu) intermetallic compounds, a total of 85 particles were analyzed. The concentration in atomic percent of Fe versus Si for the particles is shown in Figure 2h. The three dotted lines represent the expected compositions of β-AlFeSi, sc α-AlFeSi and bcc α-AlFeSi. It is noted

that most of the analysed particles with bright contrast from both Std_AA1 and Fe_AA1 are composed of slightly less Si/Fe as compared to the expected lines of bcc α-AlFeSi. As indicated by Figure 2f, this might be explained by some of the Cu substituting Si in the particles. This is not accounted for in our compositional analysis below since it is not clear to which extent this substitution takes place. Cu might also decorate the α-AlFeSi/Al interface, making it challenging to account for this when estimating the composition. The data points aligning along the x-axis in Figure 2h correspond to Mg_2Si particles.

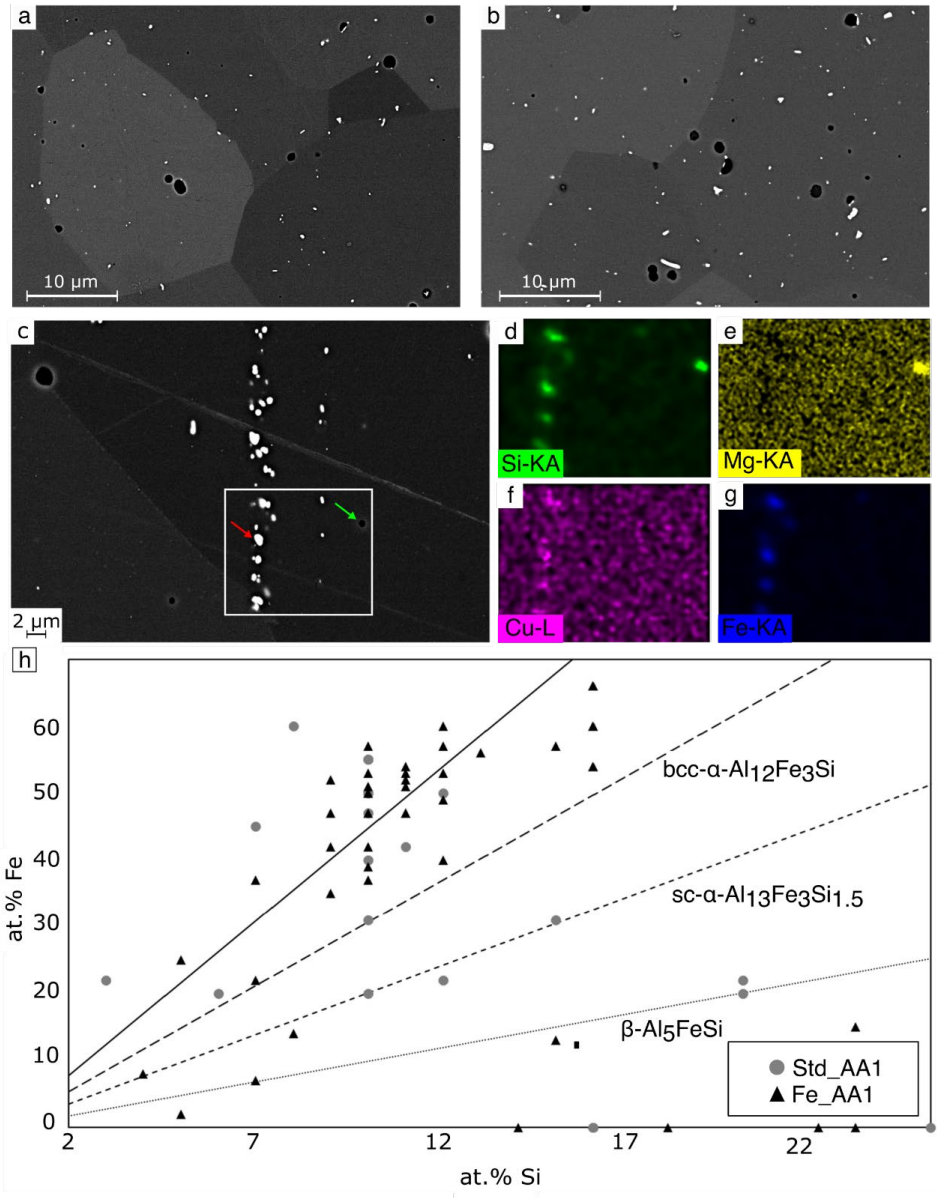

Figure 2: a, b: SEM BSE images showing two types of particles (bright and dark) in Std_AA1 and Fe_AA1, respectively. c: BSE image from Std_AA1 and (d)-(g) corresponding EDS maps from the rectangle in c for Si, Mg, Cu and Fe, respectively. h: Graph showing the concentration of Fe plotted against Si in the particles.

TEM investigations of the AlFeSi(Cu) intermetallic particles by BF imaging and SAED were also conducted to investigate their identity. The results are shown in Figure 3. A BF image of a representative AlFeSi-particle from Std_AA1 is shown in a. Figure 3b-d display SAED patterns from the [103]-, [001]-, and $[\bar{1}11]$ zone axis of AlFeSi(Cu) particles, respectively. The diffraction patterns in b and c are taken from the particle in a, while the one shown in d is from another particle. Based on these, the unit cell is indicated to be bcc with a lattice parameter between 12.57 Å and 12.61 Å, which compare well with the established value of 12.56Å [21] for bcc α-AlFeSi.

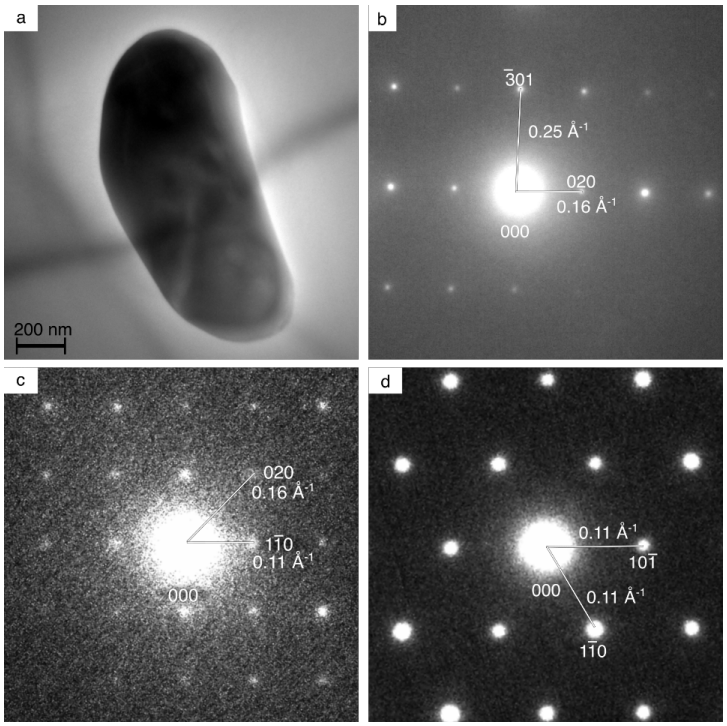

Figure 3: TEM investigations of the AlFeSi(Cu) intermetallic compound found in both Std_AA1 and Fe_AA1. a: A BF image of one representative particle. b-d: SAED patterns from the [103]-, [001]-, *and* $[\bar{1}11]$ *zone axes, respectively. The diffraction patterns in b and c are from the particle in a, while the one shown in d is from another AlFeSi(Cu)-particle. The lattice parameter was estimated to be 12.57 Å, 12.61 Å and 12.57 Å based on the diffraction patterns in b-d, respectively.*

Density, area fraction and size of the primary particles were estimated based on images like the ones in Figure 2a and b. The results are shown in Table 5: Results from SEM image analyses of primary particles. The average is the average of the corresponding quantity based on multiple images. The errors indicate the standard deviation of the estimated quantities between the analyzed images. The particle size of α-AlFeSi is similar in both samples. The Mg_2Si particles are in general larger than the AlFeSi particles. Fe_AA1 contains about twice as many α-AlFeSi particles as Std_AA1, while the amount of Mg_2Si is comparable between the two alloys.

Table 5: Results from SEM image analyses of primary particles. The average is the average of the corresponding quantity based on multiple images. The errors indicate the standard deviation of the estimated quantities between the analyzed images.

Sample	Density (10^3/mm^2)	Area fraction (%)	Mean ECD (nm)
		α-AlFeSi	
Std_AA1	10.0±2.3	0.31±0.05	607±93
Fe_AA1	21±5.8	0.67±0.12	600±95
		Mg_2Si	
Std_AA1	2.6±1.4	0.40±0.15	1515±220
Fe_AA1	3.1±1.1	0.44±0.10	1028±189

Precipitate statistics for the undeformed samples

Two types of hardening precipitates with homogenous distribution were found in the AA1 conditions of both Std- and Fe alloys, as shown in the BF images in Figure 4a and b, respectively. The first precipitate type, indicated by yellow arrows, is lath-like with lath direction along <001>Al and its cross-section elongated along <100>Al. The second type, indicated by red arrows, is much smaller and has a rod morphology. HAADF-STEM images from the Fe_AA1 alloy like the one in Figure 4c revealed that the lath-like precipitates were L phases (exemplified by the yellow rectangle), while the rods were structural units of GPB zones (see for example the precipitate enclosed by the red rectangle). These are the same types of precipitates reported in our previous work on the Std alloy in the undeformed condition [4]. To estimate the amount of Si locked in the precipitates in both samples, the average composition of the L phase was estimated from individual precipitates by overlaying HAADF-STEM images. An example is the L phase enclosed by the yellow rectangle in Figure 4c. It is enlarged and overlaid in d and e, respectively. For this individual precipitate, the composition was estimated to be $Al_{11}Mg_{34}Si_{23}Cu_{13}$. Based on HAADF-STEM images of 28 L precipitates, the average composition was estimated to be $Al_{18.8\pm3.3}Mg_{36.9\pm3.7}Si_{28.6\pm3.3}Cu_{15.7\pm3.8}$. We assume that the composition of the L phase is similar in the undeformed conditions of the Fe and Std alloy since their cross section is similar, see Table 6. The composition of the L phase has a slightly higher Mg/Si ratio than previously reported [33,34], but the higher Mg/Si ratio in the alloys studied in the present work may influence the Mg/Si ratio of the precipitates since the composition of the L phase is known to vary [2]. Even if the L phase is overall disordered, it contains local C phase atomic configurations, indicated by the red lines in Figure 4e. In addition, local symmetries seen in the GPB zones were often found at the ends of the precipitates, indicated by the blue dashed lines in e). The exact same features were found in our previous work on the standard alloy in the undeformed condition [4].

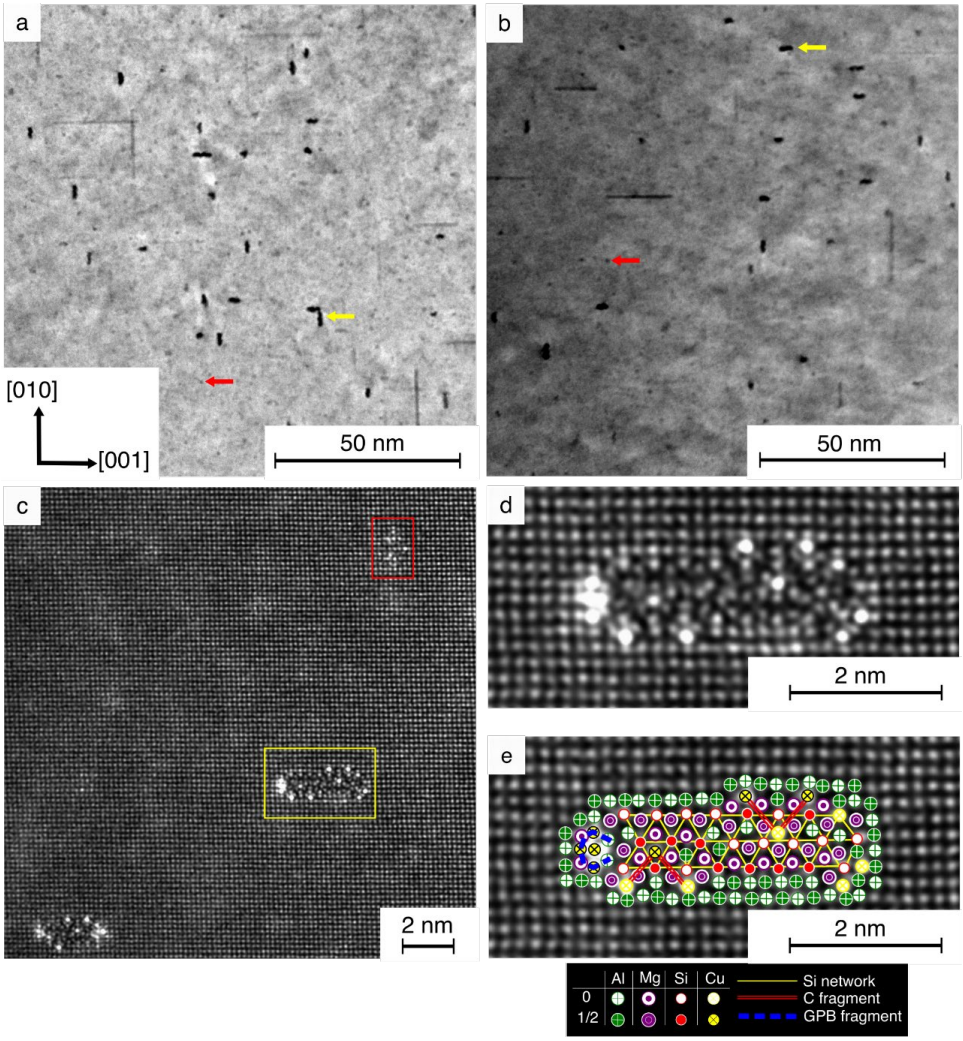

Figure 4: a, b: Overview BF images showing the existence of two precipitate types, indicated by yellow and red arrows in Std_AA1 and Fe_AA1, respectively. c: HAADF-STEM image of Fe_AA1 showing the atomic structure of the precipitates. The yellow rectangle indicates the same precipitate as the yellow arrow in a and b. This precipitate can be categorized as the L phase. The precipitate indicated by the red rectangle in c is the same type as the one indicated by red arrows in a and b. It can be categorized as structural units of GPI zones. . d: Enlarged view of the L phase indicated by the yellow rectangle in c. e: Atomic overlay of the L phase in d.

The average length, cross section, number density and volume fraction of the L phase in Std_AA1 and Fe_AA1 are shown in Table 6. Due to the small size and weak intensity of the GPB zones (not to be confused with the GP zones in the Al-Mg-Si alloy system), these were not included in the precipitate statistics. However, this will not affect the estimation of Si locked up in precipitates, since GPB zones consist of Al, Cu and Mg [14,15]. The cross section of the L phase is similar in the two alloys, Std_AA1 and Fe_AA1. The number density and volume fraction are lowest for Fe_AA1.

Table 6: Precipitate statistics for the L phase in the undeformed samples. For the cross sections, the errors indicate the standard deviation between all individual measurements. The errors for the other values are the standard deviations between the 15 analyzed images.

Sample	Length (nm)	Cross section (nm^2)	Number density (μm^{-3})	Volume fraction (%)
Std_AA1	18.6±1.6	4.8±2.1	78436±12196	0.73±0.13
Fe_AA1	13.4±1.0	5.1±1.8	50802±5555	0.34±0.03

Solute fraction

Based on the statistics from the primary particle- and precipitate analysis presented in Table 5 and Table 6, respectively, and using the parameters listed in Table 4, the solute balance for each of the particle types was estimated, summed and compared to the composition of the alloys. The results are shown in Table 7. As discussed in the Introduction, the Si distribution is very important for the final microstructure of alloys with excess Mg.

Table 7: Solute balance showing the distribution of solute between primary particles, L phase and Al matrix. All values are given in at.%.

Sample	Solute	α-AlFeSi(Cu)	Mg_2Si	L phase	Sum	Alloy composition
Std_AA1	Si	0.04	0.10	0.21	0.35	0.33
	Mg	-	0.21	0.27	0.48	1.08
	Fe	0.06	-	-	0.06	0.03
	Cu	-	-	0.11	0.11	0.50
Fe_AA1	Si	0.08	0.11	0.10	0.29	0.32
	Mg	-	0.23	0.12	0.35	1.05
	Fe	0.12	-	-	0.12	0.08
	Cu	-	-	0.05	0.05	0.50

It is evident that the primary particles and the L phase consume most of the Si from the alloy composition. This also validates our assumption that there is no significant incorporation of Si in GPB zones. It is also clear that the higher amount of Fe in the Fe added alloy results in more α-AlFeSi(Cu)-particles locking up Si, causing a lower amount of Si to be available for hardening phase precipitation as compared to Std_AA1. This explains the lower number density and volume fraction of the L phase in Fe_AA1 compared to Std_AA1. A consequence of this is that significant amounts of Mg and Cu are remaining and available for precipitation of clusters and GPB zones or they are simply left in solid solution in the matrix or aggregated on grain boundaries or other defects.

Precipitation in the deformed conditions

To investigate the precipitation in the Std- and Fe alloys in the deformed conditions, SPED and HAADF-STEM imaging were done. Due to the high density of dislocations, conventional TEM techniques gave unsatisfactory results as the contrast from the dislocations masked out the contrast from the precipitates. The chosen techniques also yield information on the precipitate type, not attainable from any conventional imaging technique.

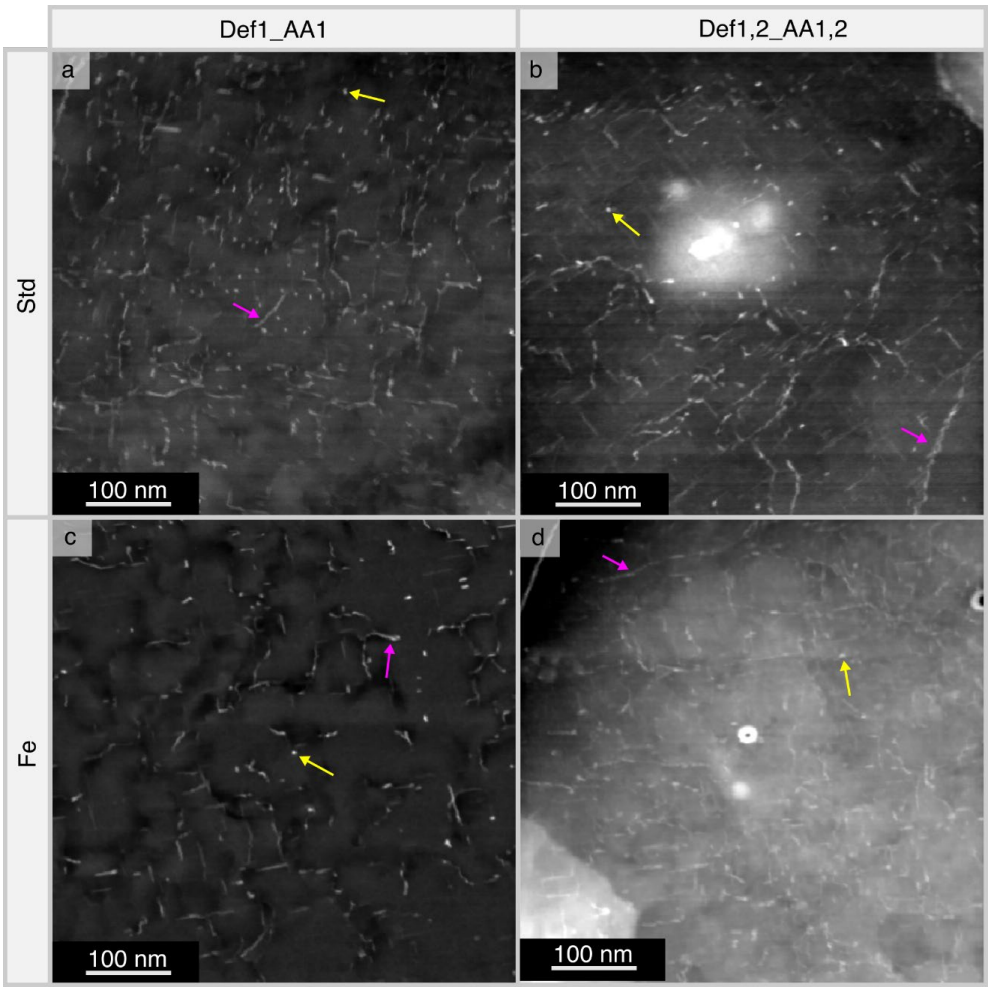

Figure 5: VDF images of the deformed conditions Def1_AA1 (a, c) and Def1,2_AA1,2 (b, d) for the Std (top)- and Fe (bottom) alloys. The yellow- and pink arrows indicate precipitation between and on deformation induced defects, respectively.

Figure 5 shows VDF images for the Def1_AA1 condition for Std and Fe in a and c, respectively. Figure 5b and d show VDF images for the Def1,2_AA1,2 condition for the Std and Fe alloy, respectively. The bright contrast stem from regions containing precipitates. It is assumed that all the elongated bright features arise from heterogeneous precipitation on deformation induced defects, e.g. on dislocation lines or subgrain boundaries. Examples of such precipitates are highlighted with the pink arrows. In addition, precipitation also occurs homogenously in the undistorted regions of the Al matrix, away from the deformation induced defects, exemplified by the yellow arrows. To get a more detailed insight into the effect of Fe on the precipitation in the deformed conditions, we aimed at differentiating between precipitates in the vicinity of deformation induced defects compared to precipitation in the bulk. I.e., quantification of the precipitates similar to the ones indicated by the pink arrows relative to the ones indicated by the yellow arrows in Figure 5. The approach is described in the Method section. In the following, the results for Def1_AA1 will be presented. For the Def1,2_AA1,2 condition, the microstructures for both alloys were too complex to be studied quantitatively. One challenge was the uneven background in the VDF images, evident in Figure 5b and

d. In addition, the PED patterns were less characteristic than in the Def1_AA1 condition, implying higher disorder in the precipitates in the Def1,2_AA1,2 condition. The SPED results from this condition will only be discussed qualitatively and phase identification using HAADF-STEM was performed.

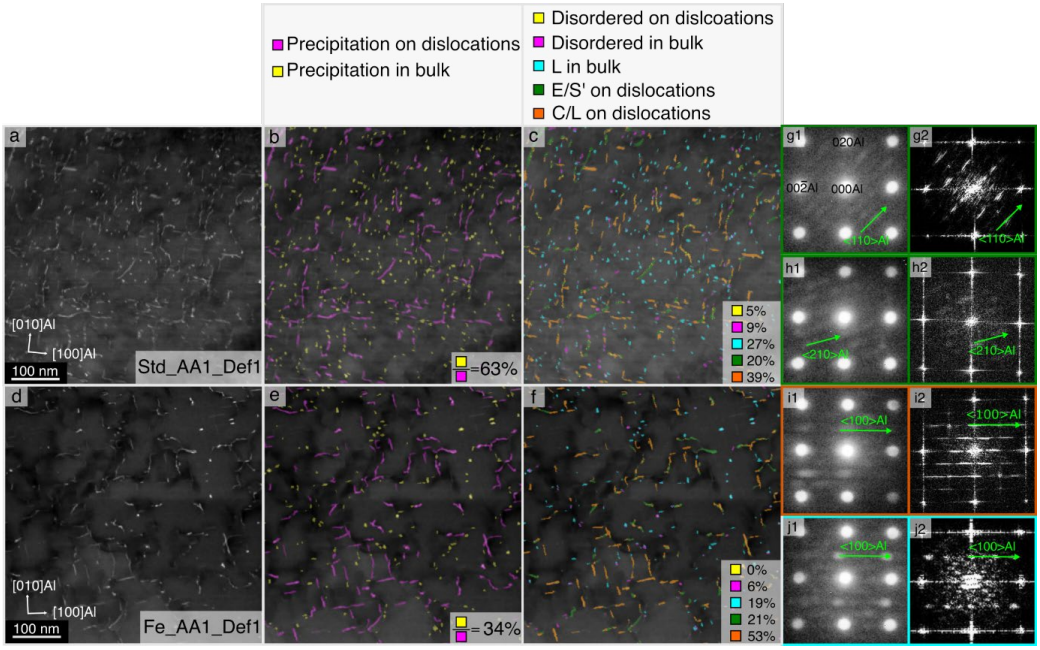

Figure 6: Results from the quantification of precipitates in the AA1_Def1 condition. a, d: VDF images from the Std- and Fe alloy, respectively. b, e: Quantification of precipitates on deformation induced defects, such as dislocations, compared to precipitation in the bulk. c, f: Phase mapping of the precipitates. g1, h1, i1, j1: Selected PED patterns from E-, S'-, C- and L phases, respectively. g2, h2, i2, j2: FFTs of E-, S-, C- and L phases, respectively. The FFTS in g2, i2 and j2 is taken from Ref. [4]*, while h2 is the FFT of Figure 7b. The colour scheme emphasizes how the different precipitates are categorized in the phase maps in c and f.*

Figure 6 shows the results from the precipitate quantification for Std_Def1_AA1 and Fe_Def1_AA1. The original VDF images are shown in a and d, while b and e show the results from the quantification of precipitation on dislocations (pink) compared to precipitation in the bulk (yellow). All percentages are given as area fractions. The results imply that the addition of Fe causes a higher fraction of precipitation to occur on deformation induced defects, since the relative area fraction of precipitation in bulk compared to on dislocations is 34% for the Fe alloy, as compared to 63% in the Std alloy.

The ordered, heterogeneously nucleated precipitates on dislocations were classified as E-, S'-, C- and L phases, while only the L phase and disordered structures were homogenously nucleated in the bulk. This is in accordance with our previous work on the Std alloy in a condition similar to the Def1_AA1 [4]. The phase maps in Figure 6c and f, for the Std- and Fe alloys, respectively, show that the same categories of precipitates were nucleated in both alloys. The precipitates are divided in five categories, based on their morphology and underlying PED pattern: Disordered precipitates, both on dislocations

and in the bulk, L in bulk, E or S' on dislocations and C or L on dislocations. NMF was unsuccessful in differentiating between the S'- and E- phase, probably due to a combination of weak signal and similarity of the two patterns. Examples of PED patterns from the E- and S' phase are shown in Figure 6g1 and h1, respectively. FFTs of HAADF-STEM images of the E and S' phase are shown in Figure 6g2 and h2, there is a good correspondence between the FFTs and PED patterns of these precipitates. Since both precipitates also appear extended in the VDF images, they could not be separated. However, both the S'- and E phases nucleate on deformation induced defects, hence this challenge is not hindering the quantification of the relative amount of precipitation on deformation induced defects compared to precipitation in the bulk. Examples of PED patterns originating from the L- and C phase are shown in Figure 6i1-j1, respectively. The patterns are similar and could not be separated by the NMF decomposition. This is not unexpected: Both phases have habit plane [001]Al and the L phase, although disordered, often contains local C symmetries. Based on their extent and the maximum Feret diameter [29], however, they could be separated during the postprocessing of the data.

To investigate which precipitate structures existed in the Def1,2_AA1,2 conditions, HAADF-STEM investigations were conducted to see the atomic structure of the precipitates. This was done for the Fe alloy. This was deemed sufficient, since there are clear indications that the addition of Fe does not affect which precipitate types nucleate, only their relative amounts. The results are shown in Figure 7. Both ordered and disordered precipitates were found. All the precipitates imaged were nucleated on dislocations. In a, an example of the C phase viewed along its [010] direction is shown. This was the most common type of ordered precipitates in this condition. The second type of ordered precipitate was the S' phase, an example is shown in b. The S' phase is known to preferentially nucleate on dislocations [14]. Most of the imaged precipitates however were disordered and these could be separated into three categories: 1) small, with well-defined cross-sections often containing local structural units of GPB zones, 2) hybrid Al-Mg-Si-Cu/Al-Mg-Cu precipitates and 3) large, disordered ones with wide cross sections. An example of the first category is shown in c. The local GPB symmetry is indicated by the blue dashed lines. In d, an example of a hybrid precipitate is shown. It consists of four distinct regions, marked by numbers in the figure. The segment enclosed by region 1 is the C phase viewed along its [001] direction, while the segment in region 2 corresponds to the S' phase. In region 3, the only instance for which the E phase [4] was found, is shown. The segment enclosed by region 4 is a disordered part of the structure. In Figure 7e, a disordered precipitate with wide cross section is shown.

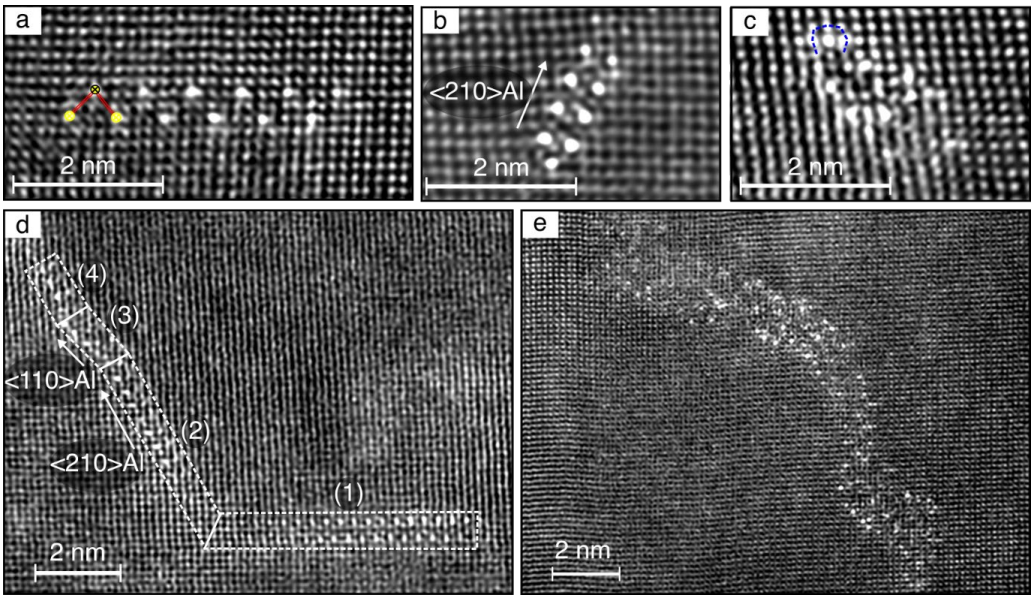

Figure 7: HAADF-STEM images of the precipitates found in Fe_Def1,2_AA1,2. a: C phase viewed along [010]C, its characteristic symmetry is indicated by the red lines. b: S' phase from the Al-Cu-Mg system. c: Disordered precipitate containing local GPB symmetries,. d: A hybrid precipitate containing the (1) C phase, (2) S' phase, (3) E phase and (4) disordering. e: Disordered precipitate with wide cross-section.

Hardness evolution and relation to microstructure

In the following, an assessment of the different mechanisms involved during each thermomechanical step will be elaborated. The discussion will be based on the TEM data from the deformed conditions, hardness measurements, the amount of Si locked in primary particles and direct observations of precipitate number densities in the undeformed conditions.

The hardness in each processing step for three different thermomechanical treatments was measured. The different thermomechanical treatments were Def1,2_AA1,2, Def1,2_AA2 and AA1,2 and the results are shown in Figure for both the Std- and Fe alloy.

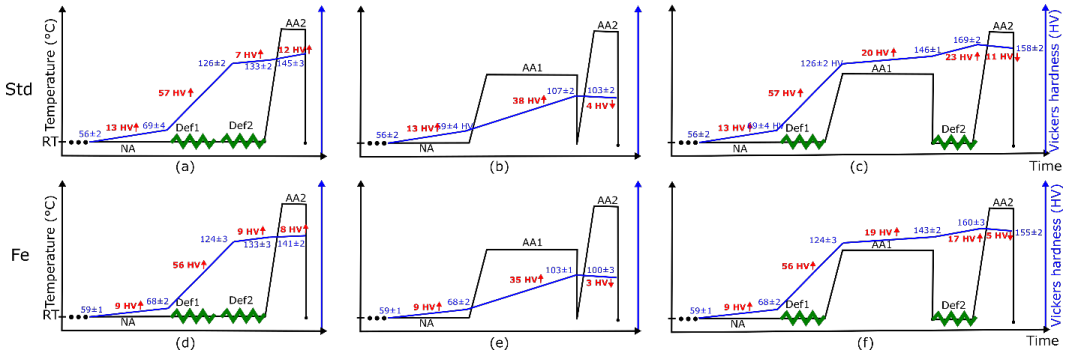

Figure 8: Hardness evolution for the two alloys in each step for 3 different thermomechanical processing routes: Def1,2_AA2 (a,d), AA1,2 (b,e) and Def1,2_AA1,2 (c, f). The top row shows hardness for the Std alloy, while the bottom row shows hardness for the Fe alloy.

During NA, the increase in HV is slightly higher in the Std alloy most likely due to the higher amount of Si available for precipitation in this alloy. It is well known that Si contributes to the clustering of solute atoms during NA and that the NA hardness increases with increasing Si content [35]. For the Def1,2_AA2 processing route shown in a and d for the Std- and Fe alloy, respectively, the Def1 and Def2 treatments yield similar increase in hardness. This indicates that the higher cluster density in the Std alloy does not affect the build-up of dislocations. Hence, the clusters are most likely shearable. This is reasonable considering their very small size. AA2 yields a higher hardness increase in the Std alloy compared to the Fe alloy, probably due to a higher number density of hardening phases following the higher amount of Si available for precipitation. Note that the hardness increases are similar, indicating that the effect of the small addition of Fe is not considerably detrimental.

The hardness for the processing route without deformation (AA1,2) is shown in Figure 8b and e for the Std and Fe alloy, respectively. After AA1, the Std alloy is slightly harder than the Fe alloy. Since the L phase is considered the main hardening precipitate in these alloys, the difference in the ageing response in the two alloys is attributed to the higher number density of the L phase in the Std alloy compared to the Fe alloy in this condition, c.f. Table 6. However, the difference in ageing response is not substantial. Thus, small additions of Fe are not particularly detrimental to the hardness in the T6 condition. During AA2, the hardness of both alloys decreases, indicating that the alloys are slightly overaged.

Hardness evolution for the Def1,2_AA1,2 processing route is shown in Figure 8c and f for the Std- and Fe alloy, respectively. The ageing response during AA1 in the pre-deformed condition is significantly reduced compared to the undeformed conditions as seen in Figure 8b, e. This is attributed to the reduction of homogeneous nucleation due to the high density of dislocations in the AA1_Def1 condition. Due to the higher diffusivity at dislocations and the favorable nucleation conditions at deformation induced defects, the precipitates on dislocations are coarser compared to the homogeneously nucleated precipitates [36,37]. It is evident from the phase maps in Figure 6c and f that the E-, S'- and C phases account for most of the precipitation on dislocations, while the homogeneously nucleated precipitates mostly consist of the L phase, which is also homogeneously nucleated in the undeformed samples, c.f. Figure 4.

The SPED data gave indications that the relative amount of homogeneous and heterogeneous nucleation differed in the two alloys, namely that the homogeneous nucleation was suppressed to a larger extent in the Fe alloy compared to the Std alloy. Teichmann *et al.* [38] found that for an Al-Mg-Si alloy, no homogeneous nucleation took place during the early stages of ageing of a 10% pre-deformed

sample. For the same alloy and pre-deformation, the authors found a small fraction of hardening phases homogeneously nucleated in the microstructure after prolonged ageing [39]. These observations confirm that the dislocations provide heterogeneous nucleation sites as well as changing the diffusivity by attracting vacancies, effectively changing the ageing kinetics. Solute atoms might also segregate at dislocations, creating a solute depleted region in the vicinity of the dislocations. Based on these observations, it is probable that the lower amount of Si available for precipitation in the Fe alloy leads to a higher fraction of heterogeneous precipitation compared to the Std alloy, since the dislocations can deplete the matrix both of solutes and vacancies. Homogeneous nucleation will be suppressed due to the fast nucleation of precipitates at the deformation-induced defects during the very early stages of AA and less Si will be available for homogeneous nucleation than in the Std alloy in the intermediate stages of AA. It is interesting to note that although there is a measurable microstructural difference in terms of precipitation between the alloys, the hardness response during AA1 after Def1 is similar between the two alloys. A material's hardness is its ability to resist deformation and is affected both by precipitates and dislocations. Based on our observations, it is probable that the heavy pre-deformation causes the contribution from the dislocations to the hardness to dominate compared to the differences observed in the precipitation. It is important to keep in mind that the precipitate fractions presented for the Def1_AA1 conditions are relative fractions, namely that we have not measured the absolute volume fractions of precipitates in the two alloys. It is, however, reasonable to assume that the volume fraction of precipitates is higher for the Std alloy than the Fe alloy, based on the precipitate statistics from the undeformed condition.

During the subsequent Def2 treatment following AA1_Def1, the hardness response is more prominent in the Std alloy compared to the Fe alloy. Since the hardness increase during Def2 was similar between the two alloys without AA1, see 8a and d, this must be attributed to a difference in the precipitate-dislocation interactions during deformation. Non-shearable precipitates are known to yield a higher work hardening due to the formation and storage of dislocation loops around the precipitates, effectively increasing the dislocation density [40]. This indicates that the Std alloy in the Def1_AA1 condition has a higher volume fraction of non-shearable precipitates than the Fe alloy. Assuming that the thicknesses of the regions in the VDF images in Figure 6a and d are similar, there is a larger fraction of precipitates nucleated in the Std alloy in this condition. This is a reasonable observation, since the α-AlFeSi(Cu) particles are unaffected by the deformation, effectively locking the same amount of Si solutes through all the processing steps.

Quantification of the microstructure in the AA1,2_Def1,2 condition was challenging, but qualitatively based on the HAADF-STEM observations exemplified in Figure 7 and VDF images in Figure 5b and d, we conclude that the microstructure in this condition mostly consists of heterogeneously nucleated precipitates, while a small amount of the precipitates is nucleated in the undistorted regions of the Al matrix. As the hardness decreases for both alloys during AA2, this is attributed to the dissolution and transformation of the homogeneously nucleated precipitates to heterogeneously nucleated precipitates. It is unclear whether the transformation is induced by Def2 or AA2 or a combination of these two.

In undeformed materials, the amount of precipitates is very important for the material's final properties. In the present study, the higher amount of L phase in the Std_AA1 condition contributed to a higher peak hardness than in the Fe_AA1. If, however, the material was deformed prior to AA1, the hardness increase during AA1 was similar. We can therefore conclude that with pre-deformation, the effect of Fe will be less detrimental to the mechanical properties of the material. By doing a second deformation and AA treatment, Def2 and AA2, the detrimental effect of Fe on the mechanical

properties is again increased, due to the lower amount of non-shearable precipitates nucleated on dislocations, yielding a lower work hardening response.

Conclusions

In summary, this study has investigated the effect of small additions of Fe on precipitation in an undeformed, and a heavily deformed Al-Mg-Si-Cu alloy. The samples were deformed twice: One deformation treatment of 80% prior to AA for 5 h at 160°C was followed by a subsequent deformation of 50% and a second AA for 10 min at 180°C to produce the final condition. The main findings include:

1. The microstructure of the undeformed samples consists of Mg_2Si- and α-AlFeSi primary particles, L phase and structural units of GPB zones. A higher amount of α-AlFeSi prevailed in the Fe added alloy decreasing the Si level available for the precipitation of hardening precipitates. The consequence was a lower number density and lower volume fraction of the L phase. This had a small, negative influence on the hardness of the Fe added alloy as compared to the standard alloy in the undeformed condition.
2. The addition of Fe affected the precipitation during artificial ageing after the first pre-deformation. The precipitation in the Fe alloy was more heterogeneous compared to the Std alloy. This was attributed to the lower amount of Si available for precipitation in this alloy. The precipitate types in the vicinity of deformation induced defects were C-, E-, S' and disordered precipitates, while the precipitation in bulk was dominated by the L phase for both alloys.
3. The precipitate types in the final condition were the ordered C-, E- and S' phases and disordered structures.
4. The hardness increase during the second deformation is highest in the standard alloy, suggesting that this condition contains a higher fraction of non-shearable precipitates as compared to the Fe added alloy.

Acknowledgements

This work was supported by the INTPART project 'Norwegian-Japanese Aluminium alloy Research and Education Collaboration Phase-2' (grant number 287965) financed by The Research Council of Norway (RCN). The (S)TEM work was carried out on the *NORTEM* (grant number 197405) infrastructure at the TEM Gemini Centre, Trondheim. E.T. and R.H. acknowledge the AllDesign project/NTNUs Digitalisation Initiative.

Data availability

The raw data required to reproduce these findings are available to download from 10.5281/zenodo.5636674.

Conflict of interest statement

On behalf of all authors, the corresponding author states that there is no conflict of interest.

References

1 C.D. Marioara, S.J. Andersen, T.N. Stene, H. Hasting, J. Walmsley, A.T.J. van Helvoort, and R. Holmestad: *Philosophical Magazine*, 2007, vol. 87, pp. 3385–413.

2 T. Saito, E.A. Mørtsell, S. Wenner, C.D. Marioara, S.J. Andersen, J. Friis, K. Matsuda, and R. Holmestad: *Advanced Engineering Materials*, 2018, vol. 20, p. 1800125.

3 J.K. Sunde, C.D. Marioara, and R. Holmestad: *Materials Characterization*, 2020, vol. 160, p. 110087.

4 E. Thronsen, C.D. Marioara, J.K. Sunde, K. Minakuchi, T. Katsumi, I. Erga, S.J. Andersen, J. Friis, K. Marthinsen, K. Matsuda, and R. Holmestad: *Materials and Design*, 2020, vol. 186, p. 108203.

5 C. Cayron, L. Sagalowicz, L. Sagalowicz, and P.A. Buffat: *Philosophical Magazine A: Physics of Condensed Matter, Structure, Defects and Mechanical Properties*, 1999, vol. 79, pp. 2833–51.

6 S.J. Andersen, C.D. Marioara, R. Vissers, A. Frøseth, and H.W. Zandbergen: *Materials Science and Engineering A*, 2007, vol. 444, pp. 157–69.

7 T. Saito, C.D. Marioara, S.J. Andersen, W. Lefebvre, and R. Holmestad: *Philosophical Magazine*, 2014, vol. 94, pp. 520–31.

8 S.J. Andersen, C.D. Marioara, J. Friis, R. Bjørge, Q. Du, I.G. Ringdalen, S. Wenner, E.A. Mørtsell, R. Holmestad, T. Saito, J. Røyset, and O. Reiso: *Materials Science Forum*, 2017, vol. 877, pp. 461–70.

9 O. Reiso, N. Ryum, and J. Strid: *Metallurgical Transactions A*, 1993, vol. 24, pp. 2629–41.

10 G. Sha, K. O'Reilly, and B. Cantor: *Materials Science Forum*, 2006, vol. 519–521, pp. 1721–6.

11 H. Tanihata, T. Sugawara, K. Matsuda, and S. Ikeno: *Journal of Materials Science*, 1999, vol. 34, pp. 1205–10.

12 M.S. Remøe, K. Marthinsen, I. Westermann, K. Pedersen, J. Røyset, and C. Marioara: *Materials Science and Engineering A*, 2017, vol. 693, pp. 60–72.

13 T. Furu, N. Telioui, C. Behrens, J. Hasenclever, and P. Schaffer: *Proceedings of the 12 ICAA*, 2010, pp. 282–9.

14 M. Mihara, C.D. Marioara, S.J. Andersen, R. Holmestad, E. Kobayashi, and T. Sato: *Materials Science and Engineering A*, 2016, vol. 658, pp. 91–8.

15 L. Kovarik, S.A. Court, H.L. Fraser, and M.J. Mills: *Acta Materialia*, 2008, vol. 56, pp. 4804–15.

16 J.A. Mir, R. Clough, R. MacInnes, C. Gough, R. Plackett, I. Shipsey, H. Sawada, I. MacLaren, R. Ballabriga, D. Maneuski, V. O'Shea, D. McGrouther, and A.I. Kirkland: *Ultramicroscopy*, 2017, vol. 182, pp. 44–53.

17 J.S. Barnard, D.N. Johnstone, and P.A. Midgley: *Ultramicroscopy*, 2017, vol. 174, pp. 79–88.

18 J. Schindelin, I. Arganda-Carreras, E. Frise, V. Kaynig, M. Longair, T. Pietzsch, S. Preibisch, C. Rueden, S. Saalfeld, B. Schmid, J.Y. Tinevez, D.J. White, V. Hartenstein, K. Eliceiri, P. Tomancak, and A. Cardona: *Nature Methods*, 2012, 9, vol. 9.

19 H.W. Ånes: Metallography-notebooks, https://github.com/hakonanes/metallography-notebooks/blob/master/particle_size_distribution_from_bse_image/particle_size_distribution_from_bse_image.ipynb, (accessed June 22, 2020).

20 S.J. Andersen: *Metallurgical and Materials Transactions A*, 1995, vol. 26, pp. 1931–7.

21 M. Cooper: *Acta Crystallographica*, 1967, vol. 23, pp. 1106–7.

22 In *Non-Tetrahedrally Bonded Elements and Binary Compounds I*, Springer-Verlag, 2005, pp. 1–4.

23 H. Tvedt, C.D. Marioara, E. Thronsen, C. Hell, S.J. Andersen, and R. Holmestad: *Ultramicroscopy*, 2022, p. 113493.

24 F. de la Peña, E. Prestat, V.T. Fauske, P. Burdet, T. Furnival, P. Jokubauskas, M. Nord, T. Ostasevicius, J. Lähnemann, K.E. MacArthur, D.N. Johnstone, M. Sarahan, J. Taillon, T. Aarholt, pquinn-dls, V. Migunov, A. Eljarrat, J. Caron, T. Poon, S. Mazzucco, B. Martineau, S. Somnath, T. Slater, C. Francis, actions-user, M. Walls, N. Tappy, N. Cautaerts, F. Winkler, and G. Donval: DOI:10.5281/ZENODO.4923970.

25 D.N. Johnstone, P. Crout, M. Nord, J. Laulainen, S. Høgås, EirikOpheim, B. Martineau, C. Francis, T. Bergh, E. Prestat, S. Smeets, andrew-ross1, S. Collins, I. Hjorth, Mohsen, T. Furnival, D. Jannis, N. Cautaerts, E. Jacobsen, AndrewHerzing, T. Poon, H.W. Ånes, J. Morzy, S. Huang, phillipcrout, T. Doherty, affaniqbal, T. Ostasevicius, mvonlany, and R. Tovey: 2021.

26 S. van der Walt, J.L. Schönberger, J. Nunez-Iglesias, F. Boulogne, J.D. Warner, N. Yager, E. Gouillart, T. Yu, and the scikit-image contributors: *PeerJ*, 2014, vol. 2, p. e453.

27 S.R. Sternberg: *Computer*, 1983, vol. 16, pp. 22–34.

28 Z. GW, R. WE, and L. SA: *The journal of histochemistry and cytochemistry : official journal of the Histochemistry Society*, 1977, vol. 25, pp. 741–53.

29 H.G. Merkus: *Particle Size Measurements*, 2009, pp. 13–42.

30 D.D. Lee and H.S. Seung: *Nature*, 1999, vol. 401, pp. 788–91.

31 J.K. Sunde, C.D. Marioara, A.T.J. van Helvoort, and R. Holmestad: *Materials Characterization*, 2018, vol. 142, pp. 458–69.

32 E. Linardi, R. Haddad, and L. Lanzani: *Procedia Materials Science*, 2012, vol. 1, pp. 550–7.

33 M. Torsæter, F.J.H. Ehlers, C.D. Marioara, S.J. Andersen, and R. Holmestad: *Philosophical Magazine*, 2012, vol. 92, pp. 3833–56.

34 C.D. Marioara, S.J. Andersen, J. Røyset, O. Reiso, S. Gulbrandsen-Dahl, T.E. Nicolaisen, I.E. Opheim, J.F. Helgaker, and R. Holmestad: *Metallurgical and Materials Transactions A: Physical Metallurgy and Materials Science*, 2014, vol. 45, pp. 2938–49.

35 M. Werinos, H. Antrekowitsch, T. Ebner, R. Prillhofer, P.J. Uggowitzer, and S. Pogatscher: *Materials & Design*, 2016, vol. 107, pp. 257–68.

36 J.D. Embury, A. Deschamps, and Y. Brechet: *Scripta Materialia*, 2003, vol. 49, pp. 927–32.

37 T. Saito, S. Muraishi, C.D. Marioara, S.J. Andersen, J. Røyset, and R. Holmestad: *Metallurgical and Materials Transactions A 2013 44:9*, 2013, vol. 44, pp. 4124–35.

38 K. Teichmann, C.D. Marioara, S.J. Andersen, K.O. Pedersen, S. Gulbrandsen-Dahl, M. Kolar, R. Holmestad, and K. Marthinsen: *http://dx.doi.org/10.1080/14786435.2011.593577*, 2011, vol. 91, pp. 3744–54.

39 K. Teichmann, C.D. Marioara, S.J. Andersen, and K. Marthinsen: *Metallurgical and Materials Transactions A*, 2012, vol. 43, pp. 4006–14.

40 W.J. Poole, X. Wang, D.J. Lloyd, and J.D. Embury: *Philosophical Magazine*, 2005, vol. 85, pp. 3113–35.

Paper VI

Scanning precession electron diffraction data analysis approaches for phase mapping of precipitates in aluminium alloys

E. Thronsen, T. Bergh, T. I. Thorsen, E. F. Christiansen, J. Frafjord, P. Crout, A. T. J. van Helvoort, P. A. Midgley, R. Holmestad

To be submitted

Author contributions

E. Thronsen developed the neural network approach. E. F. Christiansen acquired the TEM- and SPED data. T. Bergh and J. Frafjord implemented the vector-based approach. T. I. Thorsen did the template matching. E. F. Christiansen did the NMF decomposition and analysed the decomposed dataset. P. Crout assisted in the development of the neural network approach. A. T. J. Helvoort, P. A. Midgley and R. Holmestad supervised the research. E. Thronsen, T. Bergh, E. F. Christiansen and R. Holmestad initiated the study. E. Thronsen wrote the initial manuscript. T. Bergh, T. I. Thorsen and E. F. Christiansen significantly contributed to the writing of the initial manuscript. All co-authors commented on the final manuscript.

ISBN 978-82-326-6788-8 (printed ver.)
ISBN 978-82-326-5977-7 (electronic ver.)
ISSN 1503-8181 (printed ver.)
ISSN 2703-8084 (online ver.)

NTNU

Norwegian University of
Science and Technology